FLOW-FIELD IN A LINEAR CASCADE OF FILLETED VANES WITH ENDWALL FILM-COOLING

UNIVERSITEIT VAN PRETORIA
UNIVERSITY OF PRETORIA
YUNIBESITHI YA PRETORIA

Barbara Barbieri Huyssen

Submitted in partial fulfilment of the requirements for the degree

DOCTOR OF PHILOSOPHY

In Engineering

in the Department of Mechanical and Aeronautical Engineering

University of Pretoria

Supervisor: Dr G.I. Mahmood

Co-Supervisor: Prof J.P. Meyer

February 2022

To my son

La vita non è aspettare che passi la tempesta, ma imparare a ballare sotto la pioggia.

(Mahatma Gandhi)

Abstract

The optimum performance of the turbine, while adhering to certain design limitations, is to improve the aerothermal performance of axial flow turbines by reducing the total pressure losses and increasing the film-cooling coverage on the endwall of the blade and vane passages. The secondary flows near the passage endwall and film-cooling hole configurations in the endwall primarily increase the passage aerodynamic losses. According to previous studies, a leading-edge fillet, which fills the intersection of the nozzle guide vane (NGV) and the endwall, has the potential to mitigate the secondary flows. The film flow coverage on the endwall from the endwall coolant holes is also negatively affected by the secondary flows. Past investigations indicate that the interactions between the endwall secondary flows and cooling flows drag the cooling flow towards the passage suction-side and away from the endwall region leaving the pressure-side endwall unprotected from the hot combustion gas. The interactions of secondary flows with film-cooling flow often add to the total pressure losses. This thesis experimentally investigated the detailed flow field in a filleted vane cascade, employing endwall film-cooling flow. The objectives were: (i) to mitigate the endwall secondary flows in the vane passage through the benefit of a leading-edge fillet, (ii) to combine the effects of fillet with the effects of some new configurations of the leading-edge coolant holes in the endwall in order to cover the pressure-side of the passage endwall with the coolant flow, and (iii) to reduce the total pressure losses in the passage when employing film-cooling flow.

The experiments were performed in a low-speed linear vane cascade, employing the GE-E^3 first-stage nozzle guide vane profile. A new leading-edge fillet configuration was used as a method of mitigating the negative effects of the endwall secondary flows and film-cooling flow on the total pressure losses. The film cooling flow was delivered through the holes located in the endwall, upstream of the cascade as well as inside the cascade passage. The upstream coolant hole configurations included continuous and discontinuous slots, discrete cylindrical holes, and cylindrical holes with diffused exits. The passage endwall employed discrete cylindrical holes at the non-zero compound angles along an isobar line. The injection angle of all the coolant hole configurations was 30° relative to the main flow. The inlet Reynolds number of the main flow was 2.0 E+05 based on the vane chord. The average blowing ratio of the film-cooling flow ranged from 1.2 to 2.8 and the temperature ratio and the density ratio of the coolant to main flow were 0.94 and 1.05 respectively. Measurements of the flow field were obtained in four pitch-wise normal planes along the cascade passage and presented as the velocity vectors, vorticity vectors, flow angles, total pressure losses and flow temperatures. The results included baseline data with and without fillet and film-cooling flow to evaluate the effects of fillet without film-cooling flow, the effects of film-cooling configurations without fillet, and the effects of fillet combined with film-cooling flow.

The main observations from the measurements were as follows:

- The fillet reduced the total pressure losses in the vane passage because it weakened the passage vortex in the endwall region.
- The distribution of flow temperature showed that the presence of film cooling in the endwall region is better with LE discrete cylindrical holes and LE slots compared to other cases. When the coolant was added to the passage holes, the LE discrete cylindrical hole/slot film-cooling configuration still performed better than the other cooling configurations because the coolant slipped under the boundary layer separation region, cooling the entire endwall. The worst cooling behaviour was noticed for the LE discrete cylindrical hole configurations with the fillet and passage coolant holes. The coolant penetrated into the mainstream higher above the endwall before the endwall boundary layer separation region than when the LE diffused hole configuration was employed at all blowing ratios. The maximum increase in the $(C_{pt,loss})_{Mass\text{-}av}$ of the LE discrete cylindrical holes and LE slots cooling configuration is by about 40%

at M=1.4. The maximum decrease in the $(C_{pt,loss})_{Mass\text{-}av}$ of the LE diffused cylindrical holes cooling configuration is by about 11% at M=1.2

- The LE discrete diffused hole configuration provided the best performance without the filleted vanes. For the baseline configuration, the diffused cylindrical holes, with the passage coolant holes, provided slightly better performances than for the configuration provided by the LE cylindrical holes in terms of the spread of coolant coverage along the endwall, less turning of streamline coolant flows towards the suction-side, and reducing the pressure losses along the passage.

The LE discrete cylindrical holes/slots with the fillet and passage coolant hole configuration showed a higher reduction in total pressure losses and exhibited the best cooling ability for pitch-wise (PS-SS) coolant spread.

Keywords: LE fillet, film-cooling, secondary flows, nozzle guide vane, passage loss.

Publication in journals and conference proceedings

This research produced the following articles and conference papers:

- **Journal articles**

  A. S. Shote, B. Huyssen, and G. I. Mahmood, "Heat transfer and slot film-cooling effectiveness on endwall in a filleted vane cascade," International Journal of Heat and Mass Transfer, HMT-2020-776, 2020. (Under review)

- **Conference papers**
  - B. Huyssen, A. S. Shote and G. I. Mahmood, "Computational investigation of flow structure in a linear vane blade cascade with filleted endwall," Proceedings of the International Aerospace Symposium of South Africa, Pretoria, South Africa, 2016.
  - B. Huyssen and G. I. Mahmood "Flow-fields for upstream film-cooling configuration in a vane cascade," HEFAT, Wicklow, Ireland, 2019.
  - B. B. Huyssen and G. I. Mahmood, "Effects of cylindrical-hole shape and fillet on flow and temperature fields in vane cascade with endwall film-cooling," Proceedings of ASME Turbo Expo Turbomachinery Technical Conference and Exposition, London, England, GT2020-14099, 2020.

TABLE OF CONTENTS

Abstract i

Publication in journals and conference proceedings iii

LIST OF FIGURES vi

LIST OF TABLES ix

NOMENCLATURE x

Subscripts xi

Special characters xi

1. Introduction 1

1.1. Background 1

1.2. Description of the secondary flow phenomena 2

1.3. Motivation 5

1.4. Objectives 5

1.5. Thesis structure 5

2. Film-cooling technologies 6

2.1. Introduction 6

2.2. Film-cooling mass flow rate and injection angle 6

2.3. Film-cooling injection geometry 7

2.4. Leading-edge cooling 9

2.5. Endwall cooling 9

2.6. Contouring endwall effect on film-cooling 10

2.7. Fillet and film-cooling interaction 10

2.8. Closure 11

3. Fillet design 13

4. Experimental design and methodology 16

4.1. Low-speed test cascade 16

4.2. Fillet design 19

4.3. Film-cooling design 21

5. Data acquisition system and uncertainty estimates 25

5.1. Overview 25

5.2. Pressure probe measurements 26

5.3. Temperature field 29

5.4. Uncertainty analysis 30

5.4.1. Instrumentation 30

5.4.2. Pressure transducers 30

5.4.3. Thermocouples 31

5.4.4. Measurement system errors: calculated results 31

5.4.5. Five-hole probe 31
5.4.6. Local velocity and axial vorticity 33
5.4.7. Reference velocity 34
5.4.8. Coefficient of total pressure 34
5.4.9. Film-cooling inlet blowing ratio 35
5.4.10. Film-cooling flow rate 35
5.4.11. Non-dimensional temperature 35
5.5 Test matrix 36
6. Results and discussion 38
6.1. Experimental test cases of non-cooled cascade 38
6.1.1. Leading-edge contour study 38
6.2. Experimental test cases of cooled cascade 41
6.2.1. Leading-edge film-cooling 41
6.2.2. Vane Cascade 42
6.2.3. Filleted vane cascade 55
6.2.4. Filleted vane cascade with endwall film-cooling holes 58
7. Conclusions 87
7.1 Leading-edge contours 87
7.2 Effect of LE cooling configurations 87
7.3 Benefit of endwall coolant ejection within the passage 89
7.4 Suggestion for further research 90
REFERENCES 91
APPENDICES 98
APPENDIX A: FIVE-HOLE PROBE CALIBRATION 98
APPENDIX B: UNCERTAINTY CALCULATIONS 99
B.1 Pressure transducers uncertainty example calculation 99
B.2 Measurement system errors: calculated results 101
B.2.1 Five-hole probe 101
B.2.2 Local velocity and axial vorticity 105
B.2.3 Reference velocity 107
B.2.4 Coefficient of static and total pressure 107
B.2.5 Film-cooling inlet blowing ratio 108
B.2.6 Film-cooling flow rate 109
B.2.7 Non-dimensional temperature 110
APPENDIX C: SUPPLEMENTARY RESULTS 111
C.1 Discharge coefficient 111
C.2 Pitch angle contours 111
C.3 Total pressure coefficient contours 114

LIST OF FIGURES

Figure 1: *a) Endwall film-cooling, Friedrichs et al. [2], b) cooling film ejection, Wilfert and Fottner [3].* 1
Figure 2: *Schematic view of the vortical structures in the vicinity of a jet in cross-flow, Haas et al. [4].* 2
Figure 3: *a) Formation of leading-edge horseshoe vortex, b) separation lines at the endwall ahead of LE [5].* 3
Figure 4: *Vortex structure described in the literature:* (a) *1985, Langston model[6]*, (b) *1987, Sharma and Butler model [7]*, (c) *1997, Endwall Vortex structure illustrated by Wang et al. [8]*, (d) *2001, Moon and Koh [9].* 4
Figure 5*: Cooling film ejection from low to high blowing ratio, Roux [18].* 7
Figure 6*: Types of film-cooling hole geometries, Saumweber and Schulz [20].* 8
Figure 7: *Leading-edge fillet profile:(a) Sauer at al. [56], (b) Zess and Thole [57], (c) Becz et al. [58], (d) Mahmood et al. [61].* 14
Figure 8: *Experimental set-up: a) linear vane cascade, and b) measurement planes with global coordinates (X_G, Y_G, Z_G) and local coordinates (x, y, z).* 16
Figure 9: *Multiport manual scanning valve connection to wall pressure taps and pressure transducer.* 17
Figure 10: *a) Pressure taps at blade mid-span and b) comparison of static pressure distribution on the central blades.* 18
Figure 11: *Fillet geometry.* 19
Figure 12: *a) Fillet 2, b) Fillet 1 geometry and c) Fillet side view.* 20
Figure 13: *Cooling flow circuit.* 21
Figure 14: *Geometry of film-cooling configurations in mm: Case A) bleed slots, Case B) slots and holes, Case C) cylindrical holes, Case D) diffused cylindrical holes.* 22
Figure 15: *Cross-section of film-cooling configurations: a) slots, b) cylindrical holes, c) diffused cylindrical holes.* 23
Figure 16: *a) Layout of passage endwall film-cooling holes along the isobar lines and inviscid streamlines, b) isobar lines obtained by CFD study and c) cross section of endwall film cooling.* 24
Figure 17: *Schematic of the instrumentation layout.* 25
Figure 18*: Tip of the five-hole pressure probe.* 27
Figure 19: *Definition of pitch and yaw angle for the five-hole pressure probe.* 27
Figure 20: *Example of measurement points and the results of the total pressure coefficient $C_{pt,\ loss}$ contour lines at the exit plane.* 28
Figure 21: *Temperature probe sketch.* 29
Figure 22: *⊿Yaw data for a) baseline, b) Fillet 1 and c) Fillet 2 in third plane at Xg/C_{ax}=0.58.* 38
Figure 23: *Total pressure loss coefficient for a) baseline, b) Fillet 1 and c) Fillet 2 in third plane at X_g/C_{ax}=0.58.* 39
Figure 24: *⊿Yaw data for a) baseline, b) Fillet 1 case, and b) Fillet 2 case in the exit plane at X_g/C_{ax}=1.04.* 40
Figure 25: *Total pressure loss coefficient for a)baseline, b) Fillet 1 case and c) Fillet 2 case in the exit plane at X_g/C_{ax}=1.04.* 41
Figure 26: *Cooling configurations: four bleed-cooling slots (A), two bleed cooling slots and cylindrical holes (B-2A), two bleed-cooling slots and partially open cylindrical holes (B-2B), two bleed-cooling slots and cylindrical holes with Fillet 1 (B-3A), two bleed-cooling slots and cylindrical holes with Fillet 2 (B-3B), two bleed-cooling slots (B-3C), cylindrical holes (C), diffused cylindrical holes (D).* 41
Figure 27: *Contours of yaw angle deviation in third plane for cases: four slots (Case A), two bleed-cooling slots and cylindrical holes (Case B-2A), two bleed-cooling slots with cylindrical holes partially closed (Case B-2B), cylindrical holes (Case C-1) and diffused cylindrical holes (Case D-1) at M=1.8.* 43
Figure 28: *Contours of yaw angle deviation in third plane for cases: four slots (Case A), two bleed-cooling slots and cylindrical holes (Case B-2A), two bleed-cooling slots with cylindrical holes partially closed (Case B-2B), cylindrical holes (Case C-1) and diffused cylindrical holes (Case D-1) at M=2.2.* 44
Figure 29: *Total pressure loss coefficient, $C_{pt,\ loss}$ contours in third plane for cases: four slots (Case A), two bleed cooling slots and cylindrical holes (Case B-2A), two bleed cooling slots with cylindrical holes partially closed (Case B-2B), cylindrical holes (Case C-1) and diffused cylindrical holes (Case D-1) at M=1.8.* 45
Figure 30: *Total pressure loss coefficient, $C_{pt,\ loss}$ contours in third plane for cases: four slots (Case A), two bleed cooling slots and cylindrical holes (Case B-2A), two bleed cooling slots with cylindrical holes partially closed (Case B-2B), cylindrical holes (Case C-1) and diffused cylindrical holes (Case D-1) at M=2.2.* 46
Figure 31*: Total pressure loss coefficient, $C_{pt,\ loss}$ contours in the exit plane for two slots Case B-3C, cylindrical holes Case C-1, and diffused cylindrical holes Case D-1 at M=2.2.* 47
Figure 32: *Comparison of mass-averaged total pressure loss coefficient $(C_{pt,\ loss})_{mass\text{-}av}$ in the exit plane as blowing ratio, M, varies.* 48

Figure 33: *Comparison of mass-averaged total pressure loss coefficient ($C_{pt,\ loss})_{mass\text{-}av}$/MFR in the exit plane as blowing ratio, M, varies.* 48
Figure 34: *Distributions of non-dimensional axial velocity, u*=u/U near endwall in third plane at M=1.8: baseline no cooling, four slots Case A, two bleed cooling slots and cylindrical holes Case B-2A and two LE bleed cooling slots and cylindrical holes partially closed Case B-2B, cylindrical holes Case C-1, diffused cylindrical holes Case D-1* 50
Figure 35: *Distributions of non-dimensional axial velocity, u*=u/U near endwall in third plane at M=2.2: Four slots Case A, two bleed cooling slots and cylindrical holes Case B-2A and two LE bleed cooling slots and cylindrical holes partially closed Case B-2B, cylindrical holes Case C-1, diffused cylindrical holes Case D-1.* 51
Figure 36: *Contours of non-dimensional temperature (θ) distribution in the first plane for M=1.8: bleed slots Case A, cylindrical holes Case C-1, diffused cylindrical holes Case D-1.* 52
Figure 37: *Contours of non-dimensional temperature (θ) distribution in the first plane for M=2.2: bleed slots Case A, cylindrical holes Case C-1, diffused cylindrical holes Case D-1.* 52
Figure 38: *Contours of non-dimensional temperature (θ) distribution in the second plane for M=1.8: bleed slots Case A, cylindrical holes Case C-1, diffused cylindrical holes Case D-1.* 53
Figure 39: *Contours of non-dimensional temperature (θ) distribution in the second plane for M=2.2: bleed slots Case A, cylindrical holes Case C-1, diffused cylindrical holes Case D-1.* 53
Figure 40: *Contours of non-dimensional temperature (θ) distribution in third plane for M=1.8: bleed slots Case A, cylindrical holes Case C-1, diffused cylindrical holes Case D-1.* 54
Figure 41: *Contours of non-dimensional temperature (θ) distribution in third plane for M=2.2: bleed slots Case A, cylindrical holes Case C-1, diffused cylindrical holes Case D-1.* 54
Figure 42: *Cooling configurations: two bleed cooling slots - Fillet 1 Case B-3A, two bleed cooling slots and cylindrical holes Fillet 2 Case B-3B and baseline two bleed cooling slots Case B-3C.* 55
Figure 43: *Distributions of flow yaw angle deviation in third plane for baseline Case B-3C, Fillet 1 Case B-3A, and Fillet 2 Case B-3B at M=1.4.* 56
Figure 44: *Distributions of flow yaw angle deviation in third plane for baseline Case B-3C, Fillet 1 Case B-3A, and Fillet 2 Case B-3B at M=2.2.* 56
Figure 45: *Distributions of total pressure loss coefficient, Cpt, loss in third plane for baseline for Fillet 1 Case B-3A, Fillet 2 Case B-3B, baseline Case B-3C at M=1.4.* 57
Figure 46: *Distributions of total pressure loss coefficient, Cpt, loss in third plane for baseline Case B-3B, Fillet 1 Case B-3A, and Fillet 2 Case B-3B at M=2.2.* 57
Figure 47: *Cooling configurations: only passage cooling holes (E), two bleed cooling slots and cylindrical holes, passage cooling holes and fillet (B-4), cylindrical holes, passage cooling holes and fillet (C-4), diffused cylindrical holes, passage cooling holes and fillet, (D-4), cylindrical holes and (C-5), partially open cylindrical holes and passage cooling holes (C-6), diffused cylindrical holes and passage cooling holes (D-5), partially open diffused cylindrical holes and passage cooling holes (D-6).* 58
Figure 48: *⊿Yaw data in third plane: configuration Case C-5 a) M=1.4, b) M=2.4.* 60
Figure 49: *⊿Yaw data in third plane: configuration Case D-5 a) M=1.4, b) M=2.4.* 60
Figure 50: *⊿Yaw data in third plane: configuration Case E a) M=1.4, b) M=2.4.* 61
Figure 51*: ⊿Yaw data in third plane: configuration Case B-4 a) M=1.4, b) M=2.4.* 61
Figure 52: *⊿Yaw data in third plane: configuration Case C-4 a) M=1.4, b) M=2.4.* 62
Figure 53: *⊿Yaw data in third plane: configuration Case D-4 a) M=1.4, b) M=2.4.* 62
Figure 54*: ⊿Yaw data in exit plane: configuration Case C-5 a) M=1.2, b) M=2.4, c) M=2.8.* 63
Figure 55*: ⊿Yaw data in exit plane: configuration Case D-5 a) M=1.2, b) M=2.4, c) M=2.8.* 63
Figure 56: *⊿Yaw data in exit plane: configuration Case E a) M=1.2, b) M=2.4, c) M=2.8.* 64
Figure 57: *⊿Yaw data in exit plane: configuration Case B-4 a) M=1.2, b) M=2.4, c) M=2.8.* 64
Figure 58: *⊿Yaw data in exit plane: configuration Case C-4 a) M=1.2, b) M=2.4, c) M=2.8.* 64
Figure 59: *⊿Yaw data in exit plane: configuration Case D-4 a) M=1.2, b) M=2.4, c) M=2.8.* 65
Figure 60: *Total pressure loss coefficient, $C_{pt,\ loss}$ contours for Case C-5, in third plane, a) M=1.2, b) M=1.8, c) M=2.4.* 65
Figure 61: *Total pressure loss coefficient, $C_{pt,\ loss}$ contours for Case D-5, in third plane, a) M=1.2, b) M=1.8, c) M=2.4.* 66
Figure 62: *Total pressure loss coefficient, $C_{pt,\ loss}$ contours for Case E, in third plane, a) M=1.2, b) M=1.8, c) M=2.4.* 66
Figure 63: *Total pressure loss coefficient, $C_{pt,\ loss}$ contours for Case B-4, in third plane, a) M=1.2, b) M=1.8, c) M=2.4.* 67
Figure 64: *Total pressure loss coefficient, $C_{pt,\ loss}$ contours for Case C-4, in third plane, a) M=1.2, b) M=1.8, c) M=2.4.* 67
Figure 65: *Total pressure loss coefficient, $C_{pt,\ loss}$ contours for Case D-4, in third plane, a) M=1.2, b) M=1.8, c) M=2.4* 68

Figure 66: *Total pressure loss coefficient, $C_{pt,\ loss}$ contours in exit plane for Case C-5 a) M=1.2, b) M=2.4.* 69
Figure 67: *Total pressure loss coefficient, $C_{ptot,\ loss}$ contours in exit plane for Case D-5 a) M=1.2, b) M=2.4.* 69
Figure 68: *Total pressure loss coefficient, $C_{pt,\ loss}$ contours in exit plane for Case E, a) M=1.2, b) M=2.4.* 69
Figure 69: *Total pressure loss coefficient, Cpt, loss contours in exit plane for Case B-4, Slot-4, a) M=1.2, b) M=2.4.* 70
Figure 70: *Total pressure loss coefficient, $C_{pt,\ loss}$ contours in exit plane for Case C-4, Slot-4, a) M=1.2, b) M=2.4.* 70
Figure 71: *Total pressure loss coefficient, $C_{pt,\ loss}$ contours in exit plane for Case D-4, a) M=1.2, b) M=2.4.* 71
Figure 72: *Overall mass-averaged, $(C_{pt,\ loss})_{mass\text{-}av}$ vs. M (Case-E, B-4, C-5, D-5 C-4, D-4), at exit plane.* 72
Figure 73: *Overall mass-averaged, $(C_{pt,\ loss})_{mass\text{-}av}$/MFR vs. M (Case-E, B-4, C-5, D-5 C-4, D-4), at exit plane.* 72
Figure 74: *Distributions of non-dimensional axial velocity u* contours data in third plane Case C-5, a) M = 1.2, b) M=2.4.* 74
Figure 75: *Distributions of non-dimensional axial velocity u* contours data in third plane Case D-5, a) M = 1.2, b) M=2.4* 74
Figure 76: *Distributions of non-dimensional axial velocity u* contours data in third plane Case E, a) M = 1.2, b) M=2.4.* 75
Figure 77: *Distributions of non-dimensional axial velocity u* contours data in third plane Case B-4, a) M = 1.2, b) M=2.4.* 75
Figure 78: *Distributions of non-dimensional axial velocity u* contours data in third plane Case C-4, a) M = 1.2, b) M=2.4.* 76
Figure 79: *Distributions of non-dimensional axial velocity u* contours data in third plane Case D-4, a) M = 1.2, b) M=2.4.* 76
Figure 80: *Distributions of non-dimensional axial velocity u* contour Case E, exit plane, a)M= 1.2, b) M=2.4 and c)M=2.8* 77
Figure 81: *Distributions of non-dimensional axial velocity u* contour Case B-4, exit plane, a)M= 1.2, b) M=2.4 and c)M=2.8.* 77
Figure 82: *Distributions of non-dimensional axial velocity u* contour Case C-4, exit plane, a)M= 1.2, b) M=2.4 and c)M=2.8.* 78
Figure 83: *Distributions of non-dimensional axial velocity u* contour Case D-4, exit plane, a)M= 1.2, b) M=2.4 and c)M=2.8.* 78
Figure 84: *Non-dimensional x-vorticity, ω_x*, contours perpendicular to third plane: Case C-5, a) M= 1.2, b) M=2.4.* 79
Figure 85: *Non-dimensional x-vorticity, ω_x*, contours perpendicular to third plane: Case D-5, a) M= 1.2, b) M=2.4.* 79
Figure 86: *Non-dimensional x-vorticity, ω_x*, contours perpendicular to third plane: Case E, a) M= 1.2, b) M=2.4.* 80
Figure 87: *Non-dimensional x-vorticity, ω_x*, contours perpendicular to third plane: Case B-4, a) M= 1.2, b) M=2.4.* 80
Figure 88: *Non-dimensional x-vorticity, ω_x*, contours perpendicular to third plane: Case C-4, a) M= 1.2, b) M=2.4.* 81
Figure 89: *Non-dimensional x-vorticity, ω_x*, contours perpendicular to third plane: Case D-4, a) M= 1.2, b) M=2.4.* 81
Figure 90: *Contours of non-dimensional temperature (θ) distribution in third plane: Case E, a) M=1.2, b) M=2.4.* 82
Figure 91: *Contours of non-dimensional temperature (θ) distribution in third plane: Case B-4, a) M=1.2, b) M=2.4.* 82
Figure 92: *Contours of non-dimensional temperature (θ) distribution in third plane: Case C-4), a) M=1.2, b) M=2.4.* 83
Figure 93: *Contours of non-dimensional temperature (θ) distribution in third plane: Case D-4, a) M=1.2, b) M=2.4.* 83
Figure 94: *Contours of non-dimensional temperature (θ) distribution in third plane: Case D-5, a) M=1.4, b) M=2.4.* 84
Figure 95: *Contours of non-dimensional temperature (θ) distribution in third plane: Case C-5, a) M=1.4, b) M=2.4.* 84
Figure 96: *Contours of non-dimensional temperature (θ) distribution in third plane: Case D-6 a) M=1.4, b) M=2.4.* 85
Figure 97: *Contours of non-dimensional temperature (θ) distribution in third plane: Case C-6 a) M=1.4, b) M=2.4.* 85

LIST OF TABLES

Table 1: *Summary of relevant studies on injected flow.* 11
Table 2: *Summary of relevant literature on LE fillet.* 15
Table 3: *Vane geometry and flow conditions.* 16
Table 4: *Measurement plane locations* 17
Table 5*: Fillet geometric parameters* 19
Table 6: *Primary instrumentation.* 26
Table 7: *Secondary instrumentation.* 26
Table 8: *Pressure uncertainties of five-hole pressure probe in the third plane.* 32
Table 9: *Pressure uncertainties of five-hole pressure probe in the exit plane.* 32
Table 10: *Uncertainties of the pitch and yaw angles, the static and total pressure in the third plane.* 33
Table 11: *Uncertainties of the pitch and yaw angles, the static and total pressure in the exit plane.* 33
Table 12: *Uncertainties of local velocities and axial vorticity in the third plane.* 33
Table 13: *Uncertainties of local velocities and axial vorticity in the exit plane.* 34
Table 14: *Nominal values of static and total coefficient of pressure in the third plane and exit plane* 34
Table 15: *Uncertainties of static and total coefficient of pressure in third plane and exit plane.* 34
Table 16: *Uncertainties of non-dimensional temperature in the third plane and exit plane.* 35
Table 17: *Flow field measurements.* 36
Table 18: *Thermal measurements.* 37
Table 19: *Tested cooling configurations.* 42
Table 20: *MFR(m_c/m_p) of coolant to passage flow* 49
Table 21: *Endwall cooling configurations.* 59
Table 22: *MFR(m_c/m_p) of coolant to passage flow.* 73

NOMENCLATURE

C, C_{ax}	True vane chord, axial vane chord, mm
C_D	Discharge coefficient
D, L	Film-cooling hole diameter and length, mm
P, S	Pitch and span, mm
$C_{pt,loss}$	Total pressure loss coefficient
C_{ps}	Static pressure loss coefficient
M	Inlet blowing ratio of film-cooling
P	Pressure, Pa
P_s, P_t	Static pressure, total pressure, Pa
$P_{t,loc}$	Local total pressure in a plane, Pa
PS, SS	Pressure-side, suction-side
Re	Inlet Reynolds number ($\varrho UC/\mu$)
S	Blade span, mm
U	Free-stream reference velocity, m/s
u	Local axial velocity, m/s
T	Air temperature, Kelvin [K]
D	Diameter
t	Student's t-statistic
x, y, z	Cartesian axis coordinates
LE, TE	Vane leading edge, trailing edge
$\dot{m}_p$	Mainstream mass flow rate in one passage
$\dot{m}_c$	Cooling mass flow rate in one passage
MFR	Mass flow rate
YAW, PIT	Yaw angle, pitch angle, degrees

Subscripts

G, loc	Global, local coordinates
plenum, ref	Plenum, reference location
x_{loc}	Local properties in a test plane

Special characters

Δ	Change in related quantity
$\boldsymbol{\beta}$	Orifice plate diameter ratio
ρ	Density of air, kg/m^3
ω_x	Axial vorticity

1. Introduction

1.1. Background

The airline industry is still fully reliant on fossil fuel as a source of energy for aircraft propulsion systems. System efficiency has always been a high priority in turbine research. By now, fuel has become the dominant cost element in airline operations and the pursuit of even small efficiency improvements can be economically beneficial.

Overall, turbine efficiency shows an incremental improvement as turbine inlet temperatures and compression ratios are gradually increasing. At the component level, this comes from improvements in material cooling strategies and reduction in flow losses in the blade passages.

In modern gas turbines, the turbine inlet temperatures exceed the metallurgical tolerances of the passage materials. The metallurgical tolerance is accomplished by employing special thermal management by which mechanically stressed components are successfully separated from the hot free-stream flow. Cooling air bled off a late compressor stage is injected into the boundary layer of the blade passages providing a protective layer of cooling air between the material surface and the hotter gases.

Since most other turbine components are far less temperature tolerant than the turbine blades, active cooling of the turbine disk space is necessary. For this purpose, a portion of the compressed flow is purged through the interior through the gap between the stators and the rotors. Besides limiting the ingestion of hot air into the disk space, this purging offers the possibility of ejecting cooling air through the gap between the stators and the rotors. However, the purge flow comes at a cost to efficiency because it bypasses the combustion chamber and consequently does less expansion work.

In 1992, Bunker et al. [1] highlighted the problem of flow ingestion of hot mainstream gases, raising the internal temperature of the wheel space material. He advised injecting cooling air to keep the temperature within thermal limits.

The coolant air is also employed to cool the endwall vane passages of the turbine nozzle guide vanes because they are situated just downstream of the combustion chamber. The external cooling is used on the endwalls, leading edge, suction-side, pressure-side and trailing edge of the blade surface and it is usually ejected from slots or discrete holes on the surfaces (***Figure 1-a).***

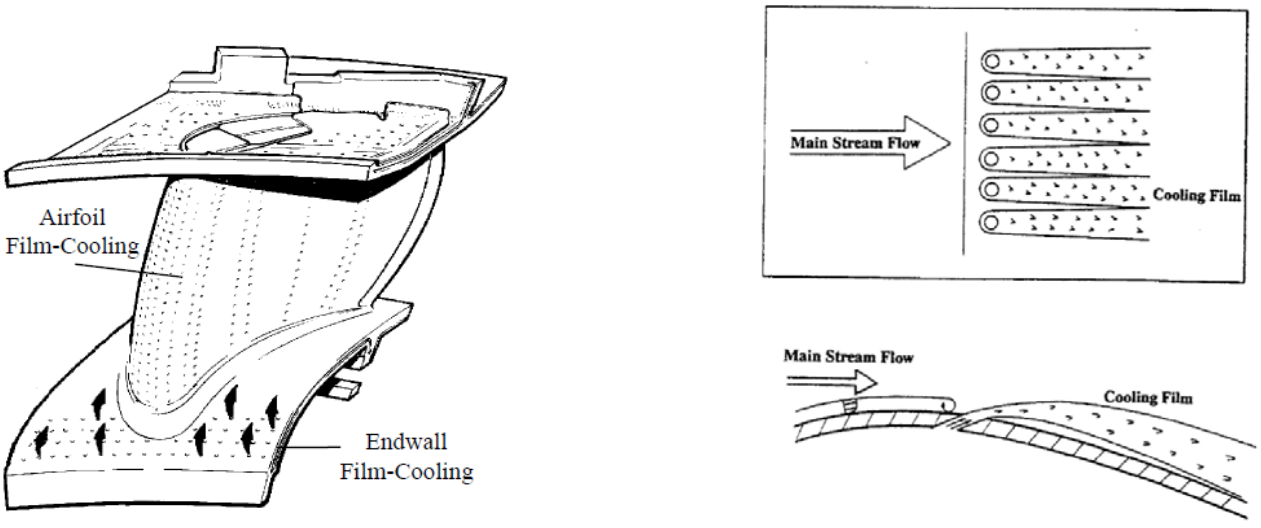

Figure 1: *a) Endwall film-cooling, Friedrichs et al. [2], b) cooling film ejection, Wilfert and Fottner [3].*

The location of endwall film-cooling extends from upstream of the vane passage to the blade. The inlet boundary layer interacts with the discharged cooling film resulting in a complex three-dimensional structure. The mixing process with mainstream flow starts immediately as the jet exits the hole (***Figure 1-b).***

The cooling flow jet bends towards the surface decelerating the flow upstream and downstream of the ejection location, while it accelerates the flow above and around the jet. The mainstream deceleration upstream of the jet causes the separation of the upcoming boundary layer, which turns into a horseshoe vortex that wraps around the jet.

A kidney-shaped vortex is formed as a result of a pair of counter-rotating vortices, according to Haas et al [4]. The bending of the jet and the strong shear action on the side of the jet intensify the pair of counter-rotating vortices and move the free-stream fluid down the endwall on the other side of the jet (***Figure 2***). Furthermore, these vortices pull surface fluid into the jet centre. In some cases, the low pressure below the jet is such that reversed flow is present on the endwall. The objective of film-cooling design is to find a configuration that allows the coolant to remain attached to a wide region of the endwall, or if it detaches, to reattach to the surface.

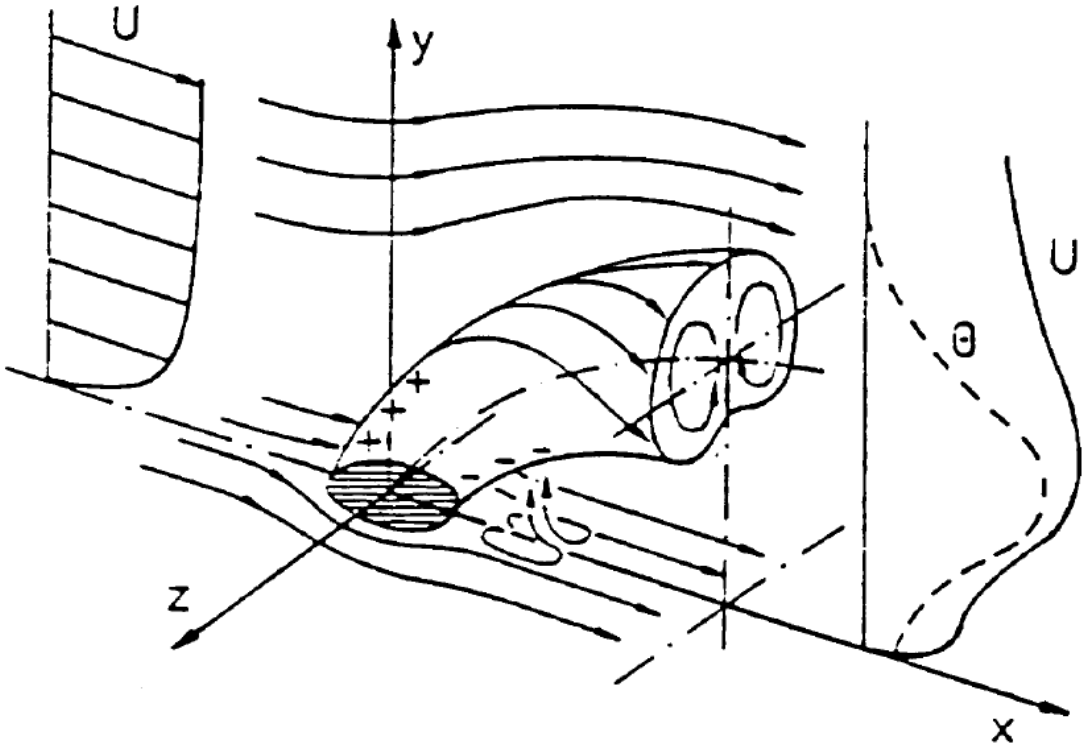

Figure 2: *Schematic view of the vortical structures in the vicinity of a jet in cross-flow, Haas et al. [4].*

1.2. Description of the secondary flow phenomena

The junction between the endwall and the blade causes a complicated three-dimensional pressure field in the flow. The incoming boundary layer rolls up at the blade base leading edge into a prominent horseshoe vortex, which causes the secondary flow along the vane passage. The nature of the flow in this area is very complex because it is characterised by a boundary layer stagnation line, strong pressure gradients and temperature gradients.

Sieverding [5] illustrates, in ***Figure 3***, the basic features of the secondary flows in turbine blade passages. ***Figure 3*** also shows where the secondary flows originate with the formation of the leading-edge vortex. The

horseshoe vortex forms at the junction of blade leading-edge and endwall (***Figure 3(a)***) and then travels between the dotted lines (S_1 and S_2) of ***Figure 3(b)*** as vortex legs on the pressure side and suction side of the blade. The endwall boundary layer detaches along the S_1 dotted line and re-attaches along the S_2 dotted line. At Saddle Point A_1 in ***Figures 3(a, b)***, the boundary layer lifts off ahead of the horseshoe vortex and then diverts on the pressure side and suction side. The dotted line along S_1 is also called the "lift-off" line of the boundary layer. The position and size of the separation region between S_1 and S_2 depend on the: (i) strength and size of the horseshoe vortex and vortex legs, (ii) inlet boundary layer characteristics, (iii) incidence angle of the blade, and (iii) shape of the blade leading edge.

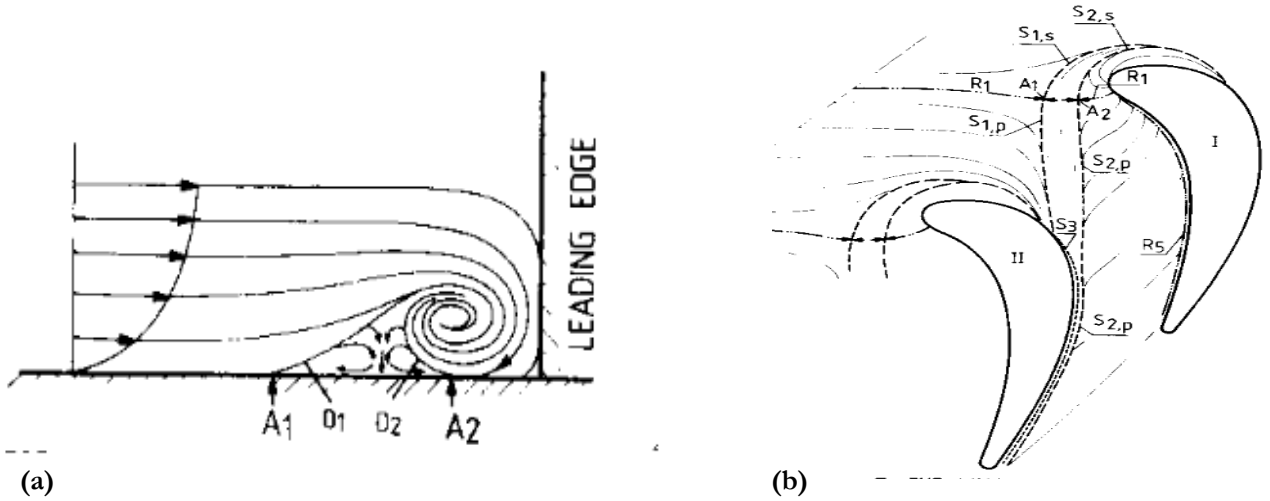

Figure 3: *a) Formation of leading-edge horseshoe vortex, b) separation lines at the endwall ahead of LE [5].*

The data presented by Langston et al. [6] indicated the position of the saddle point to be in the area of the streamwise adverse pressure gradient. The study predicted the saddle point position depending on the incidence angle of the cascade flow, and the shape and size of the blade's airfoil.

Langston [7] gave a complete literature review of secondary flow models by illustrating the progress from 1985 to 2000 in linear cascades. The review explained the development of two legs of a horseshoe vortex into the passage vortex (***Figure 4-a***).

The horseshoe develops into four major vortices: passage vortex, pressure-side leg vortex, suction-side leg vortex, and corner-vortex. When the inlet boundary layer interacts with the horseshoe vortex, the pressure-side leg vortex and suction-side leg vortex form.

The pressure leg of the horseshoe vortex gets more intense because it travels towards the suction-side of the next blade and merges with the passage pressure-side to suction-side endwall flow. This vortex intersects the suction-side vortex of the next blade and because these two vortices are rotating on the opposite side, they end up wrapping around each other. While they are going up the suction-side downstream of the leading edge, their intensity grows through the passage creating the so-called passage vortex, containing counter-rotating streamwise vortex pairs.

This interaction generates a span-wise migration of low momentum fluid from the boundary layer to the mid-span. The suction leg vortex moves to the minimum pressure point on the suction surface and adheres to the suction surface. This vortex (moved along the span) is called the counter-rotating vortex because it has the opposite rotation of the passage vortex.

In 1995, Wang et al. [8] used smoke flow visualisation with laser light at various locations inside a linear blade cascade to record the multi-vortex flow pattern at a very low Reynolds number. Their photographs

revealed the horseshoe vortex and the development of two vortex legs, passage vortex, and corner vortex within the passage. They realised that the suction leg vortex climbed the suction-side, travelled above the passage vortex, and wrapped itself around the passage vortex after the pressure leg vortex formed into the passage vortex. The suction leg vortex turned into a small branch of passage vortex structure downstream of the blade.

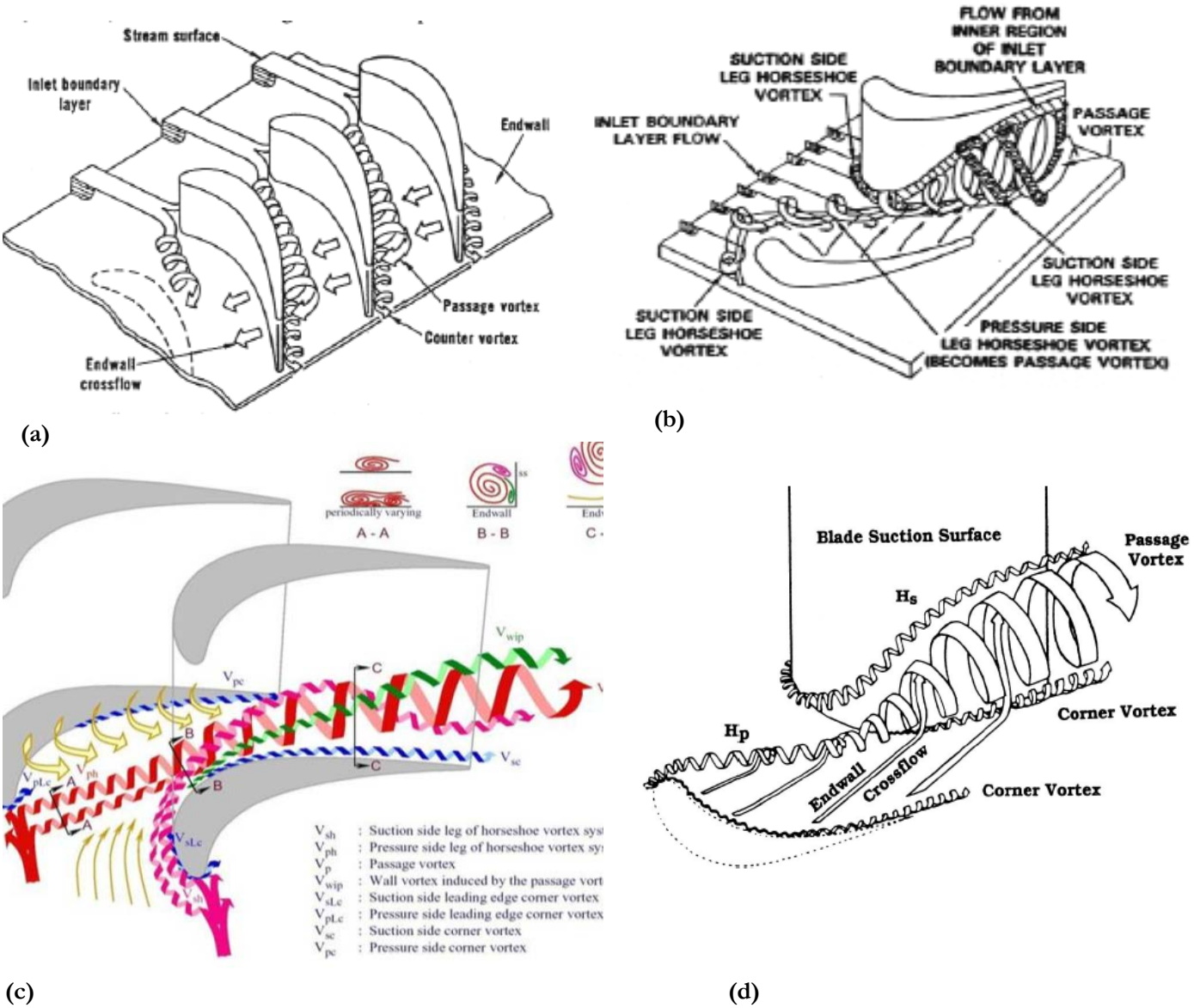

Figure 4: *Vortex structure described in the literature:* (a) *1985, Langston model[6]*, (b) *1987, Sharma and Butler model [7]*, (c) *1997, Endwall Vortex structure illustrated by Wang et al. [8]*, (d) *2001, Moon and Koh [9].*

They observed that the pressure leg of the horseshoe vortex merged with the suction leg of its counter-part at about a quarter of the surface distance from the leading edge. They identified the existence of another small but intense vortex that had a high mass transfer rate close to the suction surface, the so-called wall vortex. They realised that the main pressure loss across the cascade was a consequence of the passage vortex.

When film-cooling is introduced into this flow field, the complexity increases because the coolant interacts with the vortex flow energising the boundary layer. The mixing of the two flows changes the structure of the secondary flow in the vane passage and, at the same time, the coolant jet trajectory is diverted by it and by the cross-flow in the pitch direction.

1.3. Motivation

The secondary flow and cooling flow have a strong influence on cascade. It is necessary to implement a proper design of the endwall film-cooling configuration to achieve an effective structural modification of the flow that weakens the secondary flow and reduces the aerodynamic losses.

The criterion for increasing the efficiency of a gas turbine cycle is an optimum level of cooling air, with minimum aerodynamic losses. The challenge is to gain a detailed knowledge of the mixing behaviour between cooling flow and secondary flow and identify the parameters that influence these phenomena.

Most of the current research shows how difficult it is to cool the endwall near the pressure-side because of the high turning angle of flow and endwall flow separation due to the passage vortex system. The effectiveness of film-cooling strongly depends on film-cooling configurations and geometries.

To reduce the aerodynamic losses and heat transfer, researchers have proposed employing geometric modifications such as contoured endwalls in the vanes and filleted blades to the blade cascade. Some of the geometric modifications provide good aero-thermal performance but perform poorly in film-cooling, while other modifications provide good film-cooling on the endwall but are poor in aero-thermal performance.

1.4. Objectives

The objectives of this study were to offer some comparative experimental observations relating to leading-edge modifications together with coolant injection geometries and placements to reduce secondary flow losses or to increase the quality of the cooling flow structure. The aim of the vane stage external cooling investigations was to produce data over a wide range of cooling flow conditions, such as different cooling ejection configurations to determine and explore the aerodynamic influence of the fillet effect on the secondary flow.

1.5. Thesis structure

This research focused on detailed aerodynamic investigations of leading-edge contouring near the endwall by a proposed fillet in the presence of several injected cooling flow configurations and rates in a linear GE-E^3 vane cascade. The study investigated whether the aerodynamic improvements due to the endwall profiling were not lost in the presence of cooling flow.

The thesis is divided into two parts:

1) an investigation of leading-edge contouring at endwall by a fillet;
2) an investigation of the aerodynamic performance of a vane cascade with and without a fillet with several film-cooling configurations.

The study covered the overall blowing ratios of film-cooling ranging from 1.2 to 2.8 when the density ratio and temperature ratio of the coolant to mainstream flow were 1.05 and 0.94 respectively.

2. Film-cooling technologies

2.1. Introduction

Many literature works exist on endwall film-cooling design and on the investigation of the best cooling configuration to achieve wider coverage. The first author to publish research on endwall cooling effectiveness and heat transfer was Blair [10]. His investigation, using an upstream cooling slot, concluded that the film-cooling was affected by secondary flow. Later in 1977, Goldman and McLallin [11] reported higher aerodynamic losses and the influence on exit flow angles by conducting aerodynamic measurements of endwall cooling.

McLean et al. [12], Schuepbach et al. [13], Friedrichs et al. [14] and Barigozzi et al. [15] pointed out that mixing of the cooling air and main flow leads to increased passage flow losses. Currently, much attention is given to attempts to reduce such aerodynamic flow losses in the passages of all turbine stages. This requires optimisation of the morphology of the passage as defined by the endwalls, blade profiles and their junctions.

The success of covering a wide cooling area depends on a variety of parameters such as injection angle, location on the endwall, coolant distribution, film-cooling injection geometry (size, shape), blowing ratio, and mass flow rate.

2.2. Film-cooling mass flow rate and injection angle

In 1993, Biesinger and Gregory-Smith [16] investigated the physics of a passage flow with upstream blowing to reduce secondary flows. They reported that the blowing rates and their angle had a big role in the development of secondary flows.

Their surface flow visualisation, conducted in a linear cascade, showed that, at a low blowing rate, the first effect was the thickening of the inlet boundary layers and the strengthening of the secondary flow. At a high blowing rate, the boundary layer was re-energised and the positive streamwise vorticity counteracted the secondary vortex reducing the passage vortex and the loss.

The effect of blowing was more noticeable on the blade pressure-side rather than the suction-side, characterised by span-wise velocities away from the endwall. However, a high blowing rate produced a counter-vortex that persisted to the exit of the blade passage. Furthermore, a low angle of injection was preferable because it kept the jet closer to the endwall at the inlet to the cascade and it re-energised the low momentum fluid.

Thrift and Thole [17] evaluated the injection angle of a two-dimensional slot upstream of a vane leading edge in a low-pressure turbine blade. The high momentum injection increased the endwall heat transfer. The leading-edge vortex at the injection angles of 90° and 65° turned into the endwall, while it was turned away from the wall at 45° and 30° angles. At low momentum, the mixing of the coolant and mainstream flow was less and the leading-edge vortex turned into the endwall at all injection angles.

For the low value of ejection angles and blowing ratio, the jet bended fast enough and attached to the surface, according to Roux [18]. Increasing the angles and blowing ratio led to the jet lifting off - the surface, losing the capacity to cool off the heated area, as shown in ***Figure 5***. The flow structure depended on the coolant injection velocity and port geometry (injection angles, shape, size and distribution of holes) from which it was ejected.

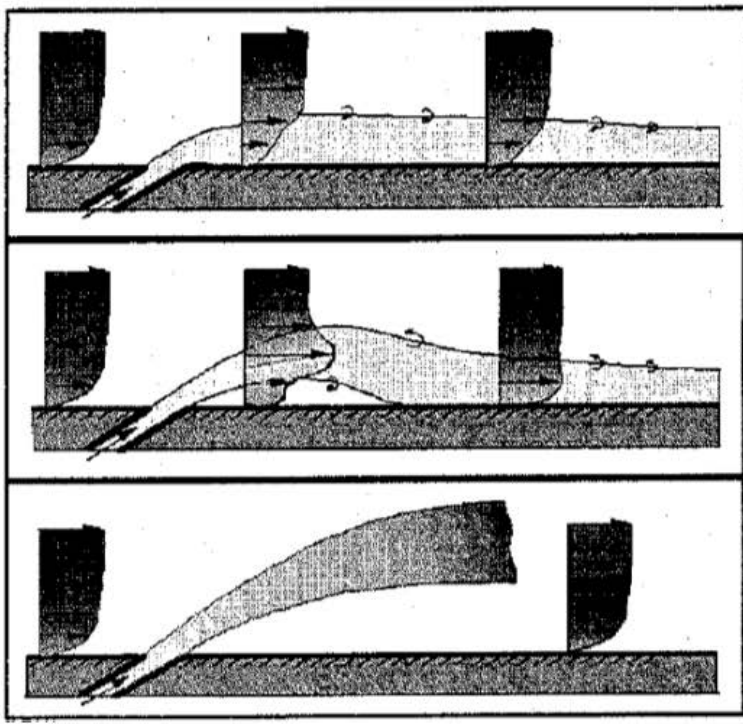

***Figure 5**: Cooling film ejection from low to high blowing ratio, Roux [18].*

The hole length to diameter parameter affected the velocity profile and the turbulence intensity at the hole exit [19]. Typical values of hole length were in the range of 2<L/D<10.

2.3. Film-cooling injection geometry

Saumweber and Schulz [20] compared the effect of a basic design of film-cooling holes, in ***Figure 6***. The study indicated that the hole angle, the expansion angle of the diffuser for a contoured hole, and the length of the cylindrical part had a significant influence on the coolant coverage. Their conclusion was that it was difficult to find a mathematical formulation for unique combinations of the mainstream flow condition and film-cooling geometry.

The experimental and computational results of [21, 22] show that the fan-shaped holes provide higher and better distribution of effectiveness and lower total pressure losses than for the cylindrical holes. Barigozzi et al. [23] investigated the effects of the exit area of four rows of fan-shaped film-cooling holes on the aerodynamic performance and endwall film-cooling effectiveness in a vane cascade. The cooling holes of [23], with a small exit area reduced aerodynamic losses and with a large exit area provided better local cooling effectiveness when the two configurations of cooling holes were compared.

Sundaram and Thole [24] investigated the effects of contaminant deposits on film-cooling along the pressure-side of a vane endwall. The film-cooling hole arrays were placed along the endwall of the pressure side of the vane passage. The study was based on semi-elliptically shaped holes placed along the pressure-side to simulate the various row depositions of the film-cooling holes that occurred from contaminants present in the hot gas path. It was discovered that the deposits hindered the mean adiabatic effectiveness level downstream of the film-cooling holes arrays by diverting the coolant jet towards the vane endwall junction on the pressure-side.

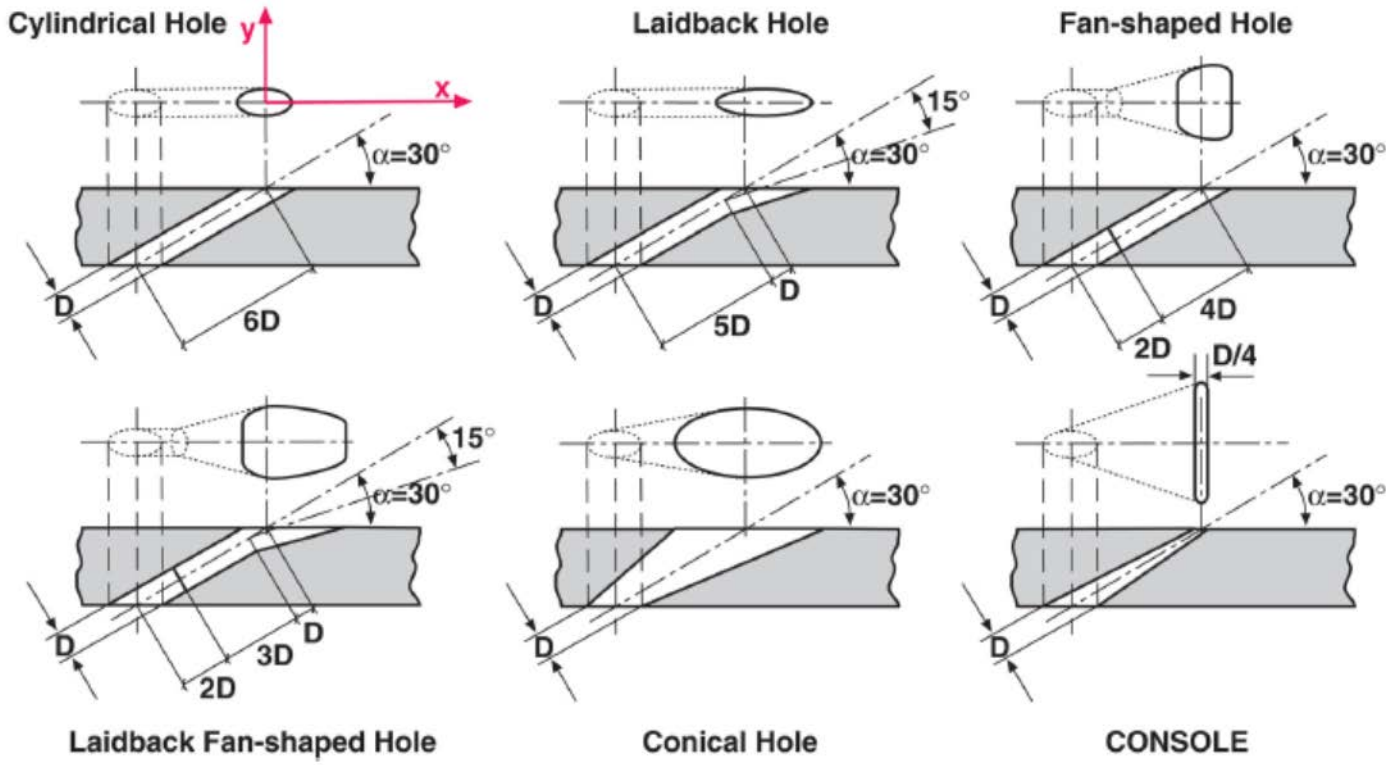

Figure 6: Types of film-cooling hole geometries, Saumweber and Schulz [20].

According to Sundaram and Thole [25], the effect of partial film-cooling hole blockage by depositions was to decrease the film-cooling performance. Film-cooling holes at the endwall were blocked at the exit by 25% conforming to the required geometrical dimensions. The results showed that deposits near the exit of the film cooling hole at times increased the cooling.

Kunze et al. [26] reported that film-cooling from the fan-shaped holes in the endwall at the cascade inlet negatively influenced the aerodynamic losses and film-cooling effectiveness distributions at the high loading condition on the vane. The fan-shaped hole film-cooling effectiveness on the endwall in Zhang et al. [27] remained largely the same with and without a filleted vane.

Fan-shaped holes outperformed cylindrical holes in the cascade endwall for the adiabatic film-cooling effectiveness in [28, 21]. However, while aerodynamic losses were lower for the fan-shaped holes in [22, 21], the same losses were higher for the fan-shaped holes in [28] than for the cylindrical holes.

Past investigations of cylindrical film-cooling holes in the upstream endwall of a vane cascade resulted in primarily good cooling effectiveness near the suction-side regions, but poor cooling effectiveness near the leading-edge and pressure-side regions. Also, the effectiveness distributions depended on the upstream locations of the cylindrical holes relative to the vane leading edge. Fan-shaped holes were employed to provide better distribution of film-cooling on the endwall than for cylindrical holes. However, aerodynamic losses across the cascade passage increased with the fan-shaped hole because of mixing between the coolant and the boundary layer. Unfortunately, the geometry of the fan-shaped hole introduced some flow losses inside the holes adding to the overall cascade aerodynamic losses [29].

2.4. Leading-edge cooling

Leading-edge cooling is achieved by injecting coolant from slots or holes just upstream of the vane. Sundaram and Thole [30] adopted an array of two-dimensional film-cooling holes in a trench with an interface slot placed upstream of a vane leading edge. Results showed that the trench produced better overall cooling than for the no-trench arrangement because the coolant was found to be attached to the endwall. The use of a trench also gave rise to flow reversal at the leading edge resulting in high vorticity. Hence adiabatic effectiveness was enhanced.

Colban et al. [31] investigated the heat transfer coefficient and adiabatic fan-shaped film-cooling hole effectiveness of a vane surface with a contoured wall. They showed that a film-cooling injection altered the boundary layer transition along the suction-side. Along the suction-side and pressure-side of the vane, adiabatic effectiveness measurement without upstream blowing showed that the jet lifted off. The jet reattached to the surface in the concave area of the vane pressure-side. The study indicated that with an increase in blowing ratio, the direction of the jets changed and the lateral coolant spreading reduced. A combined film-cooling flow from the upstream discrete holes and a continuous slot of Barigozzi et al. [32] provided desirable results in the cascade when a wall blockade was introduced upstream in the mid-pitch location. The upstream discrete slots of Xu et al. [33] predicted that the endwall film-cooling effectiveness increased and the secondary flows weakened in the cascade passage as the blowing ratio increased if the slots were positioned near the vane leading edge, and at a higher slot angle.

2.5. Endwall cooling

Thole and Knost [34] studied the effects of injecting coolant at different flow rates through a combustor turbine interface into a vane cascade. They compared the effect of the leakage flow on the downstream film cooling injection. An upstream slot and some arrays of film-cooling holes were placed on the endwall of a vane passage. The combination of film-cooling and slot flow was sufficient for significantly cooling the endwall. At constant slot flow with increased film-cooling flow rate, the measured thermal fields showed a change in the passage vortex. The slot flow was entrained in the passage vortex and transported towards the suction-side. When only the upstream slot was employed, the pressure-side regions of the endwall primarily were left uncooled. The combination of the slot and holes provided a reasonable lateral spread of the film-cooling coverage on the endwall.

Lynch and Thole [35] accomplished a larger coolant covered area with the slot film-cooling by reducing the slot width by half and positioning it further upstream of the leading edge of the vane. If a misaligned mid passage gap was present (suction-side of the endwall higher than the pressure-side of the endwall), the film cooling effectiveness was severely reduced. A thicker boundary layer had a significant effect on the jet separation from the endwall in terms of a higher blowing ratio.

Friedrichs et al. [14, 36, 37] reported that secondary flow and film-cooling trajectories influenced each other. The coolant trajectory was not affected by the angle of ejection to the flow, but film-cooling modified the endwall surface flow field with an averaged cooling effectiveness of 12.3%. Ejection into regions of low static pressure increased the loss per unit coolant mass flow. If the ejection happened upstream of the three-dimensional separation lines on the endwall, the loss due to secondary flow could be reduced.

Wang et al. [38] employed multiple rows of cylindrical holes both upstream and inside the passage of a vane cascade. The measured distributions of the endwall film-cooling effectiveness, provided by the upstream holes, dominated along the endwall and increased with the coolant flow rate and density.

Hada and Thole [39] and Du et al. [40] computationally estimated and compared film-cooling effectiveness distributions along a vane cascade endwall, employing continuous upstream slots of different geometries. The predictions of [39, 40] show that the coolant spread can be more effective by raising the upstream endwall of the slot slightly higher than for a generally level upstream endwall.

2.6. Contouring endwall effect on film-cooling

Ligrani [41] gives a detailed review of the aerodynamic losses in turbines with and without film-cooling, emphasising the difficulty in cooling the leading edge of the turbine's first stage. The effect of external vortices on the coolant's distribution can enhance cooling effectiveness with their downwash, while lifting the coolant off the endwall with their upwash. However, the flow quality can be affected by endwall contouring, by modification of the blade base junction, and by changes in the blade profile.

An example is the Rolls-Royce Trent 500, which employs non-axisymmetric endwalls in the intermediate stages of the turbine. Harvey et al. [42] ascribe a 0.9% improvement in efficiency to the contoured endwalls. Computational predictions of film-cooling and heat transfer at the endwall were carried out by Hada and Thole [39] and Lynch et al. [43]. The geometry involved in [43] included a non-axisymmetric endwall contour. Experiments on exit flow structure, endwall heat transfer and endwall film-cooling were compared. In terms of film-cooling, simulations agreed closely with the experiment; the non-axisymmetric endwall inhibited the spread of film-cooling flow at the endwall. Measurements of endwall heat transfer were reported with non-axisymmetric endwall contouring and a flat endwall without contouring in a low-pressure turbine. The contoured endwall was found to reduce the strength of the passage vortex and the heat transfer was found to reduce by about 20% in the region of high heat transfer.

The same observation was confirmed by the study of Oke et al. [44], in 2001, in a high-pressure turbine first-stage vane with axisymmetric, contoured endwall. The coolant was ejected through a single or a double slot (one behind the other) upstream of the leading edges of the vane. The secondary flow affected the cooling flow especially at a low blowing ratio, accumulating the coolant near the suction-side of the passage. Better pressure-side cooling was achieved by increasing the blowing ratio. The uniformity of coolant distribution across the leading edge was attained by a single-slot injection.

2.7. Fillet and film-cooling interaction

A promising result, showing the feasibility of the secondary flow being energised through air injection, has been achieved by several researchers. This has encouraged researchers to combine the mainstream/injected flow interaction with different blade leading edges and contoured endwall geometry in a linear cascade.

Under certain conditions, as illustrated by Simon and Piggush [45], injected flow can decrease the strength of secondary flows. They documented coolant injected from a slot with a variable step upstream of a cascade passage that had an axially contoured endwall. The injected flow with a backward-facing step entered underneath the momentum boundary layer, creating a thicker boundary layer and decreased heat transfer rate.

The aerodynamic losses, related to the horseshoe vortex, can be minimised using a leading-edge fillet, because the fillet forms a smooth transition from the NGV leading edge vane to the endwall surface. Mahmood et al. [46] investigated the effectiveness of film-cooling on the endwall of GE-E^3 nozzle guide vane through computational simulation and experimental tests. Flow streamlines obtained by a numerical study illustrated the development of secondary flow pattern along the vane passage. Along the boundary layer separation and re-attachment line, the endwall boundary layer was lifted by the passage vortices increasing the

endwall heat transfer, especially near the pressure-side. This implied that the cooling would inevitably be lifted over these lines limiting the presence of the upstream coolant in the passage downstream and cooling coverage area. The measurements showed that the film-cooling effectiveness on the pressure-side was very low if the blowing ratio was below two.

The investigations of Thomas and Povey [47] and Ornano and Povey [48] in a filleted vane cascade, with cylindrical holes in an upstream endwall, indicated that the location and angle of the holes and coolant to-mainstream mass flow ratio significantly influenced film-cooling effectiveness, coolant stream migration, and secondary flows along the cascade passage.

The effects of different geometries of the leading-edge fillet, investigated by Zhang et al. [27], on the diffused hole film-cooling effectiveness, only seem to influence the junction of the vane and endwall. Thrift et al. [49, 50] measured a decrease in endwall heat transfer and an increase in film-cooling effectiveness when the continuous slot of film-cooling flow was at a particular position and inclination.

2.8. Closure

Film-cooling on the endwall is a requirement with the increase in turbine inlet temperatures. Secondary flow strongly influences film-cooling and heat transfer. The location and geometry of the film-cooling holes require a deep understanding of the effect on the secondary flow behaviour in the vane's passage.

Table 1: Summary of relevant studies on injected flow.

Parameter	Advantages	Disadvantages
Mass flow rate	High MFR reduces loss and passage vortex [16] and increases heat transfer [17, 18].	Increasing the blowing ratio leads to the cooling jet lifting off from the surface [18].
Injection angle	A low angle helps the jets to remain attached to the endwall [16, 18]. A low angle keeps the leading-edge vortex away from the endwall [17].	
Hole shape	Fan-shaped holes have a better distribution of effectiveness and less total pressure loss than cylindrical holes [21, 22]. The small exit area of the fan-shaped holes reduces aerodynamic losses and the large exit area improves film-cooling effectiveness [23]. Slots increase the effectiveness with an increase in BR [33]. Typical values of hole length are in the range of $2<L/D<10$ [19].	Small exit areas have less total loss but less cooling effectiveness [15]. A combination of the mainstream flow condition and film-cooling geometry is unique; [20, 26] show that the fan-shaped holes negatively influence the aerodynamic losses.
Upstream and passage cooling	Film-cooling passage holes and upstream slot combination significantly cool the endwall. [34]. If the ejection happens upstream of the three-dimensional separation lines on the endwall, the loss due to secondary flow can be reduced [14, 32, 33]. Better cooling coverage with an upstream slot at 0.77 C_{ax} [31].	If only an upstream slot is employed, the pressure-side regions of the endwall primarily are left uncooled [34].
Contoured endwall	Contouring the endwall helps the spreading of the coolant [39].	
Fillet	A leading-edge fillet allows a smooth transition from the NGV leading edge to the endwall surface minimising aerodynamic losses related to the horseshoe vortex [42].	The diffused hole film-cooling only seems to be effective near the junction of the vane and endwall [45]. The continuous slot film-cooling flow is effective when it is in a particular position and inclination [46, 47].

The literature review indicated that the injection flow rate, its pressure, angle and cavity geometry influence the development of boundary layers in secondary flows within the passage. A combination of cooling holes/slots upstream of the leading edge and cooling arrays along the passage show better cooling coverage. High flow rates reduce the passage vortex at the expense of higher heat transfer.

Contoured endwalls and leading-edge blade modification, combined with film-cooling, improve secondary flow losses. Table 1 summarises the relevant studies on the effect of several parameters of cooling flow in terms of efficiency.

The current research focused on leading-edge cooling in combination with endwall cooling holes to minimise the secondary flows for minimum losses.

3. Fillet design

In 2000, Hartland et al. [51] realised that reduction in the strength of the passage vortex was achieved by using non-axisymmetric contoured endwalls as a tool to have a more homogeneous pressure field in the passage. The idea was to create a contraction in the area of the passage by profiling the endwalls with streamlined curvature to control the pressure. This method, proposed by Rose [52], aimed to remove the non-axisymmetric static pressure distribution at the nozzle guide vane exit.

By using the principle of increasing the local static pressure with a concave curvature on the endwall, or decreasing the local static pressure with the convex curvature, it was possible to reduce the cross-passage pressure gradient in the early part of the blade passage and thereby reducing the strength of the passage vortex. The designed profiled endwall was able to reduce secondary losses at the downstream exit plane by about 30% in a subsonic linear cascade.

Harvey et al. [53] compared the flat endwall and the proposed contoured endwall through flow visualisation. The effect of the contouring produced a significant change in the structure of the secondary flow and the intensity of the passage vortex. The separation line moved downstream and the profiled endwall reduced the size of the passage vortex and introduced a corner vortex.

Another passive method to reduce the leading edge vortices on the endwall, as well to reduce the pressure gradient, is by implying a fillet at the junction between the blade and the endwall.

Moore and Ransmayr [54] and Han and Goldstein [55] added a fillet at the junction of the blade leading edge and the endwall, achieving a reduction of the horseshoe vortex intensity at different Reynolds numbers. Sauer et al. [56] investigated a leading-edge contour by LE bulbs in a low-speed cascade. The contour was a convex connection between the leading edge and the endwall (***Figure 7-a***). The objective of the study was to increase the local geometric thickness, hoping to accelerate the stagnating boundary layer fluid and to reduce the total pressure profile. The suction-side vortex intensified and because it was counter-rotating to the passage vortex, it deformed the latter, moving it away from the suction-side. Even if the straightening of the suction-side vortex did lead to increased mixing losses downstream of the blade, the reduction of the endwall losses was about 50%.

Zess and Thole [57] conducted CFD simulations to design an LE fillet with an elliptically shaped asymmetric profile on the suction-side (***Figure 7-b***). The fillet had a height of one boundary layer thickness, varied linearly from the vane surface to the endwall, and a length of the double value of the boundary layer. Flow field measurements in a linear cascade agreed with computational results. The incoming boundary layer was accelerated while climbing up the fillet, eliminating the leading-edge vortex and reducing the total pressure gradient. The turbulent kinetic levels and streamwise vorticity levels were reduced near the endwall showing the effectiveness of an LE fillet.

Becz et al. [58] compared two LE bulb configurations and an LE fillet in a high-turning linear cascade (***Figure 7-c***). Only the big bulb had an undesirable result with an increase in total loss, while the other configuration showed a loss reduction of 8%. Erickson and Simon [59] compared two different endwall geometries: a dolphin and a shark nose endwall in the rotor stage of a high-pressure turbine. From CFD results, using a k-ω shear stress transport model and flow visualisation in the turbine linear cascade, they observed unsteadiness of the flow and reversing flow in the injected path slot. The computational study showed how the injected cooling flow and the horseshoe vortex mixed together and the passage loss was confirmed by measurements of adiabatic effectiveness on the contoured endwalls in the upstream region of the passage. The study indicated that the changes of the leakage flow injection rate did have a small influence on the passage loss. The dolphin nose endwall showed higher losses in the passage.

Mahmood et al. [60] further explored the asymmetrical elliptical shape of an LE fillet through four different leading-edge fillets. They observed a link between the reduction of secondary flow structures and endwall heat transfer. The fillets made the passage vortex weaker and reduced the Nusselt number between the leading edge and throat region. Downstream of the throat, the increase in total loss, and turbulence intensity indicated the strong effect of the passage vortex system due to the cross-flow and pitch-wise pressure gradients.

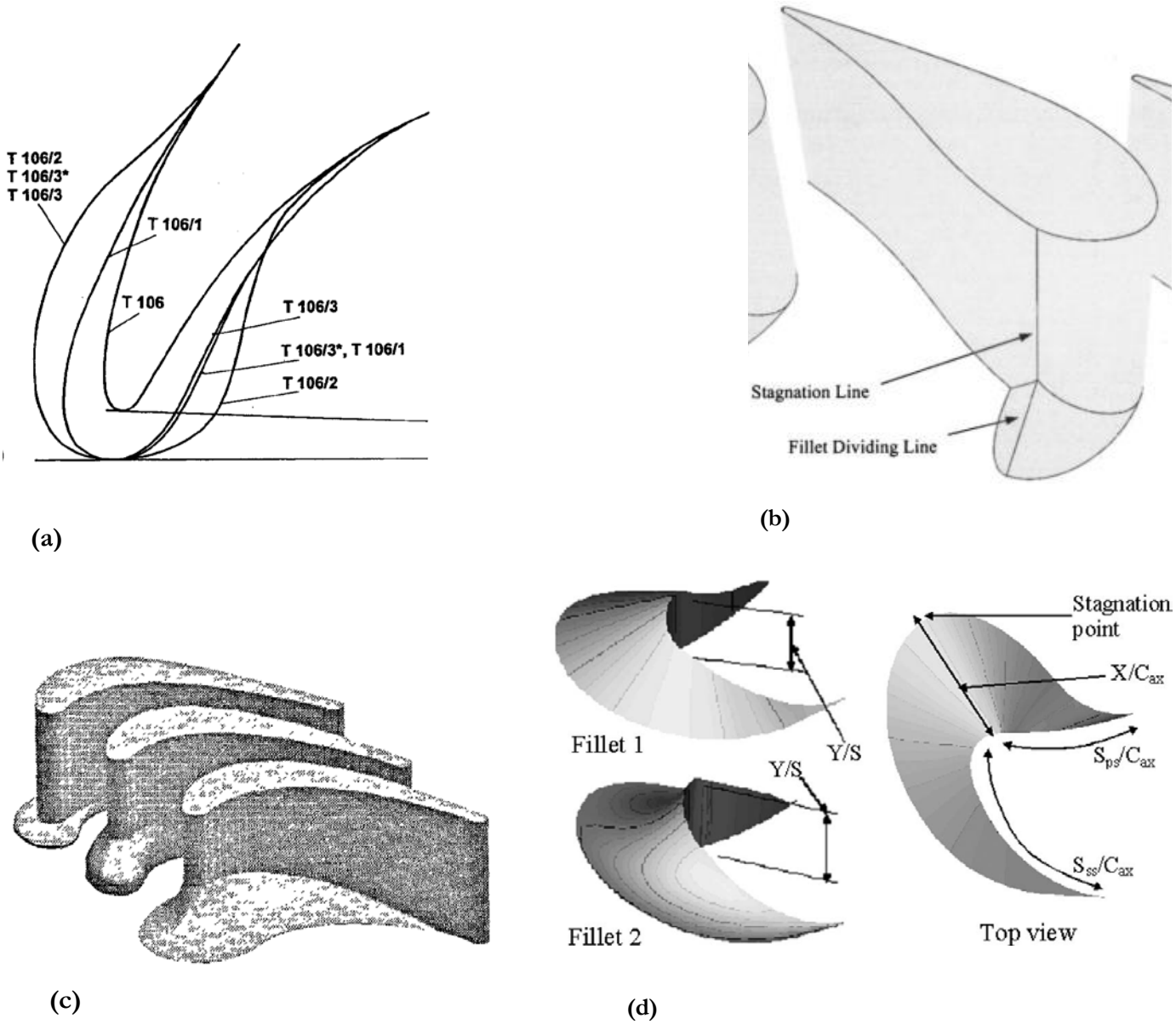

Figure 7: *Leading-edge fillet profile:(a) Sauer at al. [56], (b) Zess and Thole [57], (c) Becz et al. [58], (d) Mahmood et al. [61].*

In Ref [61], the two selected fillet profiles (***Figure 7-d)***, with smoother transitioning towards the endwall and blade, were investigated further. The linear profile fillet performed best, successfully reducing the pitch and yaw angles of the passage flow. Downstream of the leading edge, the suction vortex was much smaller and the passage vortex was weaker before than after the throat. The investigations of Becz et al. [58] and Mahmood and Acharya [61] reported an increase in the exit flow angle with the use of an LE fillet. This negative effect decreased the useful work done that stage.

Table 2 gives an overview of the main characteristics of several LE fillet shapes.

Table 2: *Summary of relevant literature on LE fillet.*

Author	Fillet shape	Fillet height	Fillet length	Horseshoe vortex
Becz et al. [58]	Bulb			Reduction, 8% total loss reduction
Zess and Thole [57]	Asymmetric pointed/sharp profile	One BL	2BL rounded increase	Reduction
Mahmood and Acharya [61]	Linear profile with more pronounced SS smoother transitioning towards the endwall and blade. SS extension of fillet more pronounced than PS to get rid of extra vortices			Reduction, but exit flow angle increased
Han and Goldstein [55]	Linear asymmetric profile			It is not observed and the passage vortex is delayed. Higher mass transfer near LE.

4. Experimental design and methodology

4.1. Low-speed test cascade

The endwall film-cooling investigations were conducted in a low-speed test cascade with a low aspect ratio, S/C=0.677. The cascade test facility was formed by seven two-dimensional vane profiles and was housed in an open-circuit wind tunnel. Atmospheric airflow in the wind tunnel was created by the suction of two axial fans, with a power rating of 7.5kW and 15 kW. The fans were connected in series, at the wind tunnel exit, to give an average free-stream flow velocity U of 10 m/s at the cascade inlet. ***Figure 8-a*** illustrates the cascade with the upstream reference measurement plane position shown and the testing area, highlighted in yellow. The fillets and film-cooling were employed in the testing area at the bottom endwall in the passage between Vanes 3, 4 and 5.

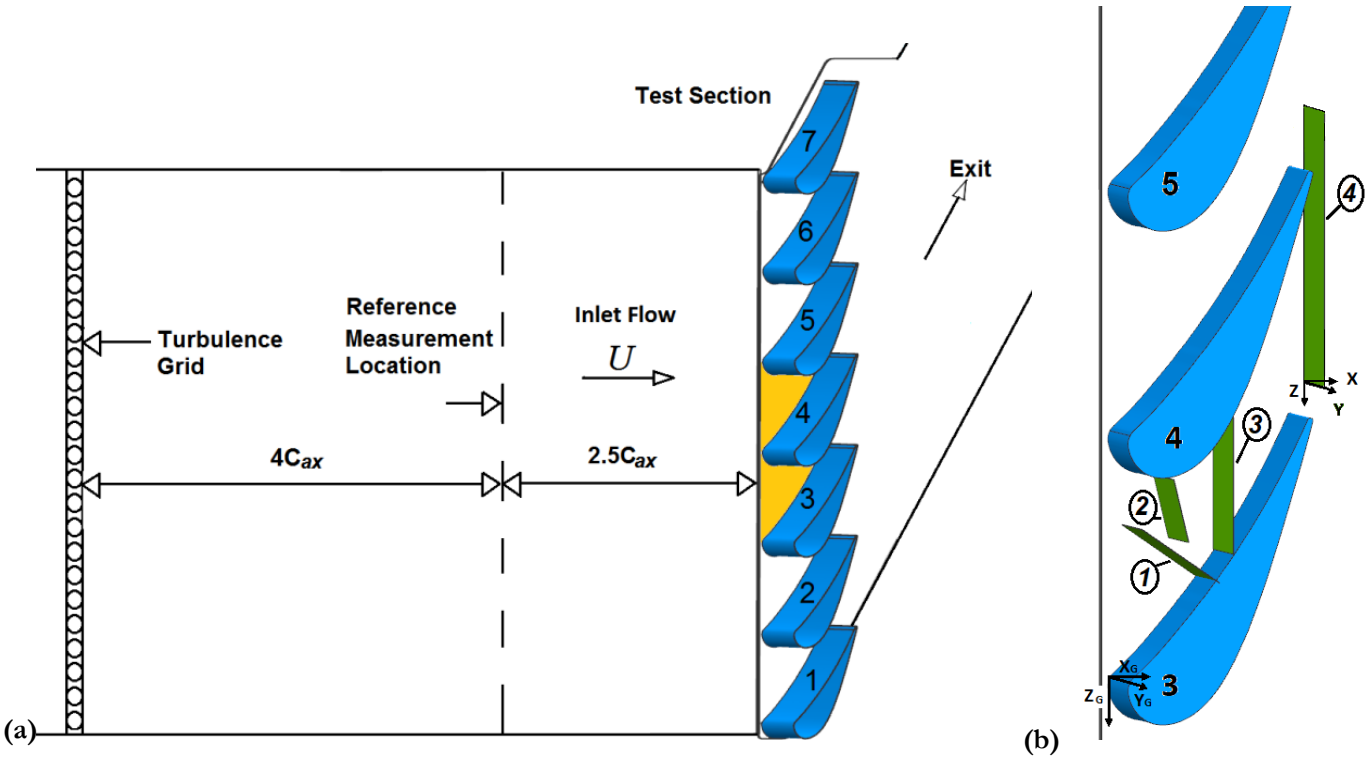

Figure 8: *Experimental set-up: a) linear vane cascade, and b) measurement planes with global coordinates (X_G, Y_G, Z_G) and local coordinates (x, y, z).*

The test section consisted of seven two-dimensional vanes marked as 1, 2, 3, ..., 7 in ***Figure 8***. The cascade geometry was obtained from the hub side of the GE-E^3 first-stage nozzle guide vane blade profiles [62] with two flat endwalls. ***Table 3*** presents all the vane geometric parameters and incoming flow characteristics.

Table 3: *Vane geometry and flow conditions.*

Cascade design details	
Blade actual chord	354.5 mm
Blade axial chord	202.6 mm
Blade span	240 mm
Blade pitch	267 mm
Inlet flow angle	0°
Blade exit angle	74°
Reference velocity	10 m/s
Reynolds number (based on reference velocity and vane actual chord)	2.0×10^5

The flow condition was considered incompressible because of the low subsonic test speed. Turbulence in the incoming flow was generated by employing a passive cylindrical grid of 6 mm cylindrical metal rods, with a spacing of 20 mm across the tunnel duct. The turbulence grid was positioned at 6.5 C_{ax} upstream of the vane cascade inlet. The reference turbulent intensity, measured with a constant temperature anemometer (CTA) system manufactured by Dante Dynamics™, was 3% in the free stream away from the endwall. The CTA software is automated to record each measurement location specified by an input file containing 36 spatial coordinates covering a rectangular grid in the inviscid region at the reference location (Y-Z plane). Each point is recorded with a frequency of 20 kHz and 40 000 samples for both channels (u- and v-velocity). The approaching boundary layer thickness was $\delta/S=0.1$ at the measurement reference plane, located at $X/C_{ax}=2.5$ upstream of the vane leading edge. All the flow and temperature measurements were obtained with the unheated endwall upstream of the cascade, i.e. no temperature boundary layer at the cascade inlet.

Cut-out slots in the top endwall, drilled holes in the bottom endwall and static pressure taps on the vane surface allowed the insertion of probes into the cascade for the flow field, temperature and pressure measurements respectively. The location of the four measurement planes is provided in ***Table 4*** and illustrated in ***Figure 8-b*** together with the coordinate systems in the test section.

Table 4: *Measurement plane locations*

Planes	Location X_G/C_{ax}
Plane 1 normal to PS	0.49
Plane 2 normal to SS	0.25
Pitchwise Plane 3 normal to X	0.58
Pitchwise Plane 4 normal to X	1.04

A separate flat-top endwall with arrays of static pressure tap holes was employed to measure the pressure distributions along the endwall. The pressure tap holes were connected to a three-channel multiport manual scanning valve with flexible PVC tubing and then to pressure transducers, as shown in ***Figure 9***.

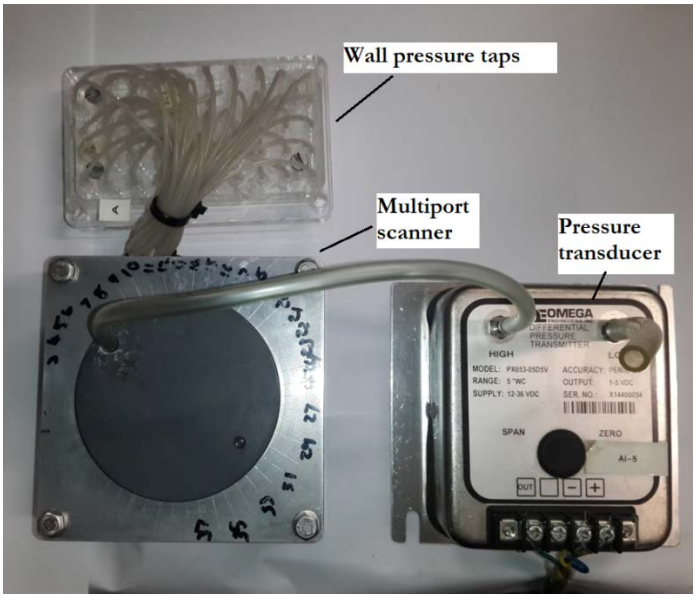

Figure 9: *Multiport manual scanning valve connection to wall pressure taps and pressure transducer.*

The circular movement of the rotary part of the scanner allowed each pressure tap location to be measured.

The walls of the cascade test section were made of commercial-grade transparent acrylic plastic. The vanes were made of acrylic plastic sheets and had hollow cores for easy access to the wall pressure taps. Layers of polyurethane coating were applied for a smooth surface finish on the vane profiles. The diameters of all the wall pressure tap holes were between 0.1 mm and 0.3 mm.

The flow temperature measurements near the bottom endwall were obtained in the first three planes (Planes 1, 2, 3 shown in ***Figure 8-b***), and the flow field measurements were obtained in the third and fourth planes. The global coordinate system (X_G, Y_G, Z_G) took its origin from the leading edge of Vane 3 and the local coordinate system (X, Y, Z) originated on the pressure-sides of Vane 3, as shown in ***Figure 8-b***. The location Z=0 refers to a position on the bottom endwall. All measurements were obtained with periodic flow conditions to simulate the turbine passage flow. Twenty-one pressure taps were located along with the vane profile at the mid-span on each of Vanes 3, 4 and 5, as shown in ***Figure 10-a***. The measured pressure along the three vane profiles was then compared for the periodic flow condition in the cascade. ***Figure 10-b*** presents the static pressure coefficients along with the vane profiles.

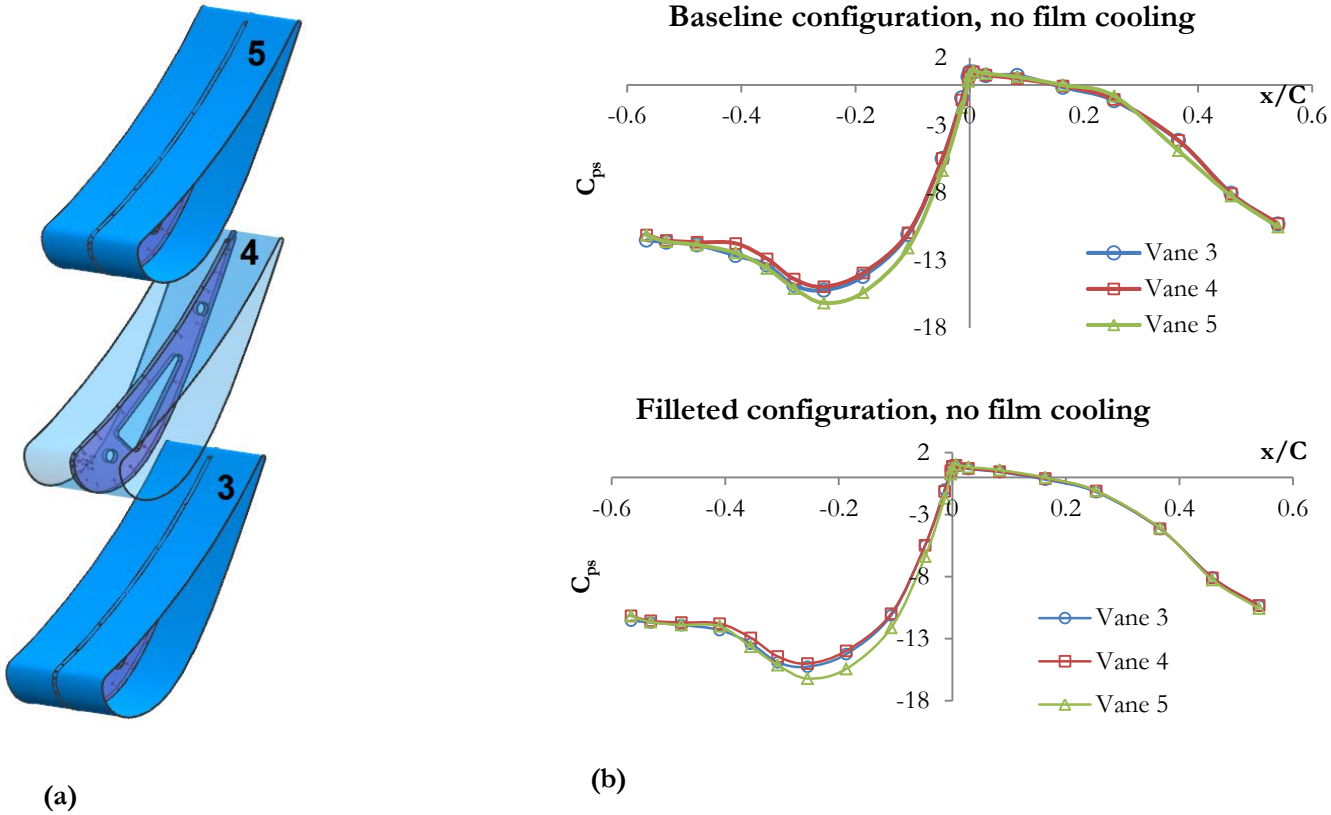

(a) **(b)**

Figure 10: *a) Pressure taps at blade mid-span and b) comparison of static pressure distribution on the central blades.*

The measured surface pressures, $P_{s,loc,}$ along the vane profiles were used to determine the C_{ps} in Eq. (1) with and without film-cooling flow.

$$C_{ps} = \frac{P_{s,ref} - P_{s,loc}}{P_{t,ref} - P_{s,ref}} \qquad (1)$$

The periodicity was confirmed by matching the C_{ps} distributions of Vanes 3, 4 and 5 with each other. The coefficients, $C_{ps,}$ for baseline case and filleted case, are shown in ***Figure 10-b.*** The values of C_{ps} are negative away from the leading-edge region, x/C=0, because of the pressure drop along the vane surface, i.e. $P_{s,\,ref} > P_{s,loc}$. The mass balance of flow, between the three passages, is reflected by the similarity in the C_{ps} distributions in each plot.

4.2. Fillet design

An asymmetric fillet was designed for the leading-edge contouring investigation, following the investigations by Zess and Thole [57], Mahmood and Acharya [61], and, Han and Goldstein [55]. The large extent of the present fillet, upstream of the leading edge, was intended to accelerate the flow in the boundary layer as it approached the leading edge in a similar way to the endwall contour [52].

Some preliminary computational fluid dynamics (CFD) analyses of the test passage of cascade were conducted with the different leading-edge fillet designs. A 2.69 million cells (structured hexahedral and quadrilateral cells) mesh was employed to simulate the secondary flows in the filleted vane passage model. The SST k-omega model with non-equilibrium wall functions and low Reynolds number correction was used for the turbulence model. The advantage of the SST k-omega model was the near-wall treatment for low Reynolds number computations and it allowed for a smooth shift from a low Reynolds number form to a wall function formulation. The flow field results of the CFD model, with the fillet designs, were primarily used for the qualitative comparisons between the fillet cases. The detailed analyses were not done for any validation and correctness and hence are not presented in the thesis. The results showed trends and effects of the leading-edge modification assessing the effectiveness of reducing the total loss in the vane passage. The magnitude of the total pressure loss at the cascade exit decreased when the fillets were fitted. The fillets reduced the exit flow turning angles in the endwall region, thereby reducing the strength and size of the passage vortex.

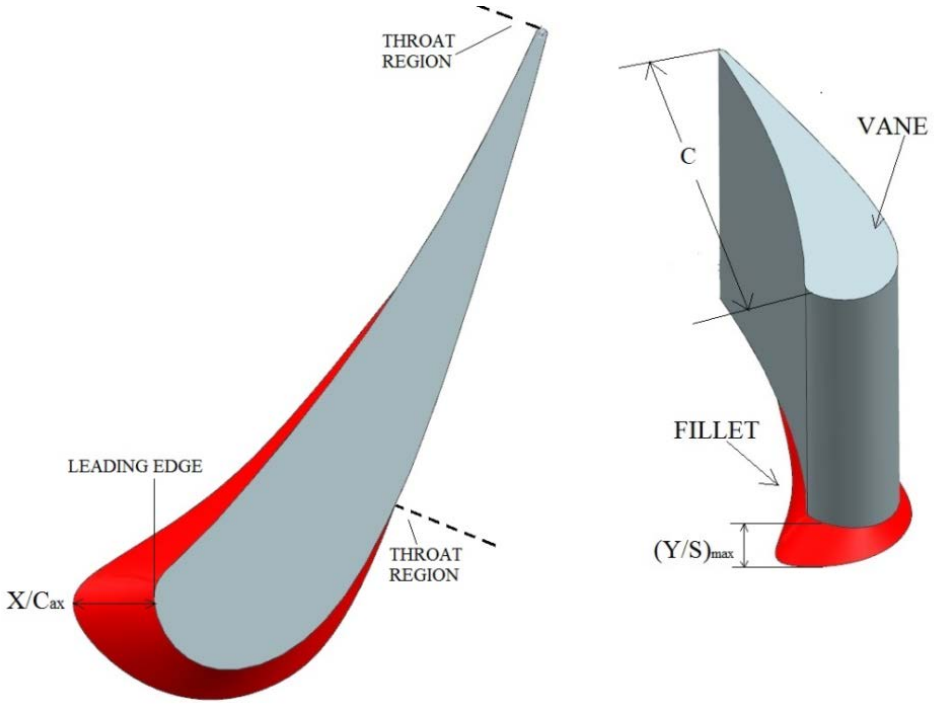

Figure 11: *Fillet geometry.*

Figure 11 displays the fillet that was finally designed for fabrication and testing. The figure shows the placement of the fillet at the vane-endwall junction. The design parameters are indicated in ***Table 5***.

Table 5: *Fillet geometric parameters*

Design parameters	
X/C_{ax}	19.7%
$(Y/S)_{max}$	0.08%
X_G	124.7 mm
X_G/C_{ax}	61.5%

The fillet was particularly large near the leading-edge area to affect the endwall secondary flows, as indicated in [27, 47, 61]. The outline of the fillet profile on the endwall closely followed the vane profile. The fillet's height was set to 0.08 S at the vane leading edge and was about the same as the inlet flow boundary layer thickness. The height of the fillet profile decreased linearly from the vane surface to the endwall, and from the vane leading edge along with the vane profile, to blend smoothly with the vane wall and endwall at the fillet trailing end. The extension of the stagnation point was 0.2 C, which was twice the boundary layers thickness, as suggested by [57]. The profile of the fillet followed the curvature of the vane profile by extending on the suction and pressure-sides until the throat region so as not to affect the vane passage throat design.

For comparison purposes, an existing fillet [63] was tested in the leading-edge cooling investigation. ***Figure 12*** shows the profiles and geometries of the two fillets. The existing fillet, called Fillet 1, extended from the blade leading edge on the blade pressure-side to the trailing edge and on the suction-side, it stopped at the throat region at the axial location of X_G = 0.62 C_{ax}. The pressure-side trailing edge was also the passage throat region.

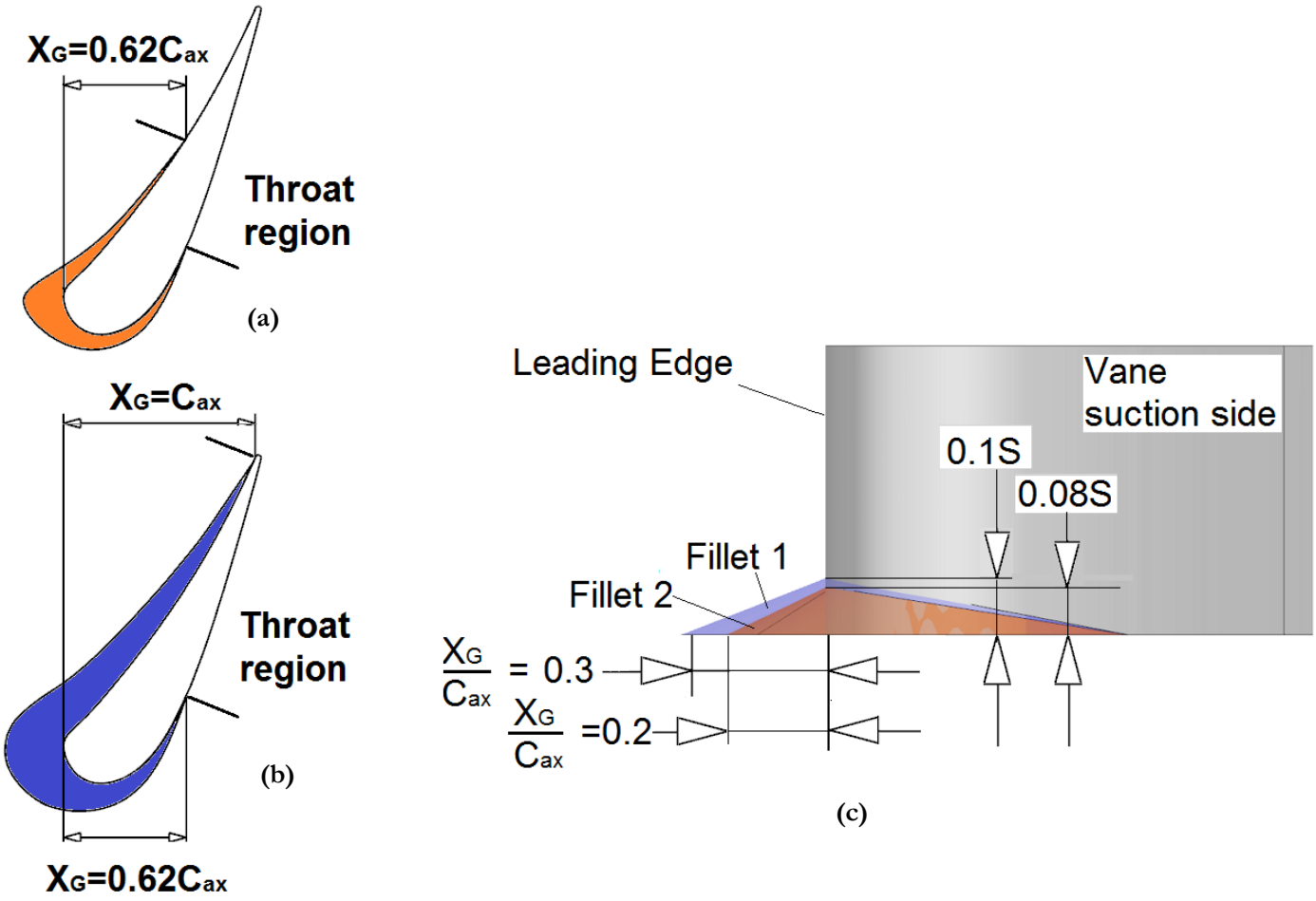

Figure 12: *a) Fillet 2, b) Fillet 1 geometry and c) Fillet side view.*

The second fillet, which was newly designed and fabricated, was called Fillet 2. It extended from the blade leading edge to the axial location of X_G = 0.62 C_{ax} on both the vane pressure and suction-side. The maximum height was different between Fillet 1 and Fillet 2, as shown in ***Figure 12-c***. Their maximum height was at the leading edge from where it varied linearly from the blade surface to the endwall and towards the trailing edge.

The two fillets, Fillet 1 and Fillet 2, were fabricated in a three-dimensional (3D) printer using the ABS material with high-density filling. The 3D printing had the surface chemically treated to reduce surface roughness and any surface leaks.

4.3. Film-cooling design

A flow circuit, depicted in ***Figure 13***, employed on the outside of the bottom endwall, supplied the film-cooling flow in the cascade test passages through the coolant holes in the bottom endwall. Metered pipe sections with ISO standard orifice plates provided the measurement of the coolant mass flow rate.

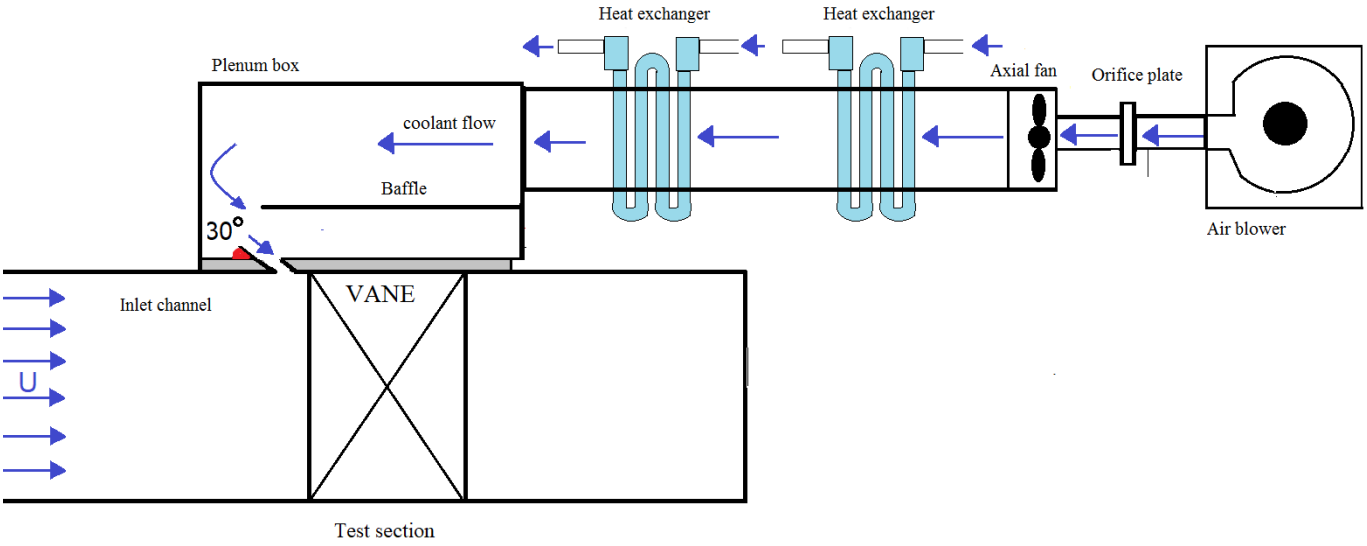

Figure 13: *Cooling flow circuit.*

The inlet overall blowing ratio, M, of the overall film-cooling flow was computed as:

$$M = \sqrt{\left(\frac{P_{t,plenum} - P_{s,ref}}{P_{t,ref} - P_{s,ref}} \right)} \tag{2}$$

The average density ratio between the coolant and upstream flow in the cooling testing was about 1.05. The mass flow rate of film-cooling flow was defined as:

$$\dot{m}_c = \rho C_d \left(\frac{\pi}{4} D_{orifice}^2 \right) \sqrt{\frac{2\Delta P_{orifice}}{\rho\left(1-\beta^4\right)}} \tag{3}$$

$\Delta P_{orifice}$ is the pressure difference in the orifice. The β ratio (ratio of orifice diameter to internal pipe diameter) of 0.7 based on ASME standards and discharge coefficient, C_d, for different holes geometries were obtained from a previous study [64].

The mass fraction ratio MFR of the film-cooling flow was defined as:

$$MFR = \frac{\dot{m}_c}{\dot{m}_p} \tag{4}$$

The chiller unit of a vapour compression system employed in the flow circuit controlled the film-cooling flow temperature. The flow was fed into the film-cooling slots and holes through a large plenum beneath the bottom endwall. The plenum covered more than the entire section of the bottom endwall in the measurement passages. The plenum walls and endwall surface on the plenum side were thermally insulated. The cooling of the

test section was achieved by LE cooling plates and passage cooling endwall. The endwall, just upstream of the cascade, had a cut-out for a replaceable insertion rectangular plate, the so-called LE cooling plate. The plate was located in the bottom endwall, at 0.079 C_{ax} upstream of the cascade inlet, and the coolant hole was always at a 30° angle to the main upstream flow. Different configurations of coolant holes were machined in the insertion plate. Once the plate with one configuration of coolant holes was investigated, it was replaced by another plate with a new configuration of coolant holes for testing. Ideally, a film coolant should come out from the endwall surface tangentially to provide a uniform layer of coolant that stays attached to the surface. Thomas and Povey [65] made used of the momentum of cooling jets to control vane secondary flows. They argued that an increase in near-wall total pressure caused by a properly designed film-cooling configuration can oppose the momentum deficit in the boundary layer and lead the flow through the passage to achieve more uniform flow streamlines at the exit. The challenge in this research was to find a cooling hole configuration that allowed the coolant to cover the large uncooled region around the vane leading edge and the pressure-side endwall due to the influence of the passage vortex on the coolant trajectory. As the coolant jets interacted with the pressure-side leg vortex and the suction-side leg vortex along the boundary layer's separation line, they were lifted away from the endwall and the coolant was swept towards the vane suction-side.

Figure 14 shows the locations and arrangements of the film-cooling configuration and cooling plate geometries relative to Vanes 3, 4 and 5 in the endwall just upstream of the cascade. Four film-cooling plates with different hole geometries were investigated: A) bleed slots of a discrete configuration, B) a combination of discrete slots and cylindrical holes, C) rows of cylindrical holes, and D) a single row of diffused cylindrical holes.

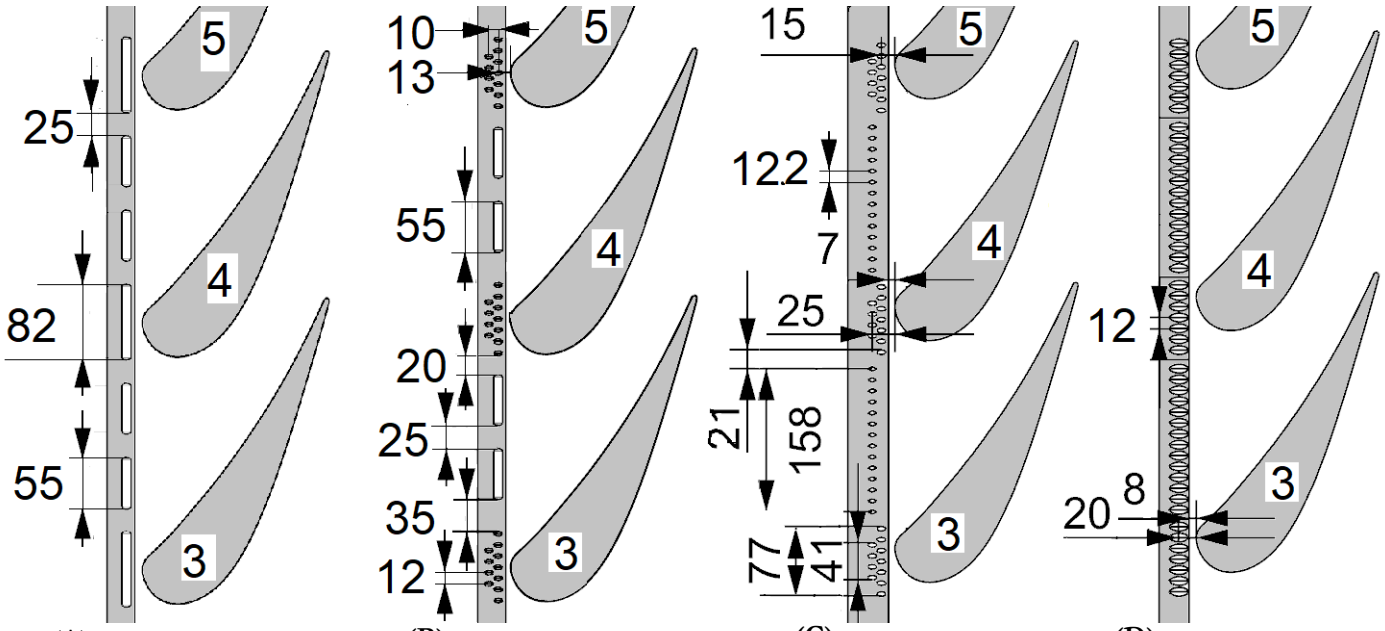

Figure 14: *Geometry of film-cooling configurations in mm: Case A) bleed slots, Case B) slots and holes, Case C) cylindrical holes, Case D) diffused cylindrical holes.*

The first plate consisted of four slots, identified as Case A in ***Figure 14***. The slots, located in front of the vane's leading edge, extended over 82 mm in length in the pitch-wise direction. Between them, there were two shorter slots of 55 mm length in the centre of the passage. Each slot was equally spaced apart by 25 mm. The second plate had two discrete slots of 55 mm length at the pitch-wise middle position and cylindrical holes placed in two rows in the leading-edge region. The holes were spaced 12 mm apart and located 35 mm apart from the slot. The slot width (D) of 5 mm and the orientation angle at 30°, relative to the endwall surface, were

the same as the hole diameter and orientation, as shown in ***Figure 15***. Both slots and holes were machined into acrylic plates.

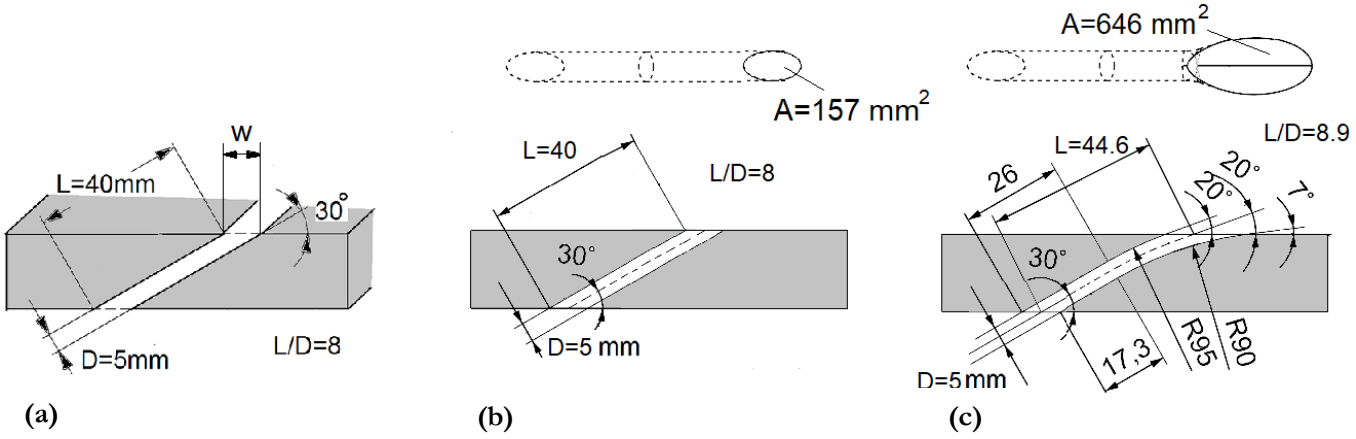

Figure 15: *Cross-section of film-cooling configurations: a) slots, b) cylindrical holes, c) diffused cylindrical holes.*

In the last two plates, identified as Case C and Case D in ***Figure 14***, two types of holes were separately employed in the film-cooling plate: simple cylindrical holes (in the Case C arrangement) with the ratio, L/D = 8 and diffused cylindrical holes (in the Case D arrangement) with the ratio, L/D = 8.9. As shown in ***Figure 14***, some of the cylindrical holes in Case C were placed in one pitch-wise row between the vanes and the others in two pitch-wise rows in the leading-edge region as Case B. Note, the pitch-wise spacing between the holes was different for Case C.

Case D consisted of a single pitch-wise row of diffused cylindrical holes, equally spaced 12 mm apart. The holes on all three plates had the same diameter of 5 mm at the inlet. The compound or yaw angle relative to the main flow direction, X_G was 0°, for both the cylindrical and diffused holes in the endwall upstream of the cascade inlet. Most of the past cascade investigations reported in the literature employed cylindrical holes at angles between 25° and 35°, with the 0° compound angle in the upstream endwall. The cylindrical holes in the current investigation were drilled in an acrylic plate, used as a film-cooling plate, as shown in ***Figure 15-b.***

The diffused cylindrical holes were designed by curving the cylindrical holes in the forward diffusion form only. They were created by diffusing the cylindrical hole in the forward direction only in the meridional plane of cross-section, as indicated in ***Figure 15-c***. As shown in the figure for the Case D hole geometry, the lines on the cylinder surface, in the meridional cross-section, started to diffuse at 17.3 mm along a circular arc towards the downstream and at 26 mm along a circular arc towards the inward or meridional axis line (broken line). The cross-sections of the diffused hole, at every point on the meridional axis, were circular to generate diffusion of the hole area primarily in the forward direction along X_G. The exit of the diffused hole was then angled at 7° at the front lip side and 20° at the rear lip side relative to the endwall in the meridional cross-section. The ratio of L/D = 8.9 for the diffused hole was then based on the camber axis length of L = 44.6 mm at the meridional cross-section. The planar area of the hole exit on the endwall was 157 mm^2 for the cylindrical hole and 646 mm^2 for the diffused hole. The geometry of diffused cylindrical hole was based on two reasons: (i) to avoid a flow separation of coolant inside the hole, and (ii) to eject the coolant smoothly to minimise the penetration into the boundary layer and transport the coolant adjacent to the endwall long distance by its momentum. An abrupt change in flow angle, in the diffusion of the fan-shaped hole, introduces flow separations [66, 67] resulting in additional pressure losses in the cascade.

The present test set-up did not allow any flow measurements inside the film-cooling holes. The work of Gritsch et al. [68] suggests any ratio of 7.5 < L/D < 11.5 is optimum for the film-cooling effectiveness. The

metering section of the current diffused hole, which was the constant diameter inlet section, had a length-to-diameter ratio of 4.3 based on [65, 68] to fully develop the coolant flow upstream of diffusion. The net forward diffusion angle of the hole was 23° (=30° -7°) based on the inlet and exit angles. This value of 23° was much larger than the common diffusion angles, between 7° and 15°, employed by many recent investigations, e.g. [22, 23, 26-29, 66-72]. Only one geometry of the diffusion hole, shown in ***Figure 15-c,*** was tested. Variations in diffused hole geometries can be the subject of future experiments.

The present diffused holes were printed in a commercial three-dimensional printer with the standard ABS plastic filament. The porosity in the printing was set at 0%. The printed film-cooling plate was chemically treated for a smooth surface finish inside the diffused hole and, to minimise leaks, through the printed plate volume. The passage cooling hole endwall, referred to as Case E, was the last cooling configuration that was tested. The cooling holes in the endwall, downstream of Blade LE, were designed according to [14, 36] to increase the film-cooling effect in the passage and reduce the secondary flow effect on the cooling jets. The locations and configurations of the holes are shown in ***Figure 16***. Six of the cooling holes were located along an isobar line on the endwall, which was identified by a static pressure coefficient value of C_{ps} =-2, shown in ***Figure 16-b***. The remaining holes were positioned to avoid the 3D separation region of the endwall boundary layer as much as possible and to provide uniform film-cooling distributions pitch-wise.

The contours of static pressure coefficient distributions, shown in ***Figure 16-b***, obtained with the CFD simulation indicate how the flow accelerated along the endwall through the passage, by illustrating the local static pressure on the endwall. The values for C_{ps} decreased along the passage in the axial direction, due to the flow accelerations caused by the area's reduction and the approach of the throat region.

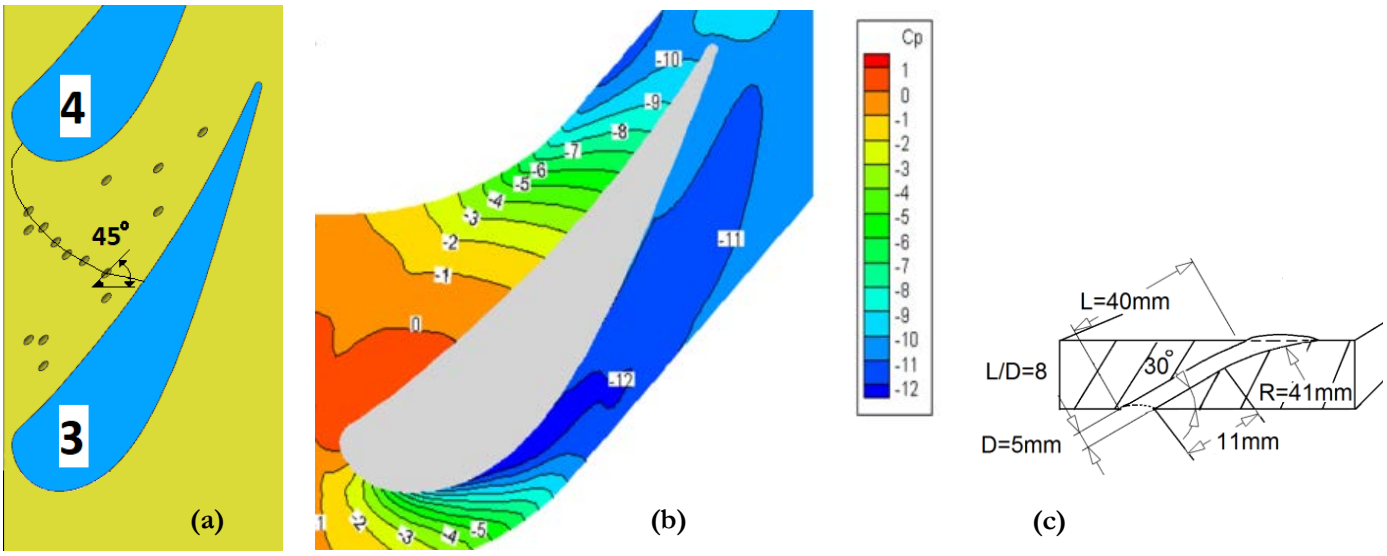

Figure 16: *a) Layout of passage endwall film-cooling holes along the isobar lines and inviscid streamlines, b) isobar lines obtained by CFD study and c) cross section of endwall film cooling.*

Furthermore, the existence of the pressure gradient between the pressure and suction-sides drove the cross-flow in the passage and enhanced the migration of the passage vortex along the endwall. The values for C_{Ps} on the endwall were negative because the wind tunnel operated under suction conditions. As the endwall pressure-side was difficult to cool [72], more film-cooling holes were positioned near the pressure-side than near the suction-side. The cooled endwall inside the measurement passage included 15 outlet cylindrical holes with the ratio L/D = 8, drilled in an acrylic plate, shown in ***Figure 16-c***. The axes of all the cooling holes were oriented at 30° at the inlet relative to the endwall surface, shown in ***Figure 16-c***, and 45° relative to the upstream main flow, shown in ***Figure 16-a.*** The holes also had the same diameter of 5 mm at the inlet.

5. Data acquisition system and uncertainty estimates

5.1. Overview

All the measurements were obtained with steady-state and periodic flow conditions in the vane passages. The inlet flow conditions were measured at the reference plane located at 2.5 C_{ax} upstream of the cascade passage inlet, as shown in ***Figure 8***. The free-stream reference temperature was measured by a thermocouple, while the reference total static pressures and velocity were measured by a Pitot static probe with the specifications provided in ***Table 7***. The flow field and local temperature measurements inside the cascade test passages were taken with a commercial five-hole pressure probe and temperature probe respectively. The probes were traversed in the four measurement planes with an automatic transverse mechanism. A schematic of the instrumentation layout is shown in ***Figure 17***.

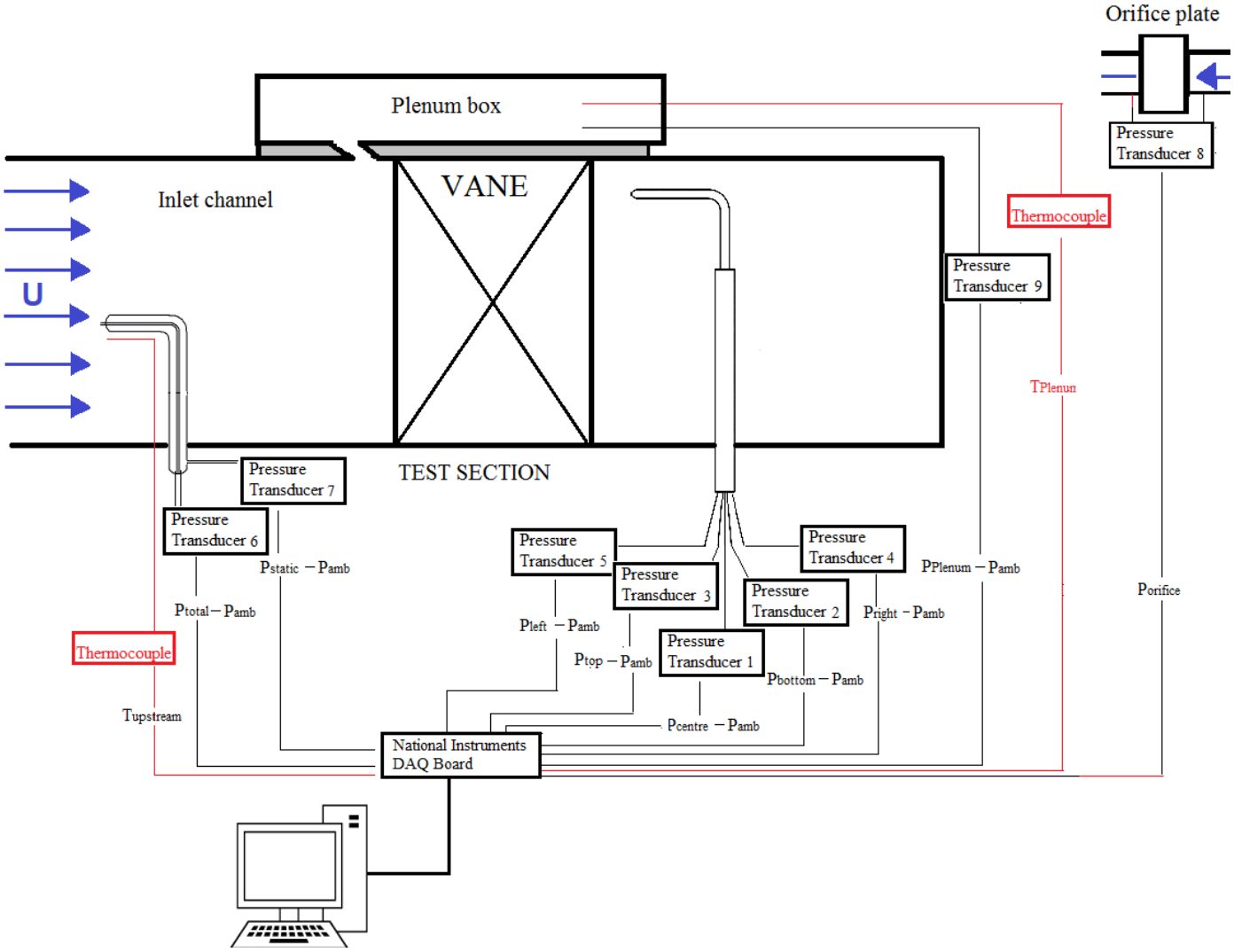

Figure 17: *Schematic of the instrumentation layout.*

An in-house configured LabView$_{TM}$ program controlled the motor controller based on a data location grid. The five-hole pressure probe measured the local velocity components (u_x, u_y, u_z), total pressure, static pressure, and pitch and yaw angles of the flow. The probe sent signals to five differential pressure transducers calibrated against the Setra MicroCal pressure calibrator. The output voltages from transducers were digitised and recorded by a National Instruments TM data acquisition system. The sampling frequency was 100 Hz for a sampling period of two seconds from each transducer. A single LabView$_{TM}$ program captured the voltage signals and time

averaged the signals as well as controlled the probe motion in the measurement plane. The five-hole pressure probe had a cylindrical tip of 2.4 mm in diameter. Flexible plastic tubes connected the five pressure ports onto independent transducers, which represented the primary instrumentation of which the specifications are shown in *Table 6*.

Table 6: Primary instrumentation.

Primary Instrumentation	Instrument	Range (kPa)	Bias error Manufacturer's component (Pa)	Max Uncertainty (Pa)	Max Uncertainty %
Differential Pressure 1	Siemens Sitrans P 7MF4433-1CA02-1BB6-Z	0-6	4.5	±12.5	13.5
Differential Pressure 2	Omega PX653	0-103.4	3.1	±17.7	4
Differential Pressure 3	Omega PX653	0-103.4	3.1	±23.1	6.2
Differential Pressure 4	Omega PX653	0-103.4	3.1	±16.4	4.3
Differential Pressure 5	Omega PX653	0-103.4	3.1	±15.9	4.6
Differential Pressure 6($P_{t, ref}$)	Omega PX2650	0-68.9	1.24	±1.5	5.8
Differential Pressure 7($P_{s, ref}$)	Omega PX2650	0-68.9	1.24	±1.7	2
Differential Pressure 8(P_{plenum})	Omega PX164	0-3.4	12.4	±12.4	4.3
Differential Pressure 9($P_{orifice}$)	Omega PX164	0-3.4	12.4	±12.8	4.1

Table 7 describes the characteristics of the secondary instrumentation, including the flow measurement probes.

Table 7: Secondary instrumentation.

Secondary Instrumentation	Instrument	Uncertainty
Reference Speed	Pitot pressure probe PDA-18-F-16-KL	0.075% of the full scale
Temperature	Thermocouple Type -T	0.1°C
Steady Flow Mapping	5-hole cobra probe -40° to 40° Pitch-40° to 40° Yaw	0.075% of the full scale
Bi-linear Transverse Mechanism	VEXTA PK268-03A driven by Velmex TM drive	0.01mm
Data Acquisition	National Instruments TM NI-USB- 6001	
Multiport Scanner Ports	Custom three output ports with 21 pressure taps	

5.2. Pressure probe measurements

A five-hole pressure probe was used for pressure measurements in all the cascade measurement planes, in the blade passage and at the blade trailing edge. The cylindrical tip of the five-hole pressure probe had the side pressure holes drilled perpendicular to the side of the cone to reduce sensitivity to change in Reynolds number [73].

***Figure 18**: Tip of the five-hole pressure probe.*

The five-hole probe was calibrated in the same wind tunnel housing the cascade. The calibration procedures were the same as in Ligrani et al. [74]. Appendix A shows the calibration results where the definitions of the different calibration pressure coefficients were also obtained from Ligrani et al. [74]. The calibration was done by rotating the probe across a range of ±25° yaw and pitch angles with increments of five degrees at a speed of 15 m/s. The bottom endwall was assumed adiabatic when film-cooling flow was present. The cobra tip arrangement ensured that the position of the probe tip and vertical stem or axis were in the same place as the probe moved. The probe coordinate system, x, y, z, was introduced at the tip to define the pitch and yaw angles. As can be seen in ***Figure 19***, the *x*-axis was in the nominal flow direction, while the *y*-axis was parallel to the stem of the probe. The coordinate and angle definitions, used in this thesis, were based on the right-handed coordinate system, as shown in ***Figure 19***, and based on Ligrani et al. [74].

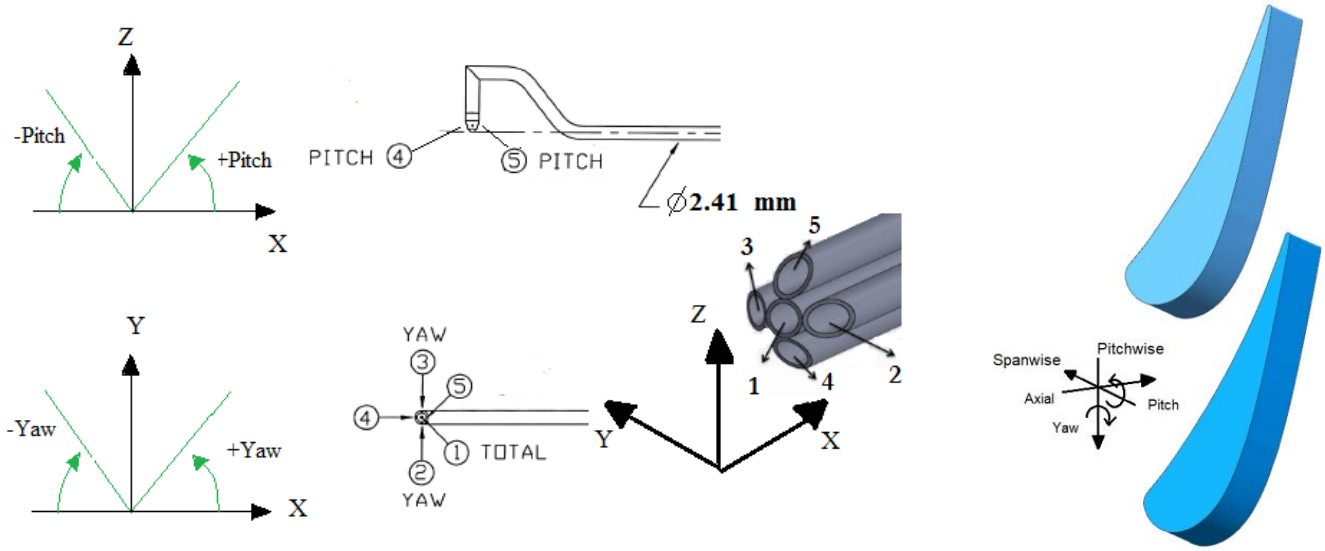

***Figure 19:** Definition of pitch and yaw angle for the five-hole pressure probe.*

The zero yaw angle was defined when the pressures at Ports 2 and 3 were about the same, with pressure margin of 1.8 Pa (49.9 Pa and 51.7 Pa respectively). The zero pitch angle was defined when the pressures at Ports 4 and 5 were the same. During calibration, yaw and pitch angles, total and static pressures were calculated using the following non-dimensional calibration pressure coefficients according to Ligrani et. al. [74]:

$$C_{p_{pitch}} = \frac{P_4 - P_5}{P_1 - P_{average}} \tag{5}$$

$$C_{p_{yaw}} = \frac{P_2 - P_3}{P_1 - P_{average}} \tag{6}$$

$$C_{p_{total}} = \frac{P_{t,ref} - P_{average}}{P_1 - P_{average}} \tag{7}$$

$$C_{p_{static}} = \frac{P_{t,ref} - P_{s,ref}}{P_1 - P_{average}} \tag{8}$$

The average pressure is defined as:

$$P_{average} = \frac{P_4 + P_5 + P_2 + P_3}{4} \tag{9}$$

Subscript 1 indicates the central port, P_2 and P_3 are measured in the yaw plane, and P_4 and P_5 are measured in the pitch plane. The pressure ports, 2, 3, 4, 5 at the probe tip, obtained data at finite distances from the tip centre location. The streamlines near the probe tip deviated due to the blockage by the probe finite tip diameter. To account for the spatial distances of the pressure data and the streamline curvature at the probe tip location, the spatial resolution corrections and one-dimensional downwash velocity corrections were applied, as suggested by Ligrani and Bradshaw [75]. The probe tip was orientated tangentially to the vane pressure surface at each measurement plane to reduce the flow yaw angle corrections. The in-house LabView$_{TM}$ program converted the voltages from the pressure transducers into the units of pressure [Pa] and calculated velocity [m/s] and flow angles after applying the probe calibration curve and correction factors.

The flow field measured in each plane was achieved by traversing the five-hole probe over a measurement grid consisting of 1 500 data points. In the span direction, the step started at 3 mm above the endwall due to the tip diameter, with finer grid resolution in the y-direction at the proximity of the endwall. The probe typically completed about 30 span-wise traverses (to mid-span) and covered about 35 to 60 pitch-wise positions depending on the measurement plane dimensions. The high-resolution measurement spacing next to the endwall aimed to capture the secondary flow structures. ***Figure 20*** presents an example of measurement points and the results of the total pressure coefficient $C_{pt,\,loss}$ contour lines at the exit plane (Plane 4).

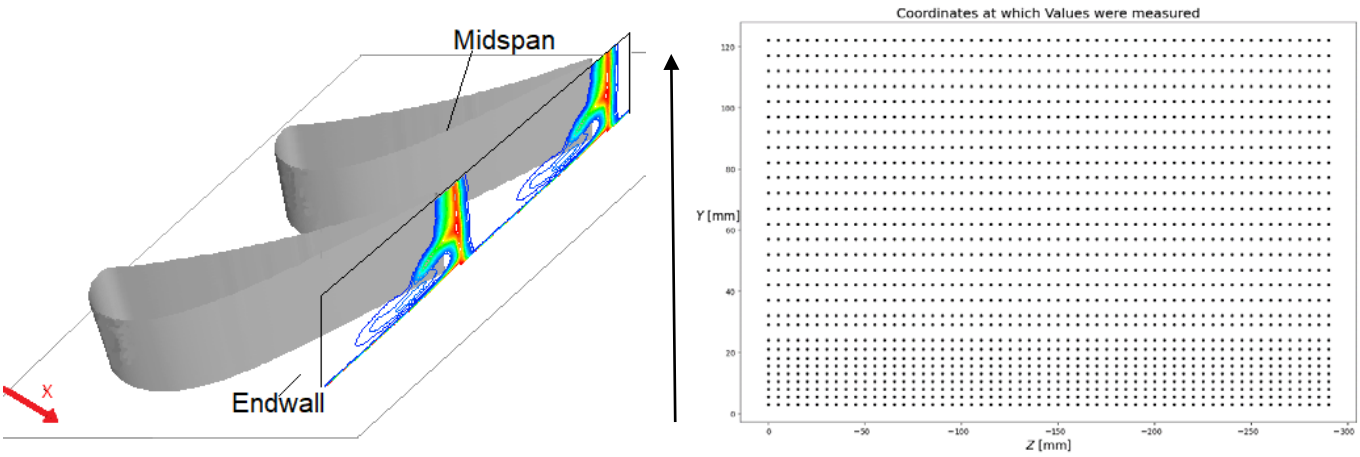

Figure 20: *Example of measurement points and the results of the total pressure coefficient $C_{pt,\,loss}$ contour lines at the exit plane.*

The local aerodynamic loss was determined by the total pressure coefficient $C_{pt,loss}$. The total pressure data were normalised by the reference conditions to determine the $C_{pt,loss}$ as shown in Eq. (10):

$$C_{pt,_{loss}} = \frac{P_{t,ref} - P_{t,loc}}{P_{t,ref} - P_{s,ref}} \tag{10}$$

For flow vector analysis, the local velocity vector components were determined by Eq. (11) to (13):

$$u_x = \mathrm{V} * \cos(YAW)\cos(PIT) \tag{11}$$

$$u_y = \mathrm{V} * \sin(PIT) \tag{12}$$

$$u_z = \mathrm{V} * \cos(PIT)\sin(YAW) \tag{13}$$

In equations (11)-(13), PIT is the pitch angle and Yaw is the yaw angle. The axial component of the vorticity along the x-direction was calculated as:

$$\omega_x = \frac{\partial u_z}{\partial y} - \frac{\partial u_y}{\partial z} \tag{14}$$

5.3. Temperature field

Temperature measurements of the flow field with film-cooling flow were obtained with an in-house built temperature probe at three measurement planes, Plane 1, 2 and 3. The temperature probe was a 5 mm diameter steel rod with K-type insulated thermocouple wires, butt-welded at the end to form a junction between two hypodermic needles, as suggested by [76]. The thermocouple ends were connected to the DAQ system, as shown in *Figure 21*.

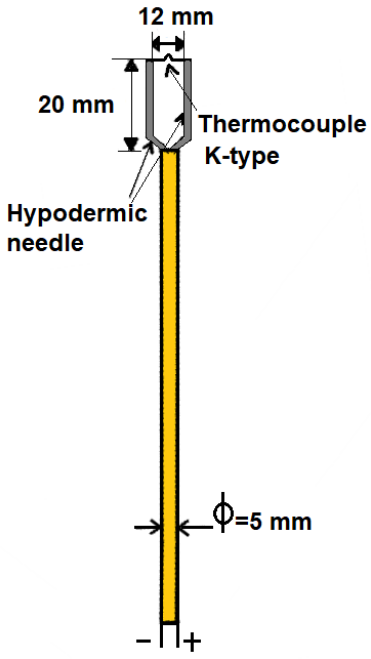

Figure 21: Temperature probe sketch.

The probe, calibrated with a water bath calibrator, was mounted on a two-axis motorised traverse system driven by a motor controller. A LabView$_{TM}$ program controlled the motor controller and captured and time

averaged the temperature signals digitised by a National Instruments$_{TM}$ data acquisition unit. The signals from the probe were time averaged at 60 Hz over 2 sec.

The non-dimensional static temperature (θ) of the flow was then mapped using the following equation:

$$\vartheta = \frac{T_{loc} - T_{plenum}}{T_{ref} - T_{plenum}} \tag{15}$$

In Eq. (15), T_{loc} and T_{plenum} respectively are the calibrated temperatures in K from the thermocouple probe and the cooling plenum box.

5.4. Uncertainty analysis

In any experimental investigation, it is important to scrutinise the uncertainty that is an estimation of the error of measurement. The uncertainty can be divided into systematic error or bias, caused by all the instruments, and random error or precision error, related to the standard deviation value of the measured data. All the detailed calculations are provided in Appendix B.

5.4.1. Instrumentation

Systematic errors are reduced by instrument calibration and correction and are stated by the manufacturer. In this analysis, the bias for all instruments was calculated and, in most cases, it was considered as the accuracy specified by the manufacturer. The precision error was acquired from the standard deviation of N=100 data points obtained during each experiment and multiplied by the Student's t-variable to fall within the 95% confidence level. Examples of the uncertainty analysis are provided in Appendix B.

5.4.2. Pressure transducers

The uncertainty of a single measurement was based on the bias, b_i, and precision error, p_i, calculated according to [77] as follows:

$$\partial u_{xi} = \sqrt{b_i^2 + p_i^2} \tag{16}$$

The bias errors of the pressure transducers that were used in the experiments were determined via linear least-squares regression analysis. The calibration curve was obtained by a linear curve fit through 14 calibration points. The precision error of the pressure transducer was calculated according to a linear regression analysis [77], which determined the mathematical relation between two or more variables x_i. The pressure transducers were calibrated through a Setra MicroCal pressure calibrator (+/-0.04% full scale, 3550Pa).

The uncertainties of total and static pressures, respectively $\partial \bar{P}_{t,ref}$ and $\partial \bar{P}_{s,ref}$, acquired with the Pitot pressure probe at the reference plane were:

$$\bar{P}_{t,ref} = 26.3\ Pa \qquad \partial \bar{P}_{t,ref} = \pm 1.5\ Pa$$

$$\bar{P}_{s,ref} = 86.8\ Pa \qquad \partial \bar{P}_{S,ref} = \pm 1.7 Pa$$

being $\bar{P}_{s,ref}$ the average(mean value) static pressure.

5.4.3. Thermocouples

The thermocouples were calibrated between -5 °C and 25 °C at 1 °C intervals through a thermostat-controlled bath, Lauda Alpha Ra 8, with a bath measurement accuracy of 0.1 °C. The uncertainty of each thermocouple was obtained with the same procedure as the one for the pressure transducers. The uncertainties of the thermocouple at the reference plane, ∂T_{ref}, and in the plenum, ∂T_{plenum}, for the nominal temperature of T_{ref} of 28.7 °C and T_{plenum} of 14.2 °C were:

$$\partial T_{ref} = \pm 0.11℃ \qquad \partial T_{ref}\% = 0.38\%$$

$$\partial T_{plenum} = \pm 0.1℃ \quad \partial T_{plenum}\% = 0.74\%$$

5.4.4. Measurement system errors: calculated results

Typically, a parametric result (R) of an experiment is estimated from a set of variables represented by:

$$R = R(x_1, x_2, x_3, \dots, x_n) \tag{17}$$

For a single known or computed uncertainty x_i, the uncertainty of the results ∂R depended on the individual uncertainties ∂x_i at P%=95% probability of the n measurements

$$\partial R = \frac{\partial \mathrm{R}}{\partial \mathrm{x_i}} \partial x_i \tag{18}$$

The uncertainty in R(x) is ∂R about mean $\bar{R}$ and the true value of calculated variable is R' calculated as:

$$R' = \bar{R} \pm \partial R, \text{ (at P\%=95\%)} \tag{19}$$

$$\partial R = \sqrt{\sum_{i=1}^{n} \left(\frac{\partial R}{\partial x_i} \partial x_i\right)^2} \tag{20}$$

In the terms ∂x_i's there are included both bias and precision errors associated with the measured variable x_i.

5.4.5. Five-hole probe

The uncertainty of the flow direction results, calculated in the data reduction, depended on the uncertainty of the five values of the probe pressures measured in the experiment and propagated uncertainty into the calculated parameters. For the experiments, the uncertainty of the five pressure holes was evaluated only in the third and exit planes where the five-hole pressure probe was used, at blowing ratio M=1.3, *Table 8* and *Table 9* respectively.

Ten measurement datasets for all pressures of the five-hole pressure probe readings were considered at three distinct regions. In the third plane, the regions were the endwall pressure-side, inviscid region and suction-side.

An in-house Fortran program used to correct the pressure reading from the five-hole probe gave the five pressure readings P_1, P_2, P_3, P_4, P_5. Minimum and maximum uncertainty values in each region are reported in *Table 8*.

Table 8: Pressure uncertainties of five-hole pressure probe in the third plane.

	Endwall pressure-side		Inviscid region		Suction-side	
	∂P (Pa)	∂P %	∂P (Pa)	∂P %	∂P (Pa)	∂P %
P_1	±1.69	3.20	±1.63	3.11	±1.72	2.95
	±2.67	8.94	±2.49	10.15	±3.71	6.19
P_2	±4.83	1.09	±4.20	1.17	±6.69	0.92
	±12.93	4.00	±10.65	2.18	±17.74	2.65
P_3	±4.82	1.39	±4.15	1.43	±5.24	1.07
	±16.79	6.19	±11.28	2.76	±23.09	4.16
P_4	±4.43	1.08	±3.99	1.33	±5.34	0.81
	±12.74	4.36	±10.28	2.36	±12.09	1.93
P_5	±4.83	1.20	±4.18	1.17	±5.77	0.89
	±13.77	4.66	±9.97	2.32	±12.47	1.97
$P_{average}$	±4.97	1.37	±4.19	1.28	±1.01	0.92
	±14.15	4.84	±10.36	2.39	±1.91	2.70

In the exit plane, the uncertainties (*Table 9*) were calculated in the following regions: close to the endwall on the pressure-side, along the blade's trailing edge, and lastly, along the span on the suction-side.

Table 9: Pressure uncertainties of five-hole pressure probe in the exit plane.

	Endwall pressure-side		Trailing edge Y=42mm		Inviscid region Z=200mm	
	∂P (Pa)	∂P %	∂P (Pa)	∂P %	∂P (Pa)	∂P %
P_1	±2.14	1.61	±1.81	7.28	±1.67	3.78
	±12.5	13.55	±3.03	12.04	±3.04	9.84
P_2	±5.32	0.92	±9.24	1.46	±7.41	1.24
	±11.29	2	±15.21	2.41	±11.99	1.97
P_3	±5.94	0.83	±8.89	1.29	±8.28	1.13
	±15.07	2.11	±16.85	2.44	±14.09	1.91
P_4	±5.76	0.82	±9.31	1.33	±8.32	1.17
	±14.13	2.04	±16.46	2.35	±13.05	1.9
P_5	±5.78	1.01	±8.37	1.36	±7.55	1.12
	±11.58	1.91	±15.29	2.57	±12.60	1.91
$P_{average}$	±5.8	0.9	±8.97	1.37	±1.01	1.21
	±13.03	2.04	±15.97	2.44	±1.91	1.92

Table 10 and *Table 11* show the range of all the uncertainty values in the three regions in the third and exit planes respectively.

Table 10: Uncertainties of the pitch and yaw angles, the static and total pressure in the third plane.

	Endwall pressure-side		Inviscid region Y=120mm		Suction-side	
	∂(°)	**∂ %**	**∂(°)**	**∂ %**	**∂(°)**	**∂ %**
PIT	±0.14	2.63	±0.001	2.3	±0.001	1.4
	±0.88	11.1	±0.008	4.5	±0.03	3.78
YAW	±0.36	7.1	±0.64	7	±0.2	7
	±0.78	10.5	±0.2	7.8	±1	8.5
	∂P (Pa)	**∂P %**	**∂P (Pa)**	**∂P %**	**∂P (Pa)**	**∂P %**
$\mathbf{P_{s,local}}$	±4.93	1.56	±4.35	1.30	±5.52	1.32
	±13.27	5.13	±9.22	2.38	±14.60	1.23
$\mathbf{P_{t,local}}$	±2.97	4.79	±2.95	4.66	±3.01	4.90
	±4.40	14.16	±3.77	10.94	±5.65	5.14

Table 11: Uncertainties of the pitch and yaw angles, the static and total pressure in the exit plane.

	Endwall pressure-side		Trailing edge Y=42mm		Inviscid region Z=200mm	
	∂ (°)	**∂%**	**∂ (°)**	**∂%**	**∂ (°)**	**∂%**
PIT	±0.024	5.93	±0.15	5.67	±0.093	5.62
	±0.17	5.49	±0.16	6.41	±0.13	6.05
YAW	±0.36	6.8	±0.18	7.03	±0.33	6.95
	±0.85	7.97	±0.25	7.63	±0.6	7.35
	∂P (Pa)	**∂P %**	**∂P (Pa)**	**∂P %**	**∂P (Pa)**	**∂P %**
$\mathbf{P_{s,local}}$	±5.61	0.97	±8.06	1.38	±7.41	1.40
	±11.79	2.04	±13.96	2.39	±11.57	1.91
$\mathbf{P_{t,local}}$	±3.53	4.57	±3.06	6.71	±2.91	5.29
	±20.14	10.74	±4.62	10.61	±4.94	7.18

5.4.6. Local velocity and axial vorticity

During the experiments, only the axial vorticity was evaluated and plotted in the results section, Chapter 6. *Table 12* and *Table 13* summarise the uncertainties of the local velocity and axial vorticity.

Table 12: Uncertainties of local velocities and axial vorticity in the third plane.

	Endwall		Inviscid region		Suction-side	
	∂(m/s)	**∂ %**	**∂(m/s)**	**∂ %**	**∂(m/s)**	**∂ %**
V	±0.27	1.02	±0.25	0.83	±0.21	0.85
	±0.62	2.86	±0.38	1.53	±0.50	0.77
Ux	±0.07	0.34	±0.04	0.16	±0.07	0.55
	±0.32	1.54	±0.13	0.52	±0.28	0.59
Uy	±1.24	70	±1.19	132	±1.68	117
	±1.88	96	±1.74	150	±1.89	192
Uz	±1.54	44	±1.47	43	±2.04	29
	±2.21	85	±2.15	61	±2.61	37
Wx	±0.56	2.9				
	±0.72	5.4				

The uncertainties of u_y (about 140% in the inviscid region and 170% in the suction side region) and u_z (about 65% in the endwall region) were very high in the expected secondary flow regions caused by the unsteadiness of the vortices as well as of the film-cooling flows (yaw and pitch angles were bigger than 25 degrees, outside the calibration map of the five-hole probe).

Table 13: *Uncertainties of local velocities and axial vorticity in the exit plane.*

	Endwall pressure-side		**Trailing edge Y=40mm**		**Inviscid region**	
	∂(m/s)	**∂ %**	**∂(m/s)**	**∂ %**	**∂(m/s)**	**∂ %**
V	±0.20	0.63	±0.27	0.83	±0.25	0.87
	±0.9	3.79	±0.43	1.33	±0.37	1.13
Ux	±0.08	0.24	±0.05	0.14	±0.08	0.33
	±0.26	1.11	±0.08	0.26	±0.14	0.44
Uy	±1.61	108	±1.85	115	±1.83	117
	±1.99	136	±2.09	149	±1.99	194
Uz	±1.76	37	±2.29	112	±2.27	47
	±2.39	70	±2.49	159	±2.40	87
Wx	±0.55	2.9				
	±0.71	5.4				

5.4.7. Reference velocity

The uncertainty of the free-stream velocity was obtained assuming a constant density of ϱ=1.006 kg/m^3. The overall uncertainty for the nominal reference velocity of 10.2 m/s was:

$$\partial U_\infty \% = 0.24\%$$

5.4.8. Coefficient of total pressure

To calculate the total pressure coefficient uncertainty, the uncertainties of the five-hole pressures, $\partial P_{t,loc}$, reference total pressure, $P_{t,\,ref}$, reference static pressure, $P_{s,ref}$ had to be known. ***Table 14*** and ***Table 15*** show the nominal values and the uncertainties of the static and total coefficient.

Table 14: *Nominal values of static and total coefficient of pressure in the third plane and exit plane*

	Third plane			**Exit plane**		
	Endwall	Inviscid region	Suction-side	Endwall	Trailing edge	Inviscid region
$\mathbf{C_{ps}}$	-7.09	-7.54	-7.88	-8.32	-8.58	-8.63
$\mathbf{C_{pt,loss}}$	0.83	0.83	0.88	3.98	0.35	0.77

Table 15: *Uncertainties of static and total coefficient of pressure in third plane and exit plane.*

	Third plane						**Exit plane**					
	Endwall		Inviscid region		Suction-side		Endwall		Trailing edge		Inviscid region	
	∂	**∂ %**	**∂**	**∂ %**	**∂**	**∂ %**	**∂**	**∂ %**	**∂**	**∂ %**	**∂**	**∂ %**
$\mathbf{C_{ps}}$	±0.37	5.27	±0.35	4.69	±0.41	5.21	±0.40	4.8	±0.42	4.97	±0.40	4.72
$\mathbf{C_{pt,loss}}$	±0.07	9.11	±0.06	7.97	±0.09	10.92	±0.54	13.68	±0.07	22.49	±0.06	8.78

5.4.9. Film-cooling inlet blowing ratio

The overall uncertainty of the nominal film-cooling inlet blowing ratio of 1.32 was:

$$\partial M = \pm 0.001 \qquad \partial M\% = 0.8\%$$

5.4.10. Film-cooling flow rate

The average orifice pressure and its uncertainty were:

$$\overline{\Delta P_{orifice}} = 102 Pa$$

$$\partial \Delta P_{orifice} = \pm 2.4 Pa$$

The overall uncertainty of the nominal film-cooling flow ratio of 0.01 kg/s was:

$$\partial \dot{m}_c = \pm 0.0001 \text{ kg/s}$$

$$\partial \dot{m}_c \% = 1.22\%$$

5.4.11. Non-dimensional temperature

The overall uncertainty of nominal non-dimensional temperature was calculated in the third plane.

Table 16 shows the uncertainty of the non-dimensional temperature for minimum and maximum θ in three regions at the endwall, at the suction-side and mid-span.

Table 16: Uncertainties of non-dimensional temperature in the third plane and exit plane.

	$\partial\theta$	$\partial\theta\%$	θ
Endwall	±0.096	17.6%	0.54
	±0.013	1.4%	0.9
Suction-side	±0.022	3.7%	0.58
	±0.015	1.6%	0.94
Mid-span	±0.084	16%	0.52
	±0.024	2.5%	0.91

5.5 Test matrix

Table 17 and *Table 18* provide an overview of all tests.

Table 17: Flow field measurements.

M	Plane	LE cooling plate	Passage cooling hole endwall	Fillet 2	Fillet 1	Baseline
1.8-2.2	3	A				X
1-2.2	3	B				X
1-2.2	3	B			X	
1-2.2	3	B		X		
1-2.8	3	B	X	X		
1.2-2.8	3	C	X	X		
1.2-2.8	3	C				X
1.4-2.4	3	C	X			X
1.4	3	C		X		
1.4	3	C			X	
1.2-2.8	3	D	X	X		
1.2-2.8	3	D				X
1.2-2.8	3	D	X			X
2.2	3	D		X		
2.2	3	D			X	
1.2-2.8	3	E	X	X		
1.2-2.6	3	E	X			X
	3			X		
	3				X	
1.2-2.8	4	B				X
1.4-2.6	4	B			X	
1.2-2.8	4	B		X		
1.2-2.8	4	B	X	X		
1.2-2.2	4	C				X
1.4-2.8	4	C	X	X		
1.4-2.8	4	C	X			X
1.2-2.8	4	D	X			X
1.2-2.6	4	D				X
1.2-2.6	4	D		X		
1.4-2.6	4	D			X	
1.4-2.8	4	D	X	X		
	4			X		
	4				X	
1.2-2.8	4	E	X			X
1.4-2.6	4	E	X	X		
	4					X

Table 18: Thermal measurements.

M	Plane	LE configuration	Passage cooling hole endwall	Fillet 2	Baseline
1.2-2.8	1	D			X
1.8-2.4	2	C			X
1.2-2.8	2	D			X
1.2-2.6	3	A	X		X
1.8	3	A	X	X	
1.2-2.6	3	B	X		X
1.4-2.2	3	B			X
1.4-2.6	3	B	X	X	
1.4-2.2	3	B		X	
1.5-2.6	3	C	X		X
1.2-2.8	3	C			X
1.5-2.6	3	C	X	X	
1.2-2.6	3	D	X		X
1.2	3	D			X
1.5-2.6	3	D	X	X	
1.2-2.8	3	E	X		X
1.2-2.8	3	E	X	X	
2.8	3		X		X

6. Results and discussion

6.1. Experimental test cases of non-cooled cascade

The measurements were obtained at flow state with a pressure variation of ±2 Pa and temperature variation to be ±0.2 °C over 10 minutes. The reference velocity, static pressure and temperature changed by only 0.2 m/s, 0.5 kPa and 0.2 °C respectively, at most between different test cases.

6.1.1. Leading-edge contour study

This section presents the effects of the fillets on the secondary flows without the film-cooling flow in the third and exit pitch-wise planes located at X_G/C_{ax}=0.58 and X_G/C_{ax}=1.04 respectively. The effects were determined by the comparisons of the flow angle deviation, ΔYaw contours, and the total pressure coefficient, $C_{pt,\,loss}$ contours, between the baseline and filleted cases. The two fillets, Fillet 1 and Fillet 2, of which the geometries are illustrated in Section 4.2, were assessed. The ΔYaw and $C_{pt,\,loss}$ distributions at the pitch-wise planes are presented in this section.

A way to visualise the passage vortex is to plot the flow yaw angle deviation values in the passage. The flow yaw angle deviation was estimated from the local yaw angle after subtracting the yaw angle at the mid-span location. As at the mid-span region, the inviscid streamlines were parallel to the passage walls, the positive ΔYaw indicated the streamline turning towards the suction-side and the negative ΔYaw indicated that the streamline was oriented towards the pressure-side of the passage. The streamline turning towards the SS was one of the primary reasons for the passage vortex strength and development near the endwall.

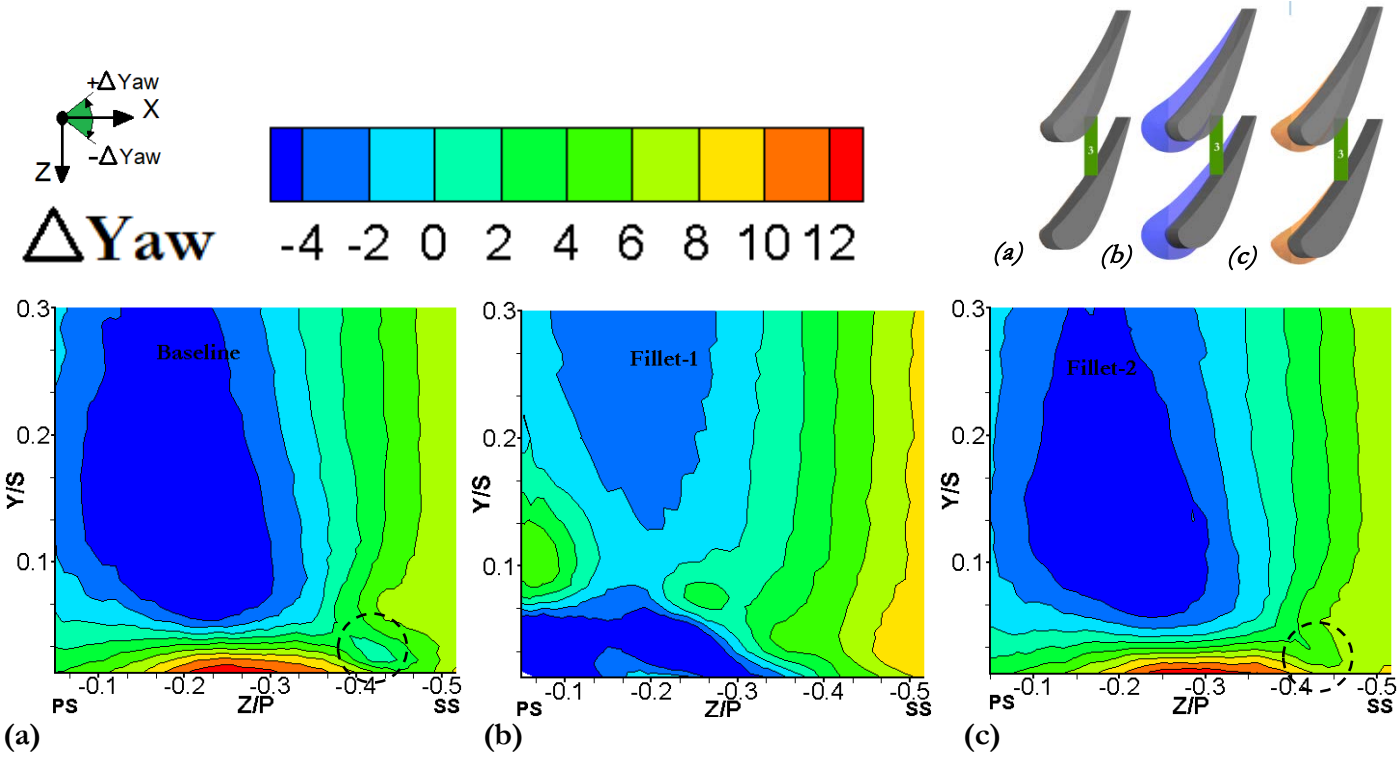

Figure 22: ΔYaw data for a) baseline, b) Fillet 1 and c) Fillet 2 in third plane at Xg/C_{ax}=0.58.

Figure 22 presents the flow yaw angle deviation values, ΔYaw contours, for the baseline and filleted cases in the pitch-wise third plane that spanned across the entire pitch in the passage.

Location Y/S = 0.0 in the plots refers to the endwall position. Flow data were not measured very close to the walls because the probe dimensions imposed flow blockages and altered the streamlines. The pressure-side blade was located at Z/P = 0.0 and the suction-side of the blade was located on the negative side of this axis at Z/P = -0.51.

The magnitude of flow angle deviation on the endwall was noticeably reduced in the passage by the presence of Fillet 1 making the flow more oriented towards the axial direction. The smaller geometry of Fillet 2 did not seem to have a great influence on the secondary flow in this pitch-wise plane.

The effects of the fillets on the secondary flow were further evident in the total pressure loss coefficient distributions, shown in ***Figure 23***, as anticipated by [57, 58, 61]. The total pressure loss coefficient distributions, $C_{pt,\,loss}$, estimated the total pressure drop from the inlet to the pitch-wise plane of interest and quantified the aerodynamic losses. Equation (10) was used to determine the $C_{pt,\,loss}$ values from the measured total pressures, $P_{t,loc}$ in the third and exit planes.

The coefficient values were high in the secondary flow region where the total pressure losses ($P_{t,\,ref} - P_{t,loc}$) were greater due to entropy generations in the secondary flows. The endwall secondary flows, including the passage vortex legs, were responsible for the additional total pressure drop and aerodynamic losses [78]. The pressure-side leg and the suction-side leg vortices combined to create the passage vortex near the suction-side of the third plane. The $C_{pt,\,loss}$ distributions also provided an insight into the boundary layer strength and streamline orientations near the endwall region in the pitch-wise plane.

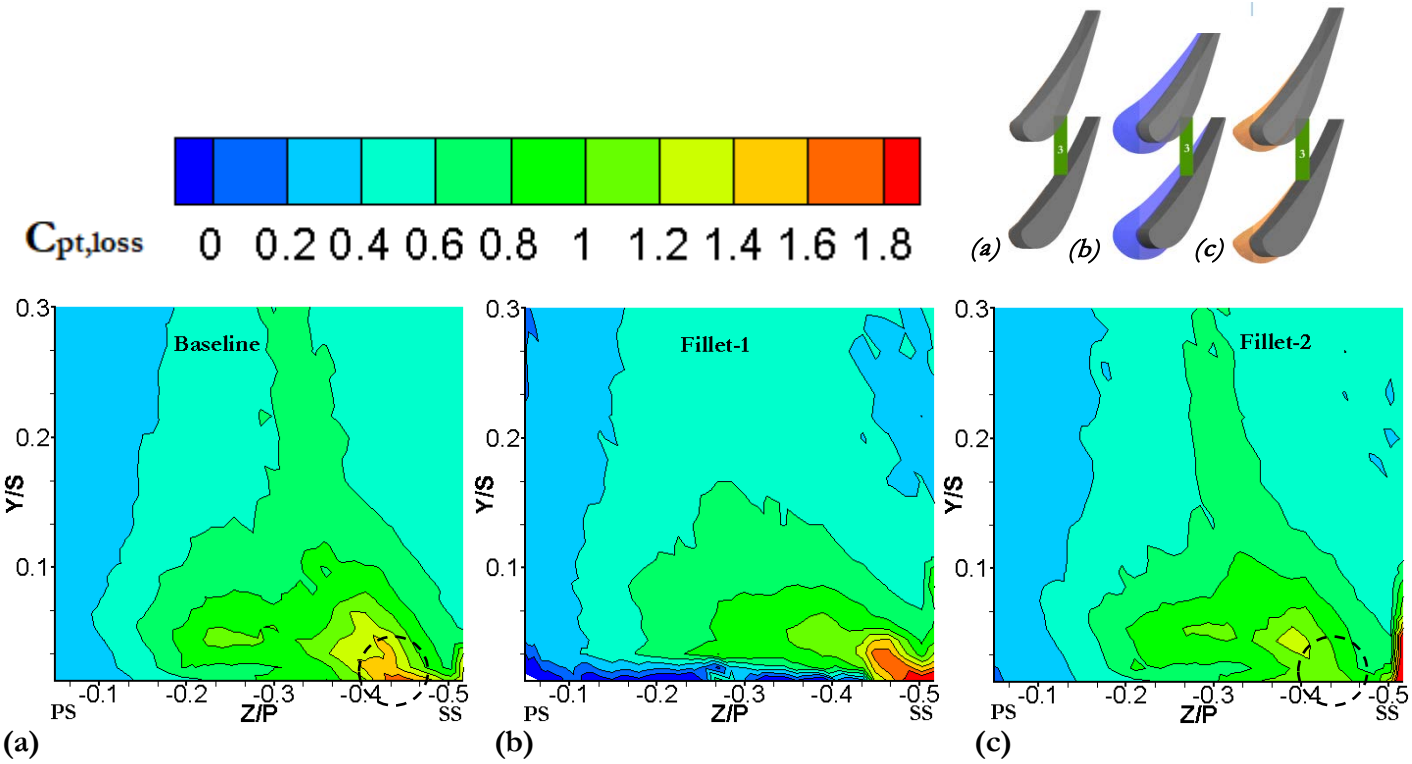

Figure 23: *Total pressure loss coefficient for a) baseline, b) Fillet 1 and c) Fillet 2 in third plane at X_g/C_{ax}=0.58.*

In ***Figure 23***, the concentrations of higher $C_{pt,\,loss}$ > 0.8 contours in the right-hand corner (SS), just above the endwall, identify the size and strength of the passage vortex core. In the baseline contour, the highest total pressure losses occurred at the suction-side blade-endwall junction around Z/P ≈-0.45, representing the passage vortex system. Comparing the baseline data with the filleted cases, the total pressure loss magnitude was reduced remarkably on the endwall for the filleted case, particularly for Fillet 1, but the secondary flow structures were not eliminated. The passage vortex size remained dominant on the endwall and the impact of the fillets seemed to

push most of its core towards the suction-side. When comparing the two fillets at the endwall, in the Fillet 1 case, the $C_{pt,\,loss}$ values, on the pressure-side, were much lower than for the Fillet 2 case due to the presence of Fillet 2. The thickening of the blade profile ultimately affected the boundary layer. The highest total pressure losses were present on the wider region on the suction-side for Fillet 1 at -0.51< Z/P <-0. 45 and for Fillet 2 at Z/P ≈-0. 51.

The overall effect of the LE fillet on the development of the passage vortex was best realised when looking at the exit plane. Lower values of ΔYaw were desirable at the exit plane for the flow uniformity as the flow entered the next row of blades in the gas turbine passages. The three cases were further tested in the exit plane. ***Figure 24*** shows the location of the vane trailing edge (TE) at Z/P ≈-1. The large deviations of the flow turning happened mainly in the near-wall region (Y/S < 0.1) and in the trailing-edge wake region. As expected, the fillet cases presented a slightly smaller magnitude of flow angle deviation along the endwall. Near the trailing edge, the passage vortex for the Fillet 1 case is oriented more in the axial direction than for the baseline case, while Fillet 2 exhibited smaller deviations of the flow on the endwall region.

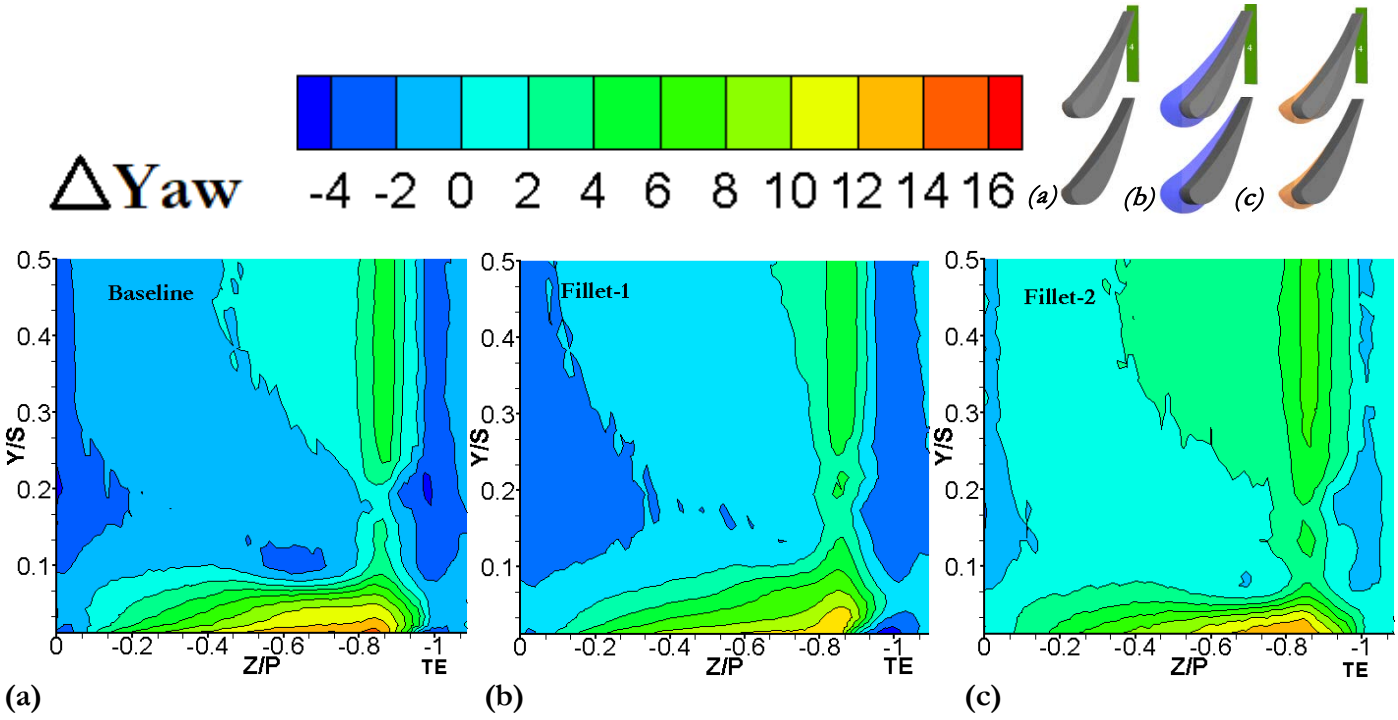

Figure 24: *ΔYaw data for a) baseline, b) Fillet 1 case, and b) Fillet 2 case in the exit plane at* X_g/C_{ax}*=1.04.*

Figure 25 indicates that, at the exit plane, the high values of $C_{pt,\,loss}$ > 4.0 at about Z/P ≈-1 in the vertical region were caused by the trailing-edge wake. Wang et al. [8] explained the high $C_{pt,\,loss}$ value contours near the trailing edge on the endwall as being the absorption of the suction-side horseshoe vortex in a larger vortex system of corner vortices. The high values of $C_{pt,loss}$ in the region approximately between -1 < Z/P < -0.7 and 0.1 < Y/S < 0.3, were caused by the passage vortex core. Part of the passage vortex interacted with the TE vortex and was not distinguishable in the TE vortex region. Compared with the baseline case, for the Fillet 2 case, a closer investigation near the endwall indicated a narrower zone of $C_{pt,\,loss}$ distribution at the trailing-edge location. ***Figure 25–b*** indicates that the Fillet 1 case showed a thicker TE zone of $C_{pt,\,loss}$ distribution but a weaker passage vortex core at 0.18<Y/S<0.24 and high $C_{pt,\,loss}$ in the proximity of the endwall at Z/P ≈-0.95.

For the baseline case, shown in ***Figure 25-a***, the maximum loss core was observed at approximately -1 < Z/P < -0.9 and at Y/S≈0.22 and approximately at Y/S≈0.20 for the Fillet 2 case in ***Figure 25 -c***. The effect of the fillets on the secondary flow appeared to be a shift of the passage vortex core towards the endwall and a secondary loss reduction.

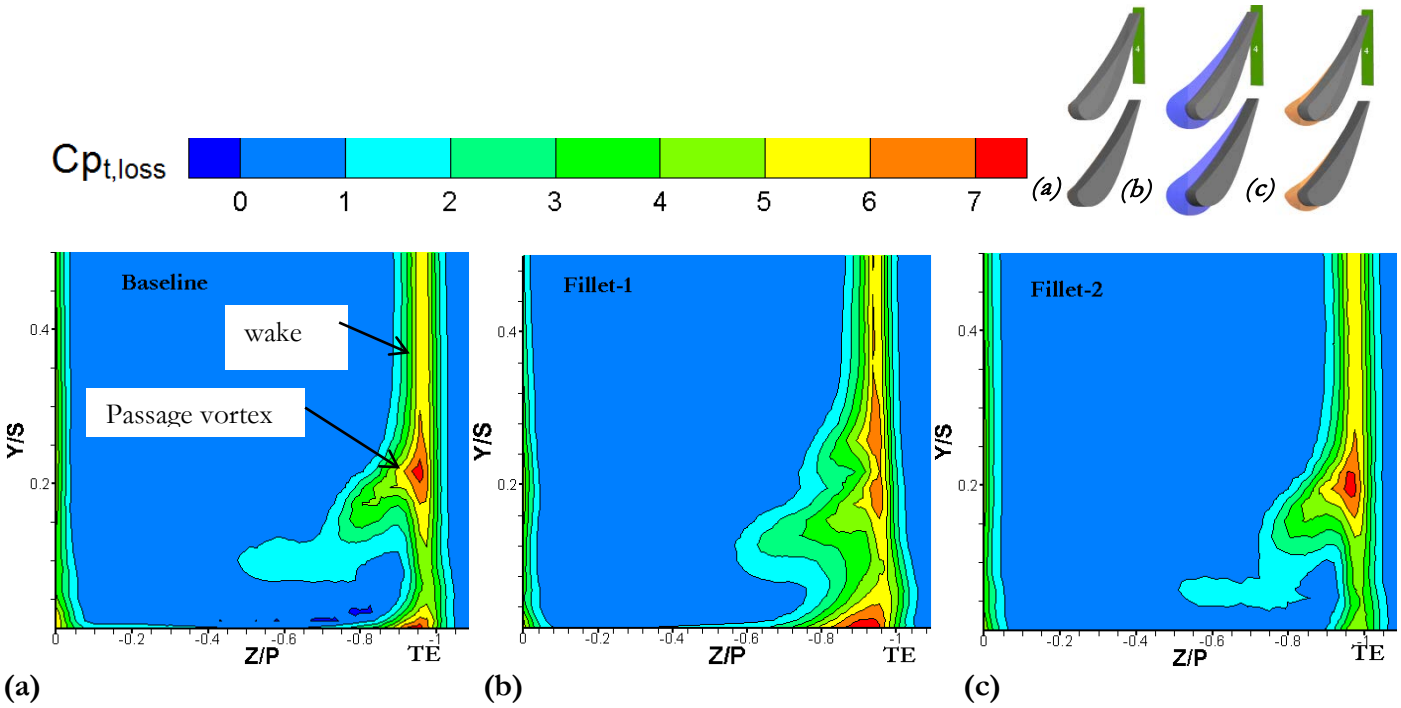

Figure 25: Total pressure loss coefficient for a)baseline, b) Fillet 1 case and c) Fillet 2 case in the exit plane at X_g/C_{ax}=1.04.

The investigation into the leading-edge contour indicated that Fillet 1 was the most effective in reducing the yaw angles in the third plane although Fillet 2 displayed the smaller size of the passage vortex migrated on suction-side. In the exit plane, Fillet 1 appeared to exhibit greater reductions in the passage vortex losses, while Fillet 2 reduced the magnitude of boundary layer losses.

6.2. Experimental test cases of cooled cascade

6.2.1. Leading-edge film-cooling

The interactions between film-cooling flow and endwall secondary flows were investigated next. Four exchangeable rectangular plates, with different film-cooling hole configurations, were employed in the endwall just upstream of the vanes.

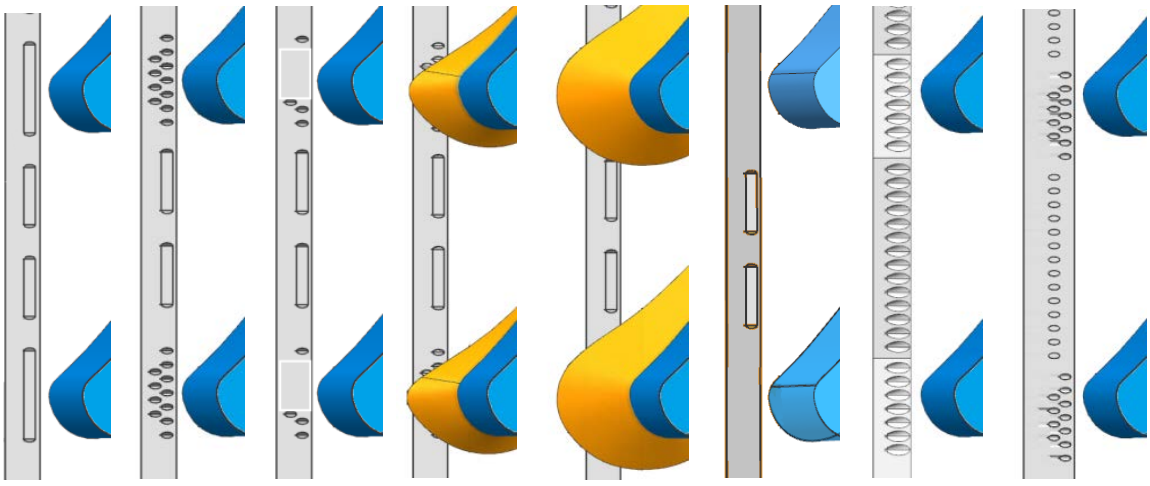

(A) (B-2A) (B-2B) (B-3A) (B-3B) (B-3C) (C) (D)

Figure 26: Cooling configurations: four bleed-cooling slots (A), two bleed cooling slots and cylindrical holes (B-2A), two bleed-cooling slots and partially open cylindrical holes (B-2B), two bleed-cooling slots and cylindrical holes with Fillet 1 (B-3A), two bleed-cooling slots and cylindrical holes with Fillet 2 (B-3B), two bleed-cooling slots (B-3C), cylindrical holes (C), diffused cylindrical holes (D).

Figure 26 illustrates the LE cooling plates: four bleed-cooling slots (configuration A), two bleed-cooling slots and cylindrical holes (configuration B-2A), the distribution of cylindrical cooling holes (configuration C), and the distribution of diffused cylindrical holes (configuration D).

Table 19 illustrate the tested configuration with all the LE cooling plates. Configuration B-2B was the LE cooling plate B-2A with partially covered cylindrical holes. These holes were covered when Fillet 2 was employed as in configuration B-3B.

All tested cooling configurations are summarised in *Table 19*.

Table 19: Tested cooling configurations.

Configurations	Description
A	Four LE bleed-cooling slots, no fillet
B-2A	Two LE bleed-cooling slots and all cylindrical holes, no fillet
B-2B	Two LE bleed-cooling slots and cylindrical holes partially closed, no fillet
B-3A	Two LE bleed-cooling slots and cylindrical holes partially closed, Fillet 1
B-3B.	Two LE bleed-cooling slots and cylindrical holes partially closed, Fillet 2
B-3C	Two LE bleed-cooling slots all cylindrical holes closed, no fillet
B-4	Two LE bleed-cooling slots and cylindrical holes partially closed, Fillet 2 + passage cooling holes
C-1	LE cylindrical holes, no fillet
D-1	LE diffused cylindrical holes, no fillet

The film-cooling analysis was conducted with and without Fillet 2 in all four measurement planes. The pressure measurements were conducted in the third and exit planes, while the thermal measurements were conducted in the first three planes.

6.2.2. Vane Cascade

6.2.2.1 Flow yaw angle deviation, ΔYaw

The flow yaw angle deviation was estimated from the local yaw angle after subtracting the yaw angle at the mid-span location. The positive ΔYaw indicated the streamline turning towards the suction-side and the negative ΔYaw was oriented towards the pressure-side of the passage. *Figure 27* and *Figure 28* show the differences in ΔYaw distributions in the third plane location for the baseline cooling configurations Case A, Case B-2A, Case B-2B, Case C-1 and Case D-1 for M values of 1.8 and 2.2 respectively. The flow field results were only shown in the region just above the endwall, where the slot film flow was assumed to interact with the boundary layer flow separation and secondary flows in the vane passage.

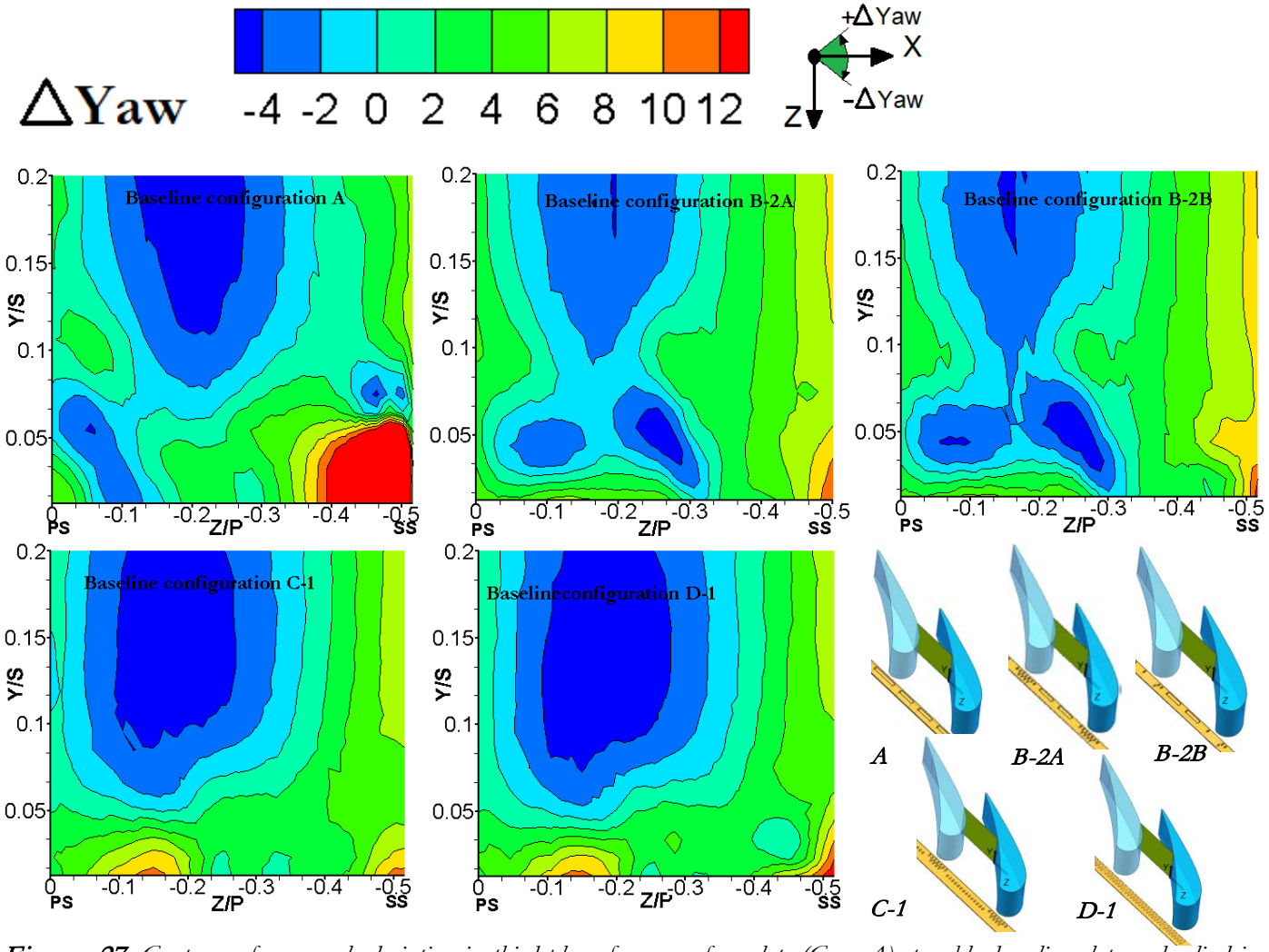

Figure 27: *Contours of yaw angle deviation in third plane for cases: four slots (Case A), two bleed-cooling slots and cylindrical holes (Case B-2A), two bleed-cooling slots with cylindrical holes partially closed (Case B-2B), cylindrical holes (Case C-1) and diffused cylindrical holes (Case D-1) at M=1.8.*

The plots showed the typical flow behaviour when the cooling was introduced, less flow turning near Y/S≈0.08 and more flow turning near Y/S≈0.05 towards the suction-side, from the mid-span towards the endwall, were present.

In ***Figure 27***, the first three cases containing LE slots (A, B-2A and B-2B) exhibited regions of negative ΔYaw values below Y/S< 0.07, implicating a complete reversal in the flow angles near the endwall on the pressure-side surface because of high momentum flow from the slots. Case A presented the highest positive ΔYaw towards the suction-side signifying the intense passage vortex located near the suction-side. The LE diffused cylindrical holes (Case D 1) and LE cylindrical holes (Case C-1) had marginal differences between them, but compared with the other cases, in the endwall region, positive ΔYaw values were present at -0.2<Z/P<-0.1.

Figure 28 indicates that at higher M, the ΔYaw values on the endwall reduced as the film-cooling gained more momentum in the boundary layer. In Case A, the high momentum jet of the film flow, from the four slots, grew stronger as M increased, travelling further into the passage before being lifted on suction-side by the secondary flows.

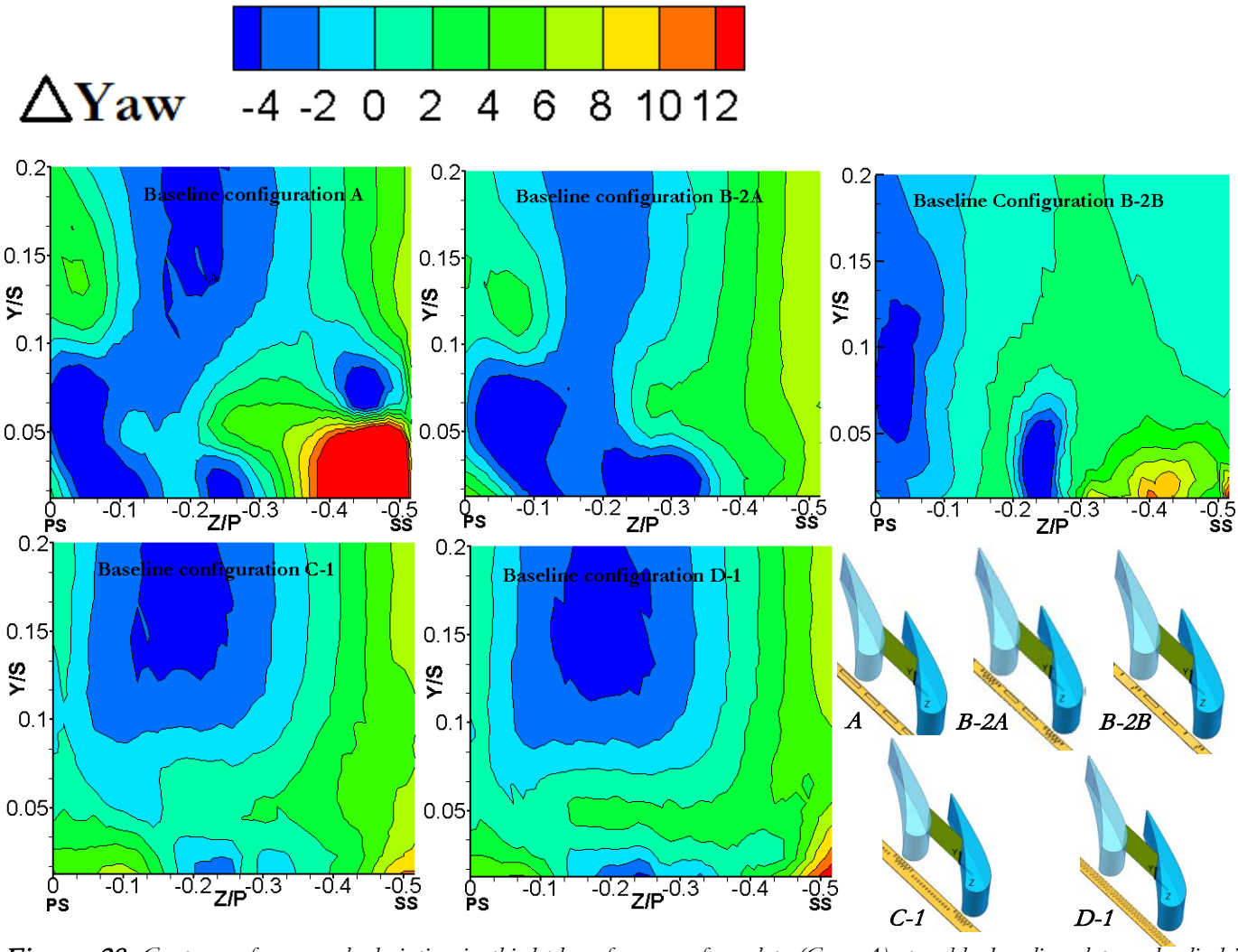

Figure 28: *Contours of yaw angle deviation in third plane for cases: four slots (Case A), two bleed-cooling slots and cylindrical holes (Case B-2A), two bleed-cooling slots with cylindrical holes partially closed (Case B-2B), cylindrical holes (Case C-1) and diffused cylindrical holes (Case D-1) at M=2.2.*

The reduction of ΔYaw on the endwall region, due to coolant flow interaction, decreased the passage vortex as confirmed by $C_{pt,\,loss}$ distributions from ***Figure 29*** to ***Figure 31***.

6.2.2.2. Total loss

The local distributions of the total pressure loss coefficient, $C_{pt,\,loss}$, revealed the location, size and strength of the passage vortex legs. The distributions of total pressure loss coefficient also partially identified the pitchwise momentum flux, the penetration depth of coolant in the endwall boundary layer and the interactions between the coolant and the passage vortex. The results of such interactions were thus either higher or lower secondary losses depending on the film-cooling flow distributions along the endwall in the turbine passage. However, it was difficult to determine the effects of endwall secondary flows on the film-cooling flow distributions from the local $C_{pt,\,loss}$.

The distributions of total pressure loss coefficient, based on the locally measured total pressure, see Eq. (10), for Case A, Case B-2A, Case B-2C, Case C-1 and Case D-1 were compared. At the location of the third plane, shown in ***Figure 29*** and ***Figure 30***, the effects of coolant flow on the endwall secondary flows indicate that the total losses were substantial in proximity to the endwall. The passage vortex and coolant jet migrated towards the suction-side (SS) corner, as suggested by Kost and Nicklas [80] and Du et al. [40]. The higher the value of

$C_{pt,\ loss}$, the higher the pressure losses and the higher the intensity of interactions as mentioned above. The presence and depth of coolant penetration into the boundary layer on the endwall were identified by the changes in the $C_{pt,\ loss}$ distributions inside the vortex core as the high jet momentums of the coolant streams decreased the pressure losses. The lower the values of the $C_{pt,\ loss}$ near the endwall, the weaker the passage vortex, and the better the film-cooling flow distributions, as implied by Du et al. [40] and Li et al. [66]. The main difference between the uncooled case shown in ***Figure 23-a*** and the cooled case, except for Case B-2B, was that the upstream cooling injection decreased the $C_{pt,\ loss}$ distributions on the pressure-side at the expense of an increase in endwall mixing losses and passage vortex on the suction-side.

On the endwall, looking at Case A, the suction vortex legs lifted the coolant along their travel paths as the coolant flows interacted with the vortex structures. Knost and Thole [81] indicate, for the LE cooling slot configuration, the tendency of the jets to separate from the surface rather than to penetrate to the pressure-side. When the coolant was present, high above the endwall, the coolant was wasted because the coolant coverage and spread were reduced on the endwall.

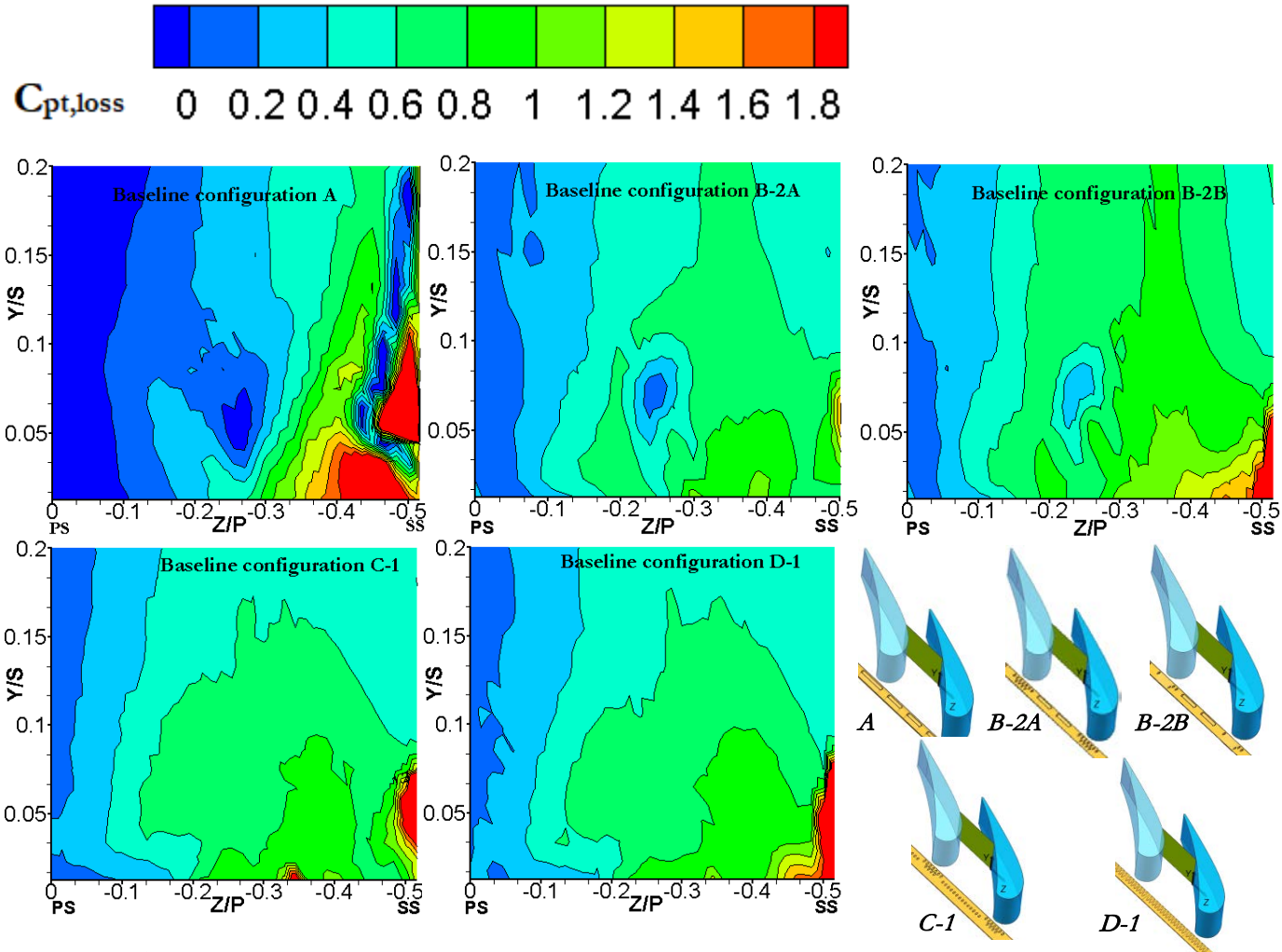

Figure 29: *Total pressure loss coefficient, $C_{pt,\ loss}$ contours in third plane for cases: four slots (Case A), two bleed cooling slots and cylindrical holes (Case B-2A), two bleed cooling slots with cylindrical holes partially closed (Case B-2B), cylindrical holes (Case C-1) and diffused cylindrical holes (Case D-1) at M=1.8.*

The high values of $C_{pt,\ loss} > 0.6$ in the location of $Z/P < -0.3$, shown in ***Figure 29*** were caused by the passage vortex core. The presence of a stronger passage vortex is evident from the figure since the $C_{pt,\ loss}$, near the suction-side at that region, was higher for Case A than for all the other configurations. The contour plots for

the configurations containing LE slots displayed a lifting cooling flow away from the endwall in the region between Z/P ≈-0.25 and 0.05<Y/S<0.8.

Both Case C-1 and Case D-1 had a similar $C_{pt,\,loss}$ distribution, with Case D-1 performing slightly better along the endwall. When the baseline configuration with no cooling, shown in ***Figure 23-a***, was compared with the cooling cases in ***Figure 29***, excluding Case A, the $C_{pt,\,loss}$ contours illustrated how the strong presence of coolant swept the passage vortex towards the suction-side corner by penetrating the boundary layer and reducing the secondary flow. ***Figure 30*** showed how the increase in the injected mass rate of the coolant to M=2.2 let the $C_{pt,\,loss}$ values decreased on the endwall and the size of the passage vortex became smaller.

For Case A, the coolant seemed to dissipate along the vane's span and not penetrate in the boundary layer towards the suction-side as far, as shown in ***Figure 29***, covering the endwall only until Z/P ≈-0.21. For Case B-2A and Case B-2B, near the pressure-side region at -0.27<Z/P <-0.2, the low $C_{pt,\,loss}$ values above the endwall indicate a lift-off of the high-momentum coolant jet above the endwall coming from the slot. With an increase in the blowing ratio, from M =1.8 to M = 2.2, the region of $C_{pt,\,loss}$ > 0.6 reduced for both Case C-1 and Case D-1 for two reasons:

(i) the cooling jet momentum increased as M increased;
(ii) the size and strength of the passage vortex core reduced as M increased.

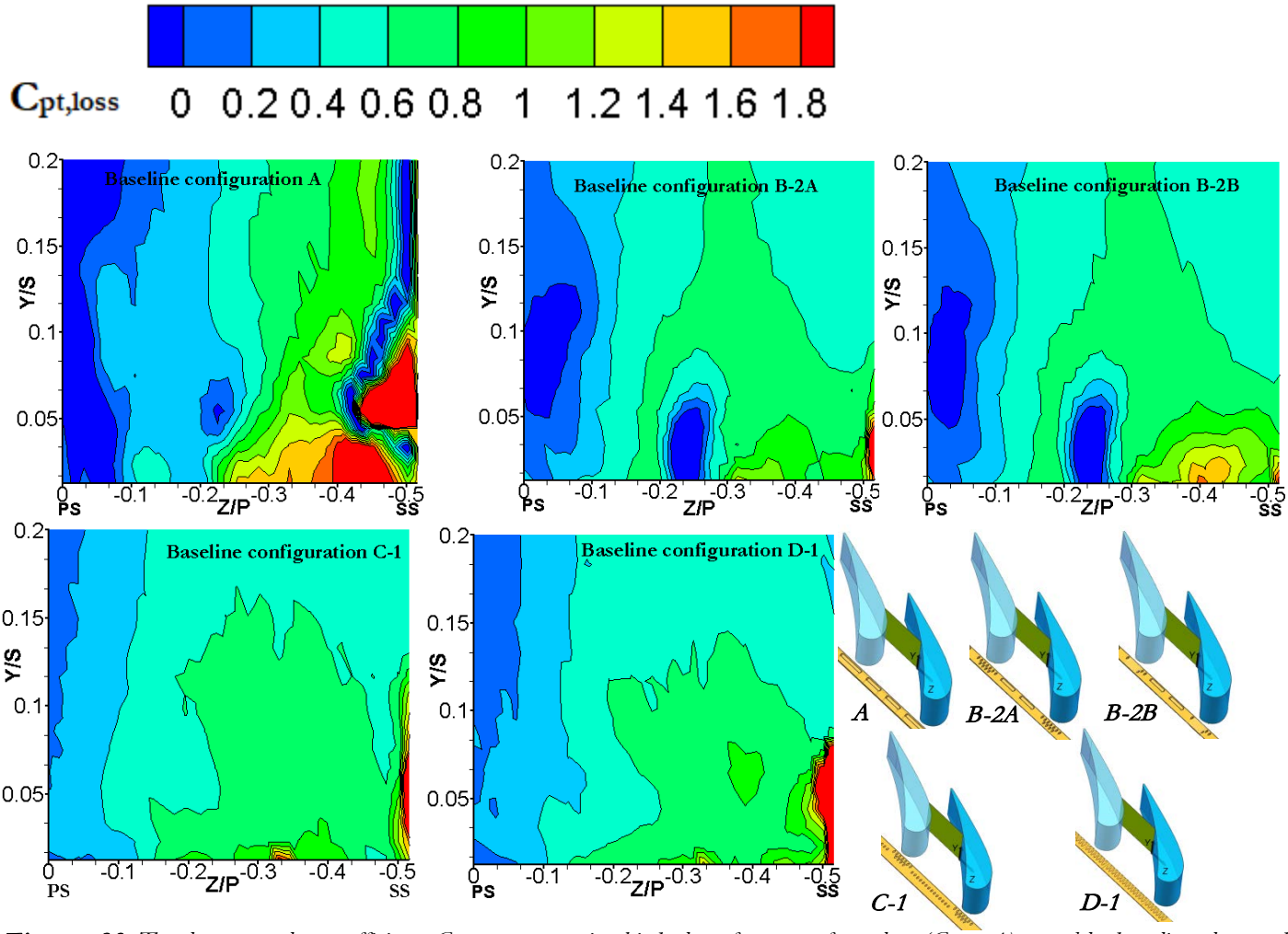

Figure 30: *Total pressure loss coefficient, $C_{pt,\,loss}$ contours in third plane for cases: four slots (Case A), two bleed cooling slots and cylindrical holes (Case B-2A), two bleed cooling slots with cylindrical holes partially closed (Case B-2B), cylindrical holes (Case C-1) and diffused cylindrical holes (Case D-1) at M=2.2.*

Moreover, the region of $C_{pt,\,loss} > 0.7$ seemed to be slightly smaller for Case C-1 than for Case D-1 indicating a weaker passage vortex core for the diffused hole film-cooling. It could be deduced that the film-cooling of Case A outperformed the other configurations in keeping the endwall highly cooled irrespective of the blowing ratio used.

A similar conclusion could be drawn for ***Figure 31*** by the comparison of the total pressure loss coefficients in the exit plane, between Case B-3C, Case-C-1, and Case-D-1 at M = 2.2. The migration of the passage vortex, high above the endwall caused by the coolant, and its interactions with the TE vortex, were also reported by previous studies on aerodynamic losses. The high values of $C_{pt,\,loss}$, adjacent to the endwall at Y/S < 0.1, shown in ***Figure 31***, were caused by the mixing of the boundary layer with the film-cooling flow. This mixing loss region of $C_{pt,\,loss}$, adjacent to the endwall, was absent in Case B-3C and slightly smaller for Case D-1 than for Case C-1, probably as a result of better distribution of coolant along the endwall for the diffused holes. The $C_{pt,\,loss}$ region in the passage vortex core was located slightly higher at Y/S ≈ 0.24 for Case C-1 than for Case D-1 at Y/S ≈ 0.2. Case B-3C resulted in the smallest aerodynamic loss with max $C_{pt,\,loss}$ <0.7. Also, the $C_{pt,\,loss}$ region in the passage vortex core was slightly smaller for Case D-1 than for Case C-1, as the passage vortex became weaker and smaller for Case D-1.

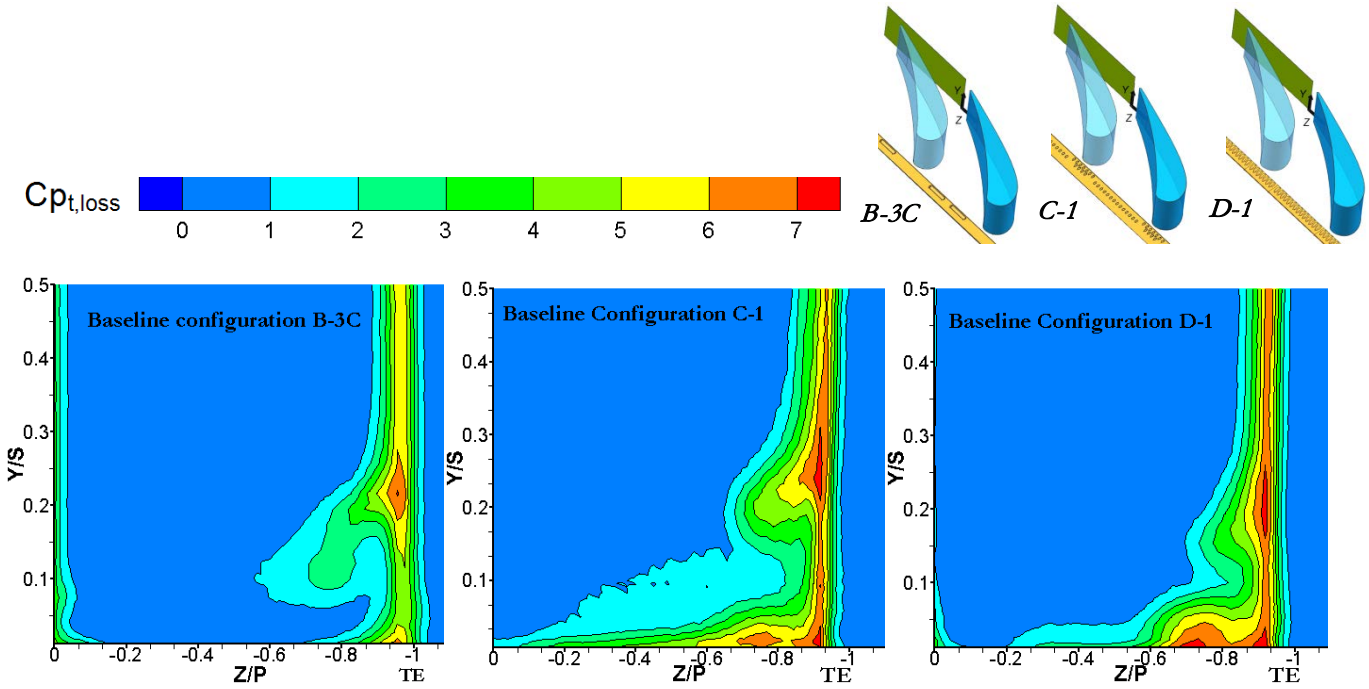

Figure 31*: Total pressure loss coefficient, $C_{pt,\,loss}$ contours in the exit plane for two slots Case B-3C, cylindrical holes Case C-1, and diffused cylindrical holes Case D-1 at M=2.2.*

As the compressor supplied the cooling fluid in the gas turbine passages, an increase in the blowing ratio means more load on the compressor, accordingly the total pressure loss performance across the turbine passage, per unit of the coolant mass flow rate is an important consideration. The influences of the blowing ratio on the overall pressure losses were shown by the mass-averaged $(C_{pt,\,loss})_{mass\text{-}av}$ and the mass-averaged loss coefficient per coolant mass fraction ratio (MFR). The $(C_{pt,\,loss})_{mass\text{-}av}$ and the $(C_{pt,\,loss})_{mass\text{-}av}$/MFR are presented in ***Figure 32*** and ***Figure 33*** respectively. The data are shown for all LE film-cooling configurations without the fillets (Case A, Case B-3C, Case C-1, and Case D-1) because the blowing ratio, M, varied. The data for Cases A and B-3C were taken from Adeola et al. [63]. The higher the value of the mass-averaged $C_{pt,\,loss,}$ the higher was loss.

The mass average was computed by the numerical integration of Eq. (21) over the entire measurement area (Y/S=0 to 0.5) in the exit plane. Simpson's trapezoidal rule was applied for the numerical integration of Eq. (21).

The area of integration, A in the Eq. 21, covered the measurement area in the exit plane and dA was determined based on the spatial resolutions between the measured points.

$$\left(C_{pt,loss}\right)_{mass-av} = \int_A \left(\frac{P_{t,ref} - P_{t,loc}}{P_{t,ref} - P_{s,ref}}\right) \frac{1}{0.5m_p} \left(\rho_{ref}\, u_{loc}\right) dA \tag{21}$$

The $0.5m_p$ in Eq. (21) indicates the mass flow rate in the measurement region between $0 \le Y/S \le 0.5$. ***Figure 32*** indicates that the mass-averaged $C_{pt,\,loss}$ increased and peaked for Case C-1 at M =1.8 and the other cases at M = 1.4. The spike in the loss distribution was caused primarily by the higher local losses just above the endwall as the film jet and boundary layer mixed. The $(C_{pt,\,loss})_{mass\text{-}av}$ distribution, shown in ***Figure 32***, was always smaller for Case D-1 than for the other configurations. The better performance might be due to a lack of separation of the diffused holes from the endwall surface, and consequently, less interaction with the free-stream and less associated mixing losses [21, 22].

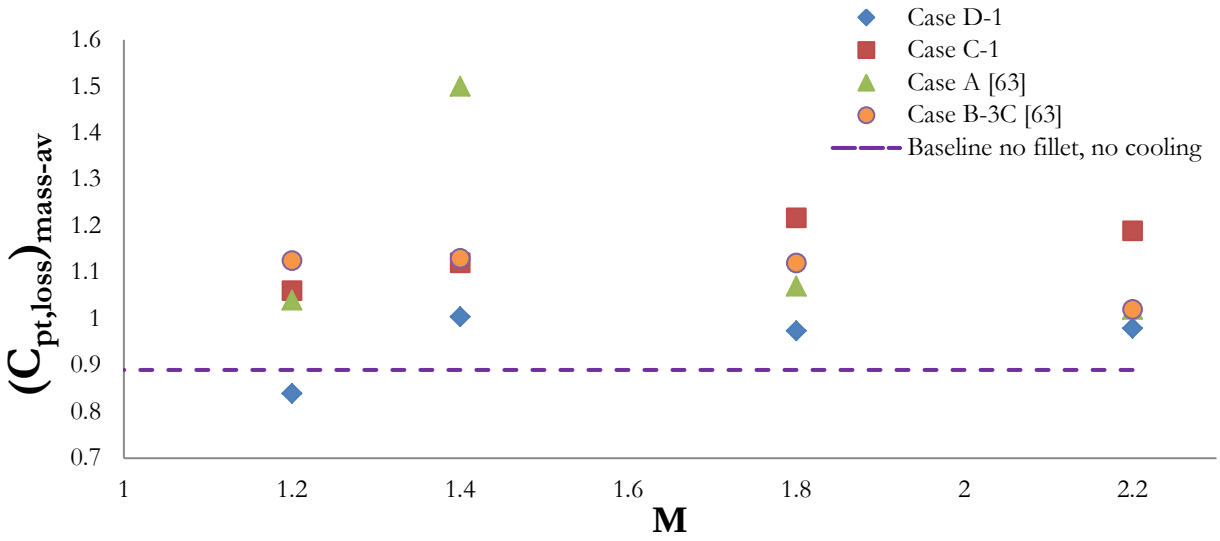

Figure 32: *Comparison of mass-averaged total pressure loss coefficient $(C_{pt,\,loss})_{mass\text{-}av}$ in the exit plane as blowing ratio, M, varies.*

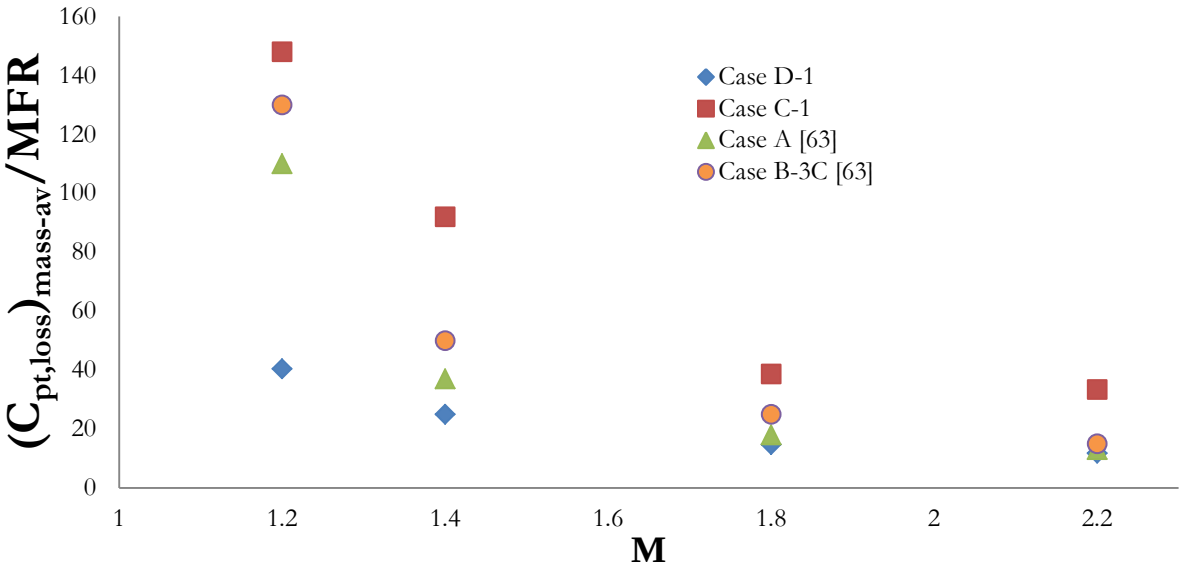

Figure 33: *Comparison of mass-averaged total pressure loss coefficient $(C_{pt,\,loss})_{mass\text{-}av}$/MFR in the exit plane as blowing ratio, M, varies.*

The comparison between the cylindrical holes and diffused holes, shown in ***Figure 32***, is in agreement qualitatively with the comparisons of the overall total pressure losses between the cylindrical holes and fan-shaped holes in Colban et al. [21]. The losses were smaller for fan-shaped holes than for cylindrical holes [21]. The overall kinetic-energy loss distributions with the cooling flow rate variations in [19, 22] suggested that the larger diffusion area of the fan-shaped hole provided smaller losses than for the cylindrical hole. In the exit plane, the local kinetic-energy loss [19, 22], was higher in the passage vortex region and in the endwall region where the coolant mixed with the endwall boundary layer. Using an analogy between the total pressure losses and kinetic-energy losses, the present Case D-1 of diffused holes was thus expected to cause less kinetic-energy losses than for Case C-1 of cylindrical holes.

The values $(C_{pt,\,loss})_{mass\text{-}av}$ were divided by the coolant mass fraction ratio (MFR), as presented in ***Figure 33***. The values of MFR were calculated at the four blowing ratios (discharge coefficient variation in function of the blowing ratio is presented in Appendix C) and are listed in ***Table 20***.

Table 20: *MFR($\dot{m}_c/\dot{m}_p$) of coolant to passage flow*

M	2.2	1.8.	1.4	1.2
Case A	**0.0911**	**0.0656**	**0.0266**	**0.0141**
Case B-3C	**0.0537**	**0.0356**	**0.0189**	**0.056**
Case C-1	**0.0397**	**0.0324**	**0.011**	**0.0092**
Case D-1	**0.1165**	**0.0862**	**0.0459**	**0.0215**

The ratio, $(C_{pt,\,loss})_{mass\text{-}av}/(MFR)$, was based on the free-stream reference velocity and it estimated the aerodynamic loss generated across the cascade passage per unit coolant mass fraction. The coolant flow rate was measured at the orifice meter in the coolant supply circuit, shown in ***Figure 13***. At any M, the diffused cylindrical hole configuration had the highest MFR.

At low M, the difference in $(C_{pt,\,loss})_{mass\text{-}av}/(MFR)$ between Case D-1 and the other cases was quite obvious, when $M \geq 1.4$, it became slim.

Comparing the LE hole configurations, shown in ***Figure 33***, the ratio, $(C_{pt,\,loss})_{mass\text{-}av}/(MFR)$, decreased significantly for Case C-1 and moderately for Case D-1 as M increased.

At any blowing ratio, $(C_{pt,\,loss})_{mass\text{-}av}/(MFR)$ was the lowest for Case D-1 and the highest for Case C-1. ***Figure 33*** indicates that Case D-1 performed better than the other configurations providing good aerodynamic performance and film-cooling coverage although Case D-1 presented the highest MFR at any M.

*6.2.2.3. Non-dimensional axial velocity, u**

The ratio of the local velocity component, u normal to the third plane (parallel to X_G) to the reference velocity, U, defined the quantity u*. The distributions of non-dimensional axial velocity, in the endwall region, illustrated the coolant distributions and concentrations along the endwall. The distributions of non-dimensional axial velocity then also represented the local mass flux ratio (local mass flux due to coolant and boundary layer near endwall divided by mainstream mass flux) for incompressible flow. The values of $u^*>1$ on the endwall related to high coolant concentration.

Figure 34 and ***Figure 35*** present the distributions of non-dimensional u* for all baseline LE film-cooling arrangements shown in ***Table 19*** and they were evaluated against the no-cooling baseline case at M=1.8 and M=2.2. In ***Figure 34***, the small value of non-dimensional axial velocity, u*≈0.8, near the endwall on the left-hand corner (PS), and the high value, u* > 1.6, near the bottom right-hand corner (SS), indicate both the high flow's acceleration in the boundary layer, from the pressure-side towards suction-side, and more coolant presence. The phenomenon of the strong cross-flow's movement, due to the pressure gradient in the pitch-wise direction, could be detected from correlating u* to ΔYaw, shown in ***Figure 27***.

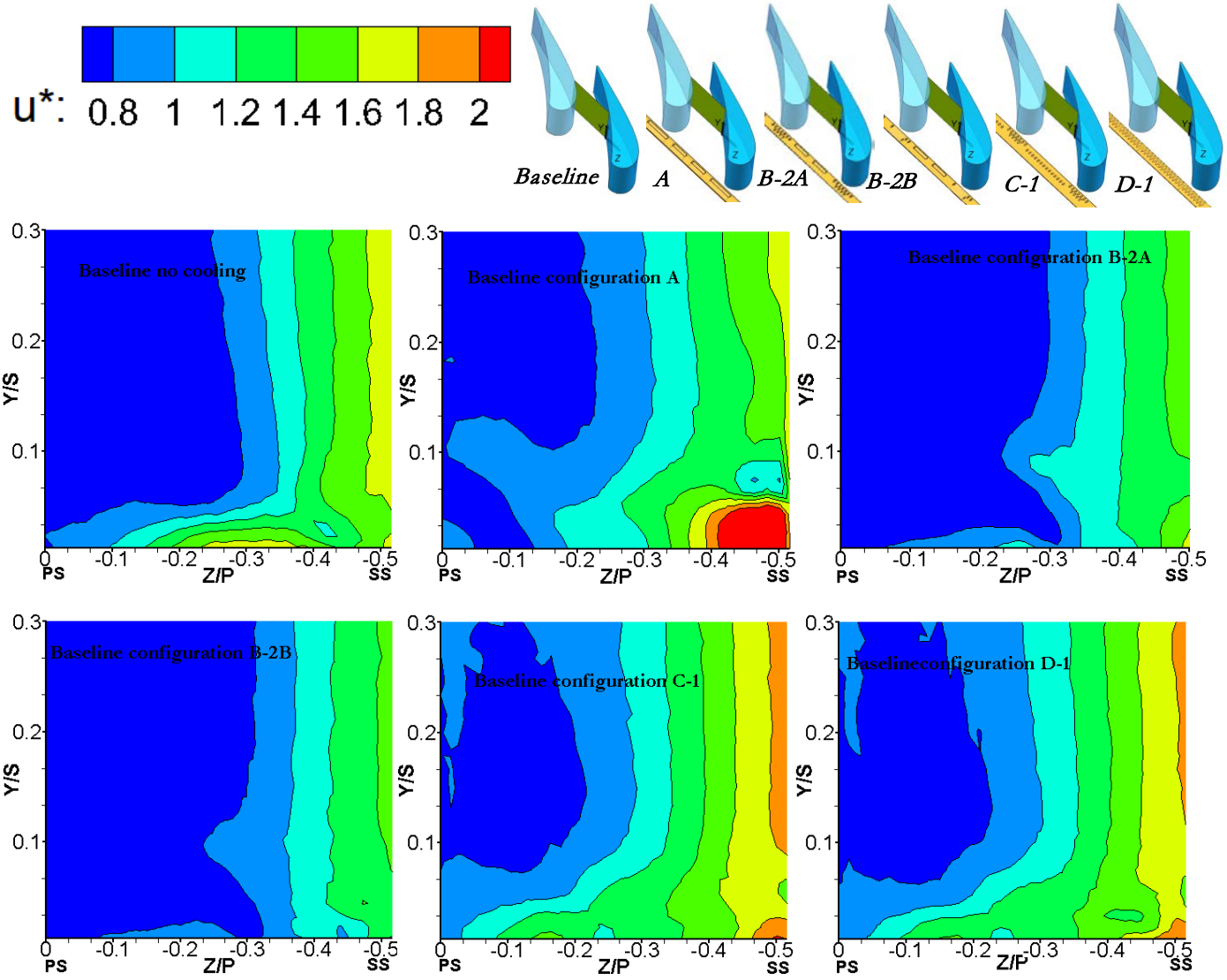

Figure 34: *Distributions of non-dimensional axial velocity, u*=u/U near endwall in third plane at M=1.8: baseline no cooling, four slots Case A, two bleed cooling slots and cylindrical holes Case B-2A and two LE bleed cooling slots and cylindrical holes partially closed Case B-2B, cylindrical holes Case C-1, diffused cylindrical holes Case D-1.*

Figure 34, the configuration with four LE slots, indicates that Case A presented the highest value, u*>2, at 0<Y/S<0.5 and at -0.5<Z/P <-0.4 where the highest pressure losses were located, due to the high momentum of the film-cooling jets and strong interaction between the coolant and passage vortex. From the ΔYaw data of Case A, shown in ***Figure 27***, the intense positive yaw angle deviation, in the same region towards the suction-side, corresponded to the high mass flux as an indicator of coolant concentration near the endwall. The differences in u*, between Case B-2A and Case B-2B, shown in ***Figure 34***, were minimum, but compared with the baseline case with no cooling, the region adjacent to the endwall towards the suction-side with u* <1 was much larger. Furthermore, Case C-1 and Case D-1 had similar trajectories and mixing patterns at both M values, showing a faster flow in the boundary layer than for Case B-2A and Case B-2B. With an increase in the mass

flux, in all the cooling configurations shown in ***Figure 35***, the spread of the coolant momentum, above the endwall and towards the pressure-side in Case A, was noticeable.

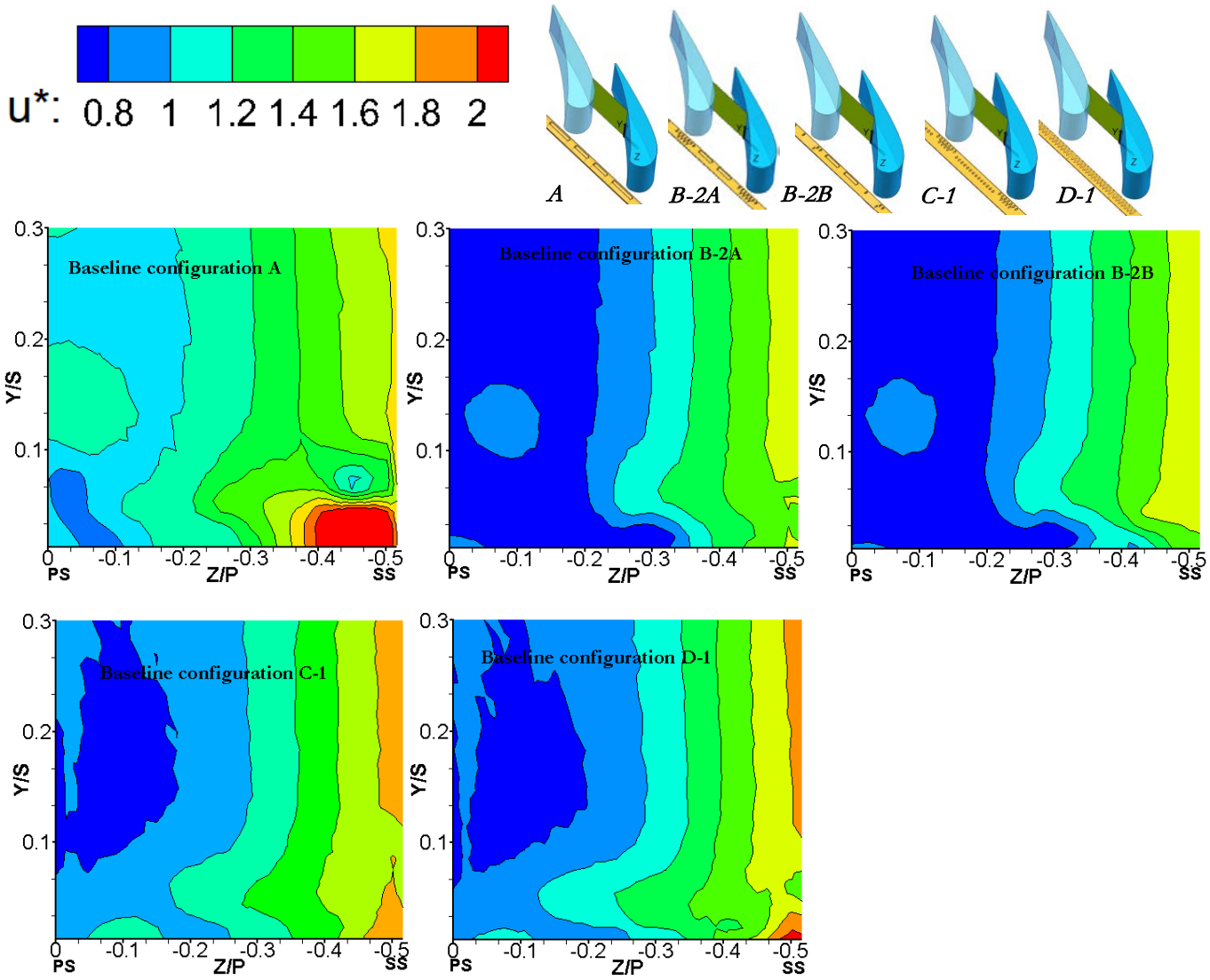

Figure 35: *Distributions of non-dimensional axial velocity, u*=u/U near endwall in third plane at M=2.2: Four slots Case A, two bleed cooling slots and cylindrical holes Case B-2A and two LE bleed cooling slots and cylindrical holes partially closed Case B-2B, cylindrical holes Case C-1, diffused cylindrical holes Case D-1.*

6.2.2.4. Thermal performance

The temperature field of flow near the endwall indicated the coolant concentration along the endwall and the depth of penetration of coolant flow into the boundary layer. The film-cooling flow, penetrating the boundary layer high above the endwall, mixed with the hot combustion gas and lost the ability to cover and cool the endwall effectively from the hot gas. The concentration of the coolant adjacent to the endwall was then beneficial to the film-cooling coverage. The high concentration or distribution of the coolant mass adjacent to the endwall, indicated by the low-temperature distributions, was thus desirable.

The measured local air temperatures, $T_{loc,}$ near the endwall in the first three planes were normalised and indicated as θ in Eq. (15). The coolant-to-mainstream temperature ratio was 0.94, while the density ratio was 1.05. In terms of the definition in the equation, the lower the $T_{loc,}$ the lower the θ due to the film-cooling streams above the endwall.

The design of LE film-cooling configurations consisted of the four slots (Case A), the cylindrical holes (Case C-1), and the diffused cylindrical holes (Case D-1). The non-dimensional temperature fields are represented in ***Figure 36*** to ***Figure 41*** for different M in the first three planes. The pressure-side (PS) of the passage in the first plane, shown in ***Figure 36*** and ***Figure 37***, is located on the left-hand side. The suction-side (SS) of the passage, shown in ***Figure 38*** and ***Figure 39***, is located on the left-hand side in the contour plots.

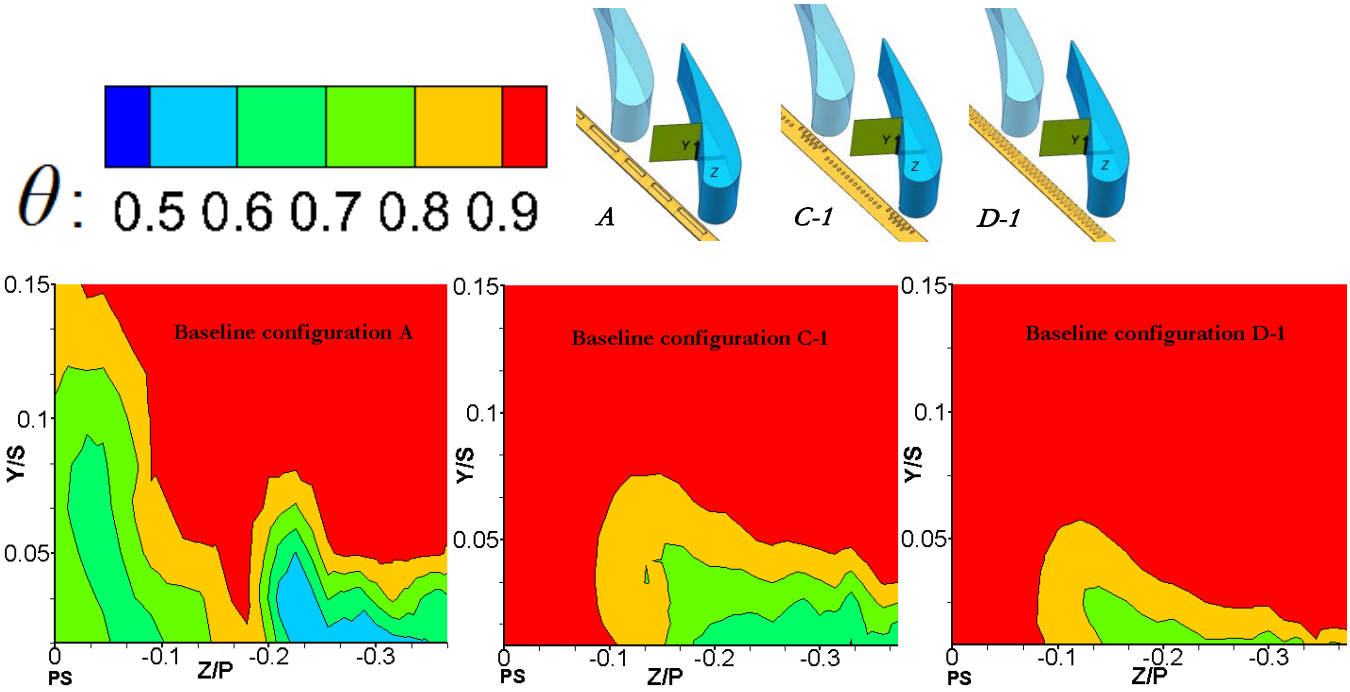

Figure 36: *Contours of non-dimensional temperature (θ) distribution in the first plane for M=1.8: bleed slots Case A, cylindrical holes Case C-1, diffused cylindrical holes Case D-1.*

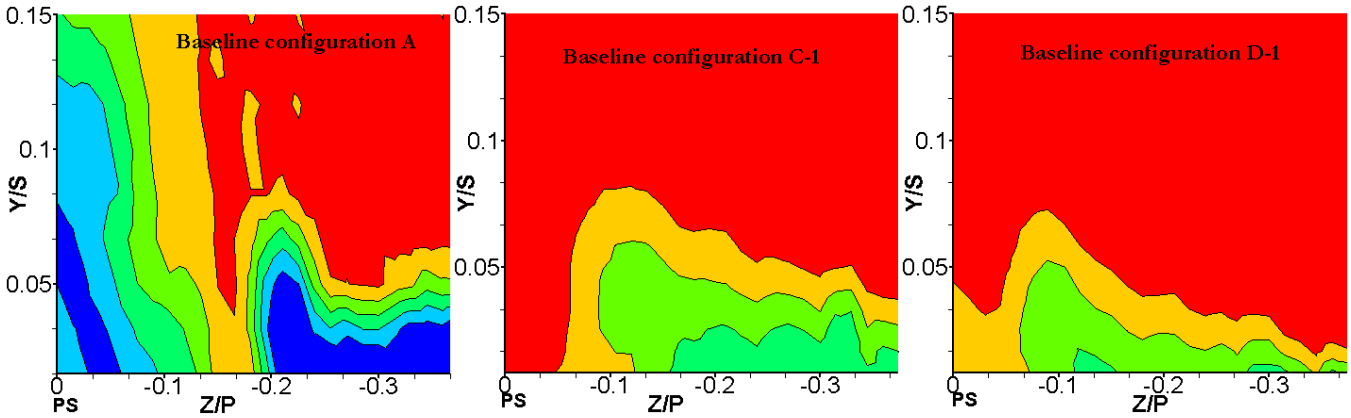

Figure 37: *Contours of non-dimensional temperature (θ) distribution in the first plane for M=2.2: bleed slots Case A, cylindrical holes Case C-1, diffused cylindrical holes Case D-1.*

The results shown in ***Figure 36*** and ***Figure 37*** confirmed that the best cooling coverage on the endwall was provided by the LE bleed slot case of Configuration A, rather than from LE cooling holes, Case C-1 and Case D-1. In fact, at any M towards the pressure-side at Z/P>-0.21, the low θ values smaller than 0.9 were present only in Case A, signifying much more concentration of the coolant ejected from the four slots around the leading edge of the vane. Indeed, the achievement of the coolant coverage on the pressure-side endwall in Case A was substantial, as according to [27, 36, 79], it was difficult for the coolant to reach the PS because of the high turning of the flow streamlines adjacent to the endwall. As the blowing ratio increased, the higher

momentum of the coolant jets at M = 2.2 transported more coolant on the endwall cooling further than the SS and PS.

However, the contour values of θ < 0.9 were seen away from the PS, for both Case C-1 and Case D-1, as the film-cooling flow was turned and swept towards the suction-side by the strong cross-pitch flow and pitch-wise pressure gradient. When the two cases were compared at both blowing ratios, shown in ***Figure 36*** and ***Figure 37***, the lower values of θ < 0.8 were distributed higher above the endwall (Y/S > 0.0) for Case C-1 than for Case D-1 meaning more losses of coolant into the boundary layer for the cylindrical holes (Case C-1). The momentum of the film-cooling jet adjacent to the endwall was higher for Case D-1, causing less convection of coolant into the boundary layer above the endwall. As observed by Bell et al. [71], the best overall protection along the endwall was provided by the diffused cylindrical holes. The Y/S distribution of θ was higher for the Case C-1 (cylindrical) holes than for the Case D-1 (diffused cylindrical) holes because of the lift-off of coolant, which was not beneficial.

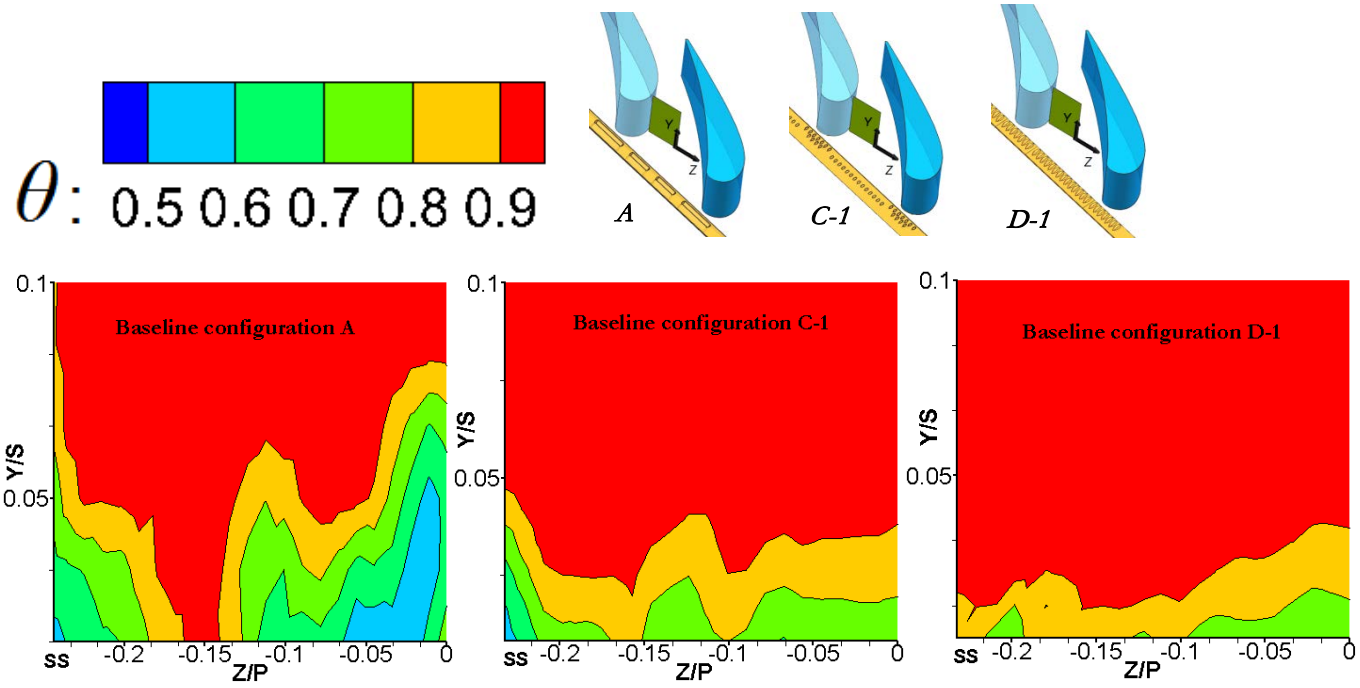

Figure 38: *Contours of non-dimensional temperature (θ) distribution in the second plane for M=1.8: bleed slots Case A, cylindrical holes Case C-1, diffused cylindrical holes Case D-1.*

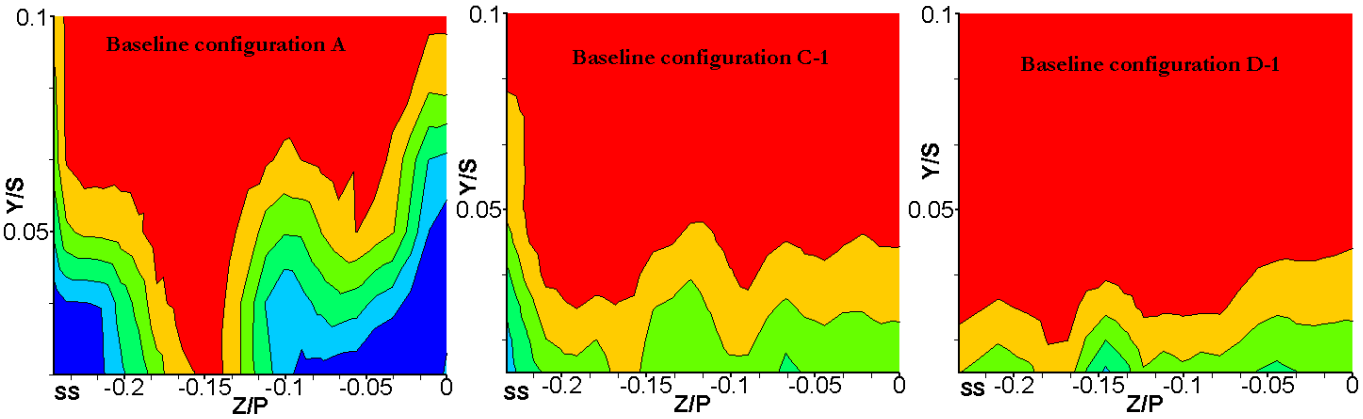

Figure 39: *Contours of non-dimensional temperature (θ) distribution in the second plane for M=2.2: bleed slots Case A, cylindrical holes Case C-1, diffused cylindrical holes Case D-1.*

As the blowing ratio was increased from M = 1.8 to 2.2, the lower values of θ moved closer to the pressure-side because the higher momentum of the coolant jet transported more coolant providing better distributions. The coolant streams penetrated deep into the boundary layer or mainstream, either due to the lift-off or due to the entrainment by the passage vortex legs and mixing with the mainstream flows.

A comparison of the same cooling configurations is presented in the second plane, shown in ***Figure 38*** and ***Figure 39***. The low values of θ < 0.8 were located along the entire endwall in the plane except for Case A, which shows a wasted coolant along the span, missing the endwall around Z/P≈-0.15. ***Figure 38*** indicates that the low values of θ < 0.8 reached higher above the endwall on the SS corner in Case C-1 than in Case D-1. Also, the θ values were smaller near the SS for Case C-1 than for Case D-1 at a blowing ratio as a consequence of the high turning of the coolant stream towards the SS. The stronger suction-side leg vortex for Case C-1 could have caused the lifting of the coolant and the lower θ values high above the endwall. ***Figure 39*** indicates that at a higher blowing ratio, the coolant was spread further in the mainstream because the low values of θ distributions reached higher above the endwall in Case-A and Case C-1.

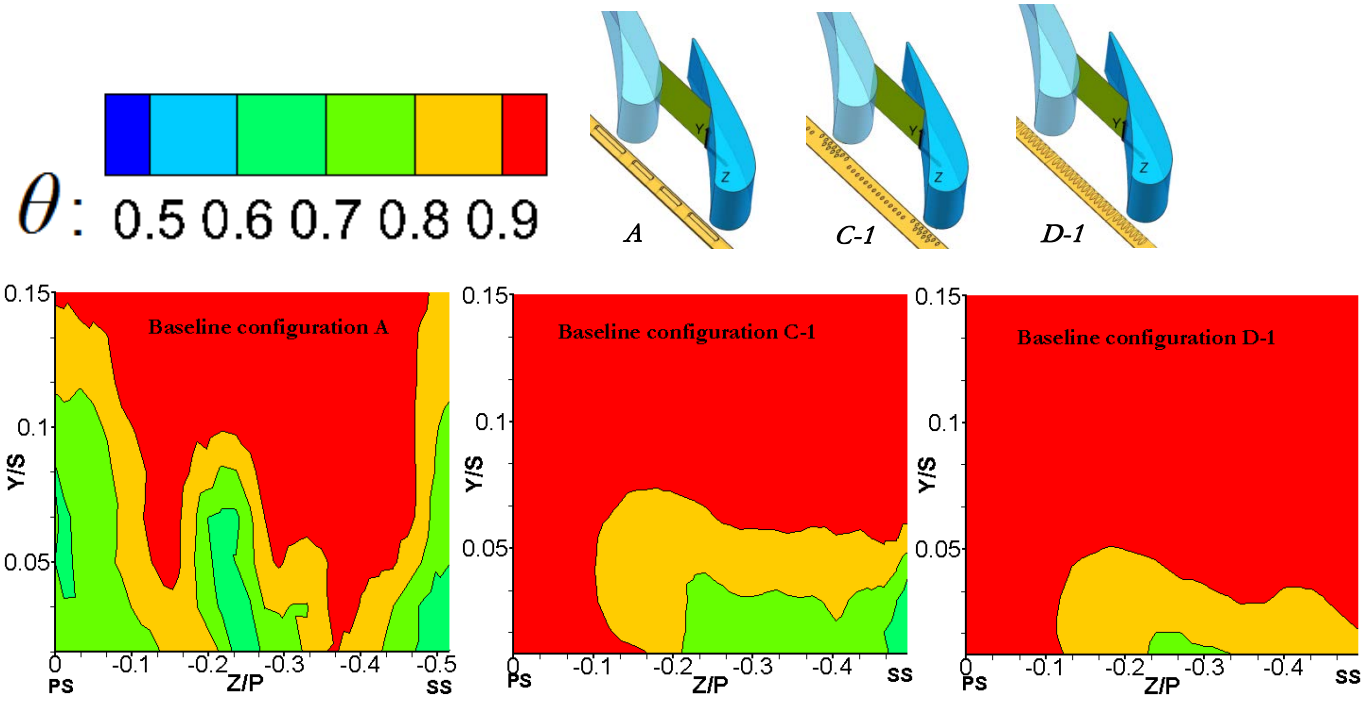

Figure 40: *Contours of non-dimensional temperature (θ) distribution in third plane for M=1.8: bleed slots Case A, cylindrical holes Case C-1, diffused cylindrical holes Case D-1.*

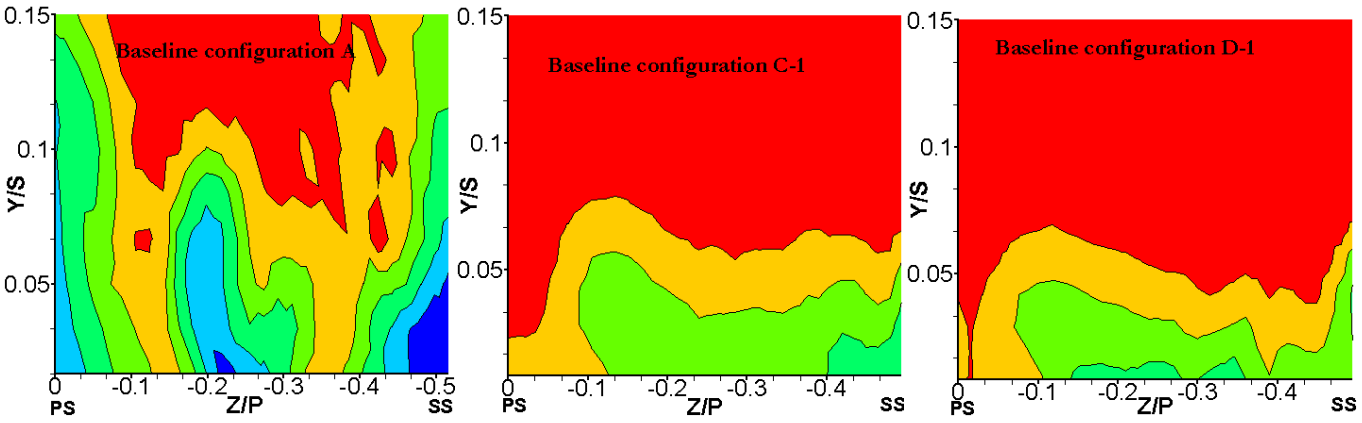

Figure 41: *Contours of non-dimensional temperature (θ) distribution in third plane for M=2.2: bleed slots Case A, cylindrical holes Case C-1, diffused cylindrical holes Case D-1.*

In Case D-1, shown in ***Figure 38*** and ***Figure 39***, the higher momentum of the film-cooling jets, adjacent to the endwall, caused less turning of coolant towards the SS as well as the convection of coolant into the boundary layer. Consequently, the diffused cylindrical holes provided better θ distributions along the endwall than the cylindrical holes did for both low and high values of M in the first and second planes.

The distributions of θ in the third plane are illustrated in ***Figure 40*** and ***Figure 41***. Also, in this pitch-wise plane, the configuration of the slots achieved the cooling of the entire endwall. At each blowing ratio, the low values of $\theta < 0.8$ were distributed closer to the endwall in Case D-1 than in Case C-1. However, more concentrations of lower values of $\theta \leq 0.7$, near the SS, appeared in Case C-1 than in Case D-1, as there was more turning and sweeping of the coolant delivered from the cylindrical holes. The migration of the coolant jet from the leading-edge endwall to the vane suction surface above the endwall was also described in [48], [65], [71].

When the blowing ratio was 2.2, the values of $\theta < 0.9$ distributed higher above the endwall as well as closer to the PS for all three cases. Therefore, the film-cooling flow covered more endwall regions when the blowing ratio was increased to M = 2.2. As in the other planes, the higher momentum of the coolant jet adjacent to the endwall for Case A was responsible for the low values of θ.

6.2.3. Filleted vane cascade

The second set of investigations explored the fillet's effect on film-cooling and the secondary flows involving the combination of the LE cooling plate Case B and two LE fillet designs (Fillet 1 and Fillet 2), of which the geometries were illustrated in Section 4.2. This section presents the pressure measurements conducted in the third plane.

The results of the filleted cases were compared with the results of the baseline case (Case B-3C) in the passage, between Vane 3 and Vane 4, where the two fillets and film-cooling were employed at the bottom endwall, shown in ***Figure 42***. The two fillets, Fillet 1 and Fillet 2, were assessed by comparing the flow angle deviation and total pressure loss coefficient between the baseline and filleted cases.

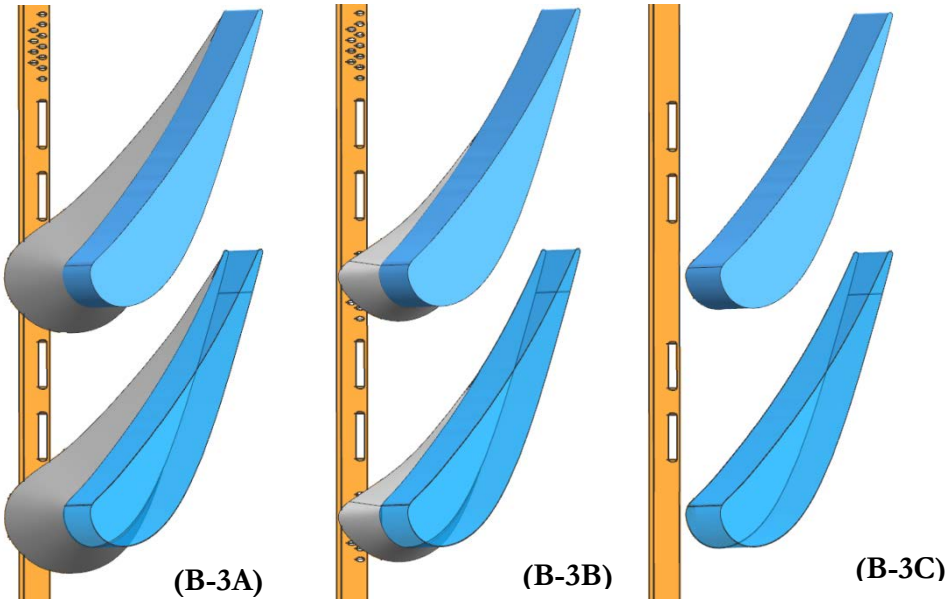

Figure 42: *Cooling configurations: two bleed cooling slots - Fillet 1 Case B-3A, two bleed cooling slots and cylindrical holes Fillet 2 Case B-3B and baseline two bleed cooling slots Case B-3C.*

6.2.3.1. Flow yaw angle deviation and total loss

The flow yaw angle deviation was estimated from the local yaw angle, after subtracting the yaw angle at the mid-span location. ***Figure 43*** indicates that the values of ΔYaw just above the endwall at 0.05<Y/S<0.2 were negative for all the configurations towards the PS. Due to pressure gradients from PS to SS, the cross flow drove the boundary layer towards the SS as illustrated by the positive ΔYaw data. For Case B-3C and Case B-3A, the negative values of ΔYaw were present adjacent to the endwall at -0.42<Z/P<-0.28 and in the proximity of the fillet at -0.4 <Z/P<-0.09 respectively. These negative values could indicate only coolant streams penetrating the boundary layer that are desirable near the endwall. Case B-3B presented the strongest passage vortex located near SS, also visible from the $C_{pt,\,loss} \geq 1.8$ in ***Figure 45***.

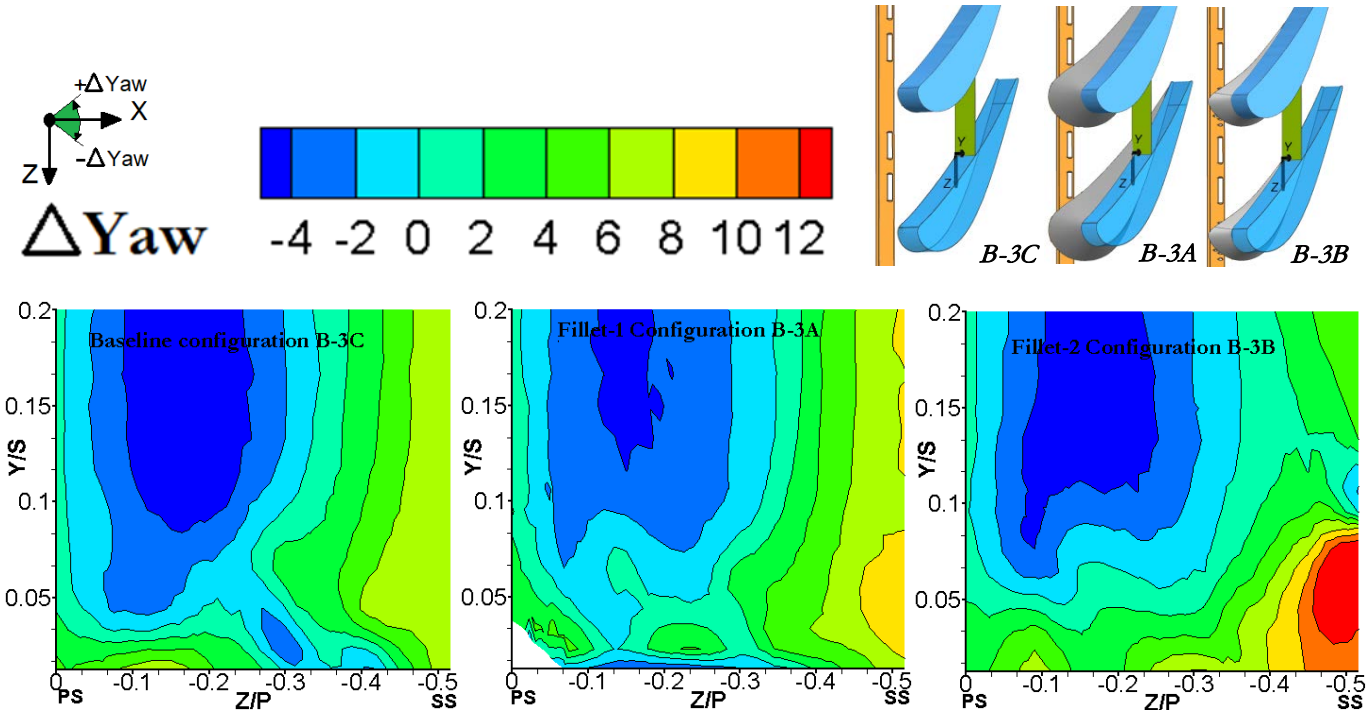

Figure 43: *Distributions of flow yaw angle deviation in third plane for baseline Case B-3C, Fillet 1 Case B-3A, and Fillet 2 Case B-3B at M=1.4.*

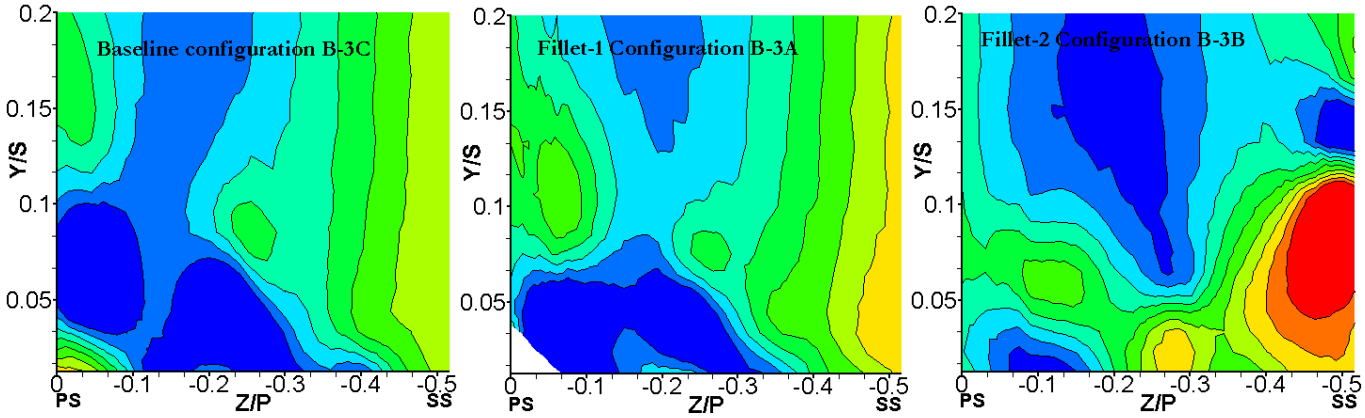

Figure 44: *Distributions of flow yaw angle deviation in third plane for baseline Case B-3C, Fillet 1 Case B-3A, and Fillet 2 Case B-3B at M=2.2.*

Figure 44 indicates that, at M=2.2, as the higher kinetic energy of the coolant streams increased along with the blowing ratio, the momentum into the boundary layer rose, the magnitudes of positive ΔYaw decreased, and the magnitudes of negative ΔYaw increased for Case B-3C and Case B-3A. Compared to ***Figure 43***, the

reduction in the flow turning of the streamlines towards the suction-side, near the endwall, made the coolant stream were less concentrated towards the SS and created more uniform coolant distributions along the pitch line. At the same M, the presence of the coolant adjacent the endwall, not occurred at low M, appeared towards the pressure side in Case B-3B as the negative values of ΔYaw were located adjacent to the endwall at -0.2 <Z/P <-0.01.

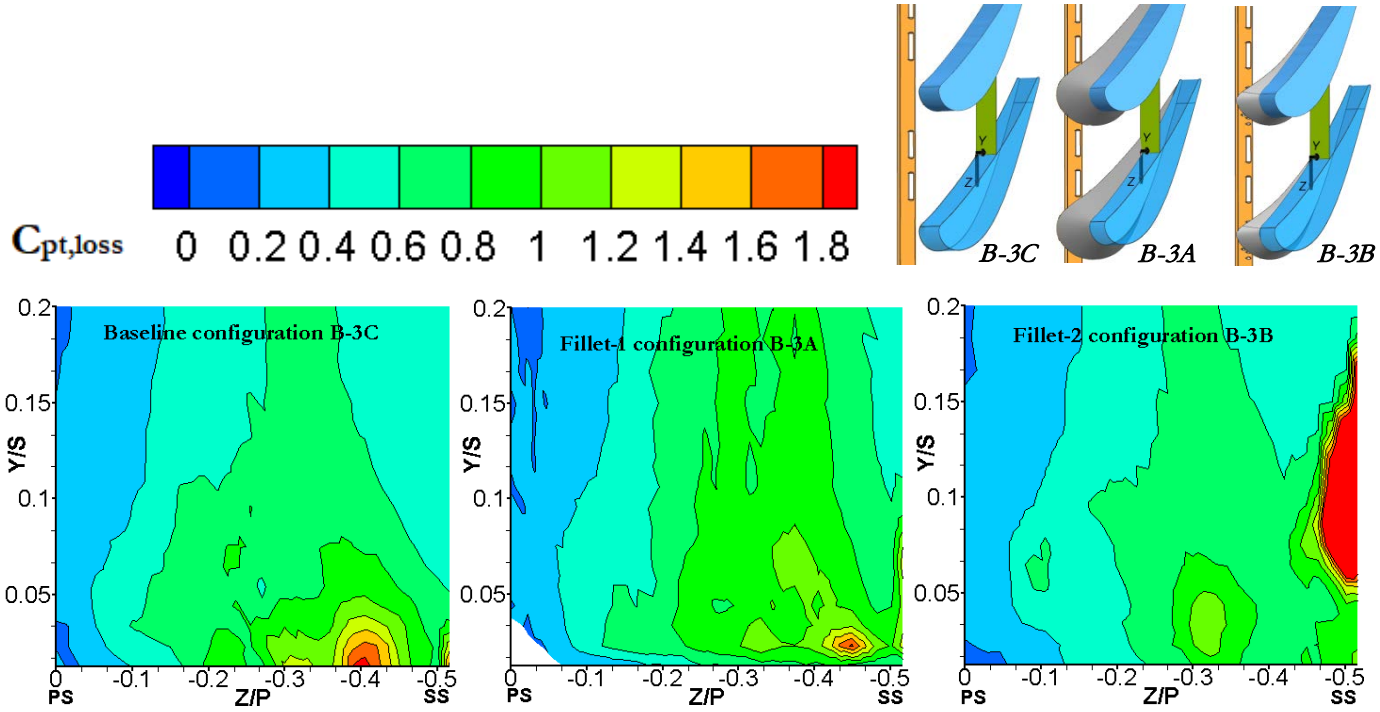

Figure 45: *Distributions of total pressure loss coefficient, Cpt, loss in third plane for baseline for Fillet 1 Case B-3A, Fillet 2 Case B-3B, baseline Case B-3C at M=1.4.*

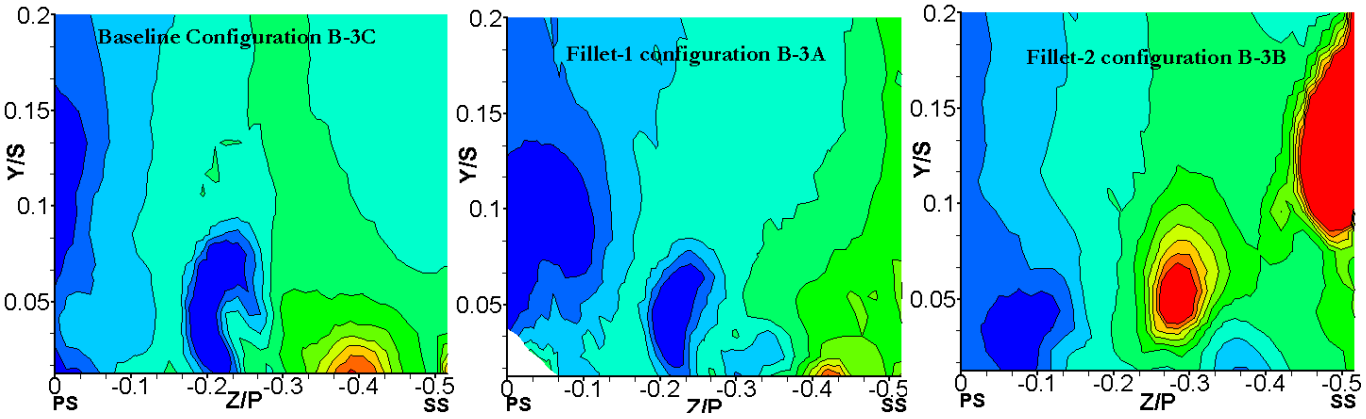

Figure 46: *Distributions of total pressure loss coefficient, Cpt, loss in third plane for baseline Case B-3B, Fillet 1 Case B-3A, and Fillet 2 Case B-3B at M=2.2.*

The distributions of $C_{pt,\,loss}$ contours in the pitch-wise plane at $X_{G/Cax}$ = 0.58 are presented in ***Figure 45*** and ***Figure 46***. Comparing the fillet's effect on the secondary flow and coolant interaction, Fillet 1 provided smaller sizes of the passage vortex core with $C_{pt,\,loss}$ > 0.8 near the SS corner, shown in ***Figure 45***, than for the baseline Case B-3C. In the baseline and fillet contours, without film-cooling (M = 0), shown in ***Figure 23***, the pressure-side leg vortex migrated towards the suction-side due to the passage cross-flow along the endwall. At a low inlet blowing ratio of M = 1.4, the pressure-side leg vortex was still present in all cases, but with reduced strength, as predicted by [45]. When the fillets were employed, the region of pressure loss along the endwall was extended along the span, but it was reduced at Z/P <-0.2 and Z/P <-0.23 for Case B-3A and Case B-3B

respectively. For Fillet 2, Case B-3B, the larger region of higher $C_{pt,\ loss} \geq 1.8$, on the suction-side above the endwall, was caused by the passage vortex lifted by the film-cooling as the endwall boundary layer was energised with high-momentum coolant jets. The coolant flow turned towards the SS along with the strong cross-pitch flow. The size and Cpt, loss values of the passage vortex were much larger for Fillet 2 than for the other cases. As the blowing ratio was increased to M = 2.2, shown in ***Figure 46***, the size of the passage vortex core with $C_{pt,\ loss} > 0.8$, near the SS corner, was significantly affected for all the cases. The slot injection at high M caused the high momentum coolant jet to reach the third plane downstream of the flow separation region. The presence of coolant in the large region on endwall in ***Figure 46*** is represented by the values of $C_{pt,\ loss} < 0$. The wider region of negative $C_{pt,\ loss}$ values along the endwall is observed for the case employing Fillet 1 (Case B-3A). The coolant distributions were located both in the mid-pitch and pressure-side for Case B-3A, while in Case B-3B, they were located towards the pressure-side.

The large region with values of $C_{pt,\ loss} \geq 1.8$ for Fillet 2, Case B-3B, showed that the passage vortex core was now located on SS, higher above the endwall than shown in ***Figure 46***. The elevated passage vortex core in Fillet 2 moved inside the trailing-edge vortex region when it travelled to the passage exit and it was not apparent at the exit. Furthermore, the coolant injection at higher M impacted the pressure-side leg vortex structure, because a new concentration of high values of $C_{pt,\ loss} \geq 1.8$, between $-0.33 < Z/P < -0.23$ and $0.03 < Y/S < 0.07$, was noticed.

The losses due to the mixing of coolant with the passage vortex structures along the vane passage contributed to the larger passage vortex for Case B-3B. The passage vortex results were thus bigger for Fillet 2 than for the other configurations. Also, the lower $C_{pt,\ loss}$ regions, shown in ***Figure 46***, indicated that the baseline configuration, Case B-3C, provided the lowest penetration of film-cooling flow into the boundary layers. Further data of $C_{pt,\ loss}$ distribution in the exit plane for Case B-3B and Case D with Fillet 2 are provided in Appendix C.

6.2.4. Filleted vane cascade with endwall film-cooling holes

The third set of investigations into film-cooling involved the combination of the LE cooling plates and the endwall film-cooling holes with and without Fillet 2. The set of configurations is displayed in ***Figure 47***.

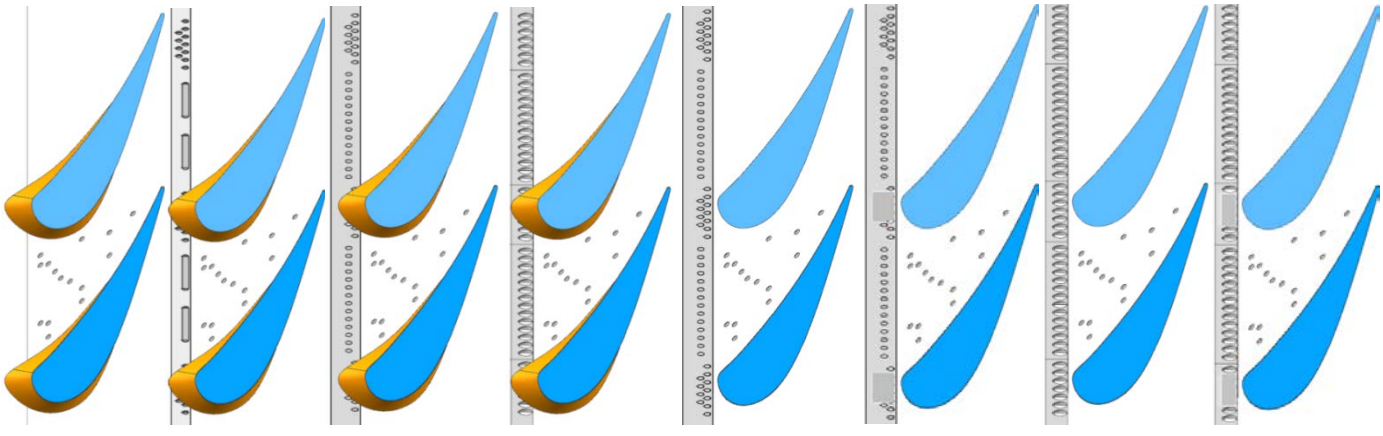

(E) **(B-4)** **(C-4)** **(D-4)** **(C-5)** **(C-6)** **(D-5)** **(D-6)**

Figure 47: *Cooling configurations: only passage cooling holes (E), two bleed cooling slots and cylindrical holes, passage cooling holes and fillet (B-4), cylindrical holes, passage cooling holes and fillet (C-4), diffused cylindrical holes, passage cooling holes and fillet, (D-4), cylindrical holes and (C-5), partially open cylindrical holes and passage cooling holes (C-6), diffused cylindrical holes and passage cooling holes (D-5), partially open diffused cylindrical holes and passage cooling holes (D-6).*

Table 21: *Endwall cooling configurations.*

Configuration	Description
E	Only endwall cooling, Fillet 2
B-4	Two LE bleed cooling slots and cylindrical holes partially closed, Fillet 2 + passage cooling holes
C-4	LE cylindrical holes, Fillet-2 + passage cooling holes
C-5	LE cylindrical holes, passage cooling holes
C-6	LE cylindrical holes partially closed, passage cooling holes
D-4	LE diffused cylindrical holes, Fillet-2 + passage cooling holes
D-5	LE diffused cylindrical holes, passage cooling holes
D-6	LE diffused cylindrical holes partially closed, passage cooling holes

Configuration E employed film cooling only from the endwall as the LE cooling plate was not used. This configuration was considered to evaluate the cooling in the passage without the flow deviation due to the LE cooling. All the measurements were conducted in the third and fourth planes from M=1.2 to M=2.8. The results were displayed in the passage between Vane 3 and Vane 4 where the endwall film-cooling was employed.

6.2.4.1. Flow angle deviation, ΔYaw (LE+passage cooling)

The flow yaw angle deviation was estimated from the local yaw angle after subtracting the yaw angle at the mid-span location. The positive ΔYaw indicated that the streamline turned towards the suction-side and the negative ΔYaw that it turned away from the suction -side of the passage. The effects of the endwall film-cooling, in the configurations shown in ***Table 21***, on the flow yaw angles were evaluated in ***Figure 48*** to ***Figure 53*** for the third plane and in ***Figure 54*** to ***Figure 59*** for the exit plane. The ΔYaw legend was the same for all plots.

For the unfilleted LE diffused cylindrical holes case in the third plane, Case D-5 shown in ***Figure 49***, at Y/S=0, the streamlines turned slightly less towards the SS than for the LE cylindrical holes case, Case C-5 shown in ***Figure 48***, indicating a better cooling penetration in the boundary layer.

At higher blowing ratios, M=2.4, the stronger jet momentum of the film-cooling flows swept the boundary layer and straightened the streamline near the endwall in the middle of the pitch line, facilitating a more uniform coolant distribution. As the blowing ratio increased, the differences in flow yaw angle deviation between the two cases were only noticeable just above the endwall at 0.02<Y/S>0.05 as the coolant seemed to be lifted towards the SS for Case D-5.

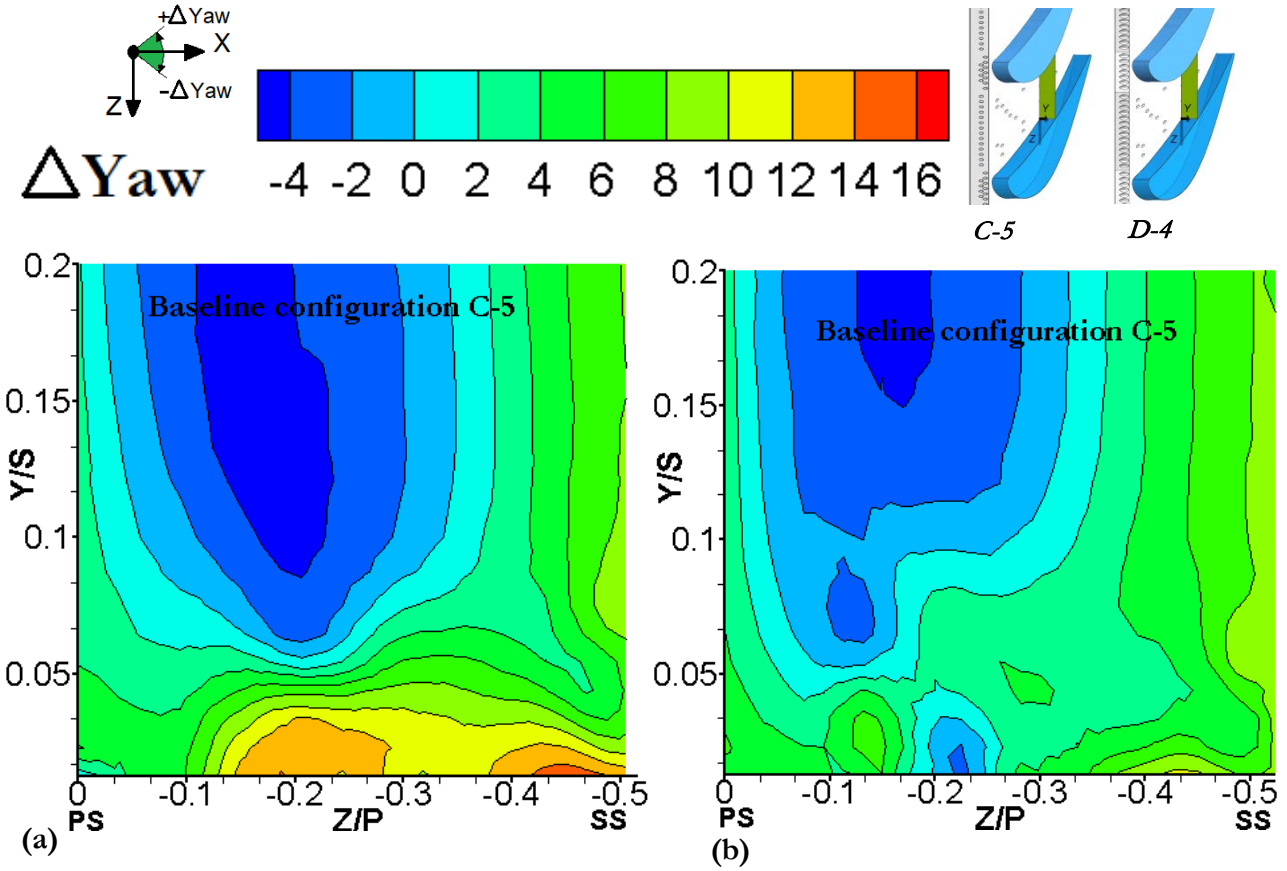

Figure 48: ⊿Yaw data in third plane: configuration Case C-5 a) M=1.4, b) M=2.4.

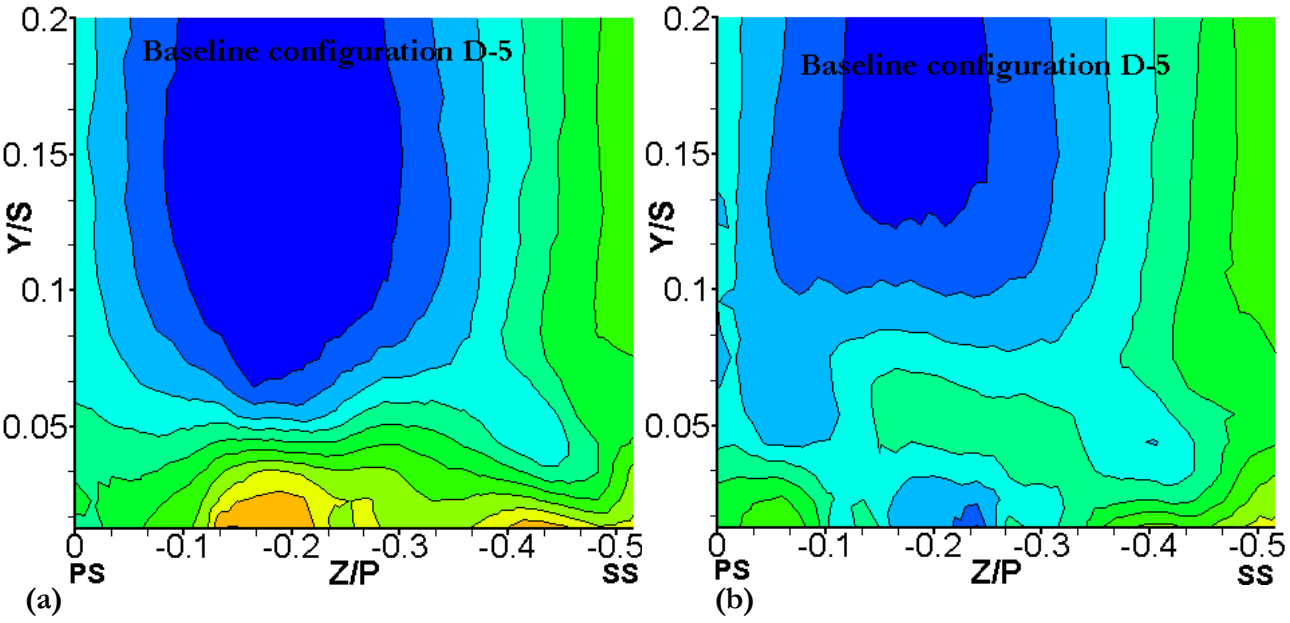

Figure 49: ⊿Yaw data in third plane: configuration Case D-5 a) M=1.4, b) M=2.4.

At 0.27<Z/P<-0.24, shown in ***Figure 48*** and ***Figure 49***, the coolant streams coming from the LE cooling holes interacted with the jet from the endwall cooling hole and forced the local streamlines towards the PS. Unfortunately, the endwall film-cooling did not successfully direct the flow's streamlines adjacent to the endwall along the passage direction as the LE cooling cases did. The best performance was exhibited by the LE slots case B-4, shown by ΔYaw contours in ***Figure 51***. By increasing the blowing ratio, because of the high momentum flow from the LE slots, Case B-4 displayed regions of ΔYaw<0 near the endwall in the middle of the pitch line, implicating a complete reversal in the flow angles.

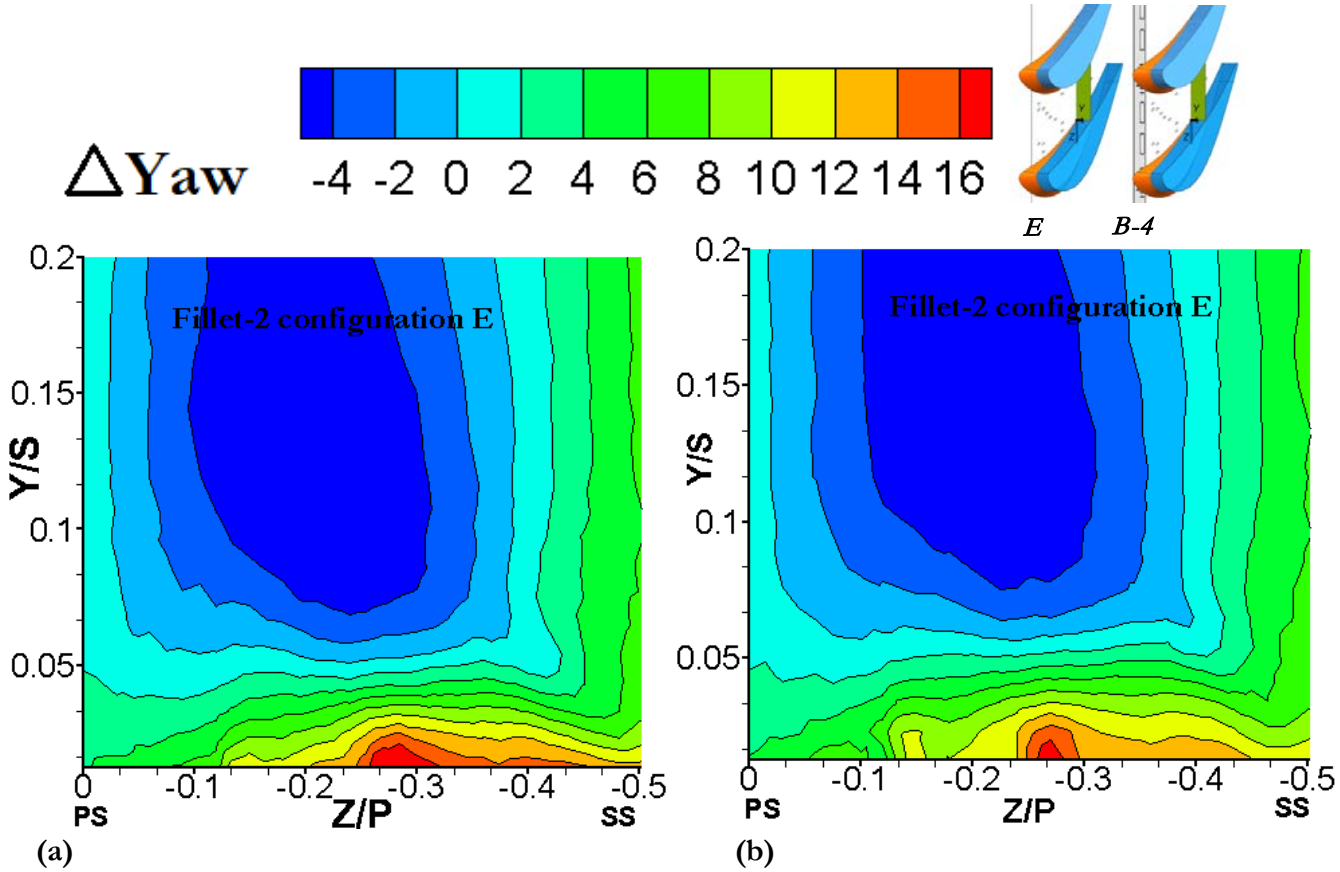

Figure 50: ⊿Yaw data in third plane: configuration Case E a) M=1.4, b) M=2.4.

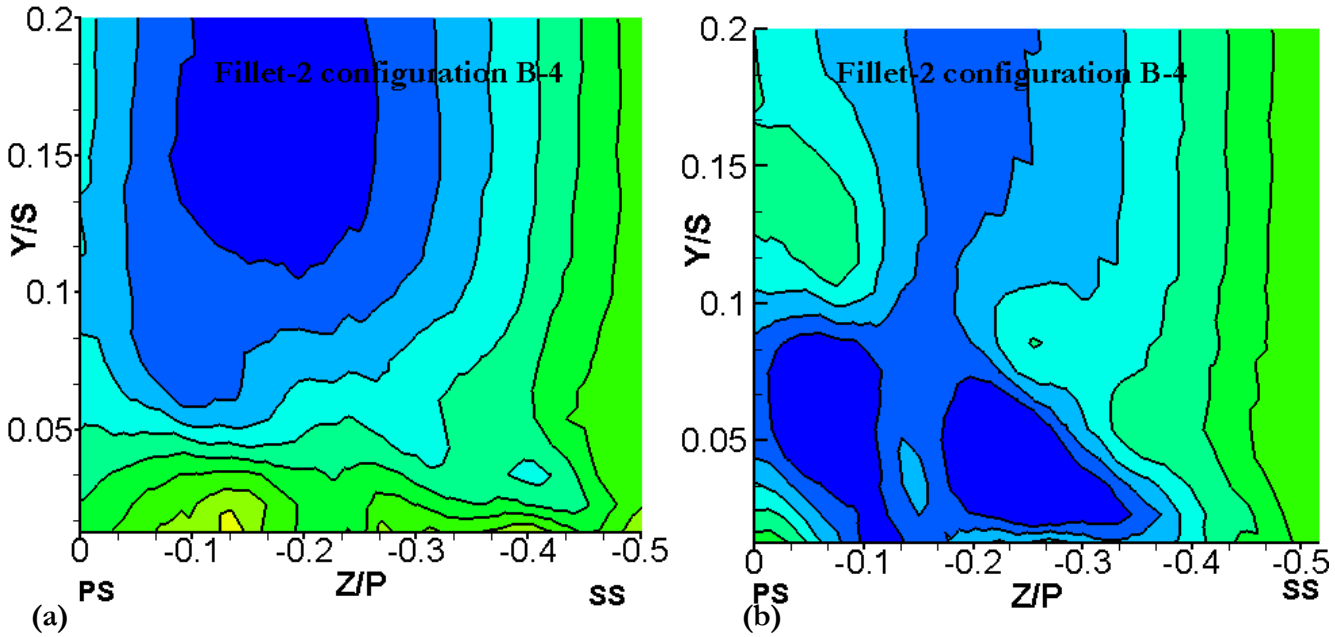

Figure 51: ⊿Yaw data in third plane: configuration Case B-4 a) M=1.4, b) M=2.4.

The filleted case with endwall film-cooling, Case E, shown in ***Figure 50***, had a wider endwall region with ΔYaw>16 towards the SS at both blowing ratios. In contrast to the case with no film-cooling shown in ***Figure 22-c***, that presents the ΔYaw contours in the same pitch-wise case for fillet-2 case but with no film-cooling, it seemed that the passage cooling holes reduced the flow yaw angle deviation on the endwall at -0.4<Z/P<-0.2. At -0.27<Z/P<-0.24, in the proximity of the endwall passage cooling hole, the coolant jet from the hole intensified the local streamlines turning towards the SS.

The effect of the fillet, combined with the LE film-cooling, quite substantially influenced the flow adjacent to the endwall. In the case of LE cylindrical cooling holes, shown in ***Figure 52***, the fillet reduced ΔYaw values adjacent to the endwall at a low blowing ratio, while it had a trivial impact on the flow at high M. However, it seemed to be detrimental when the fillet was employed on the LE of the diffused cylindrical cooling holes plate shown in ***Figure 53***. The fillet worsened the turnings of the streamlines towards the SS by lifting the coolant over the passage vortex on SS and intensifying the passage vortex. The coolant jet momentums, from both the LE diffused cylindrical holes and cylindrical holes, thus behaved differently when the fillet was present.

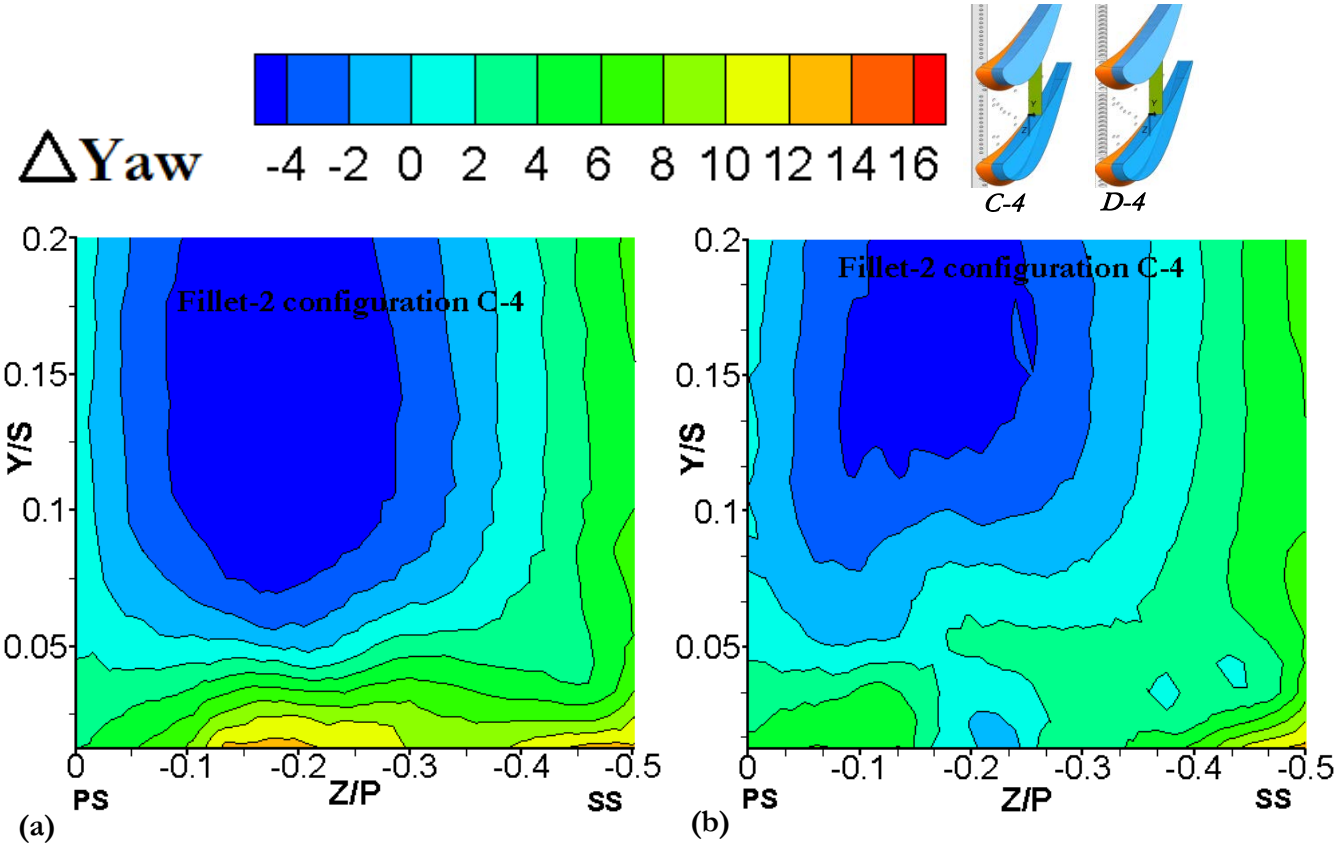

Figure 52: *ΔYaw data in third plane: configuration Case C-4 a) M=1.4, b) M=2.4.*

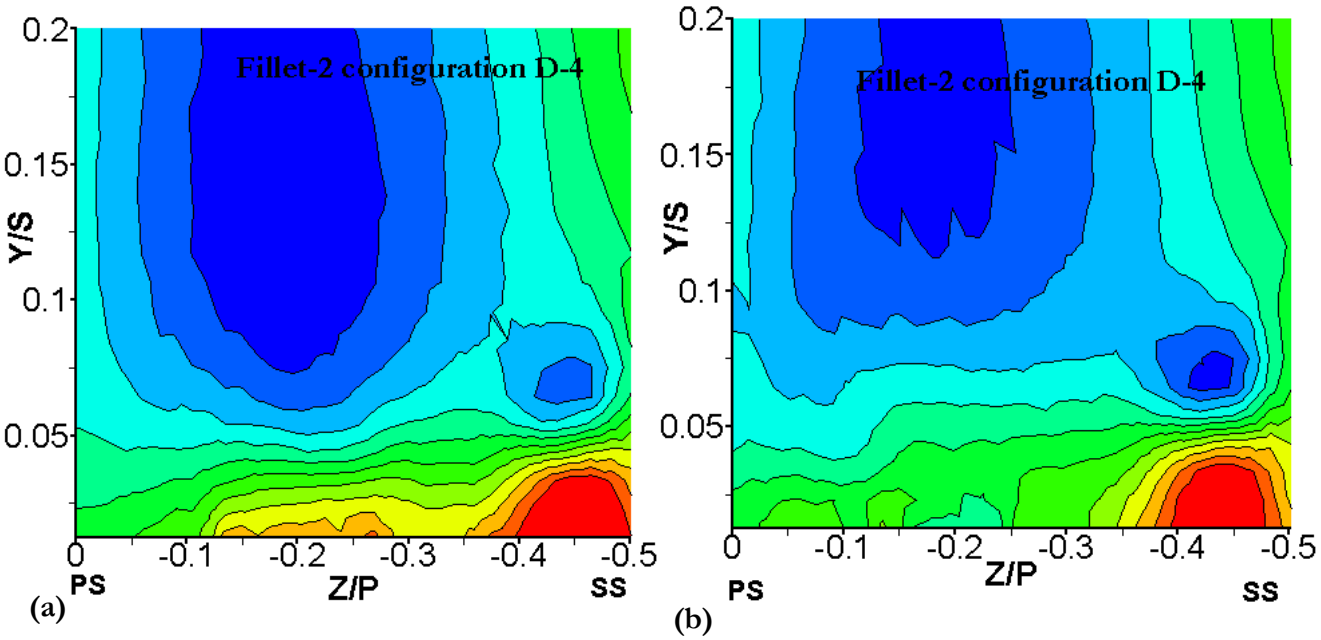

Figure 53: *ΔYaw data in third plane: configuration Case D-4 a) M=1.4, b) M=2.4.*

In the exit plane, the measurements extended to M=2.8 and the results are presented in ***Figure 54*** to ***Figure 59***. At M=1.2, strong positive yaw angle deviation, bigger than 10, was noticeable at the trailing edge at Y/S< 0.05 in all film-cooling cases except for Case B-4, as shown in the previous LE cooling investigation. By increasing the blowing ratio, the exit yaw angle deviation decreased in the endwall region, meaning that the boundary layer's streamlines, energised by the high coolant momentum, were more oriented in the axial direction.

The unfilleted cases, shown in ***Figure 54*** and ***Figure 55***, still showed a small exit yaw angle deviation in the endwall region Y/S< 0.05 even if the difference between them was small. Therefore, the coolant streams reduced the exit angle compared with the uncooled baseline, shown in ***Figure 24-a,*** on the endwall region, but it still presented interaction with the cross-flow passage in the boundary layer.

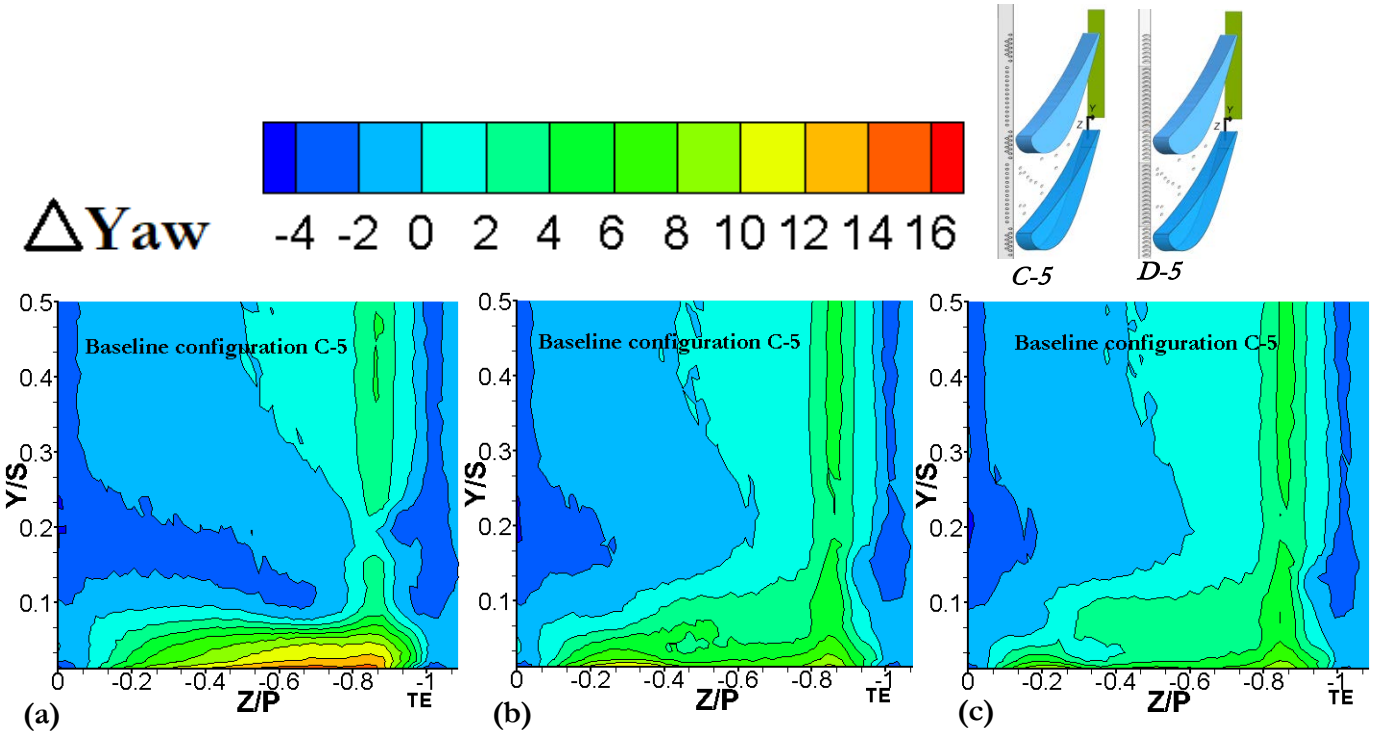

Figure 54: *⊿Yaw data in exit plane: configuration Case C-5 a) M=1.2, b) M=2.4, c) M=2.8.*

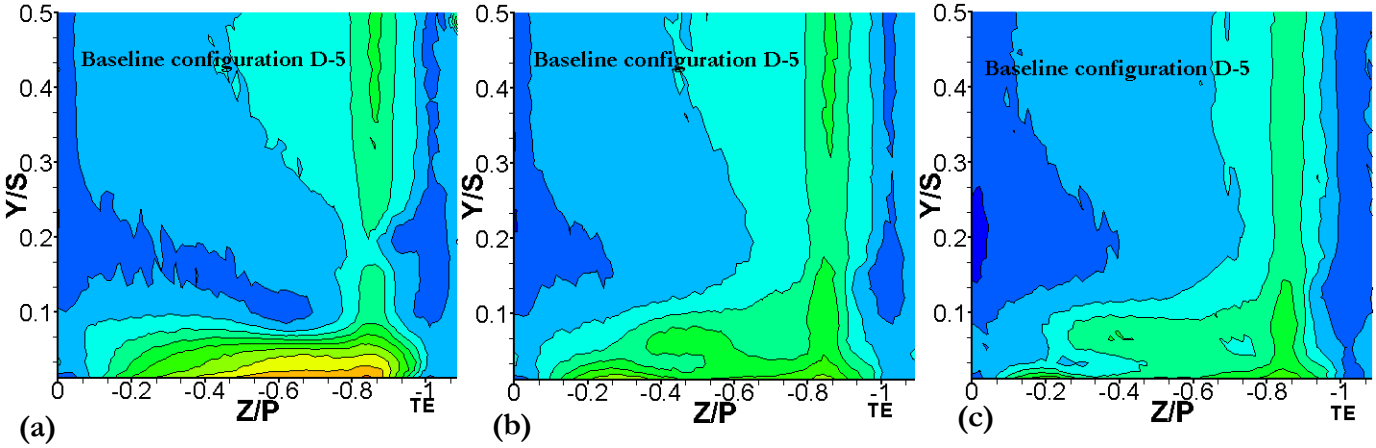

Figure 55: *⊿Yaw data in exit plane: configuration Case D-5 a) M=1.2, b) M=2.4, c) M=2.8.*

Figure 57 indicates that Case B-4 was the only case that displayed negative ΔYaw values in the endwall region at -0.4< Z/P<-0.09 because of the high momentum flow ejected from the slots. Case E, shown in ***Figure 56***, resulted in being less effective in reducing the secondary flow even at high M, as the coolant flux

from the few small openings of the discrete endwall holes was too weak to influence the passage flow significantly.

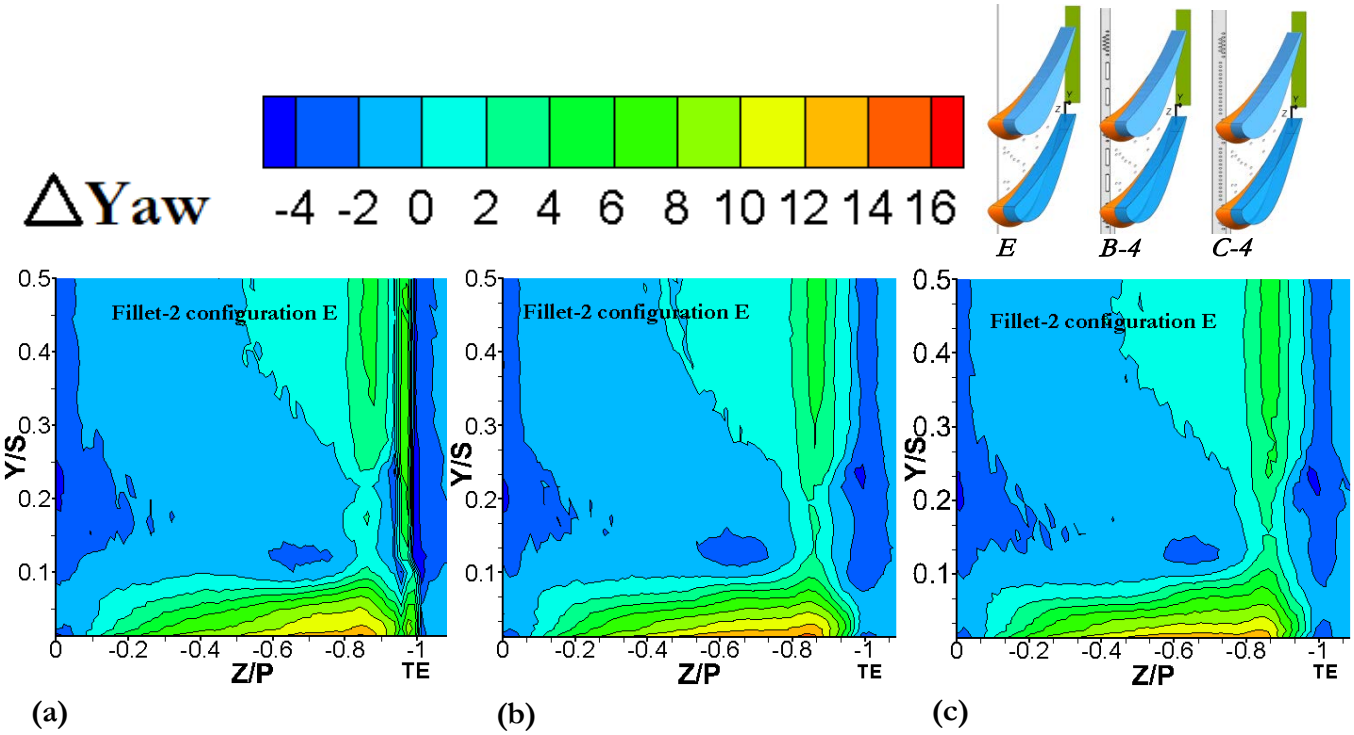

Figure 56: ⊿Yaw data in exit plane: configuration Case E a) M=1.2, b) M=2.4, c) M=2.8.

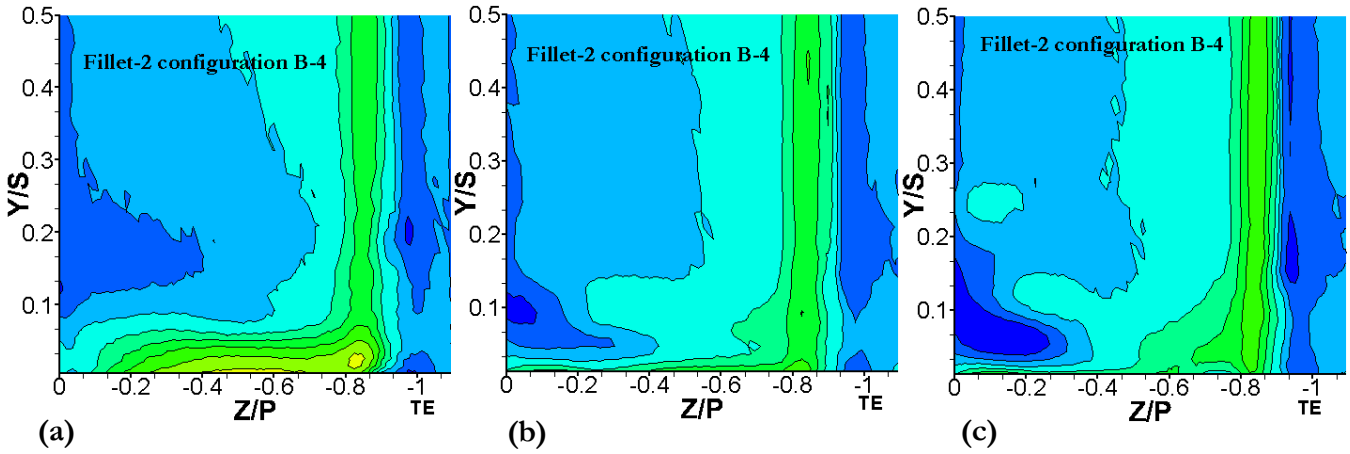

Figure 57: ⊿Yaw data in exit plane: configuration Case B-4 a) M=1.2, b) M=2.4, c) M=2.8.

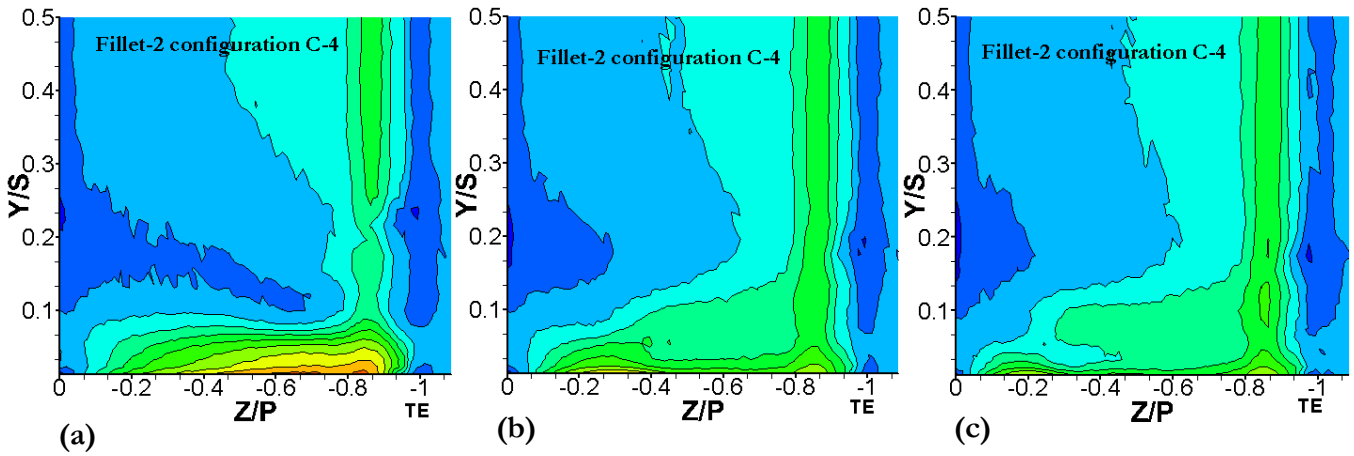

Figure 58: ⊿Yaw data in exit plane: configuration Case C-4 a) M=1.2, b) M=2.4, c) M=2.8.

Figure 58 and *Figure 59* indicate that the streamline direction of the exit flow from the passage was slightly more uniform with the LE diffused holes than with the LE cylindrical holes.

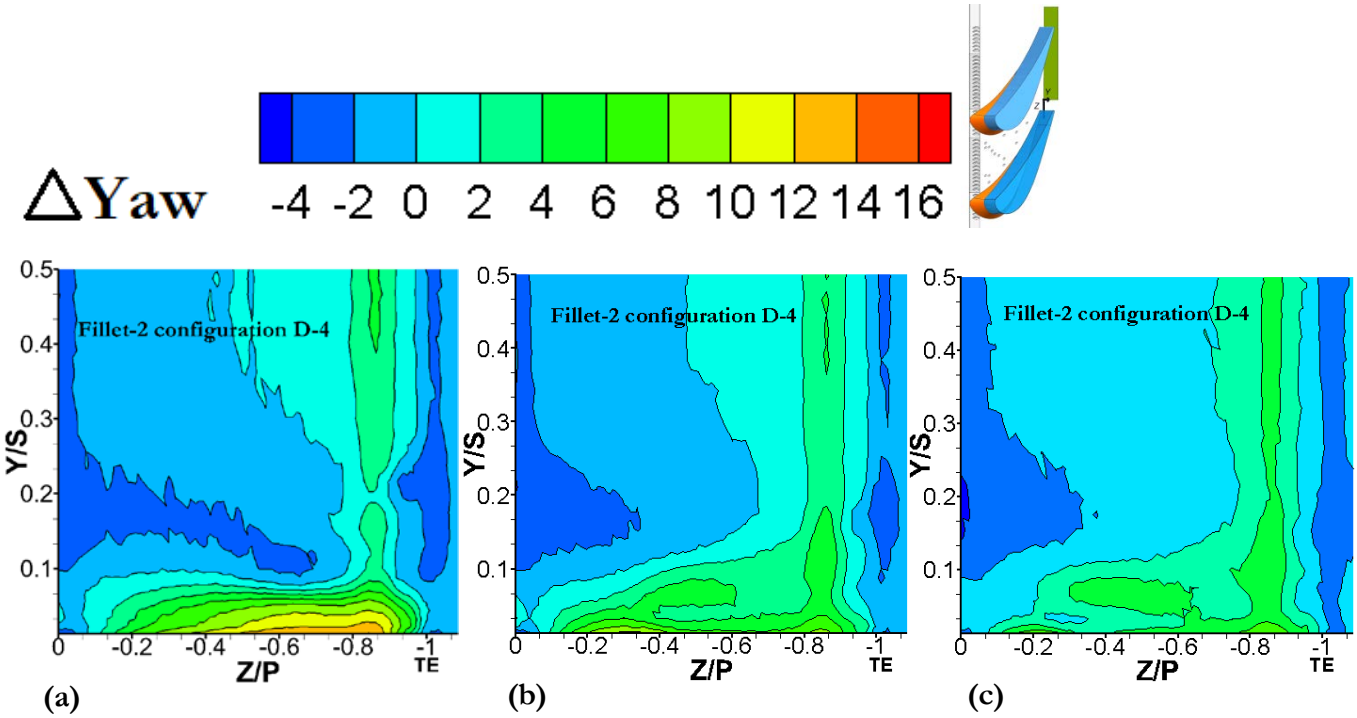

Figure 59: ⊿Yaw data in exit plane: configuration Case D-4 a) M=1.2, b) M=2.4, c) M=2.8.

6.2.4.2. Total loss(LE+passage cooling)

The distributions of the total pressure loss coefficient in the cascade, $C_{pt,\,loss,}$ based on the locally measured total pressure, Eq. (10), were presented in the third plane in *Figure 60* to *Figure 65* and in the exit plane in *Figure 66* to *Figure 71*.

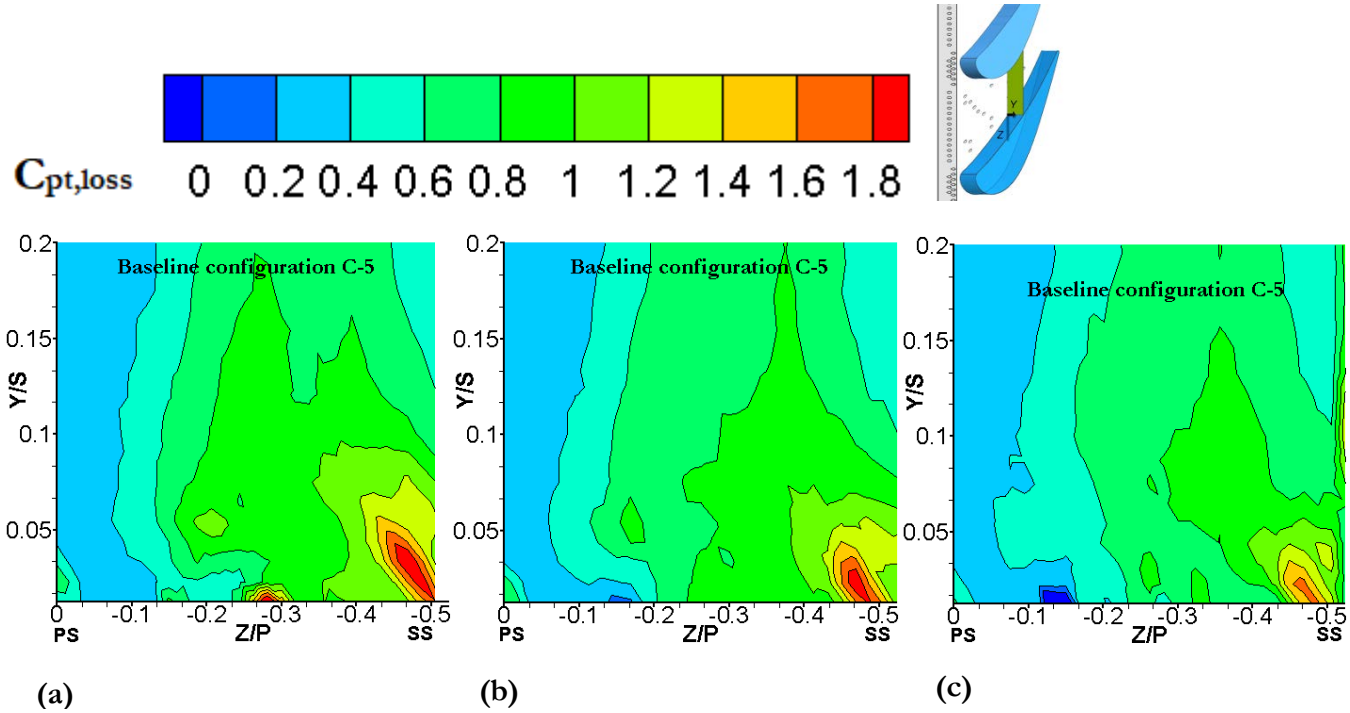

Figure 60: Total pressure loss coefficient, $C_{pt,\,loss}$ contours for Case C-5, in third plane, a) M=1.2, b) M=1.8, c) M=2.4.

The examination of the $C_{pt,\,loss}$ figures, in the third plane for the baseline cases, shown in ***Figure 60*** and ***Figure 61***, highlighted the strength of the passage vortex core and its location near the suction-side (SS) corner. As already observed in the former discussion, the LE diffused cylindrical hole configuration provided a better film-cooling performance near the endwall region than the configuration of the LE cylindrical holes did.

Compared with Case C-1 and Case D-1 with no passage cooling holes shown in ***Figure 29***

Figure 29 at M=1.8, it seemed that the coolant jet from the endwall holes, in Case C-5 and Case D-5, penetrated into the boundary layer further towards the suction-side until Z/P ≈ -0.25 at the cost of higher boundary layer mixing losses on the suction-side region.

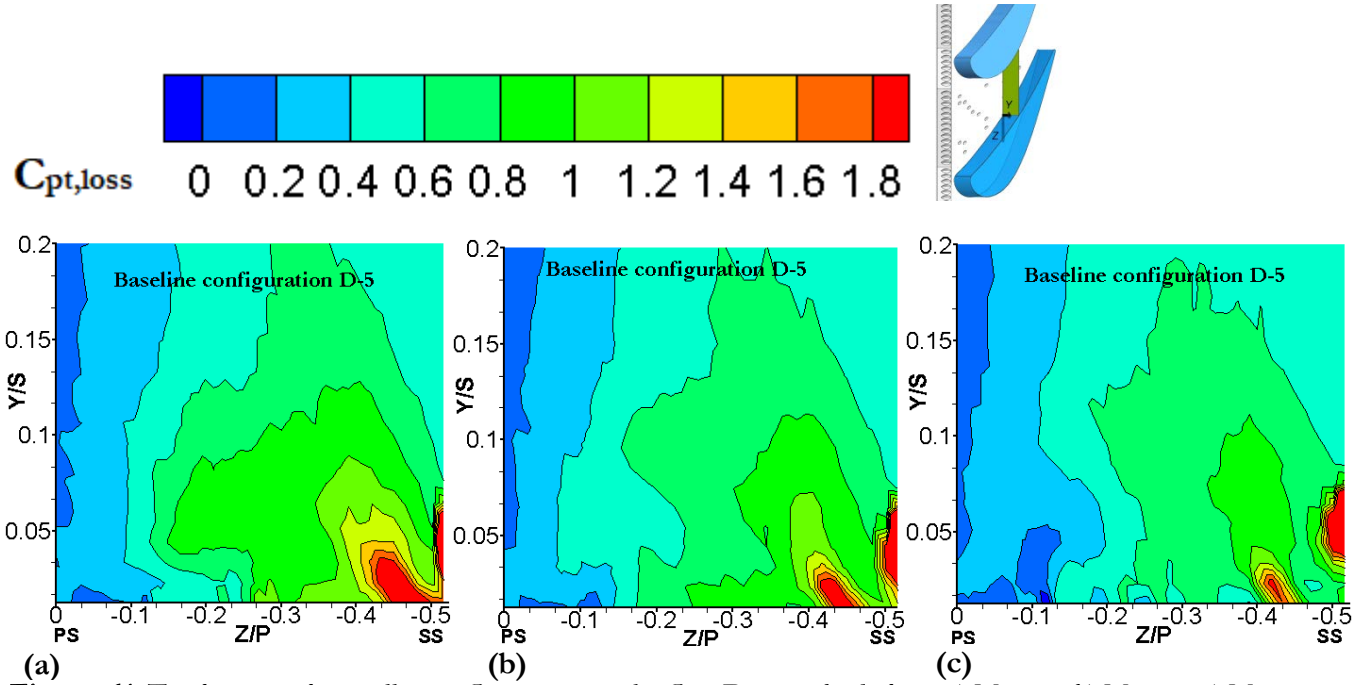

Figure 61: *Total pressure loss coefficient, $C_{pt,\,loss}$ contours for Case D-5, in third plane, a) M=1.2, b) M=1.8, c) M=2.4.*

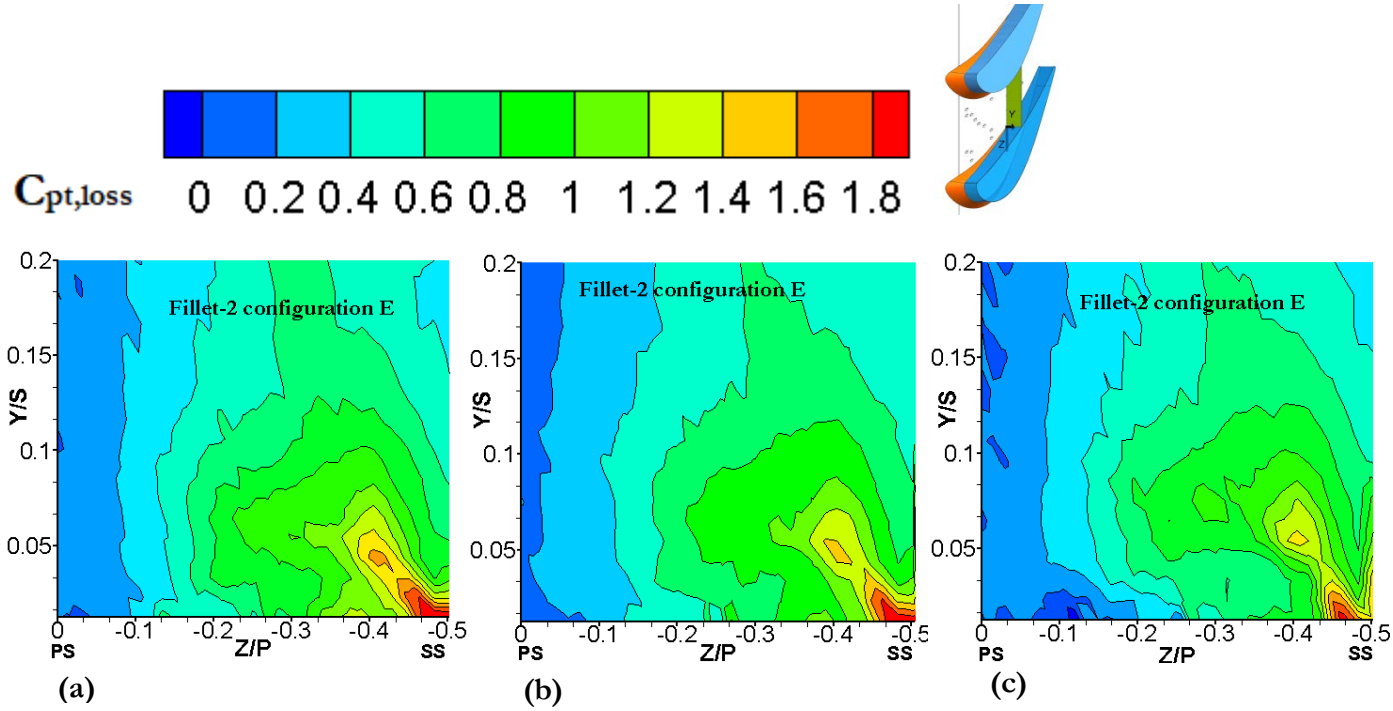

Figure 62: *Total pressure loss coefficient, $C_{pt,\,loss}$ contours for Case E, in third plane, a) M=1.2, b) M=1.8, c) M=2.4.*

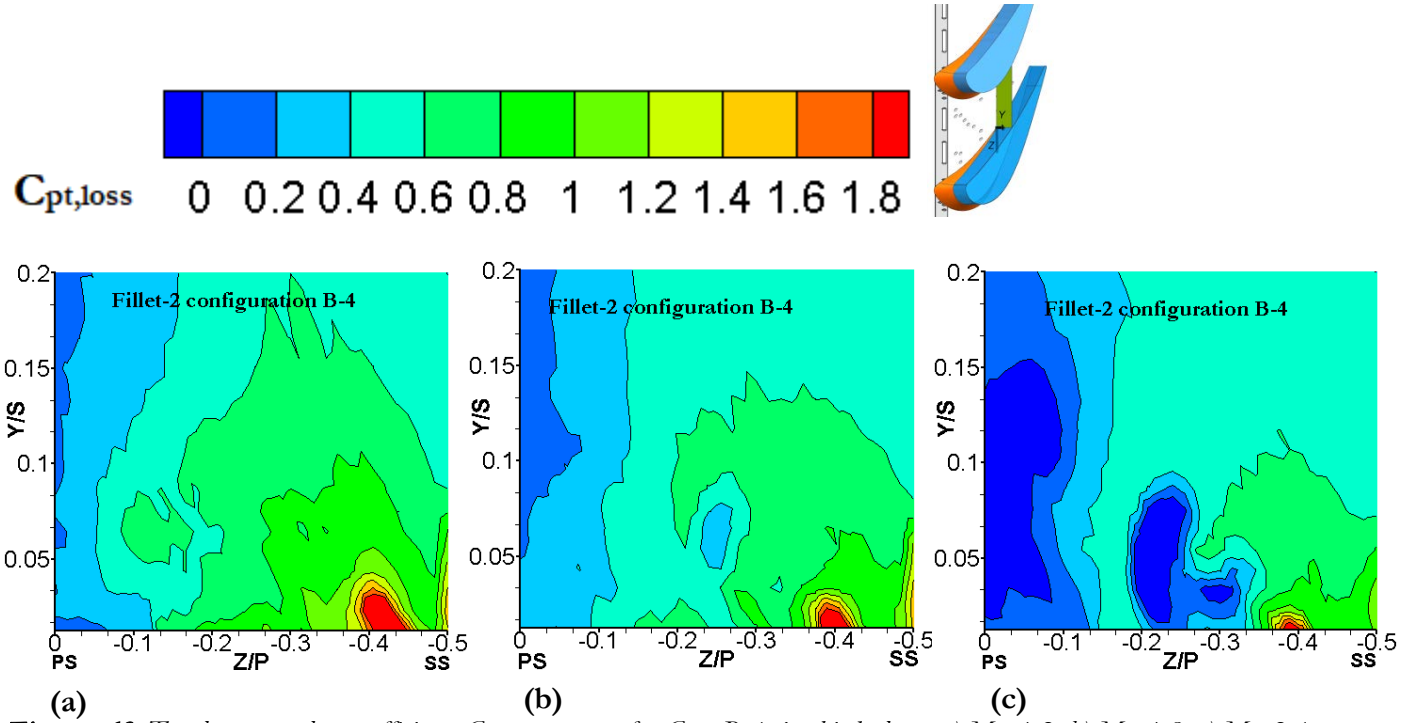

Figure 63: *Total pressure loss coefficient, $C_{pt,\,loss}$ contours for Case B-4, in third plane, a) M=1.2, b) M=1.8, c) M=2.4.*

In both filleted vane configurations, Case B-4 and Case C-4, shown in ***Figure 63*** and ***Figure 64***, the coolant covered mostly the endwall at high M but none of them extended the coverage to the SS as for Case D-4 (***Figure 65***). The coolant from the two slots, in Case B-4, was mostly wasted along the span because it was lifted off by the passage vortex separation area region located upstream.

For Case E, shown in ***Figure 62***, the endwall film-cooling flow combined with Fillet 2, achieved a cooled endwall until mid-pitch at M=2.4 and affected the passage vortex reducing the size. The filleted vane with LE diffused cylindrical holes, Case D-4 (***Figure 65***), validated the predisposition, already noticed in ***Figure 30*** (Case D-1) to intensify the passage vortex compared with the LE cylindrical holes in Case C-4 (***Figure 64***).

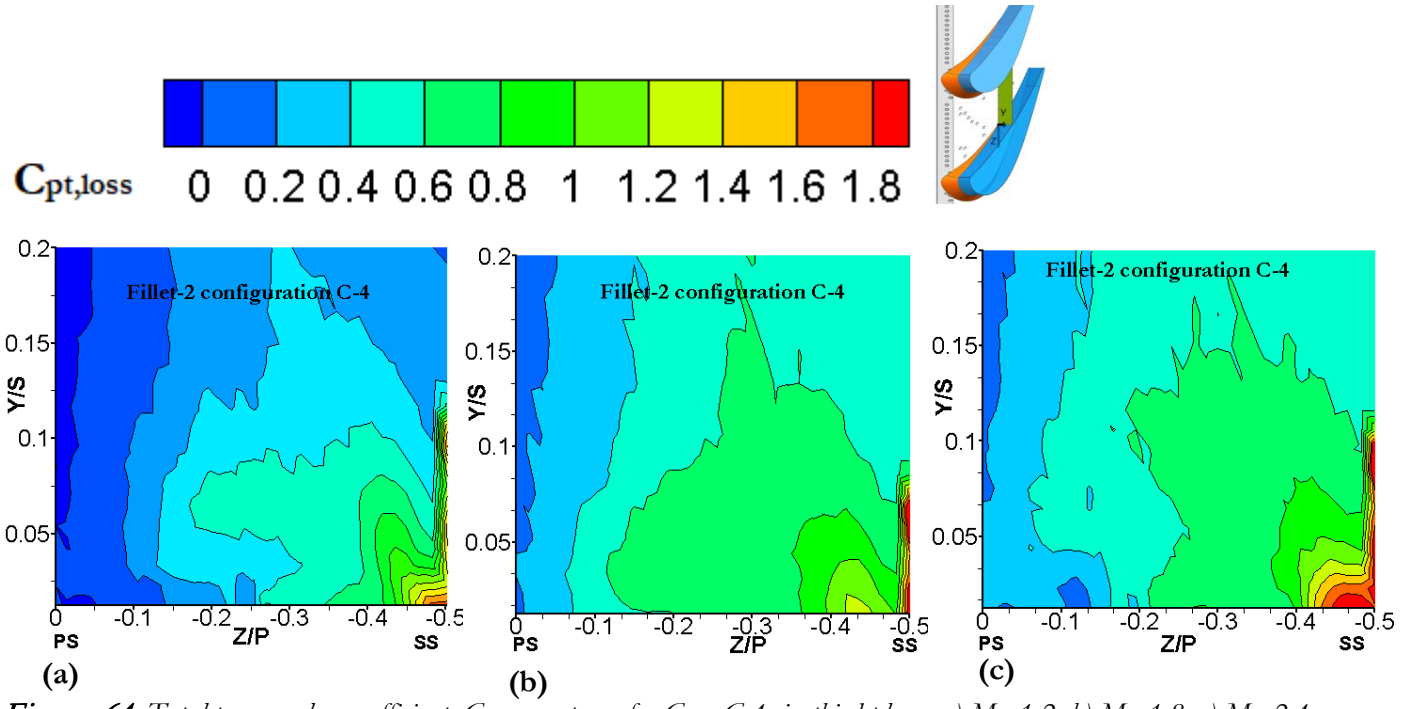

Figure 64: *Total pressure loss coefficient, $C_{pt,\,loss}$ contours for Case C-4, in third plane, a) M=1.2, b) M=1.8, c) M=2.4.*

The mixing losses due to the interactions of the coolant jets with the boundary layer had to be higher for the diffused hole cases, causing a larger and stronger passage vortex than for the cylindrical hole cases.

Nonetheless, Case D-4 diffused the coolant jet deeply in endwall boundary layers as the coolant exited the holes more tangentially to the surface reaching regions closer to SS. This phenomenon of increased cooling performance from the diffused holes, compared with cylindrical holes, was also noticed by Colban et al. [21, 31], as a consequence of the diffused hole jet not being prone to separation in the same way as the cylindrical hole jet.

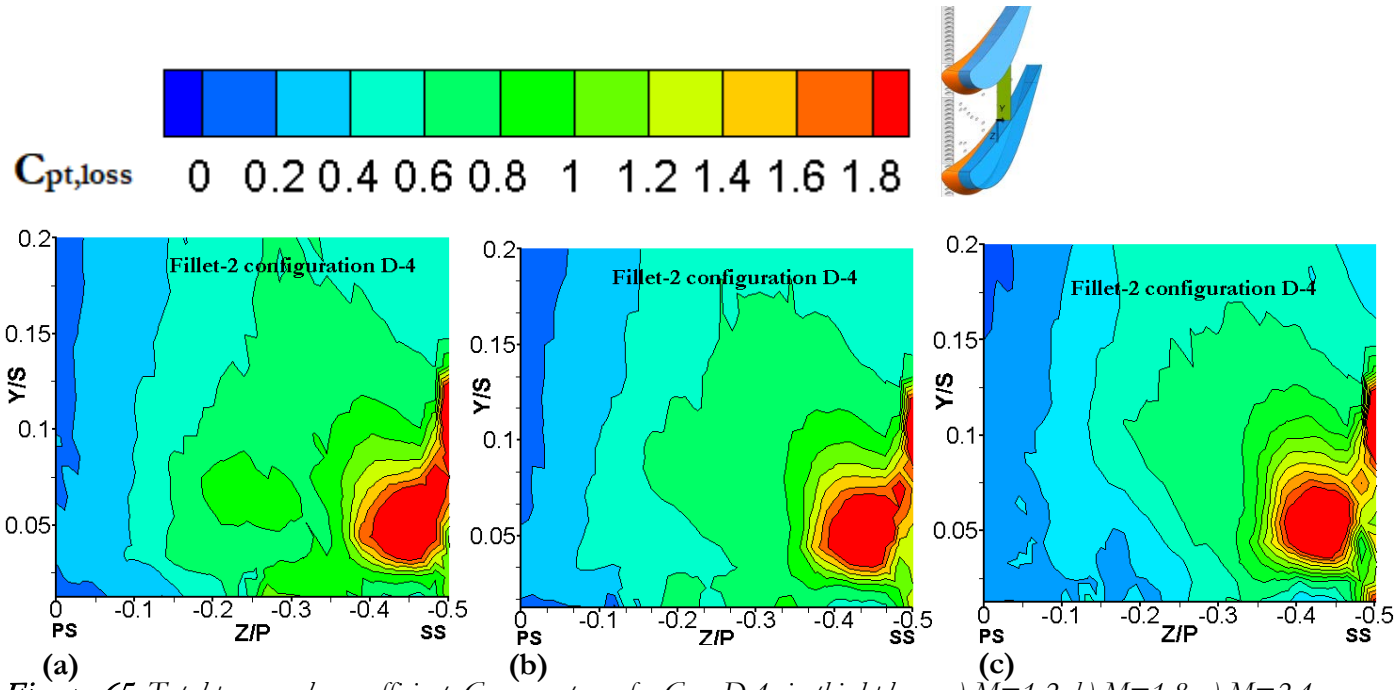

Figure 65: *Total pressure loss coefficient, $C_{pt,\,loss}$ contours for Case D-4, in third plane, a) M=1.2, b) M=1.8, c) M=2.4.*

At high M, the LE cylindrical hole combined with the filleted vane, Case C-4 shown in ***Figure 64***, in contrast with Case C-5 shown in ***Figure 60***, showed noticeable negative effects of the fillet on the $C_{pt,\,loss}$ values inside the passage vortex. The distributions of the $C_{pt,\,loss}$ inside the passage vortex were bigger than for the baseline case because the fillet's presence interacted with the film-cooling contributing to an increase in the local total pressure, $P_{t,loc}$. The size and the $C_{pt,\,loss}$ values of the passage vortex were much larger for Case D-4 than for any other case.

In contrast to Case C-4, the total pressure losses produced near the endwall for the LE diffused cylindrical holes, Case D-4 shown in ***Figure 65***, had a different pattern. The presence of the fillet caused the film-cooling to penetrate the boundary layer and cool deeper and more uniformly than for the baseline case, as shown in ***Figure 61***. The high $C_{pt,\,loss}$ concentration located at $-0.47 < Z/P < -0.37$ represented the intensified passage vortex that was lifted by the coolant jet.

The $C_{pt,\,loss}$ distributions in the exit plane are presented in ***Figure 66*** to ***Figure 71*** at two blowing ratios M=1.2 and M=2.4. The $C_{pt,\,loss} \geq 1.0$ distributions represented three regions:

(i) the trailing edge (TE) vortex with the vertical distributions of the $C_{pt,\,loss} \geq 1.0$ about $Z/P \approx -1.0$;

(ii) the exit passage vortex high above the endwall and on the left side of TE vortex with distributions of the $C_{pt,\,loss} \geq 6.0$ at about $0.2 < Y/S < 0.25$; and

(iii) the boundary layer mixing losses adjacent to the endwall with distributions of the $C_{pt,\,loss} \geq 6.0$ at about $0 < Y/S < 0.02$.

The passage vortex at the exit plane was partly located inside the TE vortex and interacted with it.

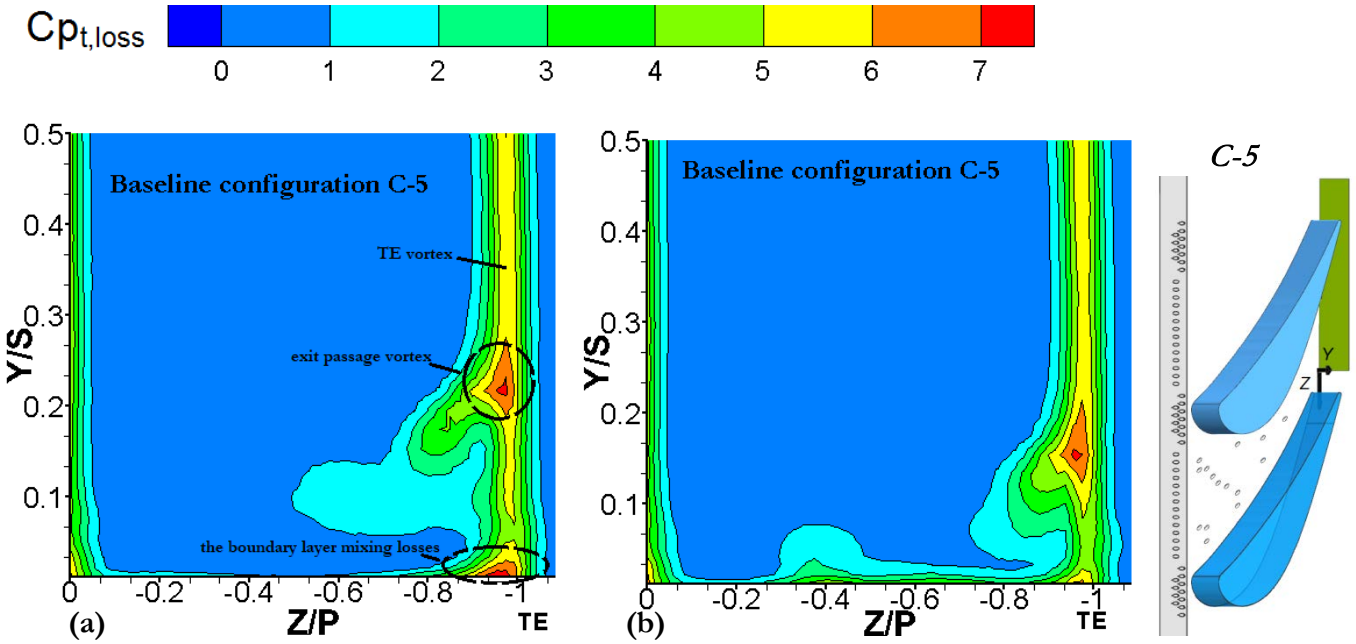

Figure 66: Total pressure loss coefficient, $C_{pt,\,loss}$ contours in exit plane for Case C-5 a) M=1.2, b) M=2.4.

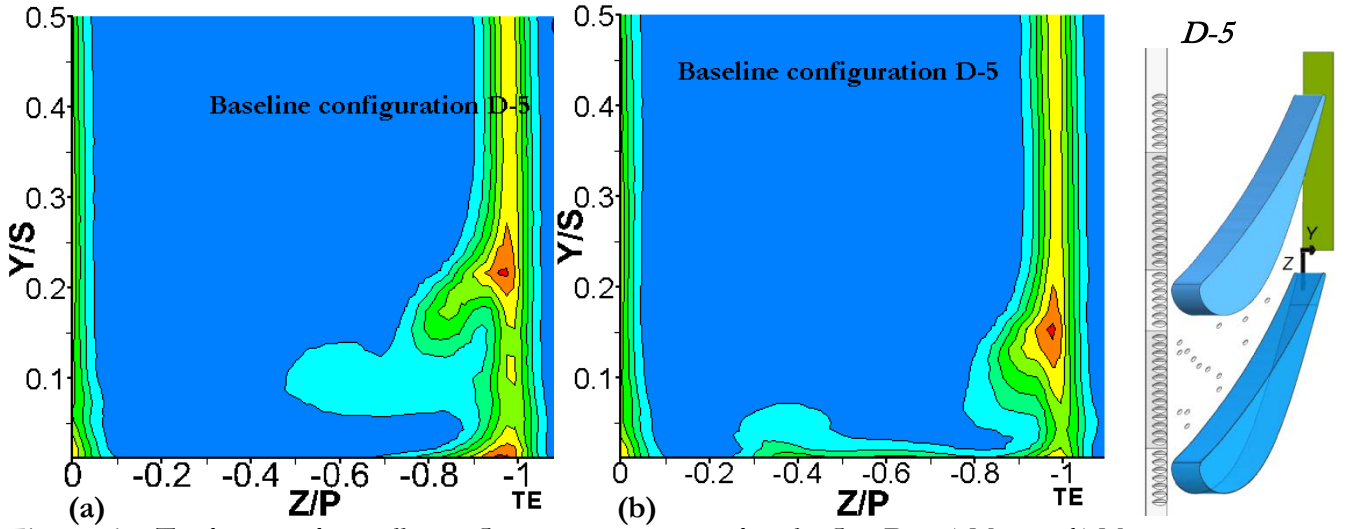

Figure 67: Total pressure loss coefficient, $C_{ptot,\,loss}$ contours in exit plane for Case D-5 a) M=1.2, b) M=2.4.

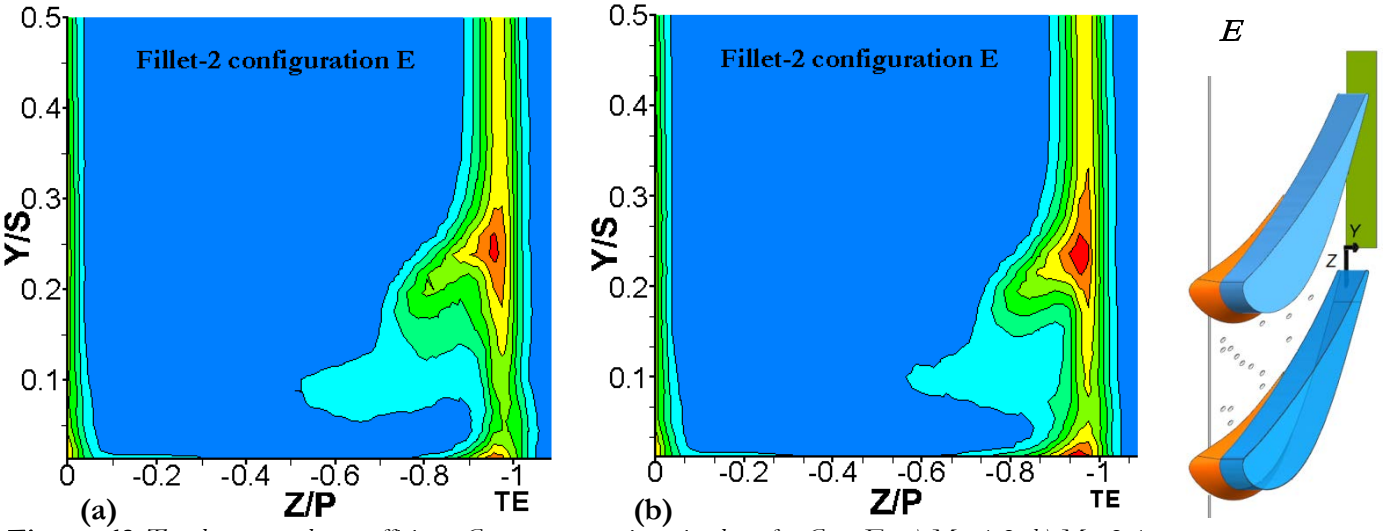

Figure 68: Total pressure loss coefficient, $C_{pt,\,loss}$ contours in exit plane for Case E, a) M=1.2, b) M=2.4.

The plots of ***Figure 66*** to ***Figure 71*** at M =1.2 or M = 2.4 show the impact of the endwall coolant ejection on the secondary flows by the $C_{pt,loss}$ distributions in the three regions. For all the cases, the $C_{pt,\,loss}$ distributions decreased in the passage vortex with increasing blowing ratio and the passage vortex core shifted closer to the endwall except for Case E. ***Figure 68*** indicates that the passage vortex kept its location at Y/S≈0.25 and strengthened. Furthermore, at high M, the boundary layer mixing losses reduced and the near-wall losses along the pitch line appeared as a result of the upstream cooling injection with high momentum.

Comparing different cases at constant M, when the fillet was present, the region of $C_{pt,\,loss}$>7 became wider as a sign of intensity gain of the exit passage vortex.

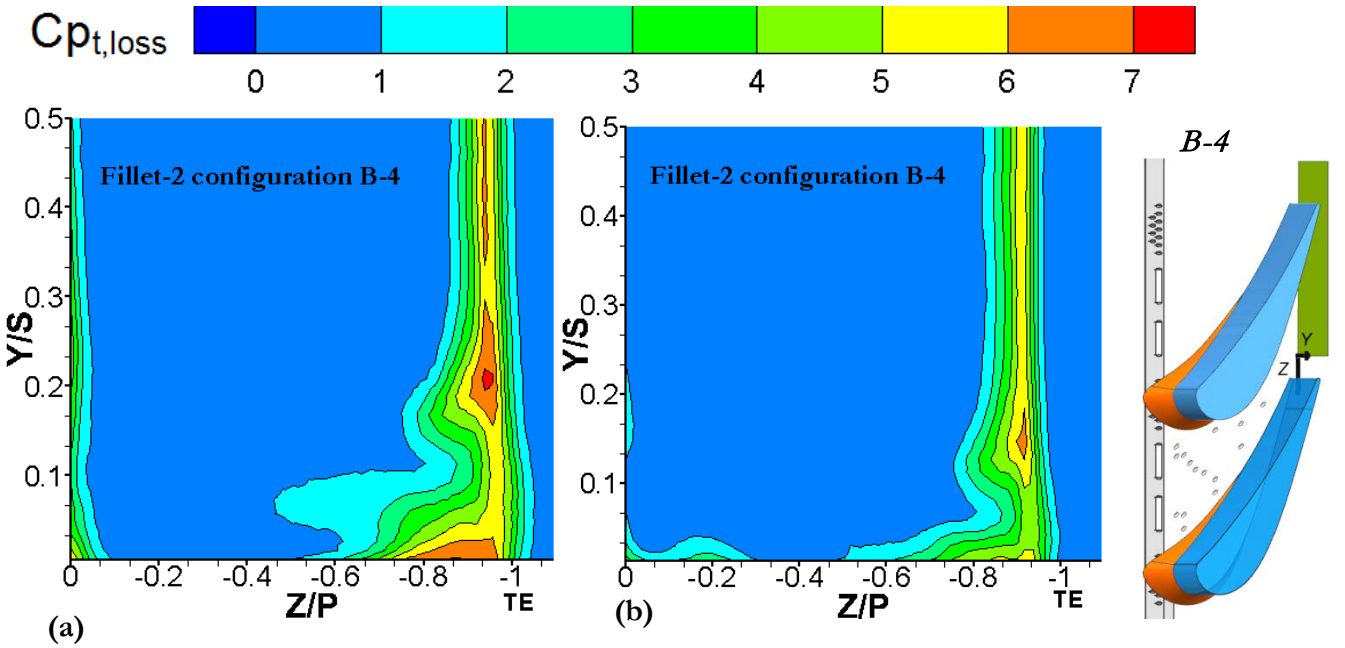

Figure 69: *Total pressure loss coefficient, Cpt, loss contours in exit plane for Case B-4, Slot-4, a) M=1.2, b) M=2.4.*

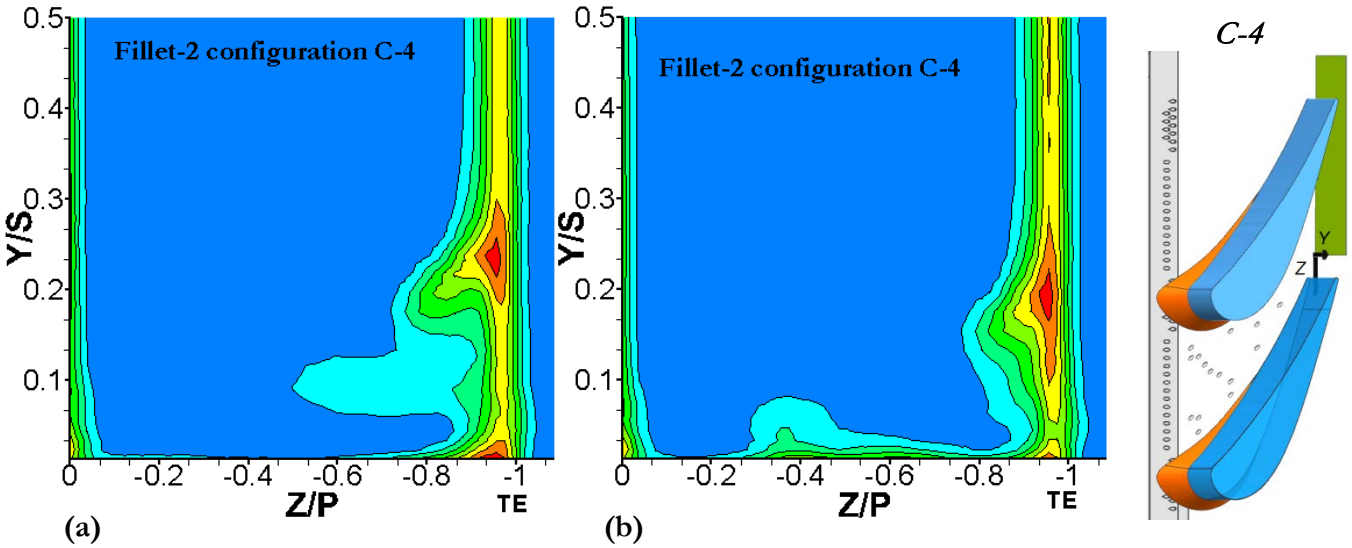

Figure 70: *Total pressure loss coefficient, $C_{pt,\,loss}$ contours in exit plane for Case C-4, Slot-4, a) M=1.2, b) M=2.4.*

In Case C-4 (***Figure 70***), the LE blocked holes from the fillet presence seemed to have the consequence to shift the exit passage vortex further away from the endwall at Y/S ≈ 0.17 and to enhance it, when compared with the baseline case, shown in ***Figure 66***.

When the LE cooling flow was absent, for Case E shown in ***Figure 68,*** the endwall cooling holes seemed to worsen the losses at a high blowing ratio. At high M, the filleted LE slot configuration shown in ***Figure 70***, Case B-4, displayed the smallest secondary losses followed by the baseline with LE diffused cylindrical holes, shown in ***Figure 71***.

Thus, the low $C_{pt,\,loss}$ value concentration at high M, indicated that Cases B-4 and D-4 were the best for reducing the losses of the passage vortex and boundary layer mixing.

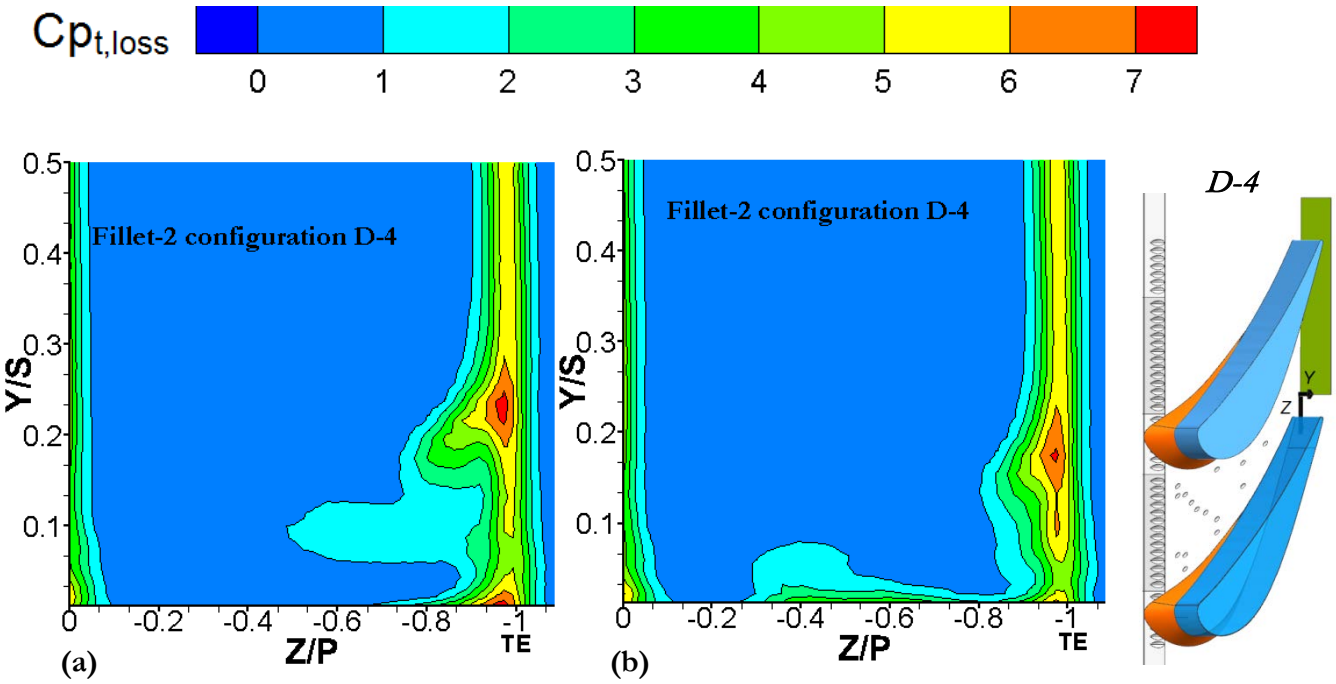

Figure 71: *Total pressure loss coefficient, $C_{pt,\,loss}$ contours in exit plane for Case D-4, a) M=1.2, b) M=2.4.*

At high M, the same conclusion on the lowest losses achieved by Case B-4 was confirmed by ***Figure 72***, which displays the mass-averaged $C_{pt,\,loss}$ at the exit plane. The $(C_{pt,\,loss})_{mass\text{-}av}$ distribution was always smaller for Case B-4 than for the other configurations.

The effects of the endwall cooling configurations and the blowing ratio on the overall pressure losses in the exit plane were revealed by the mass-average loss coefficient, $(C_{pt,\,loss})_{mass\text{-}av}$ and by the ratio $(C_{pt,\,loss})_{mass\text{-}av}$ /MFR respectively shown in ***Figure 72*** and ***Figure 73***.

The mass average was computed by the numerical integration of Equation (21) over the entire measurement area (Y/S=0 to 0.5) in the exit plane. The $(C_{pt,\,loss})_{mass\text{-}av}$ increased and peaked for all film-cooling configurations at M =1.8, and then it decreased as higher blowing ratios increased. A possible explanation for the $C_{pt,\,loss}$ increase with M < 1.8 could be because the low momentum jets entering the passage thickened the boundary layer contributing to higher mixing losses near the endwall region. However, at higher M, the high momentum jets travelled to the exit affecting the cross-flow and passage vortex. Friedrichs et al. [14] also observed that substantial cooling flow rates could delay the three-dimensional separation of the inlet boundary layer, thereby reducing the strength of the passage vortex.

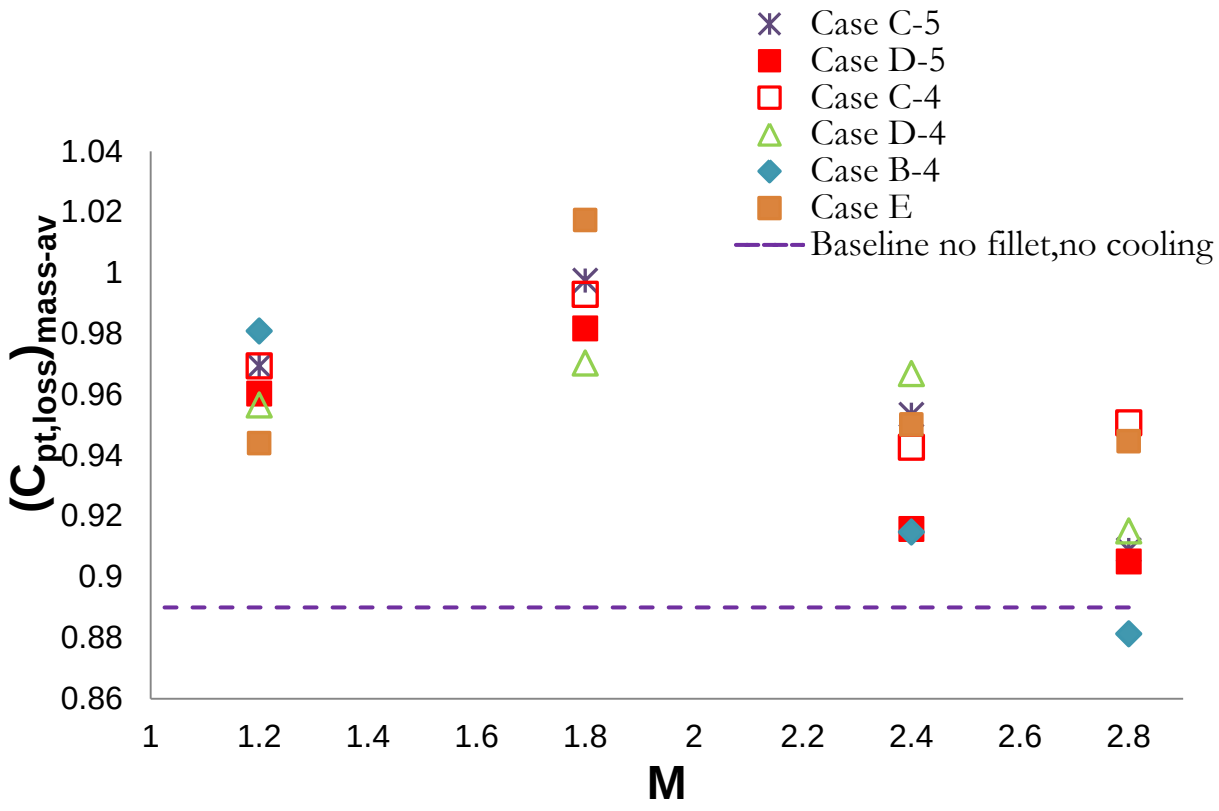

Figure 72: Overall mass-averaged, $(C_{pt,\,loss})_{mass\text{-}av}$ vs. M (Case-E, B-4, C-5, D-5 C-4, D-4), at exit plane.

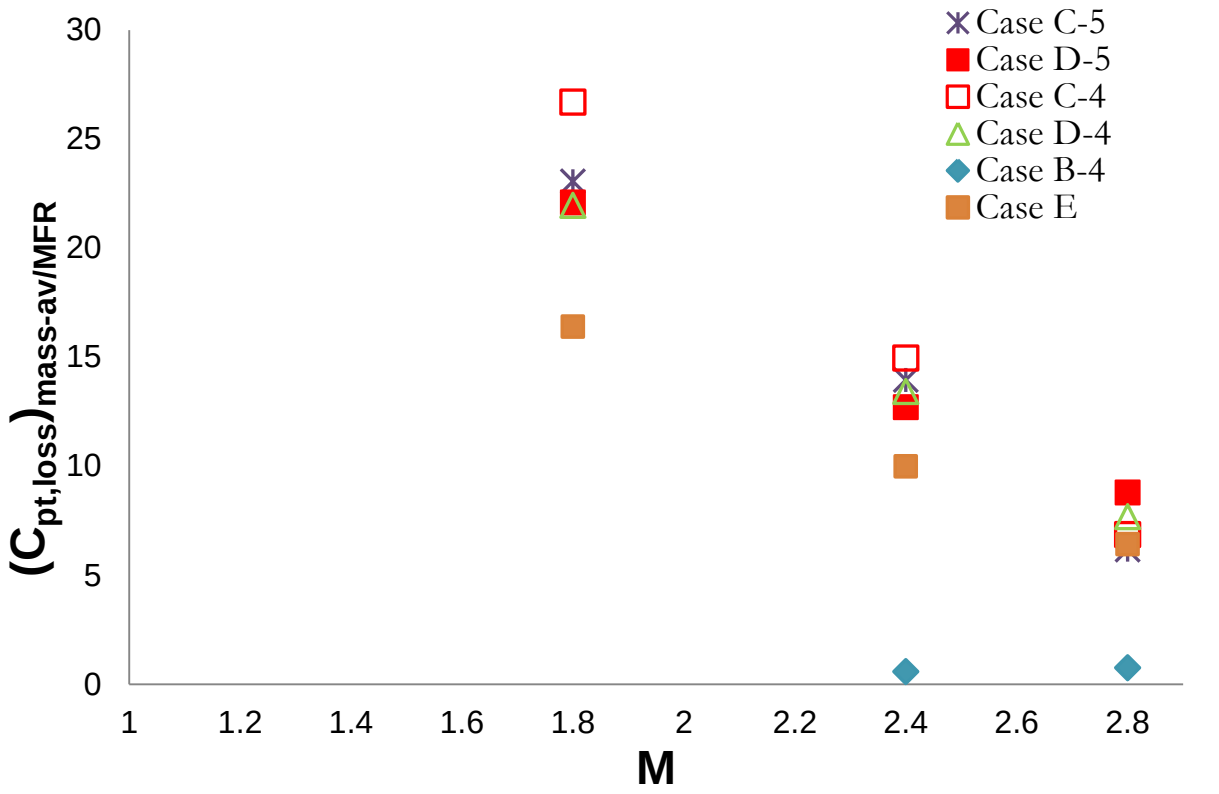

Figure 73: Overall mass-averaged, $(C_{pt,\,loss})_{mass\text{-}av}$/MFR vs. M (Case-E, B-4, C-5, D-5 C-4, D-4), at exit plane.

As predicted by [21], at any M, the losses were smaller for fan-shaped holes than for cylindrical holes except at M=2.4. An interesting phenomenon occurred for both Cases C-4 and D-4. The trend of the two cases swapped with D-4 having higher losses than for C-4 because the momentum jets from the passage cooling holes interfered with the secondary flows. The LE cylindrical diffused hole configuration, with and without fillet, always had the lowest total pressure losses through the vane passage compared with the cylindrical hole configuration. ***Figure 72*** indicates that Fillet 1 was more effective in reducing the $(C_{pt,\,loss})_{mass\text{-}av}$ for both Cases C-4 and D-4 than for the baseline Case C-5 at 1.8≤M≤2.4 and the baseline Case D-5 at 2.4≤M≤2.8.

The values of $(C_{pt,\,loss})_{mass\text{-}av}$ were divided by the coolant mass fraction ratio (MFR), shown in ***Figure 73***. In agreement with the conclusion of Friedrichs et al. [14], the ratio of the overall mass average and mass fraction decreased as the film-cooling blowing ratio increased for all cases and configurations considered.

At M=1.2, Case C-4 showed the highest pressure loss per mass fraction, thus performing better than the other configurations. At a high bleed flow rate, all cases were very close to each other. The decrease of the blowing ratio, shown in ***Figure 73***, was noteworthy only at M<1.8. At M>1.8, the pressure loss coefficient decreased, but the higher amount of coolant flow balanced the benefit of pressure loss reduction.

The values of MFR for the analysed configurations at the different blowing ratios are listed in ***Table 22***.

Table 22: *MFR($\dot{m}_c/\dot{m}_p$) of coolant to passage flow.*

M	2.8	2.4	1.8	1.2
Case E	0.1207	0.0950	0.0620	0.0036
Case C-5	0.1472	0.0683	0.0432	0.0069
Case D-5	0.1028	0.0720	0.0444	0.0062
Case C-4	0.1384	0.0630	0.0371	0.0033
Case D-4	0.1189	0.0720	0.0441	0.0036
Case B-4	1.1594	1.5637	0.0900	0.0157

At any M, since MFR was the highest, Case B-4 had the lowest mass-averaged pressure loss coefficients per unit mass fraction. As M increased, both the coolant mass flux and workload on the turbine compressor to deliver the required coolant would increase.

6.2.4.3. Non dimensional axial velocity, u(LE+passage cooling)*

The distributions of non-dimensional axial velocity u* in the endwall region are plotted in ***Figure 74*** to ***Figure 83*** in the third and exit planes for the film-cooling arrangement, shown in ***Table 21***. The ratio of the local velocity component, u normal to the third plane (parallel to X_G) to the reference velocity, U, defined the quantity u*. The distributions of non-dimensional axial velocity in the endwall region indicated a high coolant concentration near the endwall. In the middle of the vane passage, shown in ***Figure 74*** to ***Figure 79***, the coolant trajectories from the holes were towards the vane SS and provided almost complete coolant coverage on the endwall at low blowing.

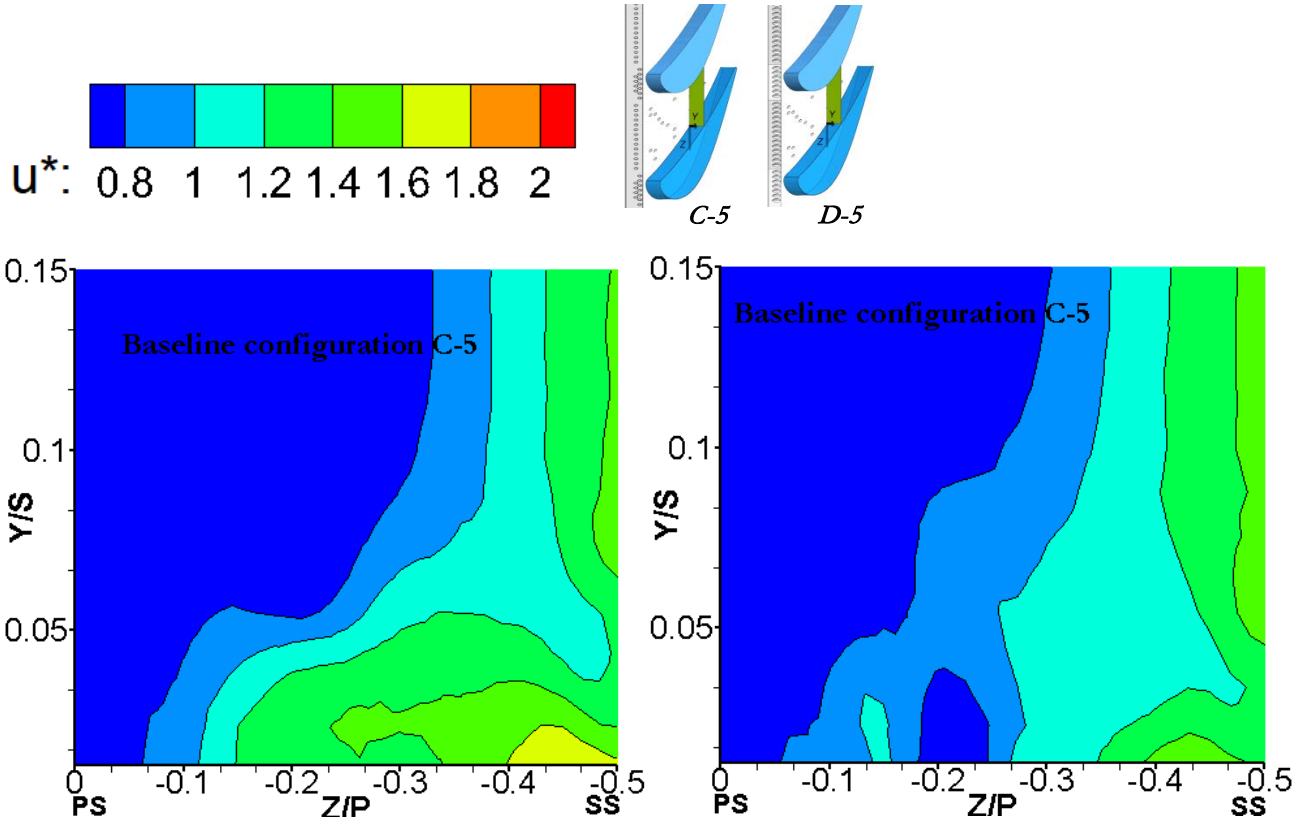

Figure 74: *Distributions of non-dimensional axial velocity u* contours data in third plane Case C-5, a) M = 1.2, b) M=2.4.*

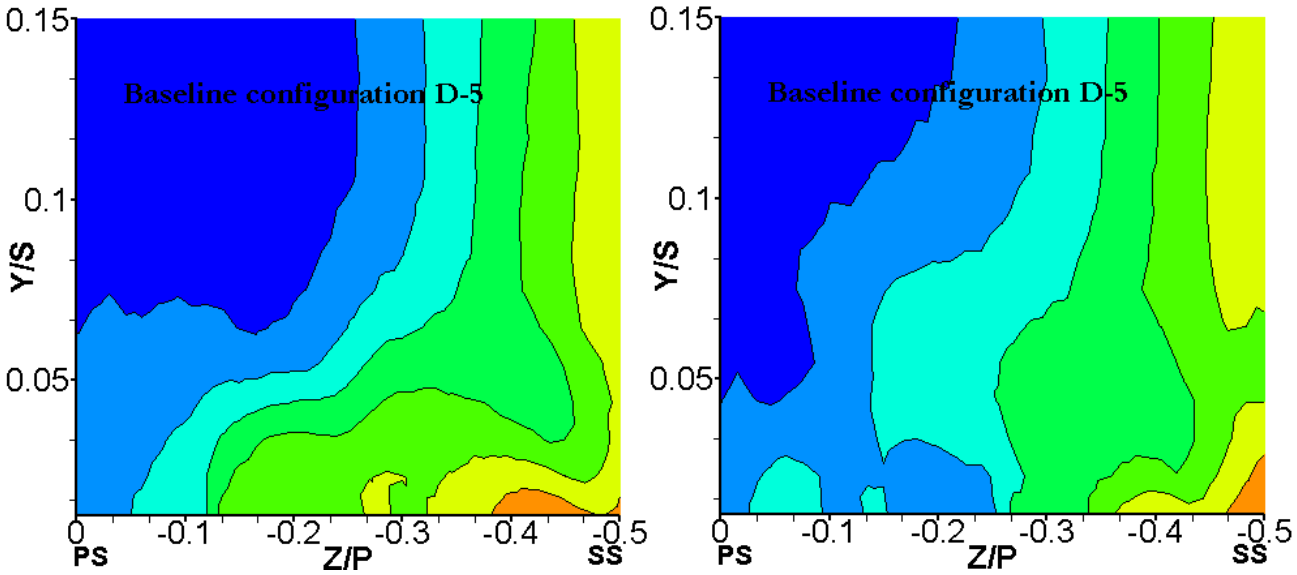

Figure 75: *Distributions of non-dimensional axial velocity u* contours data in third plane Case D-5, a) M = 1.2, b) M=2.4*

Observing the $C_{pt,\,loss}$ and u* data, in the third plane, for a given M, the momentum flux and mass flux were different for the following film-cooling configurations, resulting in different local mass flux u* distributions in the endwall region and complex flow interaction.

For the baselines case, shown in ***Figure 74*** and ***Figure 75***, the lift-off of the coolant flow, above the endwall, as it came out of the hole, interacted with the boundary layer such that the region with u*<1 increased from the middle pitch line to the pressure-side as the blowing ratio increased. For the same LE hole cooling configurations, shown in ***Figure 78*** and ***Figure 79***, the presence of Fillet 1 reduced those regions at negative u*. In Case D-4, the film-cooling somewhat seemed to energise the suction-side leg vortex.

In the absence of coolant ejection from the LE film-cooling plate, Case E (***Figure 76***), the rise of blowing ratio intensified the mass flow only locally on the endwall in proximity to the two passage cooling holes at Z/P≈-0.28 and Z/P≈-0.42.

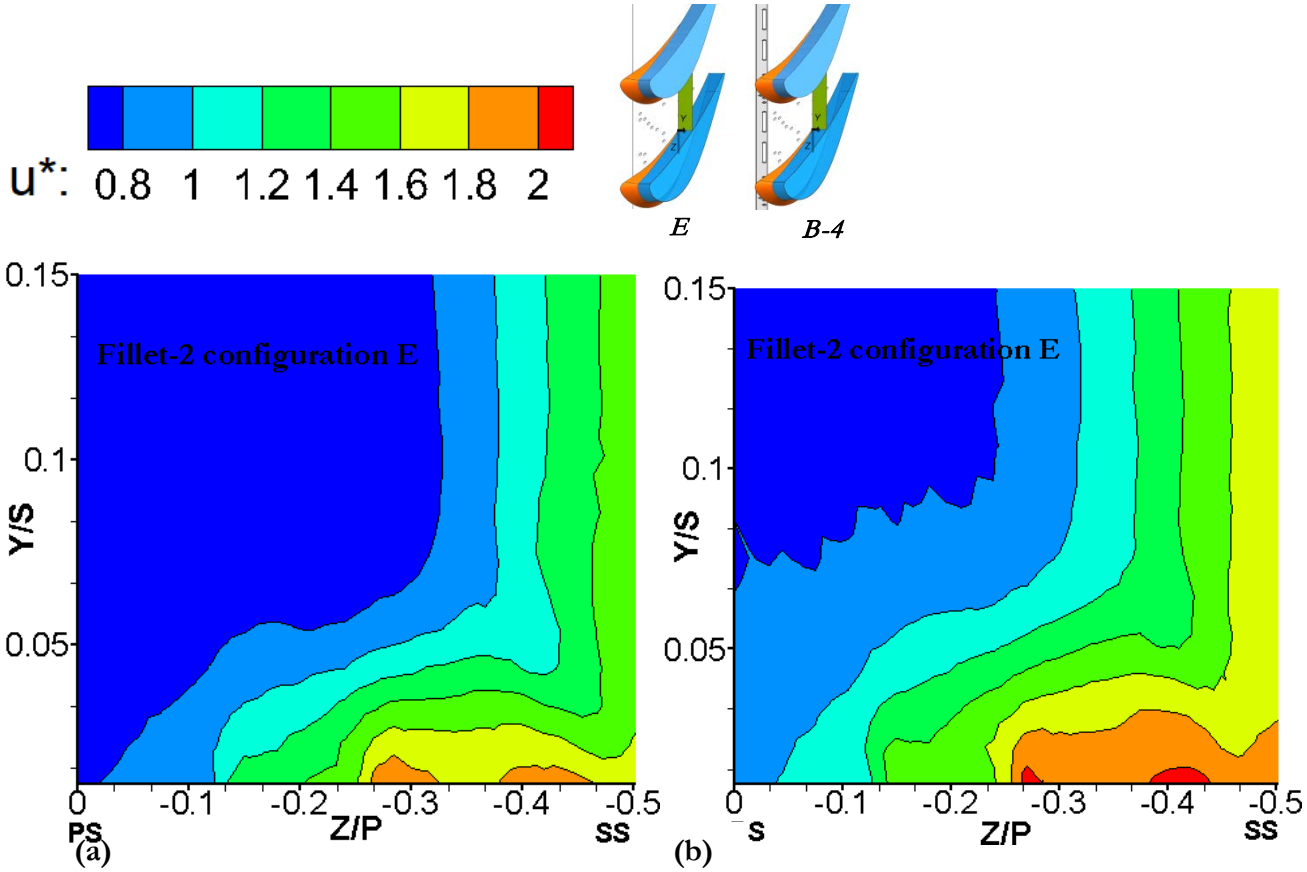

Figure 76: *Distributions of non-dimensional axial velocity u* contours data in third plane Case E, a) M = 1.2, b) M=2.4.*

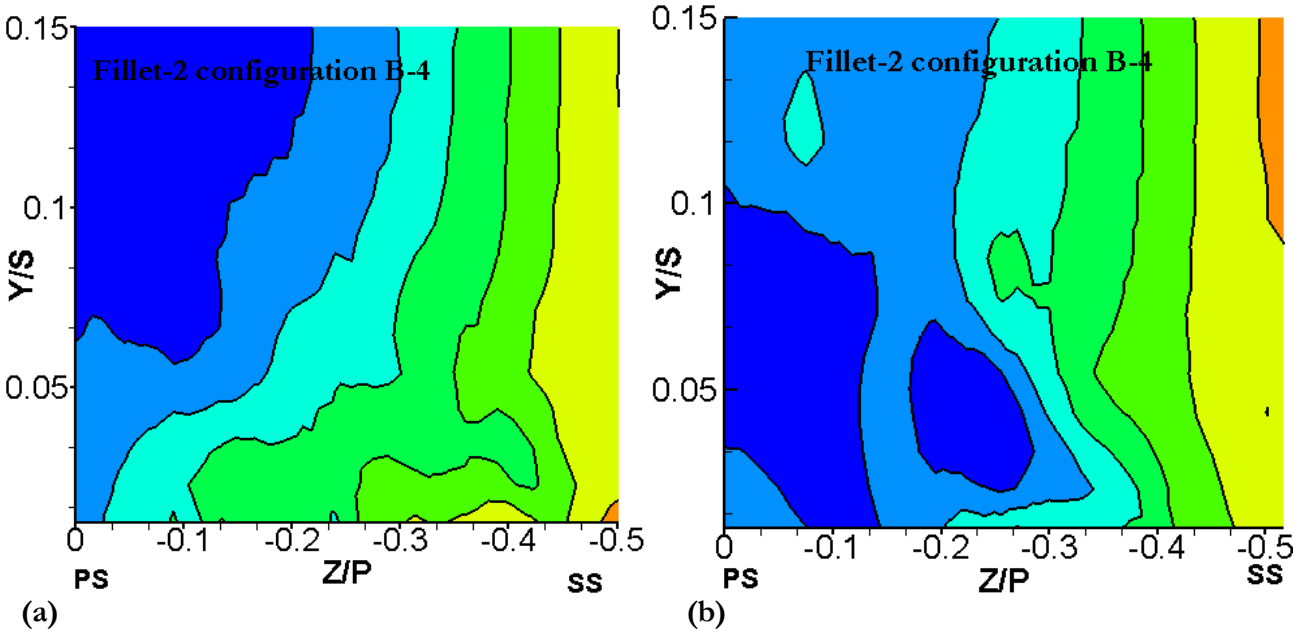

Figure 77: *Distributions of non-dimensional axial velocity u* contours data in third plane Case B-4, a) M = 1.2, b) M=2.4.*

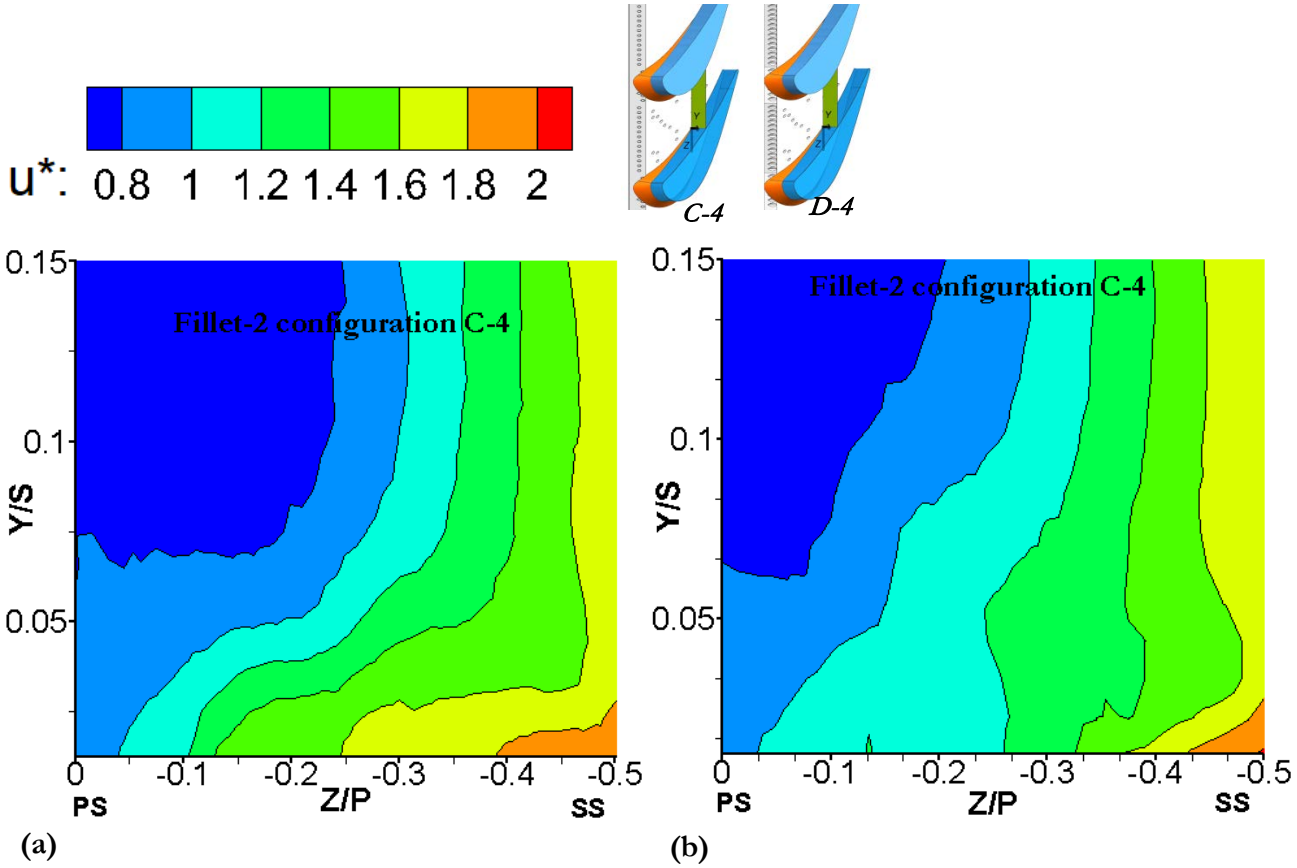

Figure 78: Distributions of non-dimensional axial velocity u contours data in third plane Case C-4, a) M = 1.2, b) M=2.4.*

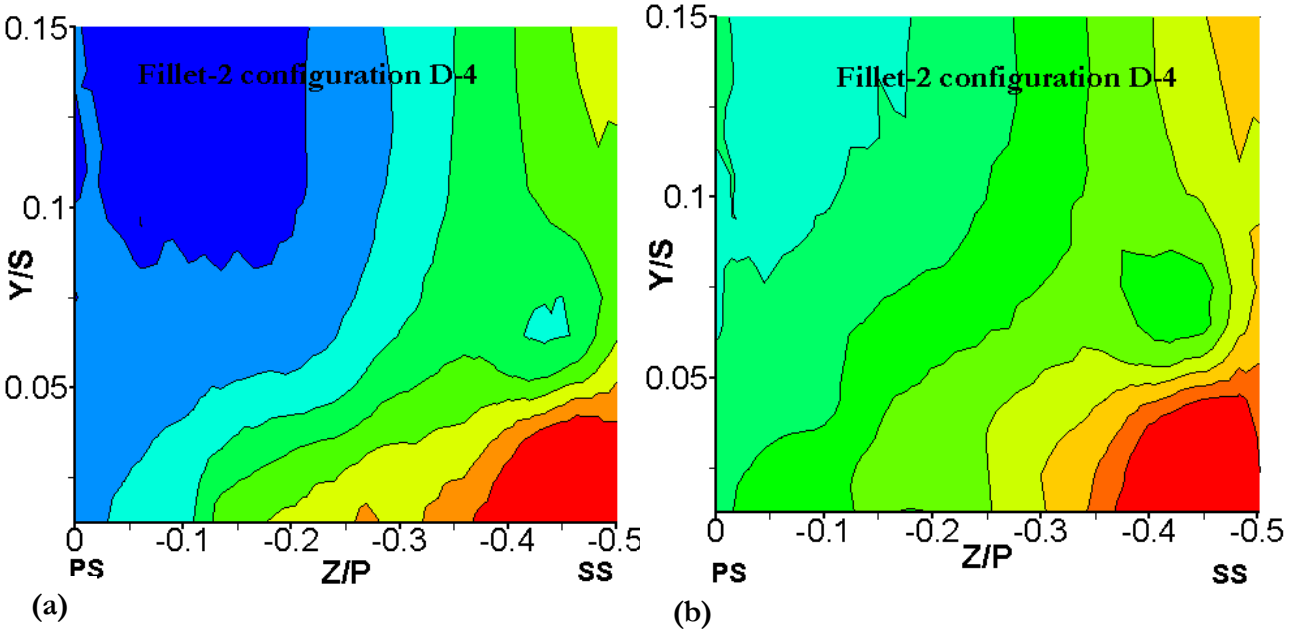

Figure 79: Distributions of non-dimensional axial velocity u contours data in third plane Case D-4, a) M = 1.2, b) M=2.4.*

The high values of non-dimensional axial velocity near the endwall at -0.5<Z/P<-0.38 for Case D-4, shown in ***Figure 79***, occurred because of the strong interaction of the suction-side leg vortex with the boundary layer. Observing the $C_{pt,\,loss}$ and u* data, the higher mass flux and momentum flux of the coolant, as M increased, seemed to add momentum to the boundary layer increasing u* and decreasing $C_{pt,\,loss}$ near the endwall, as shown in ***Figure 65***, at the same location. However, in Case C-4, shown in ***Figure 78***, the higher mass and momentum flux of the coolant seemed to cause mixing losses in the boundary layer at -0.4<Z/P<-0.5 decreasing u* and increasing $C_{pt,\,loss}$ near the endwall, shown in ***Figure 64***.

The high mass flux was severe in the other configurations, mostly in Case B-4. ***Figure 77*** indicates that as M changed, the interaction between the coolant jets from the two LE slots at high jet momentum and the boundary layer changed. The boundary layers were more energised; the streamlines turning towards the suction side were reduced together with the secondary loss, as displayed in ***Figure 51*** and ***Figure 63*** respectively.

In the exit plane, shown in ***Figure 80***, Case E displayed higher mass flux u* at the region -0.9<Z/P<-0.2 at any M, whereas in the other cases, shown in ***Figure 81*** to ***Figure 83***, with an increase in the blowing ratio, such regions reduced or even did not appear, Case B-4 and D-4. The coolant from the passage cooling holes seemed to have an influence only at the endwall region by accelerating the flow and interacting with the boundary layer. The trend was supported by the high ΔYaw distributions adjacent to the endwall for Case E, shown in ***Figure 56***, and low ΔYaw distributions adjacent to the endwall, shown in ***Figure 57*** to ***Figure 59***, for the other cases.

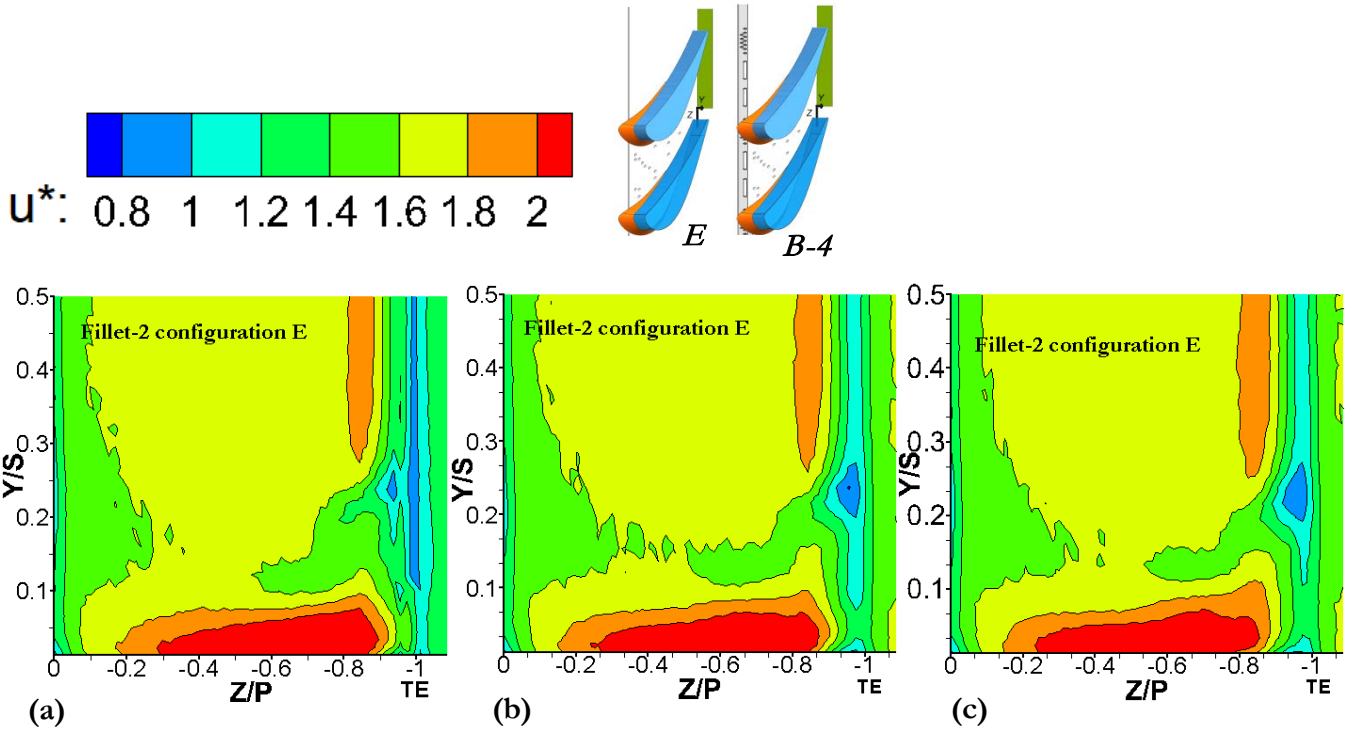

Figure 80: *Distributions of non-dimensional axial velocity u* contour Case E, exit plane, a)M= 1.2, b) M=2.4 and c)M=2.8.*

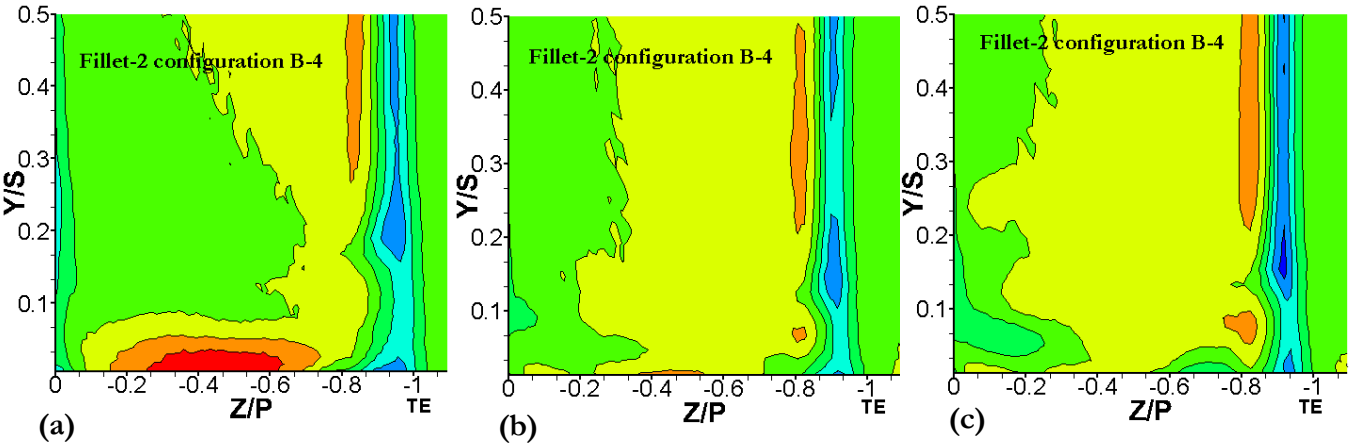

Figure 81: *Distributions of non-dimensional axial velocity u* contour Case B-4, exit plane, a)M= 1.2, b) M=2.4 and c)M=2.8.*

As already noticed in $C_{pt,\ loss}$ distributions, for all cooling cases except for Case E, shown in ***Figure 66*** to ***Figure 71***, the passage vortex core at TE, specified by u*<1 at Z/P≈-0.98 and Y/S≈0.2, translated towards the

endwall at Y/S≈0.1 at a higher blowing ratio. At the exit plane, Case B-4 presented the lowest non-dimensional axial velocity in the proximity of the endwall region indicating a slower flow.

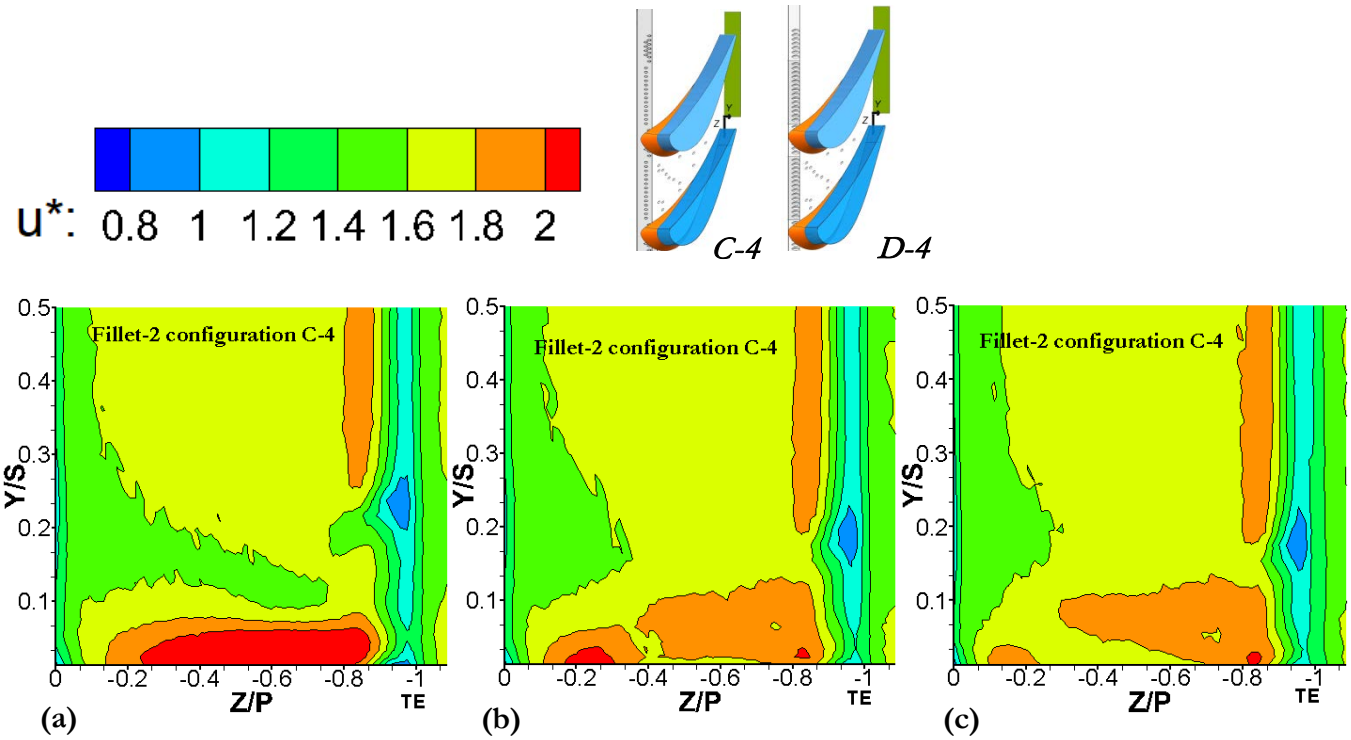

Figure 82: Distributions of non-dimensional axial velocity u contour Case C-4, exit plane, a)M= 1.2, b) M=2.4 and c)M=2.8.*

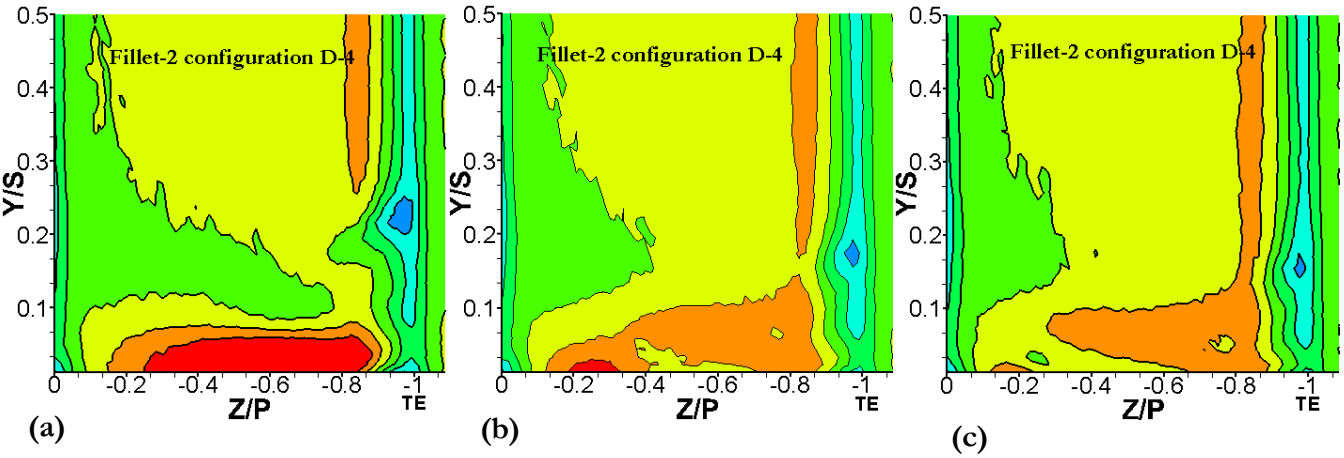

Figure 83: Distributions of non-dimensional axial velocity u contour Case D-4, exit plane, a)M= 1.2, b) M=2.4 and c)M=2.8.*

6.2.4.4. Non-dimensional axial vorticity, ω_x(LE+passage cooling)*

The axial vorticity, defined in the Eq. (22), describes the rotation location and size of the passage vortex core structures, with a positive magnitude indicating clockwise rotation.

$$\omega_x^* = \frac{\omega_x C}{U_{ref}} \tag{22}$$

The negative vorticity regions adjacent to the endwall and the spread along the pitch line were a sign of lateral movement towards the pressure-side, opposite to the cross-flow direction of the passage. The effects of the high momentum of the film-cooling flow were further evaluated by comparing the contour plots of normalised axial vorticity distributions in the third plane between the film-cooling cases, shown in ***Table 21*** and ***Figure 84*** to ***Figure 89***. In all the figures, the axial vorticity contours illustrate two adjacent regions of vorticity of opposite sign on the endwall towards the suction-side. The positive axial vorticity identified the passage vortex.

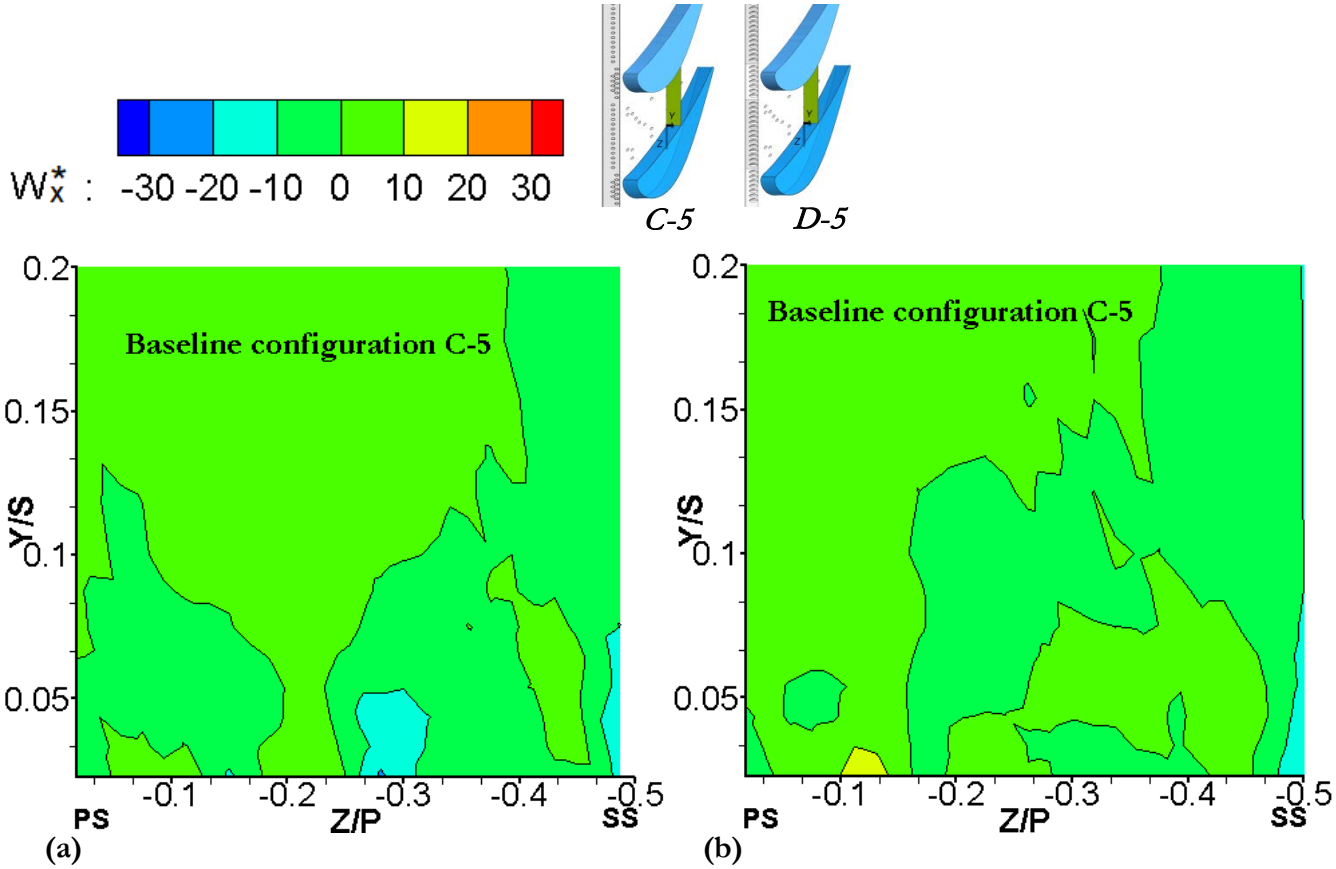

***Figure 84**: Non-dimensional x-vorticity, ω_x*, contours perpendicular to third plane: Case C-5, a) M= 1.2, b) M=2.4.*

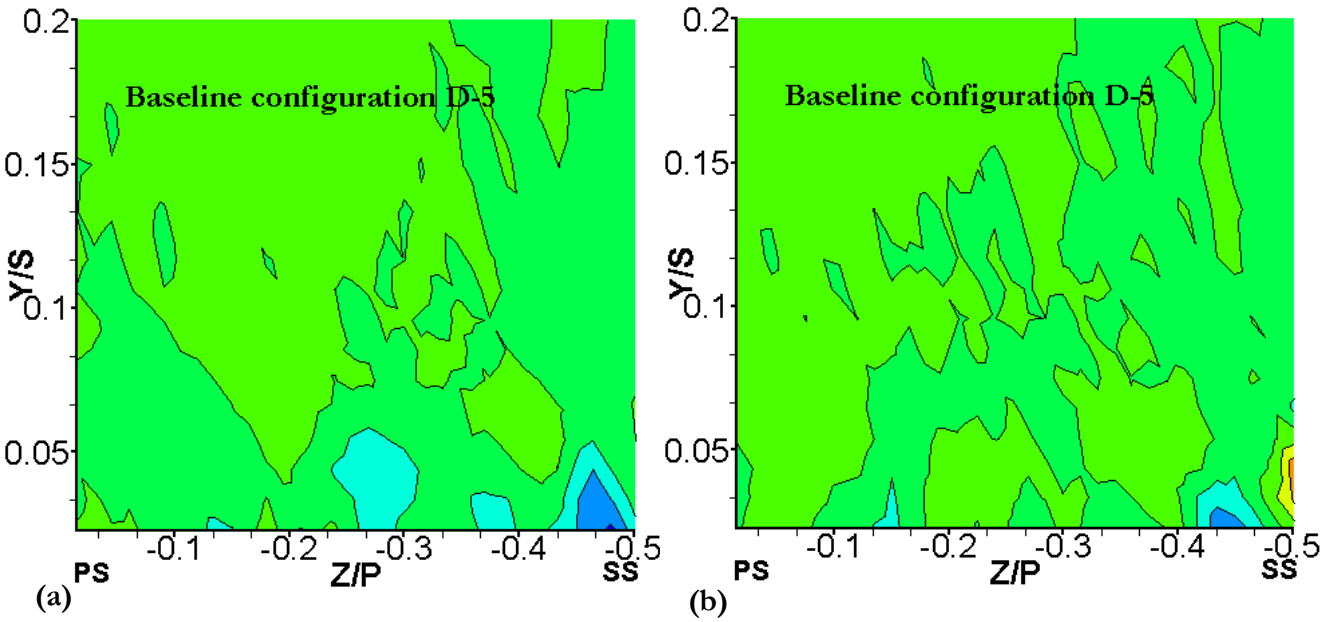

***Figure 85**: Non-dimensional x-vorticity, ω_x*, contours perpendicular to third plane: Case D-5, a) M= 1.2, b) M=2.4.*

The region of negative axial vorticity, about Z/P ≈ -0.45, represented the suction-side leg vortex that was close to the suction-side. The negative vorticity, away from the SS at Z/P > -0.4 at Y/S<0.05 along the pitch line, was caused by the coolant flows and the wall vortex that interacted with the coolant flow.

The unfilleted cases, shown in ***Figure 84*** and ***Figure 85***, indicated the interaction between the coolant jets and the passage flow mainly on the SS. The absence of the fillet seemed to reduce the axial vorticity on the endwall.

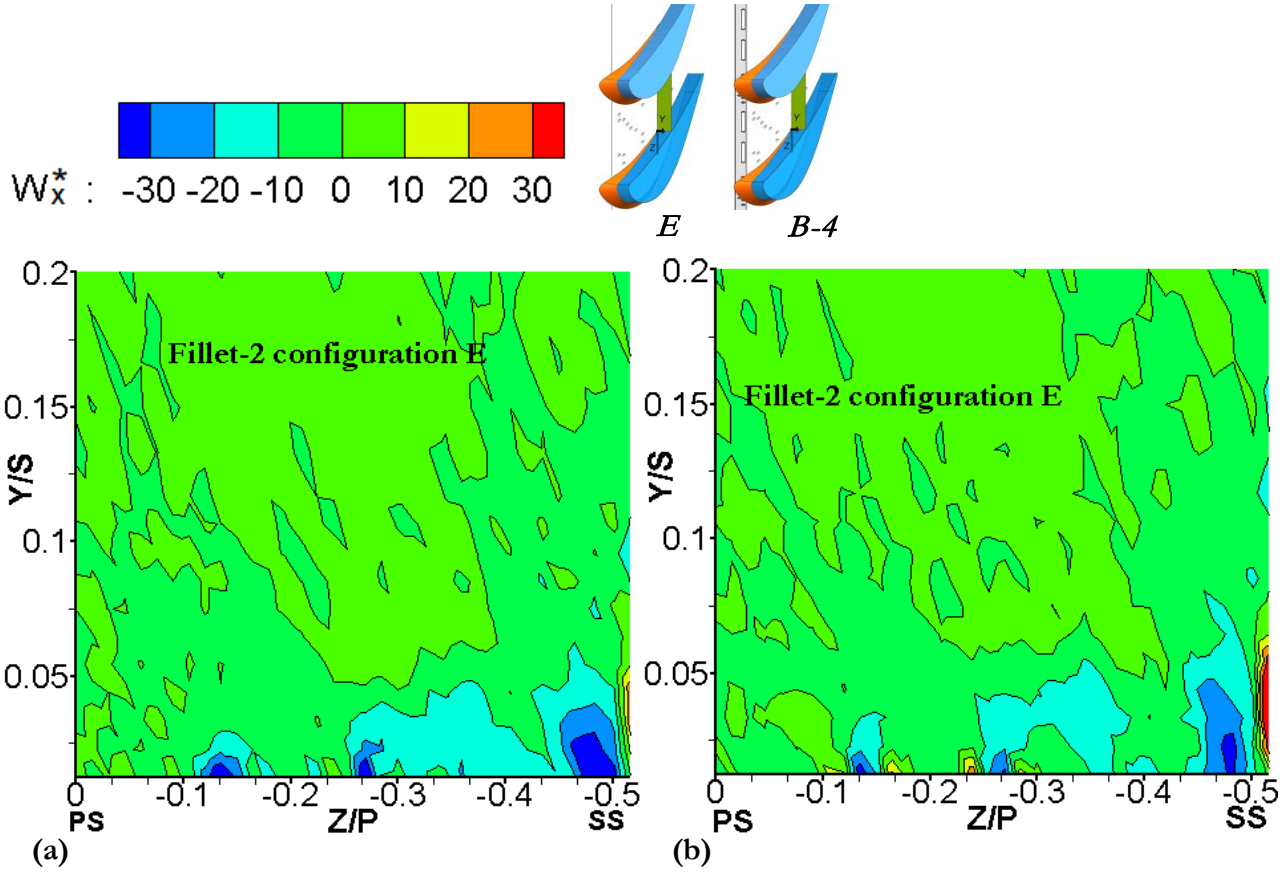

Figure 86: *Non-dimensional x-vorticity, ω_x^*, contours perpendicular to third plane: Case E, a) M= 1.2, b) M=2.4.*

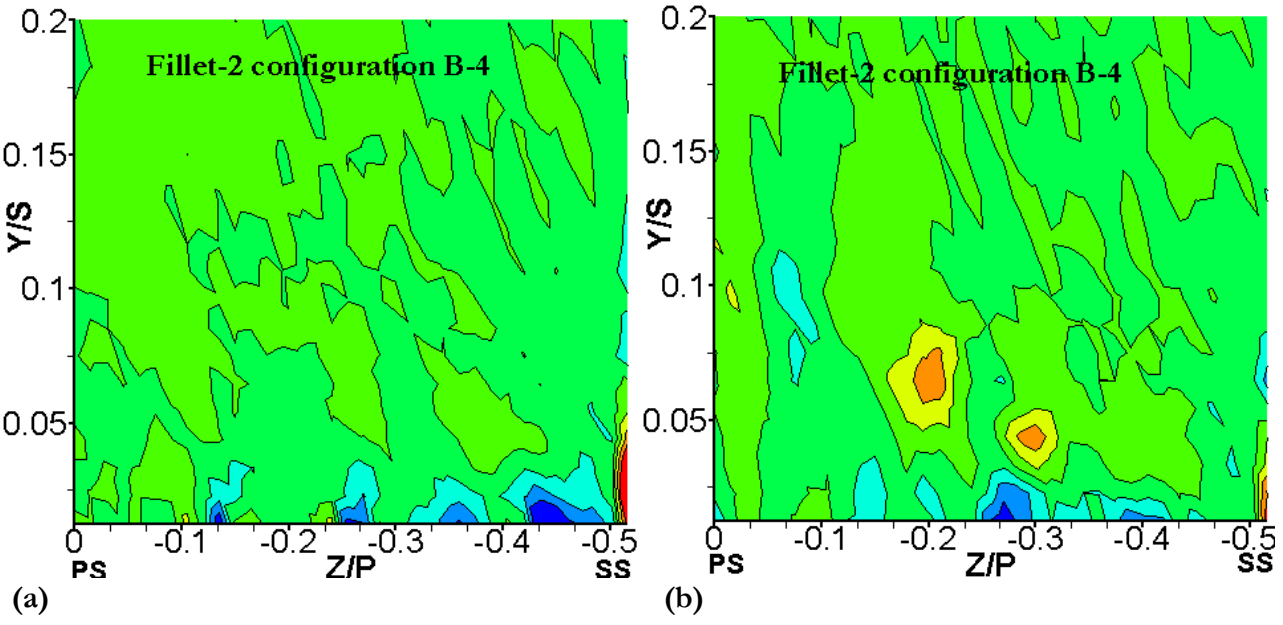

Figure 87: *Non-dimensional x-vorticity, ω_x^*, contours perpendicular to third plane: Case B-4, a) M= 1.2, b) M=2.4.*

For the filleted case with the same LE film-cooling plates, as the coolant supply increased, shown in ***Figure 88*** and ***Figure 89***, the high values of positive and negative ω_x*, at Y/S>0.04 on the suction-side, became more visible as the coolant travelled further into the passage before being lifted by the secondary flows, mostly for Case D-4, shown in ***Figure 89***. In this case, the coolant ejected from the LE diffused holes managed to drift the secondary flow vortices on the suction-side away from the endwall towards the mid-span. The effects of the coolant injection became more prominent, shown in ***Figure 88***, at M=2.4. In comparison with the other cases, the film jets ejected from the LE slots, B-4 configuration, reduced the non-dimensional axial vorticity on SS making smaller the passage vortex, but it caused additional ω_x* >10 at -0.35<Z/P>-0.25 and 0.03<Y/S<0.09.

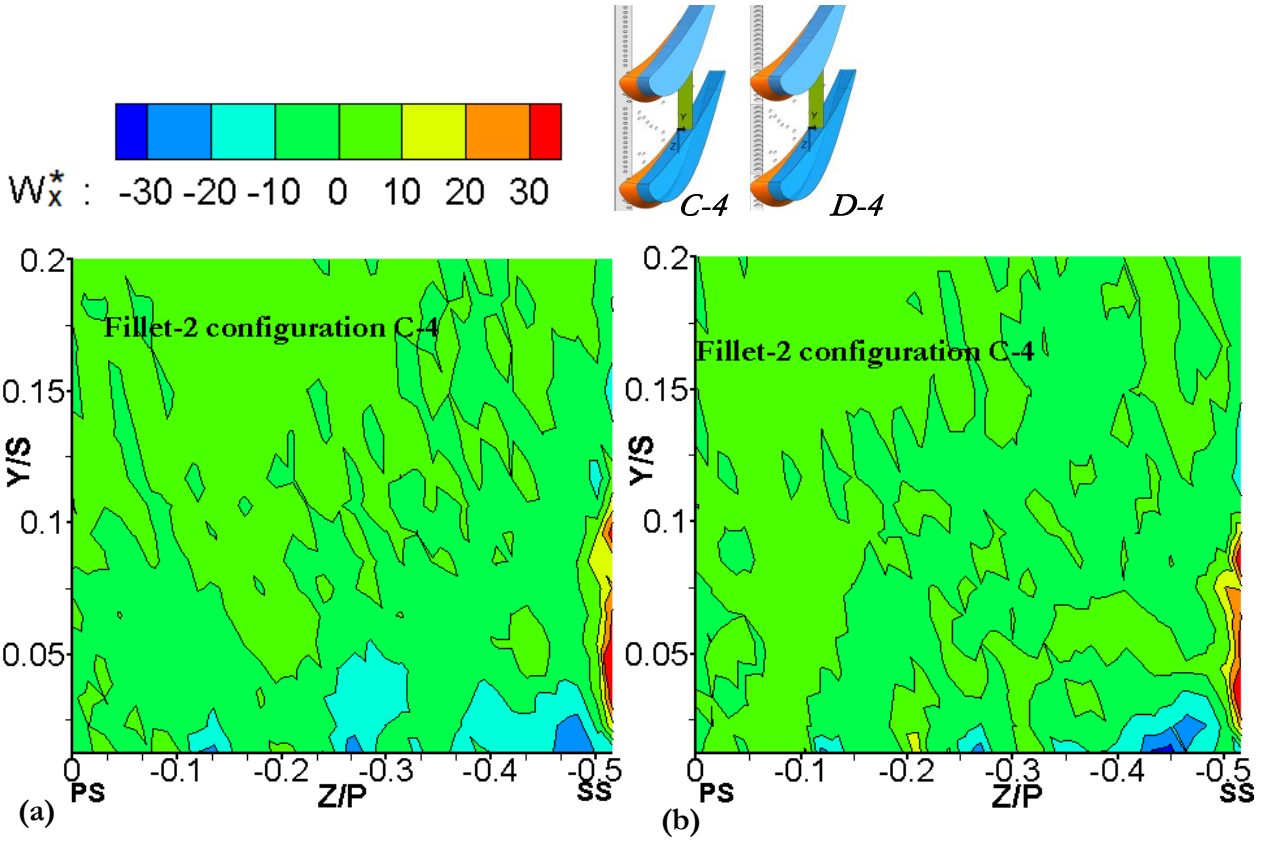

Figure 88: *Non-dimensional x-vorticity, ω_x*, contours perpendicular to third plane: Case C-4, a) M= 1.2, b) M=2.4.*

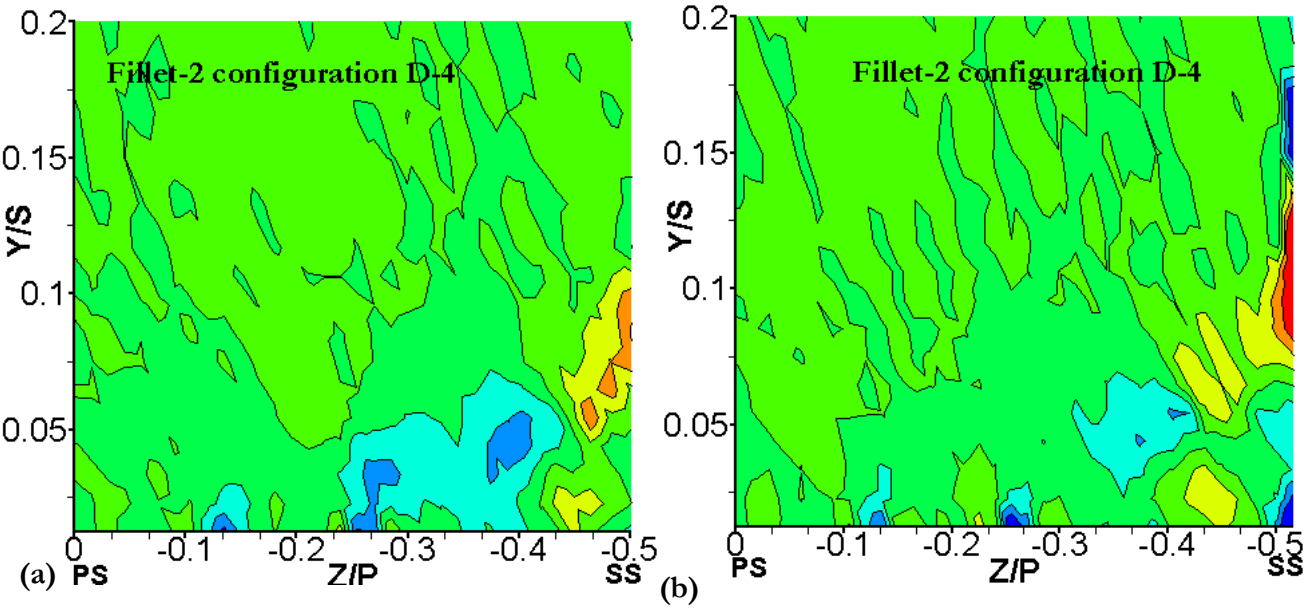

Figure 89: *Non-dimensional x-vorticity, ω_x*, contours perpendicular to third plane: Case D-4, a) M= 1.2, b) M=2.4.*

6.2.4.5. Thermal performance(LE+passage cooling)

The measured local air temperatures, $T_{loc,}$ near the endwall in the first three planes were normalised and indicated as θ in Equation (15). In accordance with the definition in the equation, the lower the $T_{loc,}$ the lower is the θ due to the film-cooling streams above the endwall. The non-dimensional temperature fields obtained in the third plane, as shown in ***Figure 90*** to ***Figure 97***, covered all the cooling cases with and without the fillet, provided in ***Table 21***.

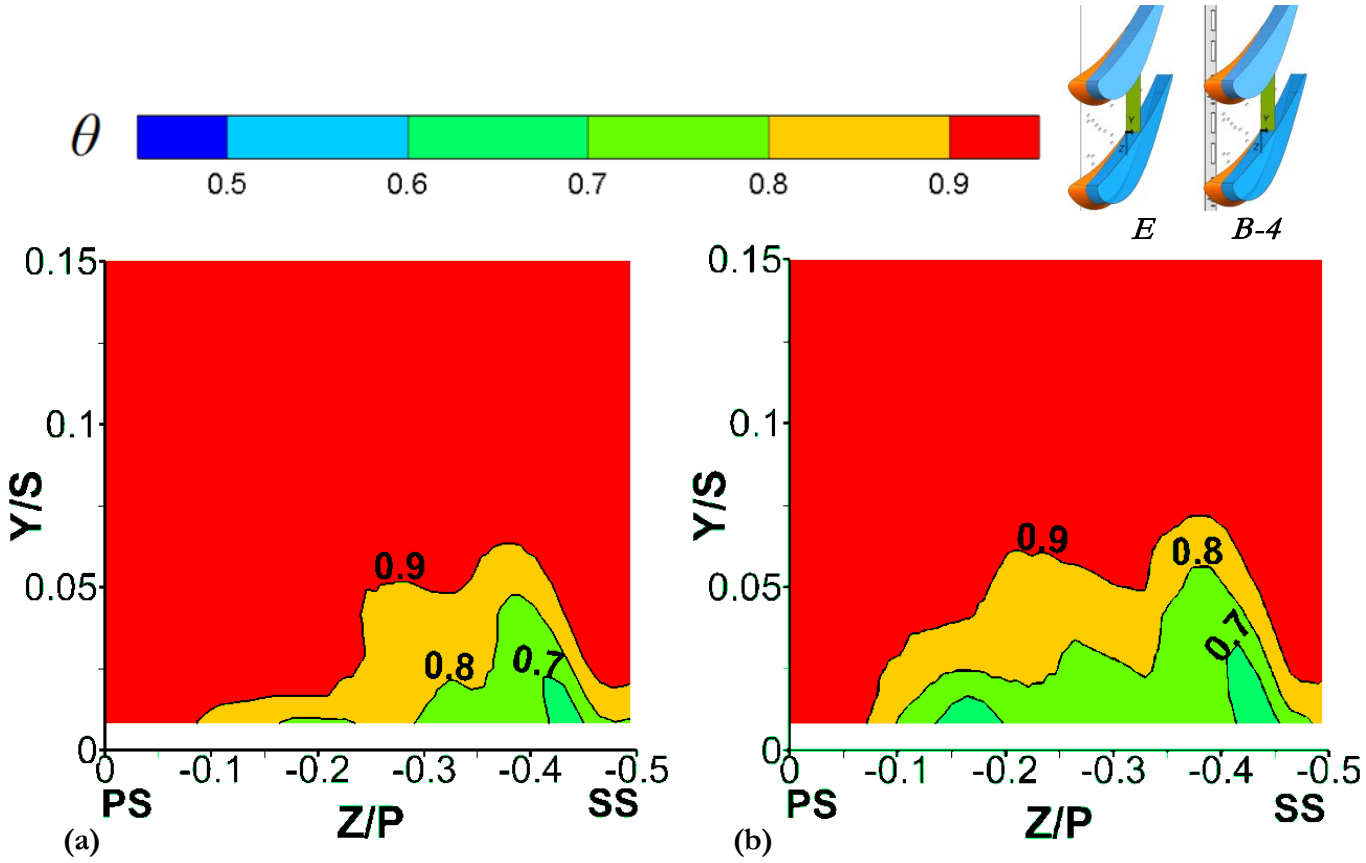

Figure 90: *Contours of non-dimensional temperature (θ) distribution in third plane: Case E, a) M=1.2, b) M=2.4.*

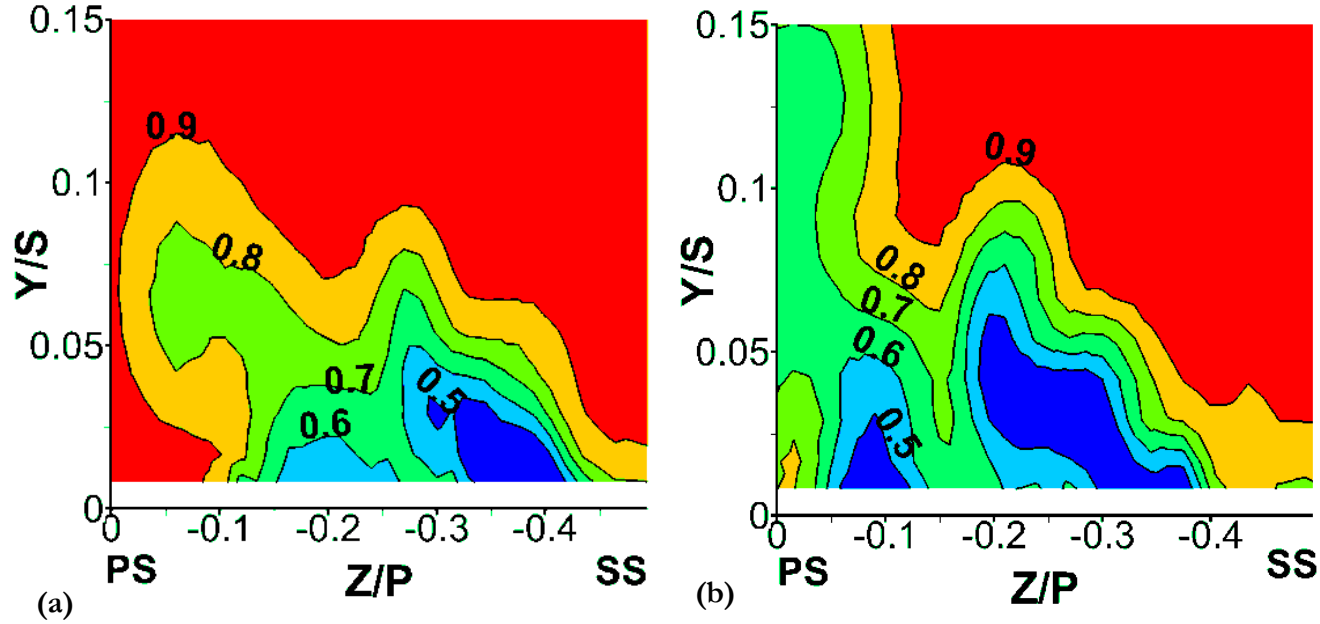

Figure 91: *Contours of non-dimensional temperature (θ) distribution in third plane: Case B-4, a) M=1.2, b) M=2.4.*

The flow mixing and lifting of the coolant by the endwall flows were responsible for low values of θ high above the endwall. The low θ distributions above the endwall were an indication of the coolant mixing with the boundary layer and the losses of film-cooling coverage on the endwall. Therefore, the desirable coolant flow trajectories were represented by the distributions of low values of θ adjacent to the endwall. The pitch-wise spread of low values of *θ* along the endwall meant uniform distributions of the coolant flows along the endwall. Furthermore, greater values of *θ,* higher above the endwall, showed the lift-off of the coolant, which did not contribute to the film-cooling of the endwall.

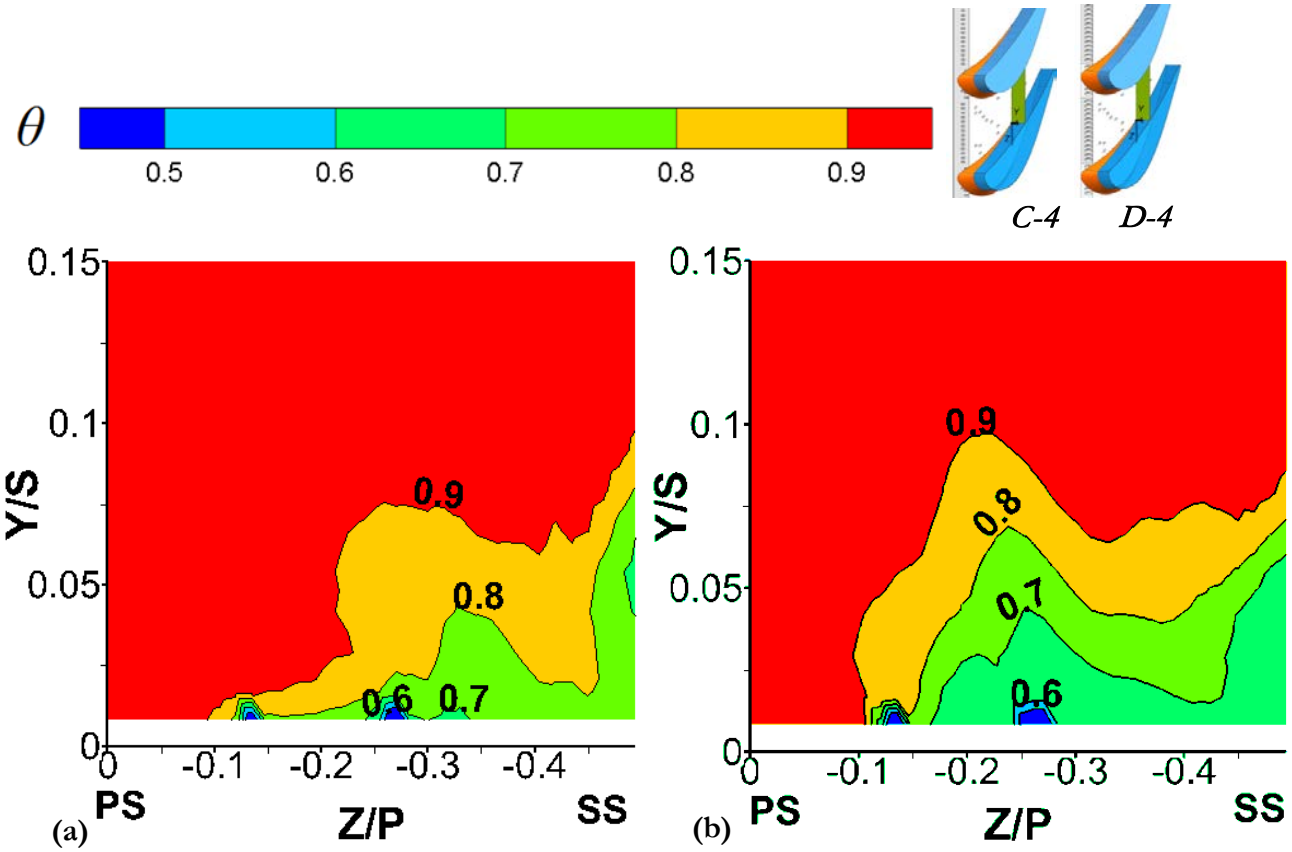

Figure 92: Contours of non-dimensional temperature (θ) distribution in third plane: Case C-4), a) M=1.2, b) M=2.4.

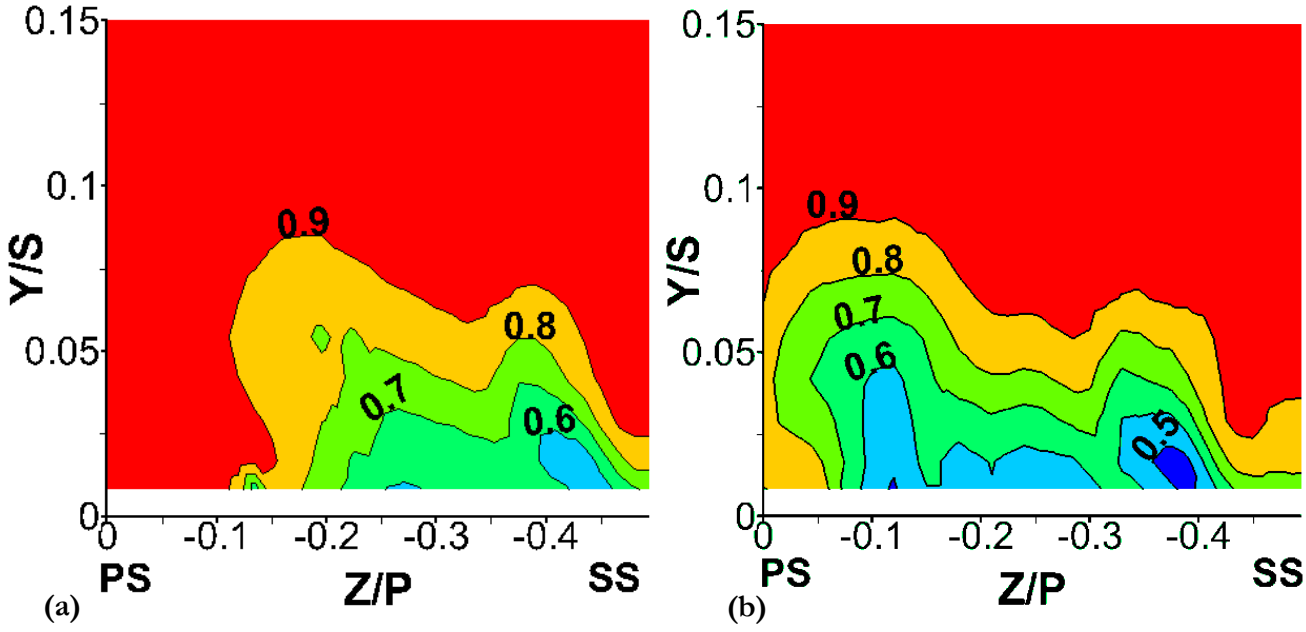

Figure 93: Contours of non-dimensional temperature (θ) distribution in third plane: Case D-4, a) M=1.2, b) M=2.4.

The worst thermal endwall protection was obtained by Case E. The high non-dimensional temperature distribution indicated a lack of upstream injection from the LE film-cooling holes, as shown in ***Figure 90***. The endwall was cooled from the SS to Z/P≈ -0.1. Even at higher blowing ratios, the coolant jets from the passage holes did not manage to reach the PS. Compared with Case B-4, ***Figure 91*** illustrates the capacity of the coolant jets from the two slots and cylindrical holes to cool the same pitch-wise endwall region but at lower θ distributions, smaller than 0.8. Furthermore, at M=2.4, the film-cooling managed to reach the pressure-side at the price of wasting coolant along the span (greater values of θ above the endwall).

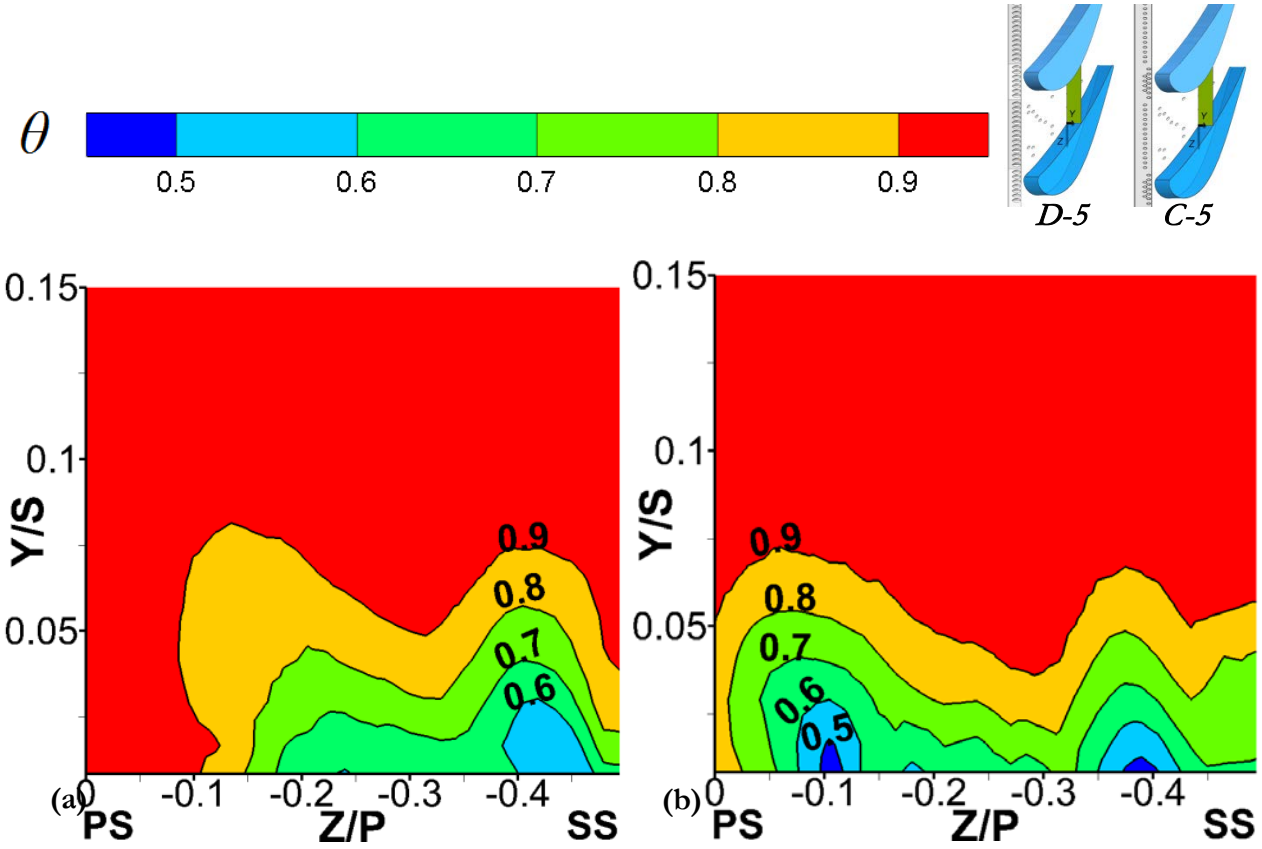

Figure 94: *Contours of non-dimensional temperature (θ) distribution in third plane: Case D-5, a) M=1.4, b) M=2.4.*

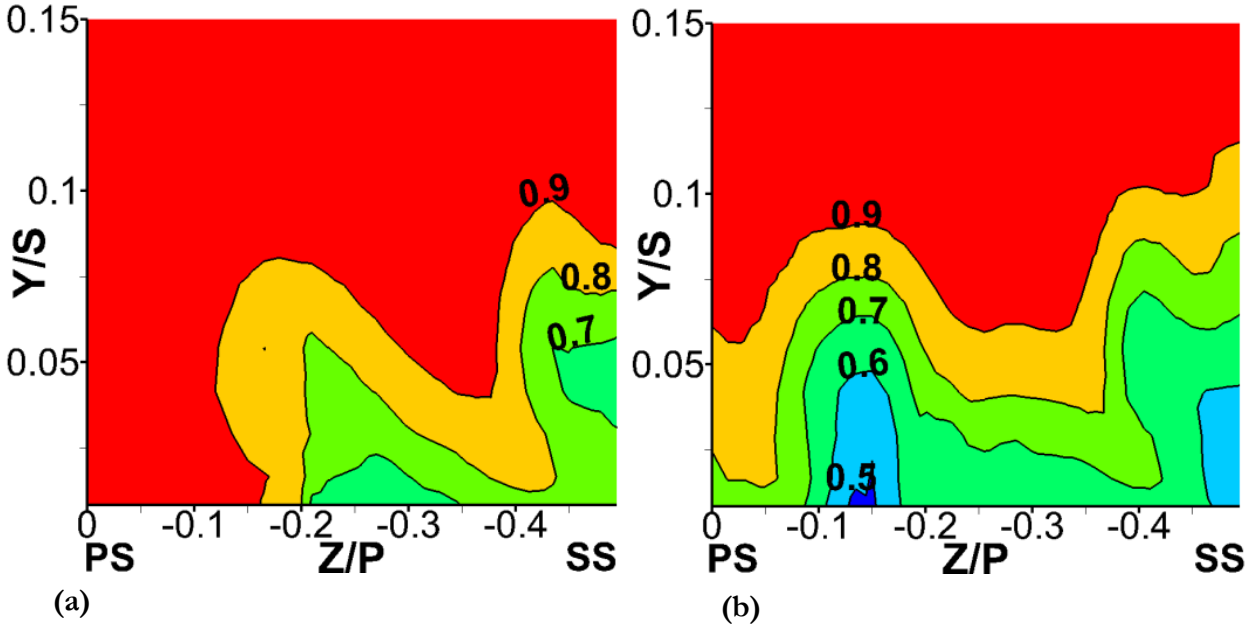

Figure 95: *Contours of non-dimensional temperature (θ) distribution in third plane: Case C-5, a) M=1.4, b) M=2.4.*

Following the results shown in ***Figure 87***, the coolant from upstream slots provided an effective coverage downstream of the boundary layer separation region by slipping under the separation region and reaching the PS. The θ distributions, shown in ***Figure 93*** and ***Figure 94***, for the diffused cylindrical holes case always showed a better cooling performance (lower θ values on the endwall) than for the cylindrical holes shown in ***Figure 92*** and ***Figure 95***.

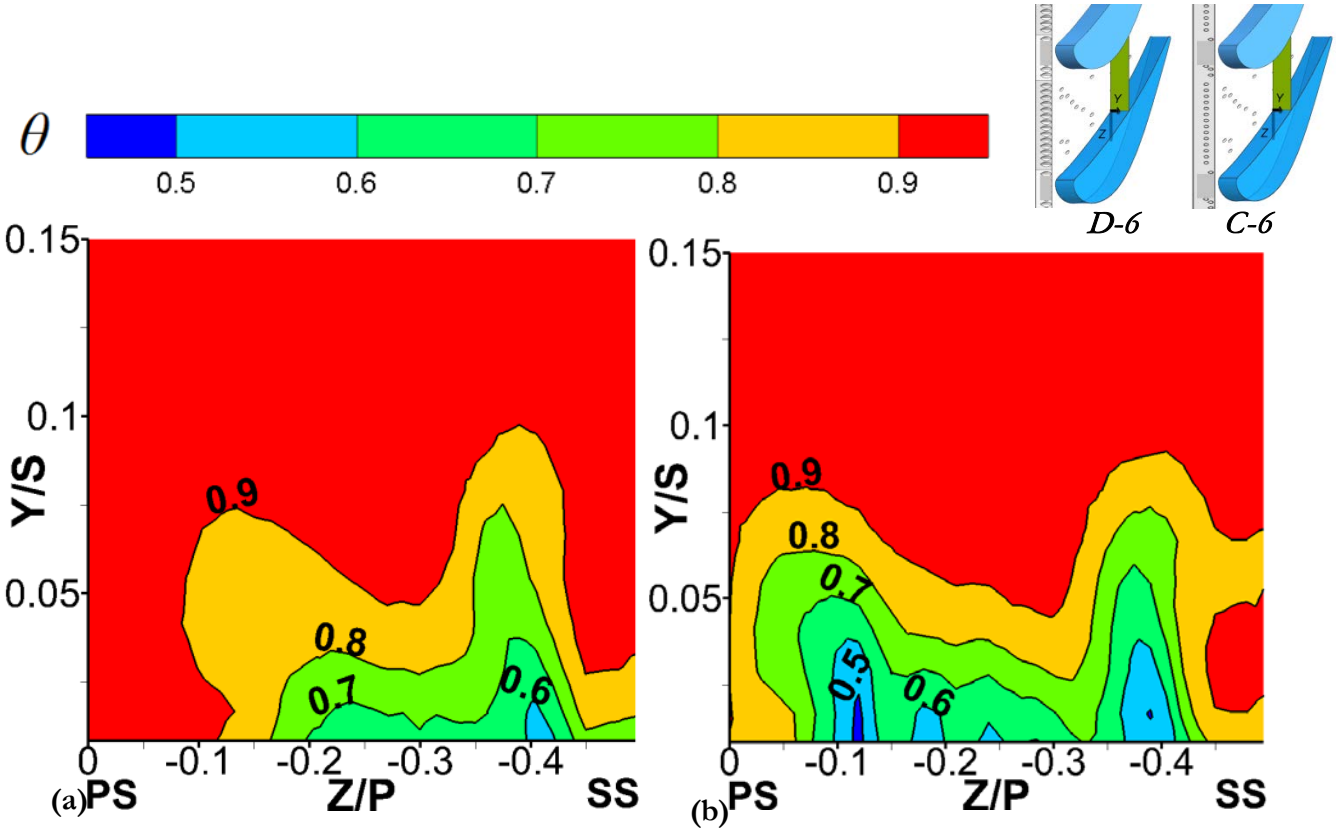

Figure 96: *Contours of non-dimensional temperature (θ) distribution in third plane: Case D-6 a) M=1.4, b) M=2.4.*

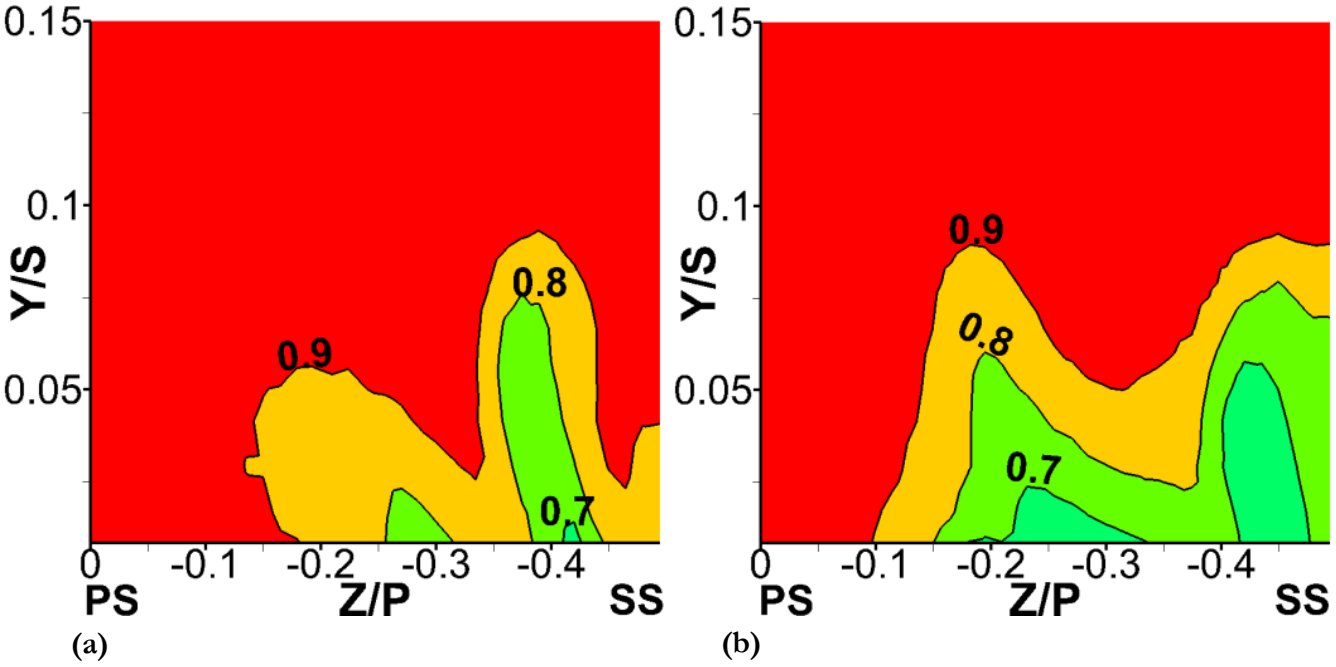

Figure 97: *Contours of non-dimensional temperature (θ) distribution in third plane: Case C-6 a) M=1.4, b) M=2.4.*

When the filleted case, Case D-4, shown in ***Figure 93***, was compared with the baseline Case D-5, shown in ***Figure 94***, the θ distributions had similar coolant trajectories and the effects of fillet seemed to cool the endwall slightly better. However, from the comparisons of the LE cylindrical hole cases, shown in ***Figure 92*** and ***Figure 95***, it appeared that Fillet 2 had a negative effect on the coolant jets. At the corresponding M, Case C-4 worsened the pitch-wise θ distributions on the endwall and at higher M, the coolant did not reach the endwall on the PS as Case C-5 did. The thermal analysis reinforced the observation that the LE diffused cylindrical holes provided a better coolant distribution than the cylindrical holes did.

The comparison between Case C-6 and Case C-5 indicated that the addition of film-cooling holes at the LE vane had a thermal benefit as expected, shown in ***Figure 95*** and ***Figure 97***. The closing few LE discrete holes, eight in Case D-6 and fourteen Case C-6, shown in ***Figure 96*** and ***Figure 97***, reduced the coolant on the endwall region when compared with the same configurations shown in ***Figure 94*** and ***Figure 95***. Furthermore, it seemed that the cylindrical holes were more affected by the absence of the LE coolant than the diffused cylindrical holes were.

Relating the θ data, shown in ***Figure 90*** to ***Figure 97***, to the ω_x* data, shown in ***Figure 84*** to ***Figure 89***, in the third plane, it can be concluded that the coolant coverage on the endwall at given M was essentially dependent on a combination of mass flux, momentum and trajectory of the coolant as well as the lifting of the coolant. The low values of the θ data revealed the presence of coolant streams, but did not properly illustrate the amount of coolant mass flux and momentum. At higher blowing ratio and coolant flux, the thermal performance confirmed the same tendency of passage vortex reduction, providing better distributions at the corresponding cooling configuration. In Case B-4, the LE slots achieved successful coolant coverage with low aerodynamic losses, followed by the LE diffused cylindrical hole configuration.

7. Conclusions

The nozzle guide vane endwall, at high pressure, is an exposed surface directly downstream of the combustor exhaust and needs a uniform cooling-film distribution. Due to complex secondary flow structures on the endwall surfaces, the uniform cooling-film distribution becomes a challenge. The objective of the study was to explore the potential of LE film-cooling configurations in a filleted vane that could overcome such challenges at low secondary flow losses. The film-cooling flow performance of several LE film-cooling configurations, with and without the passage cooling holes were experimentally measured in a linear vane cascade housed in an atmospheric (low pressure) wind tunnel. Furthermore, the experimental results of the aerothermal performance of film-cooling were presented to show the effects of the leading-edge modification on the endwall cooling scheme combined with different film-cooling injections. A fillet, blended on the NGV blade surface, was employed on the endwall to evaluate the effects on the interaction between film-cooling and the endwall. The inlet Reynolds number to the cascade was 2.0E+05 based on the actual chord length of the vane profile, the coolant-to-mainstream temperature ratio was 0.94, while the density ratio for all the tests was approximately 1.05. The tests were conducted for several blowing ratios of film-cooling flow, from M=1.2 to M=2.8. The results of the measurements of total pressure loss distributions, flow yaw angle deviation, non-dimensional axial velocity and non-dimensional vorticity were presented in the last two planes, while the flow temperature field was plotted for the first three planes. The current investigation aimed to compare the performance across all the cooling configurations.

7.1 Leading-edge contours

A first analysis involved the effects of two fillet profiles, Fillet 1 (fillet towards the TE) and Fillet 2 (fillet stopping at the throat section) at the junction of the vane and the endwall. The fillets were evaluated against the baseline case without film-cooling. The LE contouring study revealed that both LE fillets had a positive influence on the flow and secondary losses in the endwall region of the investigated NGV. Near the endwall, in the third plane, compared with the baseline case, Fillet 1 presented the smallest flow angle deviation on the endwall of the flow indicating that the streamlines were more oriented towards the axial direction. The total pressure loss magnitude was reduced remarkably on the endwall for the filleted case, particularly for Fillet 1, although a wider zone of loss on the suction-side for Fillet 1 was present.

In the exit plane, Fillet 2 shifted the location of the passage vortex core towards the endwall and reduced the boundary layer mixing losses. Fillet 1 presented a more uniform exit yaw angle, diminished the passage vortex core but enhanced the boundary layer mixing losses. In the absence of film-cooling, the filleted cases reduced the static pressure differences between the pressure-side and the suction-side of the passage in the endwall region. As a result, the passage vortex system at the exit plane was minimised. Both fillets induced favourable endwall boundary layer conditions along the passage by minimising the pitch-wise velocity components and therefore the aerodynamic losses.

7.2 Effect of LE cooling configurations

The interactions between the film-cooling flow and endwall secondary flows were analysed next. Experiments were conducted to investigate the impact of a range of coolant-to-mainstream flux ratios on the flow field for three different LE film-cooling configurations. For baseline cases, LE film-cooling plates

containing slots, cylindrical holes, and cylindrical holes with diffused exits were employed in the pitch-wise rows in the endwall slightly upstream of the cascade inlet. They were located in front of the vane's leading edge and they extended over 82 mm in length in the pitch-wise direction.

One LE slot plate had two slots of 5 mm width, separated by two shorter slots in the centre of the passage, equally spaced 25 mm apart and orientated at 30° relative to the endwall surface. In the second plate, the two middle slots were substituted by cylindrical holes spaced apart by 12 mm, placed in two rows in the leading-edge region.

Two types of LE film-cooling holes were assessed: cylindrical holes and diffused cylindrical holes. The cylindrical hole of diameter 5 mm was machined in the endwall at 30° relative to the endwall surface. The diffused hole was designed by diffusing the cylindrical hole in the forward direction smoothly to create a net diffusion angle of 13° at the hole exit. The compound angle of both types of holes was zero at the endwall surface.

Among the baseline cases, better endwall cooling coverage was achieved with the slotted film-cooling configurations at the cost of a stronger passage vortex. From the distributions of total pressure loss coefficients, the results revealed that the slot configurations provided the best performance because the coolant did not penetrate sufficiently into the boundary layer in the discrete hole configurations. Comparing diffused cooling holes to cooling cylindrical holes, the distributions of the loss coefficients indicated that the total pressure losses were lower for the diffused holes than for the cylindrical holes. Just downstream of the exit, the passage vortex was slightly weaker and smaller for the diffused hole film-cooling. However, the boundary layer mixing losses due to the film-cooling flow and passage vortex structure were more enhanced. The effects of coolant blowing were evaluated on the overall mass-averaged total pressure losses experienced at the passage exit. The peak of losses occurred at a blowing ratio of 1.4. The largest reduction in total pressure losses for all film-cooling configurations was mostly at the highest blowing ratio. The baseline of LE diffused holes performed best at any blowing ratio value, as predicted by previous studies.

The mass flux distributions just above the endwall provided the estimates of film-cooling jet momentum. In the LE four-slot configuration, Case A, in the pitch-wise plane located halfway inside the passage, the coolant concentration near the endwall on suction-side was highlighted by the non-dimensional axial velocity distributions. The high momentum of the film-cooling jets interacted with the suction-side leg vortex where the highest pressure losses were located. When the leading-edge slot was replaced by the cylindrical holes, Case B-2B, the value of the normal velocity component became very small near the endwall because of the strong pitchwise flow from the pressure-side to the suction-side. The differences in u* were minimal between the cylindrical and diffused holes and occurred much closer to the endwall. As the blowing ratio increased, the momentum of the film-cooling jets intensified and the coolant accumulated towards the suction-side.

The thermal field was presented in a non-dimensional form. The distributions of the non-dimensional temperature in the first plane revealed that the region around the leading edge was completely cooled only by the film slot coolant jets from the four LE slots, in Case A. The higher momentum of the coolant jet from the LE slots transported more coolant near the pressure-side and penetrated deeper into the boundary layer. At any M and in all four planes, the endwall was always cooled for this configuration, but unfortunately, most of the coolant was wasted along the span. Regarding the LE hole configurations, the coolant jets, adjacent to the endwall, from the diffused cylindrical holes, were responsible for better coolant distributions along the endwall than for the cylindrical holes. The pitch-wise concentrations and distributions of the coolant adjacent

to the endwall for the diffused holes caused distributions of low values of non-dimensional temperature adjacent to the endwall but the PS remained an uncooled region at low M.

For the cylindrical holes, the coolant streams migrated more towards midstream, were more concentrated towards the passage suction-side, and were lifted higher above the endwall by the suction-side leg vortex in contrast to the diffused holes.

The observed distributions of non-dimensional temperature on the endwall for the diffused hole were certainly beneficial for better cooling film coverage of the endwall. Therefore, the secondary flow was affected by the coolant flow and by its injection geometry.

7.3 Benefit of endwall coolant ejection within the passage

The third set of investigations required a combination of the LE cooling plates previously evaluated and the endwall film-cooling holes. Experimental results were presented to show the effects of the leading-edge modification on the endwall cooling scheme with different configurations of LE film-cooling plates combined with endwall ejection cooling.

It was observed that for the baseline cases in the third plane, the introduction of the film-cooling from the passage holes decreased the pressure gradients and the flow yaw deviation angles near the endwall. Therefore, the cross-flow from the pressure-side to suction-side weakened. Consequently, the intensity of the passage vortex core and the boundary layer mixing losses were reduced at the exit plane. Remarkably, the total pressure loss coefficients were smaller when extra coolant from the passage was present, especially at the higher coolant flow rate. As already observed in the former discussion of the temperature field, the diffused cylindrical holes still behaved slightly better than the cylindrical holes in terms of the spread of coolant coverage, less turning of streamlines, and fewer pressure losses along the passage.

The main observations from the study indicated that at any M, the most effective cooling of the endwall was achieved by the filleted and the LE slots, Case B-4, implying effective cooling coverage of the endwall. Furthermore, this filleted case resulted in the lowest total pressure losses only at high M. Unfortunately, since the amount of coolant mass flux was very large at the higher blowing ratios, the requirement of high coolant flow rate overshadowed the benefit of reducing the overall total pressure losses by putting more load on the compressor.

Moreover, in the other cooling configurations, the effective cooling of the endwall depended on the blowing ratio of the film-cooling. In the third plane, it was observed that the introduction of Fillet 2 combined with the LE cylindrical hole configuration decreased the local total pressure loss coefficients on the endwall for $M<2.4$ Consequently, the total pressure loss coefficients and the turnings of the streamlines towards the suction-side were smaller than for the filleted case, especially at the higher coolant flow rate. However, the diffused cylindrical holes caused a larger turning of the boundary layer streamlines towards the suction-side inside the passage. Consequently, the passage vortex was lifted from the endwall by the coolant and became stronger when the filleted vane was employed with the diffused cylindrical holes.

The thermal analysis showed that both baseline cases, LE diffused cylindrical holes and cylindrical holes with the endwall coolant ejection, reached uniform coolant distributions along the pitch line at $M=2.4$ in contrast to the filleted vane with LE cylindrical holes. Contrary to the LE cylindrical holes, Fillet 1 negatively

influenced the secondary flow interaction with the coolant because the coolant injection enhanced the suction-side leg vortex structure. The diffused cylindrical holes reached the pressure-side at M=2.4, but the baseline case was prone to cool the endwall surface more.. In the exit plane, the largest reduction in total pressure losses for all film-cooling configurations occurred at the highest blowing ratio. The peak of losses occurred at a blowing ratio of 1.8, as predicted by previous studies; while for the baseline, it occurred at high blowing ratios.

The analysis indicated that when the passage cooling holes were added to the LE cooling configuration, among all configurations, except for Case B-4, filleted Case D-4 performed best at the lower blowing ratio values. Moreover, at the higher blowing ratio, the LE diffused cylindrical holes case, Case D-6 without the fillet, provided the best performance because the jet penetrated deep into the boundary layer and the total pressure losses, due to the mixing of coolant streams with the boundary layer, decreased.

The study emphasised the active role of coolant flow in the development of the aerodynamic field in the near-wall region. The influences of the film-cooling hole geometry and the LE fillet changed with the blowing ratio. Therefore, the mechanism of cooling prediction is very complex and depends on upstream conditions hence affecting the cooling performance.

7.4 Suggestion for further research

The coolant jet core of the laidback fan-shaped holes being much closer to the surface showed a better lateral spread on the surface than for the cylindrical hole. Compared with the cylindrical hole film-cooling, the present arrangement of diffused cylindrical hole film-cooling had the potential to provide better aerodynamic performance and higher film-cooling effectiveness at the expense of overall gas-turbine efficiency. Consequently, the outcome of the current research would be improved by optimising the fillet in conjunction with LE diffused cylindrical holes and passage holes in terms of reducing the passage vortex structure and endwall region flow deviations. Such an analysis should be done with the aid of a proper CFD investigation.

REFERENCES

[1] S. Bunker, D. E. Metzger and S. Wittig, "Local heat transfer in turbine disk-cavities part I: rotor and stator cooling with hub injection of coolant," Gas Turbine and Aeroengine Congress and Exposition, 1990.

[2] S. Friedrichs, H. Hodson and W. Dawes, "Distribution of film-cooling effectiveness on a turbine endwall measured using the ammonia and diazo technique," ASME Journal of Turbomachinery, vol. 118(4), pp. 613-621, 1996.

[3] G. Wilfert and L. Fottner, "The aerodynamic mixing effect of discrete cooling jets with the mainstream flow on a highly loaded turbine blade," Proceedings of ASME Turbo Expo, pp. 94-GT-235, 1994.

[4] W. Haas, W. Rodi and B. Schönung, "The influence of density difference between hot and coolant gas on film-cooling by a row of holes: predictions and experiments," ASME Journal of Turbomachinery, vol. 114(4), pp. 747–755, 1992.

[5] C. H. Sieverding, "Recent progress in the understanding of basic aspects of secondary flows in turbine blade passage," ASME Journal of Engineering for Gas Turbines and Power, vol.107, pp.248–257, 1985.

[6] L. S. Langston, M. L. Nice and R. M. Hooper,, "Three dimensional flow within a turbine cascade passage," Journal of Engineering for Power, vol. 99, pp. 21-28 , 1977.

[7] L. S. Langston, "Secondary Flows in Axial Turbines-A Review," Heat Transfer in Gas Turbine Systems, Annals of the New York Academy of Sciences, vol. 934, pp. 11-26, 2001.

[8] H. P. Wang, S. J. Olson, R. J. Goldstein and E. R. Eckert, "Flow visualization in a linear turbine cascade of high performance turbine blades," ASME Journal of Turbomachinery, vol. 119(1), pp. 1-8, 1995.

[9] Y. J. Moon and S. R. Koh, "Counter-rotating streamwise vortex formation in the turbine cascade with endwall fence," Computer & Fluids, vol. 30, pp. 473-490, 2001.

[10] M. F. Blair, "An Experimental study of heat transfer and film-cooling on large-scale turbine endwalls," ASME Journal of Heat Transfer, vol. 96(4), pp. 524-529, 1974.

[11] L. J. Goldman and K. L. McLallin, "Effect of endwall cooling on secondary flows in turbine stator vanes," AGARD-CPP-214, 1977.

[12] C. McLean, C. Camci and B. Glezer, "Mainstream aerodynamic effects due to wheelspace coolant injection in a high pressure turbine stage: Part I-aerodynamic measurements in the rotational frame," ASME Journal of Turbomachinery, vol. 123(4), pp. 687-696, 2001.

[13] P. Schuepbach, R. S. Abhari, M. G. Rose, T. Germain, I. Raab and J. Gier, "Effects of suction and injection purge-flow on the secondary flow structures of high-work turbine," ASME Journal of Turbomachinery, vol. 132(2) , 2008.

[14] S. Friedrichs, H. P. Hodson and W. N. Dawes, "Aerodynamic aspects of endwall film-cooling," ASME Journal of Turbomachinery, vol. 119(4), pp. 786–793, 1997.

[15] G. Barigozzi, G. Franchini, A. Perdichizzi and M. Quattrore, "Endwall film-cooling effects on secondary slows in a contoured endwall nozzle vane," ASME Journal of Turbomachinery, vol. 132(4), p. 041005, 2010.

[16] T. E. Biesinger and D. G. Gregory-Smith, "Reduction in secondary flows and losses in a turbine cascade by upstream boundary layer blowing," International Gas Turbine and Aeroengine Congress and Exposition, 1993.

[17] A. A. Thrift and K. A. Thole, "Influence of flow injection angle on a leading-edge horseshoe vortex," International Journal of Heat and Mass Transfer, vol. 55, pp. 4651–4664, 2012.

[18] J. Roux, "Experimental investigation of nozzle guide vanes in a sector of an annular cascade," Licentiate Thesis, Department of Energy Technology, Division of Heat and Power Technology, KTH Royal Institute of Technology, no. ISBN 91-7283-672-5.

[19] J. H. Leylek and R. D. Zerkle, "Discrete-jet film-cooling: a comparison of computational results with experiments," ASME Journal of Turbomachinery, vol. 116(3), pp. 358-368, 1994.

[20] C. Saumweber and A. Schulz, "Effect of geometry variations on cooling performance of fan shaped cooling holes," ASME Journal of Turbomachinery, vol. 134(6), p. 061008, 2012.

[21] W. Colban, K. A. Thole and M. Haendler, "A comparison of cylindrical and fan-shaped film-cooling holes on a vane endwall at low and high freestream turbulence levels," ASME Journal of Turbomachinery, vol. 130(3), pp. 031007-031009, 2008.

[22] W. Colban and K. A. Thole, "Influence of hole shape on the performance of a turbine vane endwall film-cooling scheme," International Journal of Heat and Fluid Flow, vol. 28, pp. 341-356, 2007.

[23] G. Barigozzi, G. Franchini and A. Perdichizzi , "End-wall film-cooling through fan-shaped holes with different area ratios," ASME Journal of Turbomachinery, vol. 129(2), pp. 212-220, 2007.

[24] N. Sundaram, M. D. Barringer and K. A. Thole, "Effects of deposits on film-cooling of a vane endwall along the pressure-side," ASME Journal of Turbomachinery, vol. 130, p. 041006, 2008.

[25] N. Sundaram and K.A. Thole, "Bump and trench modifications to film-cooling holes at the vane-endwall junction," ASME Journal of Turbomachinery, vol. 130(4), p. 041013, 2008.

[26] M. Kunze, Vogeler, K., Brown, G., Prakash, C., and Landis, K., "Aerodynamic and endwall film-cooling investigations of a gas turbine nozzle guide vane applying temperature-sensitive paint.," ASME Journal of Turbomachinery, vol. 133(3), pp. 0310271-0310279, 2011.

[27] Y. Zhang , X. Yuan and P. Ligrani, "Film-cooling effectiveness distribution on first-stage vane endwall with and without leading-edge fillets," International Journal of Heat and Mass Transfer, vol. 66, pp. 642–654, 2013.

[28] G. Barigozzi, G. Benzoni, G. Franchini and A. Perdichizzi "Fan-shaped hole effects on the aero-thermal performance of a film-cooled endwall," ASME Journal of Turbomachinery, vol. 128(1), pp. 43-52, 2006.

[29] R. S. Bunker, 'A review of shaped hole turbine film-cooling technology', ASME Journal of Heat Transfer, vol. 127, pp. 441-453, 2005.

[30] N. Sundaram and K. A. Thole, "Film-cooling Flowfields With Trenched Holes on an Endwall," ASME Journal of Turbomachinery, vol. 131, pp. 1-10, 2009.

[31] W. Colban, A. Gratton, K. A. Thole and M. Haendler "Heat transfer and film-cooling measurements on a stator vane with fan-shaped cooling holes," ASME Journal of Turbomachinery, vol. 128, pp. 53-61, 2006.

[32] G. Barigozzi, H. Abdeh, A. Perdichizzi, M. Henze and J. Krueckels, "Aerothermal performance of a nozzle vane cascade with a generic nonuniform inlet flow condition—part II: influence of purge and film-cooling injection," ASME Journal of Turbomachinery, vol. 139(10), p. 101004, 2017.

[33] Xu QZ, Du Q, Wang P, Liu J, Liu G, "Computational investigation of film-cooling and secondary flow on turbine endwall with coolant injection from upstream interrupted slot," International Journal of Heat and Mass Transfer, vol. 123, pp. 285-296, 2018.

[34] K. A. Thole and D. G. Knost, "Heat transfer and film-cooling for the endwall of a first stage turbine vane," International Journal of Heat and Mass Transfer, vol. 48(25), pp. 5255-5269, 2005.

[35] S. P. Lynch and K. A. Thole, "The effect of combustor-turbine interface gap leakage on the endwall heat transfer for a nozzle guide vane," ASME Journal of Turbomachinery, vol. 130(4), pp. 041019-10, 2008.

[36] S. Friedrichs, H. P. Hodson and W. N. Dawes, "The design of an improved endwall film-cooling configuration," ASME Journal of Turbomachinery, vol. 130(4), pp. 772-780, 1999.

[37] S. Friedrichs, H. P. Hodson and W. N. Dawes, "Distribution of film-cooling effectiveness on a turbine endwall measured using the ammonia and diazo technique," ASME Journal of Turbomachinery, vol. 118, pp. 613-621, 1996.

[38] N. Wang , C.-C. Shiau , J.-C. Han , H. Xu and M. Fox, "Turbine vane endwall film-cooling from mid-chord or downstream rows and upstream coolant injection," International Journal of Heat and Mass Transfer, vol. 133, pp. 247–255, 2019.

[39] S. Hada and K. A. Thole, "Computational study of a mid-passage gap and upstream slot on vane endwall film-cooling," ASME Journal of Turbomachinery, vol. 133, p. 011024, 2011.

[40] K. Du, Z. Li and J. Li, "Effects of the leading edge injection slot on the film-cooling and heat transfer performance of the vane endwall," International Journal of Heat and Mass Transfer, vol. 102, pp. 1308-1320, 2016.

[41] P. Ligrani, "Aerodynamic losses in turbines with and without film-cooling, as influenced by mainstream turbulence, surface roughness, airfoil shape, and Mach number," International Journal of Rotating Machinery, vol. 2012, Article ID 957421, 2012.

[42] N. W. Harvey , G. Brennan, D. A. Newman and M. G. Rose "Improving turbine efficiency using non-axisymmetric end walls: validation in the multi-row environment and with low aspect ratio blading," ASME Turbo Expo: Power for Land, Sea, and Air, no. DOI: 10.1115/GT2002-30337, pp. 119-126, 2002.

[43] S. P. Lynch, K. A. Thole, A. Kohli and C. Lehane, "Computational predictions of heat transfer and film-cooling for a turbine blade with nonaxisymmetric endwall contouring," ASME Journal of Turbomachinery, vol. 133(4), p. 041003, 2011.

[44] R. Oke, T. Simon, , T. Shih, B. Zhu, Y. L. Lin, and M. Chyu, "Measurements over a film-cooled, contoured endwall with various coolant injection rates," ASME Turbo Expo: Power for Land, Sea, and Air, DOI:10.1115/2001-GT-0140, 2001.

[45] T. W. Simon, J. D. Piggush, "Turbine Endwall Aerodynamics and Heat Transfer," Journal of Propulsion and power, vol. 22(2), 2006.

[46] G. I. Mahmood, A. K. Saha and S. Acharya, "Secondary flows and upstream film-cooling in a linear NGV cascade in compressible flows: computations and experiments," International Conference on Heat Transfer, Fluid Mechanics and Thermodynamics, paper number: MG1, 2008.

[47] M. Thomas and T. Povey, "Improving turbine endwall cooling uniformity by controlling near-wall secondary flows," Proceedings of the Institution of Mechanical Engineers, Part G: Journal of Aerospace Engineering, vol. 231(14), pp. 2689-2705, 2016.

[48] F. Ornano and T. Povey, "Experimental and computational study of the effect of momentum-flux ratio on high-pressure nozzle guide vane endwall cooling systems," ASME Journal of Turbomachinery, vol. 139(12), p. 121002, 2017.

[49] A. Thrift, K. A. Thole and S. Hada, "Effects of an axisymmetric contoured endwall on a nozzle guide vane: adiabatic effectiveness measurements," ASME Journal of Turbomachinery, vol. 133(4), p. 041007, 2011.

[50] A. Thrift, K. A. Thole and S. Hada, "Effects of an axisymmetric contoured endwall on a nozzle guide vane: convective heat transfer measurements," ASME Journal of Turbomachinery, vol. 133, pp. 041008-1, 2011.

[51] J. C. Hartland, P. C. Gregory-Smith, N. W. Harvey and M. G. Rose, "Nonaxisymmetric turbine endwall design: part II-experimental validation," ASME Journal of Turbomachinery, vol. 122, pp. 286-293, 2000.

[52] M. G. Rose, "Non-axisymmetric endwall profiling in the HP NGV's of an an axial flow gas turbine," ASME Turbo Expo: Power for Land, Sea, and Air, DOI:10.1115/ 94-GT-249, V001T01A090 , 1994.

[53] N. W. Harvey, M. G. Rose, M.D. Taylor, S. Shahpar, J. Hartland and D.G. Gregory-Smith "Nonaxisymmetric turbine end wall design: part I— three-dimensional linear design system," ASME Journal of Turbomachinery, vol. 122(1), pp. 278-285, 2000.

[54] J. Moore and A. Ransmayr, "Flow in a turbine cascade: part 1—losses and leading-edge effects," Journal of Engineering for Gas Turbines and Power, vol. 106(2), pp. 400-407, 1984.

[55] S. Han and R. J. Goldstein, "Influence of Blade Leading Edge Geometry on Turbine Endwall Heat(Mass) Transfer," ASME Journal of Turbomachinery, vol. 128(4), pp.798-813 , 2006.

[56] H. Sauer, R. Muller and K. Vogeler, "Reduction of secondary flow losses in turbine cascades by leading edge modifications at the endwall," ASME Journal of Turbomachinery, vol. 123(2), pp. 207-213, 2001.

[57] G. Zess and K. Thole, "Computational design and experimental evaluation of using a leading edge fillet on a gas turbine vane," ASME Journal of Turbomachinery, vol.124(2), pp. 167-175, 2002.

[58] S. Becz, M. S. Majewski and L. S. Langston, "Leading edge modification effects on turbine cascade endwall loss," ASME Turbo Expo: Power for Land, Sea, and Air, DOI:10.1115/ GT2003-38898, pp. 359-367, 2003.

[59] R. Erickson and T. W. Simon, "Effects of stator/rotor leakage flow and axisymmetric contouring on endwall adiabatic effectiveness and aerodynamic loss," Heat Transfer Research, vol. 42(1), pp. 45-64, 2011.

[60] G. Mahmood, R. Gustafson and S. Acharya, "Experimental investigation of flow structure and Nusselt number in a low-speed linear blade passage with and without leading-edge fillets," ASME Journal of Heat Transfer, vol. 127(5), pp. 499-512, 2005.

[61] G. Mahmood and S. Acharya, "Experimental investigation of secondary flow structure in a blade passage with and without leading edge fillets," ASME Journal of Fluids Engineering, vol. 129(3), pp. 253-262, 2007.

[62] L. P. Timko, "Energy efficient engine high pressure turbine component test performance report," Contract Report for NASA, 1990.

[63] S. A. Shote, G. I. Mahmood and J. P. Meyer, "Influences of large fillets on endwall flows in a vane cascade with upstream slot film-cooling", Journal of Experimental Thermal and Fluid Science, vol.112, 2020.

[64] Z. Dlamini, "Experimental investigation of film-cooling hole performance," MEng Thesis, University of Pretoria, 2020.

[65] M. Thomas and T. Povey, "Improving turbine endwall cooling uniformity by controlling near-wall secondary flows", Proceedings of the Institution of Mechanical Engineers, Part G: Journal of Aerospace Engineering, vol. 231(14), pp. 2689-2705, 2017.

[66] W. Li, X. Li, J. Ren and H. Jiang, "A novel method for designing fan-shaped holes with short length-to-diameter ratio in producing high film-cooling performance for thin-wall turbine airfoil," ASME Journal of Turbomachinery, vol. 140(9), p. 091004, 2018.

[67] Y. Li, Y. Zhang, X. Su and X . Yuan, "Experimental and numerical investigations of shaped hole film-cooling with the influence of endwall cross flow," International Journal of Heat and Mass Transfer, vol. 120, pp. 42-55, 2018.

[68] M. Gritsch, W. Colban, H. Schär and K. Döbbeling, "Effect of hole geometry on the thermal performance of fan-shaped film-cooling holes," ASME Journal of Turbomachinery, vol. 127(4), pp. 718-725, 2005.

[69] P. Aghasi, E. Gutmark, and D. Munday, "Dependence of film-cooling effectiveness on three-dimensional printed cooling holes," ASME Journal of Heat Transfer, vol. 139(10), pp. 1020031-10200315, 2017.

[70] R. P. Schroeder and K. A. Thole, "Adiabatic effectiveness measurements for a baseline shaped film-cooling hole," ASME Turbo Expo: Power for Land, Sea, and Air, DOI:10.1115/GT2014-25992, V05BT13A036, 2014.

[71] C. M. Bell, H. Hamakawa and P. Ligrani, "Film-cooling from shaped holes," ASME Journal of Heat Transfer, vol. 122(2), pp. 224-232, 2000.

[72] K. Du and J. Li, "Numerical study on the effects of slot injection configuration and endwall alignment mode on the film-cooling performance of vane endwall," International Journal of Heat and Mass Transfer, vol. 98, pp. 768-777, 2016.

[73] R. G. Dominy and H. P. Hodson, "An investigation of factors influencing the calibration of five-hole probes for three-dimensional flow measurements," ASME Journal of Turbomachinery, vol.115(3), pp. 513-519, 1993.

[74] P. Ligrani, B. Singer and L. Baun, "Miniature five-hole pressure probe for measurement of three mean velocity components in low-speed flows," Journal of Physics E: Scientific Instruments, vol. 22, no. 10, p. 868, 1989.

[75] P. Ligrani and P. Bradshaw, "Spatial resolution and measurement of turbulence in the viscous sublayer using subminiature hot-wire probes," Experiments in Fluids, vol. 5, no. 6, pp. 407-417, 1987.

[76] S. Han and R. J. Goldstein, "The heat/mass transfer analogy for a simulated turbine blade," International Journal of Heat and Mass Transfer, vol. 51, pp. 5209-5225, 2008.

[77] P. F. Dunn, "Measurement and data analysis for engineering and science", second edition, CRC Press, 2010.

[78] S. Acharya and G. I. Mahmood, " Turbine blade aerodynamics in gas turbine: handbook", NETL of the US Department of Energy, Ch. 4.3, pp. 363-388, 2007.

[79] G. I. Mahmood and A. Keenesh, "Effects of upstream endwall film-cooling on a vane cascade flowfield", manuscript no. 2017-02-B36640, Journal of propulsion and power, vol. 34(2), pp. 460-468, 2018.

[80] F. Kost and M. Nicklas, "Film-cooled turbine endwall in a transonic flowfield: Part I-aerodynamic measurement," ASME Journal of Turbomachinery, vol. 123(4), pp. 709-719, 2001.

[81] D. G. Knost and K. A. Thole, "Adiabatic Effectiveness Measurements of Endwall Film-cooling for a First-Stage Vane," ASME Journal of Turbomachinery, vol. 127(2), pp.297-305, 2005.

APPENDICES

APPENDIX A: FIVE-HOLE PROBE CALIBRATION

The five-hole probe calibration was conducted in the upstream section of the turbulence grid where the free-stream velocity was 15 m/s. The procedure involved manually positioning the probe at a known yaw angle and then rotating the tip over the range of pitch angles. The calibration range was taken between -25° to +25° for both the pitch and yaw angle. The calibration coefficients were presented next and showed good agreement with Ligrani et al. [74].

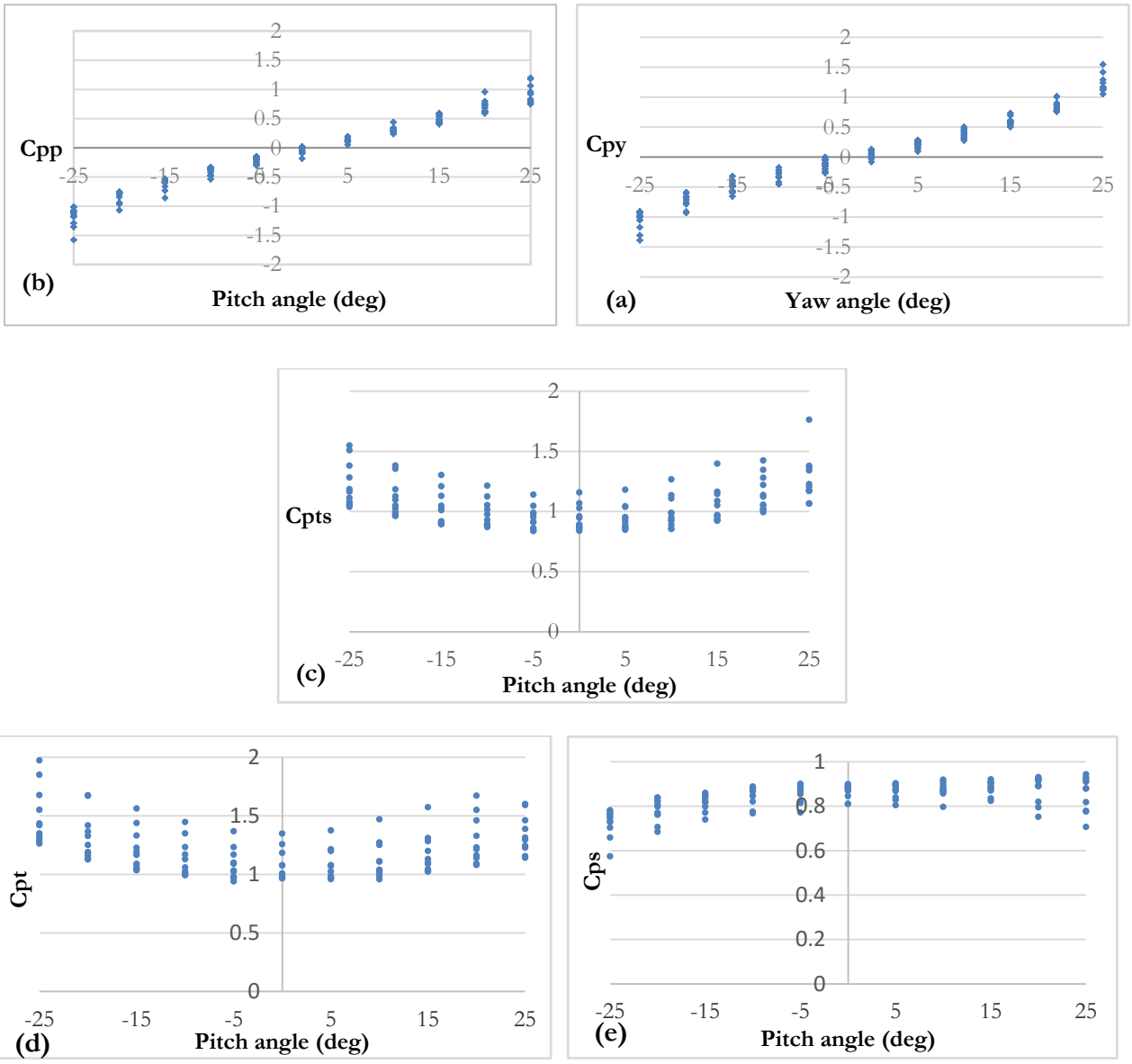

Figure A 1: *Five-hole pressure probe calibration data: a) yaw angle calibration with yaw angle and pitch angle, b) pitch angle calibration, variation of C_{pp}, with pitch angle and yaw angle, c) P_t - P_s calibration, variation of C_{pts} with pitch angle and yaw angle, d) P_t calibration, variation of C_{pt} with pitch angle and yaw angle, e) P_s calibration, variation of C_{ps} with pitch angle and yaw angle.*

APPENDIX B: UNCERTAINTY CALCULATIONS

B.1 Pressure transducers uncertainty example calculation

The uncertainty of a single measurement was based on the bias and precision error calculated according to [77], as follows:

$$\boldsymbol{\partial x_i = \sqrt{b_i^2 + p_i^2}} \tag{23}$$

The bias errors of the pressure transducers that were used in the experiments were determined via linear least-squares regression analysis. The bias error of the Siemens pressure transducer was 0.156 Pa, accuracy specified by the Setra Micro-cal pressure calibrator (+/-0.04% full scale, 3550Pa) used during the calibration. The calibration of the Siemens pressure transducer consisted of M=14 data points from zero to maximum pressure value, 390Pa. The calibration curve was obtained by a linear curve fit through the calibration points.

The precision error of the pressure transducer was calculated according to the linear regression analysis [76], which determines the mathematical relation between two or more variables x_i.

In the case of the pressure transducer, the x-variable was the pressure reading from the calibrator and the depending variable, the y-variable, was represented by the pressure reading from the output voltage of the pressure transducer. The x-variable was known, the y-variable was obtained from the measurement and therefore, the uncertainty lay in the y-variable. The precision error at 390 Pa for the Siemens pressure transducer was derived from the standard deviation of about 14 measuring points logged and calculated as follows:

$$\mathrm{p_{P1}} = \pm \mathrm{t_{95}} \mathrm{S_{yx}} \sqrt{\frac{1}{\mathrm{N}} + \frac{1}{\mathrm{M}} + \frac{(\mathrm{x_i} - \bar{\mathrm{x}})^2}{\mathrm{S_{xx}}}} = \pm 0.0074 \tag{24}$$

The Student's t variable was t_{95}=2.16 for measurements 13 degrees of freedom where

$$\partial \mathrm{S_{xx}} = \sum_{\mathrm{i=1}}^{\mathrm{N}} (\mathrm{x_i} - \bar{\mathrm{x}})^2 = (0-30)^2 + (30-195)^2 + (60-195)^2 + (90-195)^2 + (120-195)^2 + (150-195)^2 + (180-195)^2 + (210-195)^2 + (240-195)^2 + (270-195)^2 + (300-195)^2 + (330-195)^2 + (360-195)^2 + (390-195)^2 = 204.7\mathrm{kPA} \tag{25}$$

$$\boldsymbol{\partial S_{xy} = \sum_{i=1}^{N} (x_i - \bar{x})(y_i - \bar{y}) = (0-195)(-1.88-194.84) + +(30-195)\ \ (29.77-194.84) + (60-195)\ \ (59.84-194.84) + (90-195)\ \ (90.04-194.84) + (120-195)\ \ (119.8-194.84) + (150-195)\ \ (150.05-194.84) + (180-195)\ \ (180.05-194.84) + (210-195)\ \ (210.24-194.84) + (240-195)\ \ (240.17-194.84) + (270-195)\ \ (270.13-194.84) + (300-195)\ \ (300.06-194.84) + (330-195)\ \ (329.89-194.84) + (360-195)\ \ (359.9-194.84) + (390-195)\ \ (389.78-194.84) = 205.1 kPa} \tag{26}$$

$$b = \frac{\partial S_{xy}}{\partial S_{xx}} = 1 \; a = \bar{y} - b\bar{x} = -0.523 \qquad y_{ci} = a + bx_i \tag{27}$$

$$\partial S_{yx} = \sqrt{\sum_{i=1}^{N} \frac{(y_i - y_{ci})^2}{N-2}} = \sqrt{\frac{2.775}{12}} = 0.481 \tag{28}$$

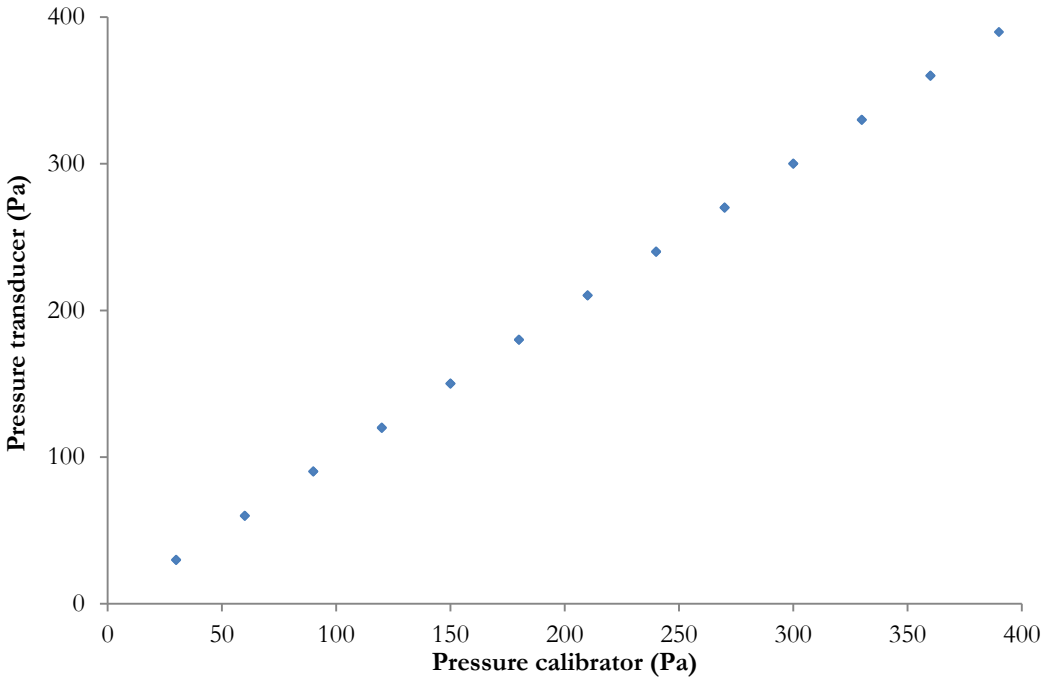

Figure B 1: *Sample plot of the pressure transducer measurement as a function of the pressure measured by the calibrator.*

The overall uncertainty for a nominal pressure of 390 Pa for the pressure transducer was

$$\boldsymbol{u_{bias} = \sqrt{b_{cal}^2 + p_i^2} = \sqrt{1.42^2 + 0.517^2} = 1.518\ Pa} \tag{29}$$

This overall uncertainty of the pressure transducer was lower than the manufacturer's accuracy; therefore, the latest was considered as total bias error. The overall uncertainty for the Siemens pressure transducer was taken as the bias calibration error of the pressure transducer over the entire pressure range.

The uncertainty of a single measurands or variable $\bar{x}_{\iota,}$ could be expressed with the odds of 20 to 1 or a 95% confidence level of probability that the actual error would not be more or less than the estimate. This was computed via Eq. (30)

$$x_i = \bar{x}_\iota \pm \partial x_i \tag{30}$$

In probability and statistics, the x_i term represents a single observation with δ being the uncertainty that is obtained from the product of the standard deviation multiplied with the Student's t-

distribution variable, which is used when estimating the mean of a dataset for which the sample size is small (number of degrees of freedom: n < 30).

The precision error u_p with P% probability was estimated through repeated measurements of the dataset of P_1 taken by the Siemens pressure transducer and statistical analysis.

$$u_p = t_{v,p} S_x \tag{31}$$

The sample standard deviation was

$$S_x = \sqrt{\frac{1}{N-1}\sum_{i=1}^{N}(P_i - \overline{P})} \tag{32}$$

The uncertainty of P_1 at mid-span was calculated as:

$$\partial P_1 = \sqrt{u_{bias}^2 + u_P^2} = \sqrt{1.42^2 + 0.53^2} = \pm 1.51 \text{ Pa} \tag{33}$$

The true calibrated pressure value of P_1 in the inviscid region at mid-span at the probability of 95% was:

$$P_1' = \bar{P}_1 \pm \partial P_1 = 27.35 \pm 1.51(Pa)$$

At the reference plane, the averaged corrected total pressure and static pressure were respectively:

$$P'_{t,ref} = \bar{P}_{t,ref} + \partial x_i = -26.3 \pm 1.5\ (Pa) \tag{34}$$

$$P'_{s,ref} = \bar{P}_{s,ref} + \partial x_i = -86.8\ \pm 1.7(Pa) \tag{35}$$

The overall uncertainty of all pressures of the five-hole pressure probe, in three regions along the exit plane, at a minimum and maximum value, is provided in *Table 8* and *Table 9*.

B.2 Measurement system errors: calculated results

B.2.1 Five-hole probe

The uncertainty of the flow direction results calculated in data reduction depended on the uncertainty of the five values of probe measured in the experiment and the uncertainty of each measurement of the five-hole probe pressure and the flow angles acquired in probe calibration.

$$P_{ave} = \frac{P_4 + P_5 + P_2 + P_3}{4} \tag{36}$$

$$\boldsymbol{\partial P_{ave}} = \sqrt{\left(\frac{\partial P_{ave}}{\partial \overline{P_2}}\partial \overline{P_2}\right)^2 + \left(\frac{\partial P_{ave}}{\partial \overline{P_3}}\partial \overline{P_3}\right)^2 + \left(\frac{\partial P_{ave}}{\partial \overline{P_4}}\partial \overline{P_4}\right)^2 + \left(\frac{\partial P_{ave}}{\partial \overline{P_5}}\partial \overline{P_5}\right)^2} =$$

$$\frac{1}{2}\sqrt{\partial \overline{P_2}^2 + \partial \overline{P_3}^2 + \partial \overline{P_4}^2 + \partial \overline{P_5}^2} \tag{37}$$

$$\frac{\partial P_{ave}}{\partial \overline{P_2}} = \frac{1}{4} \tag{38}$$

For the calculation of the bias uncertainty of yaw and pitch angles, Eqs. 4-7 were used from the calibration at yaw and pitch and a statistical analysis was conducted for 10 values angle dataset at 0, 10, and 20 degrees.

$$C_{p_{yaw}} = \frac{P_2 - P_3}{P_1 - P_{ave}} \tag{39}$$

$$C_{p_{pitch}} = \frac{P_4 - P_5}{P_1 - P_{ave}} \tag{40}$$

$$\boldsymbol{u_{bias} = t_{v,P} S_x} \tag{41}$$

The sample standard deviation is

$$S_x = \sqrt{\frac{1}{N-1}\sum_{i=1}^{N}\left(C_{pyaw,i} - \overline{C_{pyaw}}\right)} \tag{42}$$

For the experiments, the uncertainty of the five-hole pressure probe was evaluated in the third plane and the exit plane. Ten measurement datasets for all pressures of the five-hole pressure probe reading were considered at three distinct regions along the plane at blowing ratio M=1.3. An in-house Fortran program used to correct the pressure reading from the five-hole probe gave the five pressure readings P_1, P_2, P_3, P_4, P_5. ∂P_{ave}. In the third plane, ***Figure B 2*** illustrates the following regions: close to the endwall, close to the suction-side, and along the span through the pitch direction.

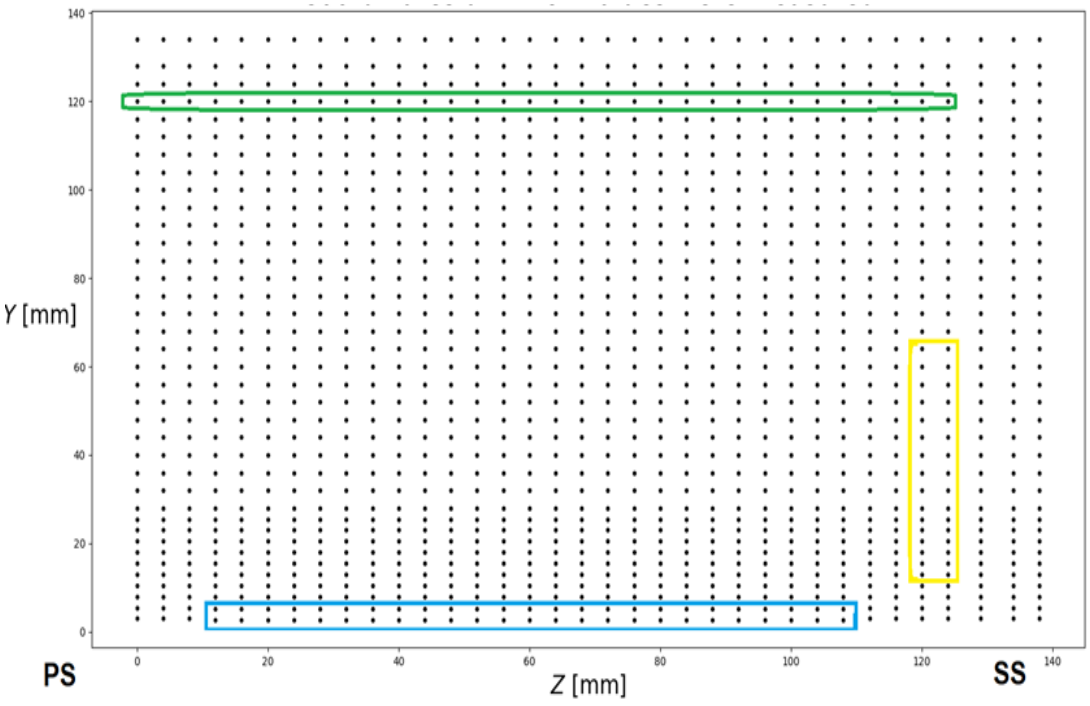

Figure B 2: *Uncertainty measurement regions at the third plane.*

In the exit plane, ***Figure B 3*** illustrates the following regions: close to the endwall on the pressure-side, along the blade's trailing edge, and lastly, along the span on the suction-side.

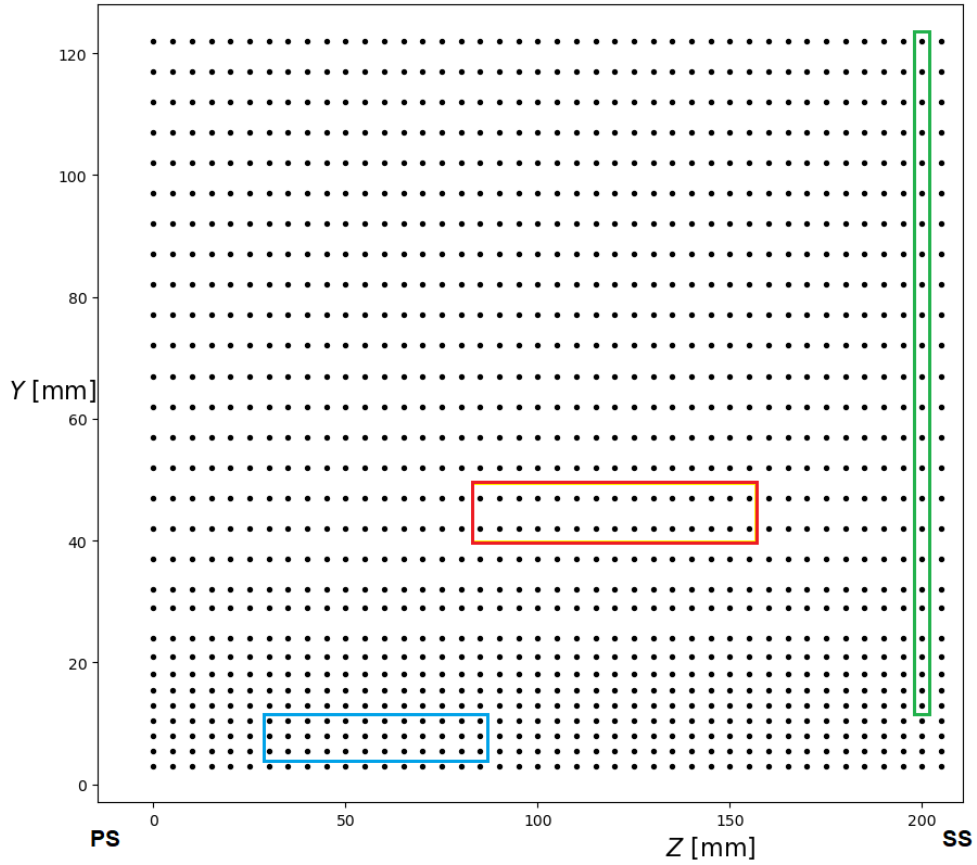

***Figure B 3**: Uncertainty measurement regions at the exit plane.*

The precision uncertainty of yaw and pitch angles in the three measurement regions was obtained as follows:

$$\partial C_{Py} = \sqrt{\left(\frac{\partial C_{Py}}{\partial \overline{P_2}}\partial \overline{P_2}\right)^2 + \left(\frac{\partial C_{Py}}{\partial \overline{P_3}}\partial \overline{P_3}\right)^2 + \left(\frac{\partial C_{Py}}{\partial \overline{P_1}}\partial \overline{P_1}\right)^2 + \left(\frac{\partial C_{Py}}{\partial \overline{P_{ave}}}\partial \overline{P_{ave}}\right)^2} \tag{43}$$

The uncertainty of the yaw coefficient was:

$$\frac{\partial C_{Py}}{\partial \overline{P_2}} = \frac{1}{\overline{P_1} - \overline{P_{ave}}} \tag{44}$$

$$\frac{\partial C_{Py}}{\partial \overline{P_3}} = -\frac{1}{\overline{P_1} - \overline{P_{ave}}} \tag{45}$$

$$\frac{\partial C_{Py}}{\partial \overline{P_1}} = -\frac{\overline{P_2} - \overline{P_3}}{(\overline{P_1} - \overline{P_{ave}})^2} \tag{46}$$

$$\frac{\partial C_{Py}}{\partial \overline{P_{ave}}} = \frac{\overline{P_2} - \overline{P_3}}{(\overline{P_1} - \overline{P_{ave}})^2} \tag{47}$$

The uncertainty of the pitch coefficient was:

$$\boldsymbol{\partial C_{Pp}} = \sqrt{\left(\frac{\partial C_{Pp}}{\partial \overline{P_4}}\boldsymbol{\partial \overline{P_4}}\right)^2 + \left(\frac{\partial C_{Pp}}{\partial \overline{P_5}}\boldsymbol{\partial \overline{P_5}}\right)^2 + \left(\frac{\partial C_{Pp}}{\partial \overline{P_1}}\boldsymbol{\partial \overline{P_1}}\right)^2 + \left(\frac{\partial C_{Pp}}{\partial \overline{P_{ave}}}\boldsymbol{\partial \overline{P_{ave}}}\right)^2} \quad (48)$$

$$\frac{\boldsymbol{\partial C_{Pp}}}{\boldsymbol{\partial \overline{P_{ave}}}} = \frac{\overline{P_4} - \overline{P_5}}{(\overline{P_1} - \overline{P_{ave}})^2} \quad (49)$$

$$\frac{\boldsymbol{\partial C_{Pp}}}{\boldsymbol{\partial \overline{P_4}}} = \frac{1}{\overline{P_1} - \overline{P_{ave}}} \quad (50)$$

$$\frac{\boldsymbol{\partial C_{Pp}}}{\boldsymbol{\partial \overline{P_5}}} = -\frac{1}{\overline{P_1} - \overline{P_{ave}}} \quad (51)$$

$$\frac{\boldsymbol{\partial C_{Pp}}}{\boldsymbol{\partial \overline{P_1}}} = -\frac{\overline{P_4} - \overline{P_5}}{(\overline{P_1} - \overline{P_{ave}})^2} \quad (52)$$

$$\boldsymbol{\partial Yaw} = \sqrt{\boldsymbol{C_{P\_bias}^2 + C_{Py\_p}^2}} \quad (53)$$

$$\boldsymbol{\partial Pitch} = \sqrt{\boldsymbol{C_{Pp\_bias}^2 + C_{Pp\_p}^2}} \quad (54)$$

In the same way, the uncertainty of the total pressure coefficient was calculated:

$$\partial C_{Pt} = \sqrt{\left(\frac{\partial C_{Pt}}{\partial \overline{P_{t,ref}}}\partial \overline{P_{t,ref}}\right)^2 + \left(\frac{\partial C_{Pt}}{\partial \overline{P_1}}\partial \overline{P_1}\right)^2 + \left(\frac{\partial C_{Pt}}{\partial \overline{P_{ave}}}\partial \overline{P_{ave}}\right)^2} \quad (55)$$

$$\frac{\boldsymbol{\partial C_{Pt}}}{\boldsymbol{\partial \overline{P_{ave}}}} = \frac{\overline{P_{t,ref}} - \overline{P_1}}{(\overline{P_1} - \overline{P_{ave}})^2} \quad (56)$$

$$\frac{\boldsymbol{\partial C_{Pt}}}{\boldsymbol{\partial \overline{P_{t,ref}}}} = \frac{1}{\overline{P_1} - \overline{P_{ave}}} \quad (57)$$

$$\frac{\boldsymbol{\partial C_{Pt}}}{\boldsymbol{\partial \overline{P_1}}} = -\frac{\overline{P_{t,ref}} - \overline{P_{ave}}}{(\overline{P_1} - \overline{P_{ave}})^2} \quad (58)$$

The uncertainty of the static pressure coefficient was:

$$\boldsymbol{\partial C_{Ps}} = \sqrt{\left(\frac{\partial C_{Ps}}{\partial \overline{P_t}}\boldsymbol{\partial \overline{P_t}}\right)^2 + \left(\frac{\partial C_{Ps}}{\partial \overline{P_s}}\boldsymbol{\partial \overline{P_s}}\right)^2 + \left(\frac{\partial C_{Ps}}{\partial \overline{P_1}}\boldsymbol{\partial \overline{P_1}}\right)^2 + \left(\frac{\partial C_{Ps}}{\partial \overline{P_{ave}}}\boldsymbol{\partial \overline{P_{ave}}}\right)^2} \quad (59)$$

$$\frac{\boldsymbol{\partial C_{Ps}}}{\boldsymbol{\partial \overline{P_{ave}}}} = \frac{\overline{P_t} - \overline{P_s}}{(\overline{P_1} - \overline{P_{ave}})^2} \quad (60)$$

$$\frac{\boldsymbol{\partial C_{Ps}}}{\boldsymbol{\partial \overline{P_t}}} = \frac{1}{\overline{P_1} - \overline{P_{ave}}} \quad (61)$$

$$\frac{\boldsymbol{\partial C_{Ps}}}{\boldsymbol{\partial \overline{P_s}}} = -\frac{1}{\overline{P_1} - \overline{P_{ave}}} \quad (62)$$

$$\frac{\boldsymbol{\partial C_{Ps}}}{\boldsymbol{\partial \overline{P_1}}} = -\frac{\overline{P_t} - \overline{P_s}}{(\overline{P_1} - \overline{P_{ave}})^2} \quad (63)$$

The local total pressure was given by

$$P_t=P_{ave}+C_{pt}(P_1- P_{ave}) \quad (64)$$

The uncertainty of the local total pressure was:

$$\partial P_t = \sqrt{\left(\frac{\partial P_t}{\partial \overline{C_{pt}}}\partial\overline{C_{pt}}\right)^2 + \left(\frac{\partial P_t}{\partial \overline{P_1}}\partial\overline{P_1}\right)^2 + \left(\frac{\partial P_t}{\partial \overline{P_{1ave}}}\partial\overline{P_{ave}}\right)^2} \quad (65)$$

$$\frac{\partial P_t}{\partial \overline{C_{ave}}} = \mathbf{1} - \boldsymbol{C_{pt}} \quad (66)$$

$$\frac{\partial P_t}{\partial \overline{C_{pt}}} = \overline{\boldsymbol{P_1}} - \overline{\boldsymbol{P_{ave}}} \quad (67)$$

$$\frac{\partial P_t}{\partial \overline{P_1}} = \boldsymbol{C_{pt}} \quad (68)$$

The local static pressure was given by

$$P_S=P_1-C_{ps}(P_1- P_{ave}) \quad (69)$$

The uncertainty of local static pressure was:

$$\partial P_s = \sqrt{\left(\frac{\partial P_s}{\partial \overline{C_{ps}}}\partial\overline{C_{ps}}\right)^2 + \left(\frac{\partial P_s}{\partial \overline{P_1}}\partial\overline{P_1}\right)^2 + \left(\frac{\partial P_s}{\partial \overline{P_{ave}}}\partial\overline{P_{ave}}\right)^2} \quad (70)$$

$$\frac{\partial P_s}{\partial \overline{P_{ave}}} = \boldsymbol{C_{ps}} \quad (71)$$

$$\frac{\partial P_s}{\partial \overline{C_{ps}}} = \boldsymbol{P_{ave}} - \overline{\boldsymbol{P_1}} \quad (72)$$

$$\frac{\partial P_s}{\partial \overline{P_1}} = \mathbf{1} - \boldsymbol{C_{ps}} \quad (73)$$

The overall uncertainty of the yaw and pitch angles, yaw and pitch coefficients, local static and total pressure coefficients, in three regions along the third and exit planes, at a minimum and maximum value, was given in *Table 10* and *Table 11*.

B.2.2 Local velocity and axial vorticity

The local velocity was obtained by the five-hole pressure probe reading. The density was considered constant.

$$\mathbf{V} = \sqrt{\mathbf{2}\left(\frac{|\overline{\boldsymbol{P_{t,loc}}}-\overline{\boldsymbol{P_{s,loc}}}|}{\boldsymbol{\rho}}\right)} \quad (74)$$

The uncertainty of the local velocity was calculated as

$$\partial V = \sqrt{\left(\frac{\partial V}{\partial \overline{P_{s,loc}}}\partial\overline{P_{s,loc}}\right)^2 + \left(\frac{\partial V}{\partial \overline{P_{t,loc}}}\partial\overline{P_{t,loc}}\right)^2} \quad (75)$$

$$\frac{\partial V}{\partial \overline{P_{s,loc}}} = -\frac{1}{\rho\sqrt{\frac{\left|P_{t,loc}-P_{s,loc}\right|}{\rho}}\sqrt{2}} \tag{76}$$

$$\frac{\partial V}{\partial \overline{P_t}} = \frac{1}{\rho\sqrt{\frac{\left|P_{t,loc}-P_{s,loc}\right|}{\rho}}\sqrt{2}} \tag{77}$$

The components of the local velocities were:

$$u_x = \mathbf{V} * \cos(Yaw)\cos(PIT) \tag{78}$$

$$u_y = \mathbf{V} * \sin(PIT) \tag{79}$$

$$u_z = \mathbf{V} * \cos(PIT)\sin(yaw) \tag{80}$$

Their uncertainties were:

$$\partial u_x = \sqrt{\left(\frac{\partial u_x}{\partial \overline{PIT}}\partial \overline{PIT}\right)^2 + \left(\frac{\partial u_x}{\partial \overline{Yaw}}\partial \overline{Yaw}\right)^2 + \left(\frac{\partial u_x}{\partial V}\partial V\right)^2} \tag{81}$$

$$\partial u_y = \sqrt{\left(\frac{\partial u_y}{\partial \overline{PIT}}\partial \overline{PIT}\right)^2 + \left(\frac{\partial u_y}{\partial V}\partial V\right)^2} \tag{82}$$

$$\partial u_z = \sqrt{\left(\frac{\partial u_z}{\partial \overline{PIT}}\partial \overline{PIT}\right)^2 + \left(\frac{\partial u_z}{\partial \overline{Yaw}}\partial \overline{Yaw}\right)^2 + \left(\frac{\partial u_z}{\partial V}\partial V\right)^2} \tag{83}$$

$$\frac{\partial u_x}{\partial \overline{PIT}} = -\mathbf{V}\cos(Yaw)\sin(PIT) \tag{84}$$

$$\frac{\partial u_x}{\partial \overline{Yaw}} = -\mathbf{V}\cos(PIT)\sin(Yaw) \tag{85}$$

$$\frac{\partial Uu_x}{\partial V} = \cos(Yaw)\cos(PIT) \tag{86}$$

$$\frac{\partial u_y}{\partial \overline{PIT}} = \mathbf{V}\cos(PIT) \tag{87}$$

$$\frac{\partial u_y}{\partial \overline{Yaw}} = \mathbf{0} \tag{88}$$

$$\frac{\partial u_y}{\partial V} = \sin(PIT) \tag{89}$$

$$\frac{\partial u_z}{\partial \overline{PIT}} = -\mathbf{V}\sin(Yaw)\sin(PIT) \tag{90}$$

$$\frac{\partial u_z}{\partial \overline{Yaw}} = \mathbf{V}\cos(PIT)\cos(Yaw) \tag{91}$$

$$\frac{\partial u_z}{\partial V} = \cos(PIT)\sin(yaw) \tag{92}$$

The uncertainty of the axial vorticity was calculated considering two measurement points along with the pitch at distance d.

$$\partial w_x = \frac{\sqrt{(u\partial U_z)^2+(u\partial U_y)^2}}{d} \quad (93)$$

The overall uncertainty of the local velocity components and axial vorticity, in three regions along the third and exit planes, at a minimum and maximum value, was given in *Table 12* and *Table 13*.

B.2.3 Reference velocity

The uncertainty of the free-stream velocity was obtained assuming a constant density of ϱ=1.006 kg/m^3. Since the linear cascade is a suction facility, the dynamic pressure was:

$$\overline{P_{t,ref}} - \overline{P_{s,ref}} = \frac{1}{2}\rho\overline{U_{ref}^2} \quad (94)$$

$$\overline{U_{ref}} = \sqrt{\frac{2*(\overline{P_{t,ref}}-\overline{P_{s,ref}})}{\rho}} \quad (95)$$

$$\frac{\partial\overline{U_{ref}}}{\partial\overline{P_{t,ref}}} = \frac{\sqrt{2}}{2\sqrt{\rho(\overline{P_{t,ref}}-\overline{P_{s,ref}})^2}} = \mathbf{0.011} \quad (96)$$

$$\frac{\partial\overline{U_{ref}}}{\partial\overline{P_{s,ref}}} = \frac{-\sqrt{2}}{2\sqrt{\rho(\overline{P_{t,ref}}-\overline{P_{s,ref}})^2}} = \mathbf{-0.011} \quad (97)$$

The uncertainty of U_{ref} can be evaluated by:

$$\partial\overline{U_{ref}} = \sqrt{\left(\frac{\partial U_{ref}}{\partial\overline{P_{t,ref}}}\partial\overline{P_{t,ref}}\right)^2 + \left(\frac{\partial U_{ref}}{\partial\overline{P_{s,ref}}}\partial\overline{P_{s,ref}}\right)^2} = \pm\mathbf{0.026} \quad (98)$$

The overall uncertainty of the nominal reference velocity of 10.8 m/s was:

$$\partial U_\infty\% = \frac{\partial U_\infty}{\overline{U_\infty}} * 100\% = 0.24\% \quad (99)$$

B.2.4 Coefficient of static and total pressure

To calculate the static pressure coefficient uncertainty, the uncertainties of the five-hole pressures, $\partial P_{t,\,loc,}$ had to be known. The uncertainty of the static pressure coefficient was calculated as follows:

$$C_{Ps} = \frac{\overline{P_{s,ref}}-\overline{P_{s,loc}}}{\overline{P_{t,ref}}-\overline{P_{s,ref}}} \quad (100)$$

$$\partial C_{Ps} = \sqrt{\left(\frac{\partial C_{Ps}}{\partial\overline{P_{t,ref}}}\partial\overline{P_{t,ref}}\right)^2 + \left(\frac{\partial C_{Ps}}{\partial\overline{P_{s,ref}}}\partial\overline{P_{s,ref}}\right)^2 + \left(\frac{\partial C_{Ps}}{\partial\overline{P_{s,loc}}}\partial\overline{P_{s,loc}}\right)^2} = 0.011 \quad (101)$$

$$\frac{\partial C_{Ps}}{\partial P_{s,ref}} = \frac{(\overline{P_{t,ref}}-\overline{P_{s,ref}})-(\overline{P_{s,ref}}-\overline{P_{s,loc}})}{(\overline{P_{t,ref}}-\overline{P_{s,ref}})^2} \quad (102)$$

$$\frac{\partial C_{Ps}}{\partial P_{t,ref}} = \frac{\overline{P_{s,ref}} - \overline{P_{s,loc}}}{\left(\overline{P_{t,ref}} - \overline{P_{s,ref}}\right)^2} \tag{103}$$

$$\frac{\partial C_{Ps}}{\partial P_{s,loc}} = -\frac{1}{\overline{P_{t,ref}} - \overline{P_{s,ref}}} \tag{104}$$

The uncertainty of the total pressure coefficient was calculated as follows:

$$C_{Pt,loss} = \frac{\overline{P_{t,ref}} - \overline{P_{t,loc}}}{\overline{P_{t,ref}} - \overline{P_{s,ref}}} \tag{105}$$

$$\partial C_{Pt,loss} = \sqrt{\left(\frac{\partial C_{Pt,loss}}{\partial P_{t,ref}} \partial \overline{P_{t,ref}}\right)^2 + \left(\frac{\partial C_{Pt,loss}}{\partial P_{s,ref}} \partial \overline{P_{s,ref}}\right)^2 + \left(\frac{\partial C_{Pt,loss}}{\partial P_{t,loc}} \partial \overline{P_{t,loc}}\right)^2} \tag{106}$$

$$\frac{\partial C_{Pt,loss}}{\partial P_{t,ref}} = \frac{\left(\overline{P_{t,ref}} - \overline{P_{s,ref}}\right) - \left(\overline{P_{t,ref}} - \overline{P_{t,loc}}\right)}{\left(\overline{P_{t,ref}} - \overline{P_{s,ref}}\right)^2} \tag{107}$$

$$\frac{\partial C_{Pt,loss}}{\partial P_{s,ref}} = \frac{\overline{P_{t,ref}} - \overline{P_{t,loc}}}{\left(\overline{P_{t,ref}} - \overline{P_{s,ref}}\right)^2} \tag{108}$$

$$\frac{\partial C_{Pt,loss}}{\partial P_{t,loc}} = -\frac{1}{\overline{P_{t,ref}} - \overline{P_{s,ref}}} \tag{109}$$

The overall uncertainty of the static and total pressure coefficient, in three regions along the plane, was given in ***Table 15*** at a minimum and maximum $C_{pt,loss}$.

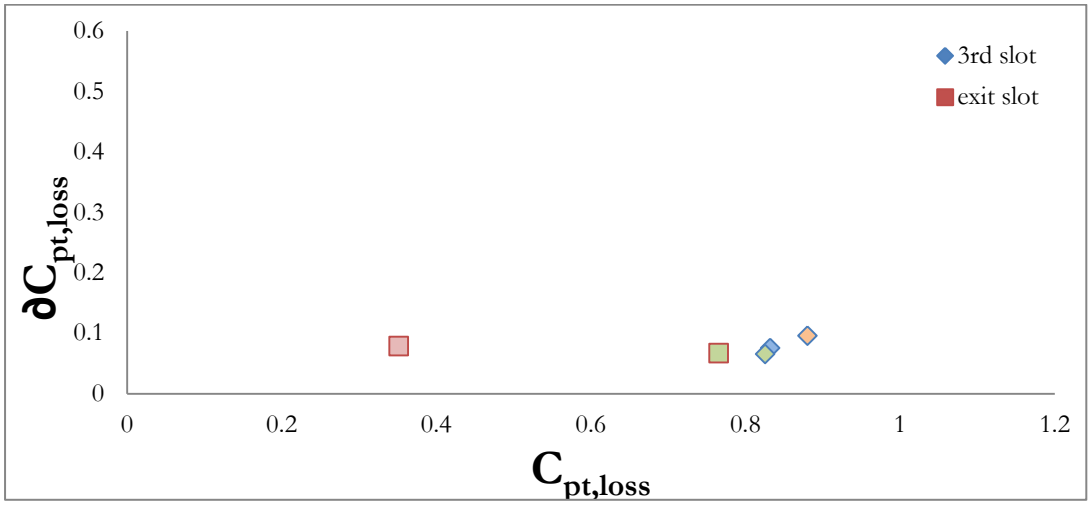

Figure B 4*: Uncertainty of the total pressure coefficient at the third plane and exit plane.*

B.2.5 Film-cooling inlet blowing ratio

The uncertainty of the film-cooling inlet blowing ratio was calculated as follows:

$$M = \sqrt{\frac{\overline{P_{t,plenum}} - \overline{P_{s,ref}}}{\overline{P_{t,ref}} - \overline{P_{s,ref}}}} \tag{110}$$

$$\partial M = \sqrt{\left(\frac{\partial M}{\partial \overline{P_{t,ref}}}\partial \overline{P_{t,ref}}\right)^2 + \left(\frac{\partial M}{\partial \overline{P_{s,ref}}}\partial \overline{P_{s,ref}}\right)^2 + \left(\frac{\partial M}{\partial \overline{P_{t,plenum}}}\partial \overline{P_{t,plenum}}\right)^2} \quad (111)$$

$$\frac{\partial M}{\partial P_{t,plenum}} = \frac{1}{2}\frac{1}{\overline{P_{t,ref}}-\overline{P_{s,ref}}}\left(\frac{\overline{P_{t,plenum}}-\overline{P_{s,ref}}}{\overline{P_{t,ref}}-\overline{P_{s,ref}}}\right)^{-\frac{1}{2}} = \frac{1}{2}\frac{1}{\sqrt{(\overline{P_{t,ref}}-\overline{P_{s,ref}})(\overline{P_{t,plenum}}-\overline{P_{s,ref}})}} \quad (112)$$

$$\frac{\partial M}{\partial \overline{P_{s,ref}}} = \frac{1}{2}\frac{(\overline{P_{t,plenum}}-\overline{P_{s,ref}})^{1/2}}{(\overline{P_{t,ref}}-\overline{P_{s,ref}})^{3/2}} - \frac{1}{2}\frac{1}{(\overline{P_{t,plenum}}-\overline{P_{s,ref}})^{1/2}(\overline{P_{t,ref}}-\overline{P_{s,ref}})^{1/2}} \quad (113)$$

$$\frac{\partial M}{\partial \overline{P_{t,ref}}} = -\frac{1}{2}\frac{(\overline{P_{t,plenum}}-\overline{P_{s,ref}})^{\frac{1}{2}}}{(\overline{P_{t,ref}}-\overline{P_{s,ref}})^{\frac{3}{2}}} \quad (114)$$

$\overline{P_{plenum}} = 19.91Pa$

$\partial \overline{P_{plenum}} = \pm 2.8Pa$

The overall uncertainty of the nominal film-cooling inlet blowing ratio of 1.32 was:

$$\partial M = \pm 0.001$$

$$\partial M\% = 0.8\%$$

B.2.6 Film-cooling flow rate

The uncertainty of the film-cooling flow rate was calculated as follows:

$$\dot{m}_{cooling} = \rho C_d\left(\frac{\pi}{4}D_{orifice}^2\right)\sqrt{\frac{2\Delta P_{orifice}}{\rho\left(1-\beta^4\right)}} \quad (115)$$

$$\partial \dot{m}_{cooling} = \sqrt{\left(\frac{\partial \dot{m}_{cooling}}{\partial \Delta P_{orifice}}\partial \Delta P_{orifice}\right)^2} \quad (116)$$

$$\frac{\partial \dot{m}_{cooling}}{\partial \Delta P_{orifice}} = \frac{C_d\left(\frac{\pi}{4}D_{orifice}^2\right)}{\left(1-\beta^4\right)\sqrt{\frac{2\Delta P_{orifice}}{\rho\left(1-\beta^4\right)}}} \quad (117)$$

$\overline{\Delta P_{orifice}} = 102Pa$

$\partial \Delta P_{orifice} = \pm 2.4Pa$

The overall uncertainty of the nominal film-cooling flow ratio of 0.01 kg/s was:

$\partial \dot{m}_{cooling} = \pm 0.0001$ kg/s

$\partial \dot{m}_{cooling}\,\% = 1.22\%$

B.2.7 Non-dimensional temperature

The uncertainty of the non-dimensional temperature was calculated in the *third* plane as follows:

$$\boldsymbol{\theta} = \frac{\overline{T_{local}} - \overline{T_{plenum}}}{\overline{T_{ref}} - \overline{T_{plenum}}} \tag{118}$$

$$\partial\theta = \sqrt{\left(\frac{\partial\theta}{\partial\overline{T_{ref}}}\partial\overline{T_{ref}}\right)^2 + \left(\frac{\partial\theta}{\partial\overline{T_{plenum}}}\partial\overline{T_{plenum}}\right)^2 + \left(\frac{\partial\theta}{\partial\overline{T_{local}}}\partial\overline{T_{local}}\right)^2} \tag{119}$$

$$\frac{\partial\boldsymbol{\theta}}{\partial\overline{T_{plenum}}} = -\frac{\overline{T_{ref}} - \overline{T_{local}}}{\left(\overline{T_{plenum}} - \overline{T_{ref}}\right)^2} \tag{120}$$

$$\frac{\partial\boldsymbol{\theta}}{\partial\overline{T_{ref}}} = \frac{\overline{T_{plenum}} - \overline{T_{local}}}{\left(\overline{T_{ref}} - \overline{T_{plenum}}\right)^2} \tag{121}$$

$$\frac{\partial\boldsymbol{\theta}}{\partial\overline{T_{local}}} = \frac{1}{\overline{T_{ref}} - \overline{T_{plenum}}} \tag{122}$$

The overall uncertainty of the nominal non-dimensional temperature, in three regions at the endwall, at the suction-side and mid-span, was given in ***Table 16*** at a minimum and maximum θ.

APPENDIX C: SUPPLEMENTARY RESULTS

This section serves as an additional representation of the experimental results which are not discussed in Chapter 6. Hence, these results are not discussed but are presented here for completeness to the reader.

C.1 Discharge coefficient

Figure C 1 shows the discharge coefficient variation in the function of the blowing ratio for the two types of cooling holes obtained in a different test facility used by Dlamini [64].

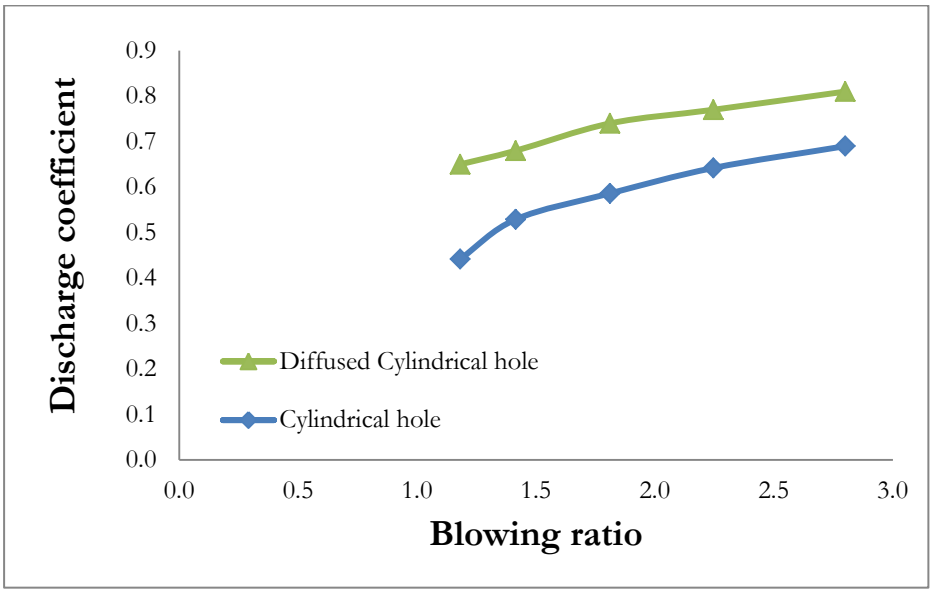

Figure C 1: *Discharge coefficient results with M varying for the cylindrical hole and diffused cylindrical hole at zero compound angle.*

At all blowing ratio the discharge coefficient of the diffused cylindrical hole is about 12% higher than the cylindrical hole.

C.2 Pitch angle contours

The pitch angles together with the yaw angles provide a measure of the direction of the secondary flow. For completeness the pitch angle contours for most configurations in the third plane are plotted from ***Figure C 2*** to ***Figure C 7*** , where positive x is out of the paper. The positive pitch angle indicates that the flow is directed away from the endwall while the negative pitch angles indicate that the flow is directed towards the endwall. On the SS, the large local positive pitch angle indicates the vertical velocity component associated with the passage vortex that skews the streamwise velocity.

In ***Figure C 2*** the baseline case has the highest pitch angles. The fillets reduced the passage vortex. By increasing the blowing ratio in the cooling configurations from ***Figure C 3*** to ***Figure C 7***, the interaction of the coolant with the boundary layer becomes more intense and the flow structure change significantly on the endwall.

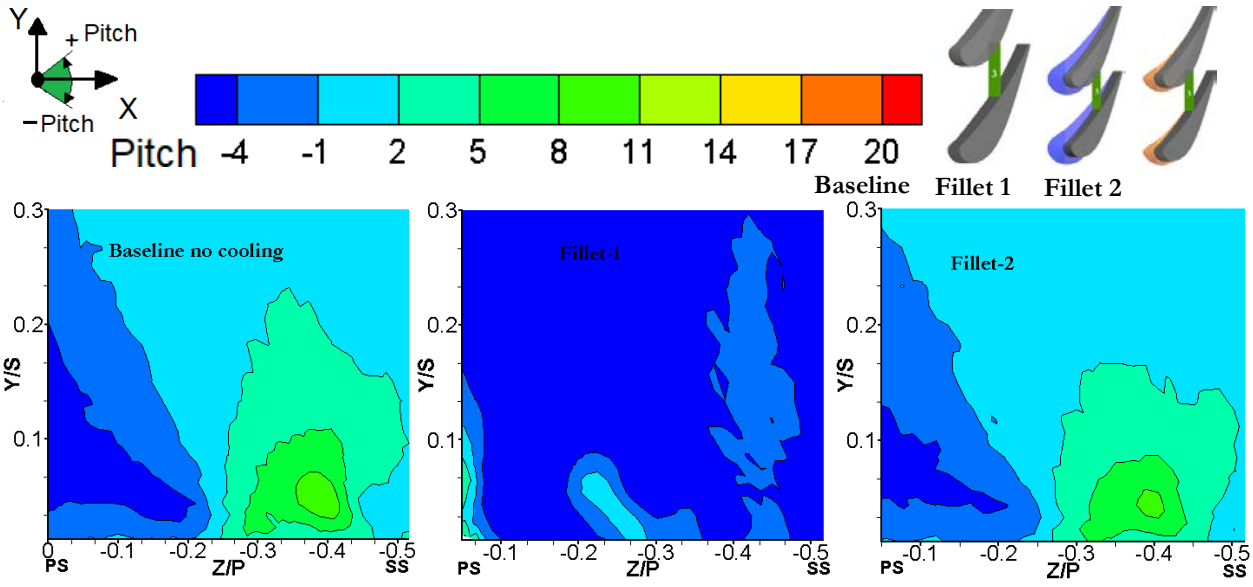

Figure C 2: Distributions of pitch angle in third plane for cases: Baseline, Fillet 1 and Fillet 2.

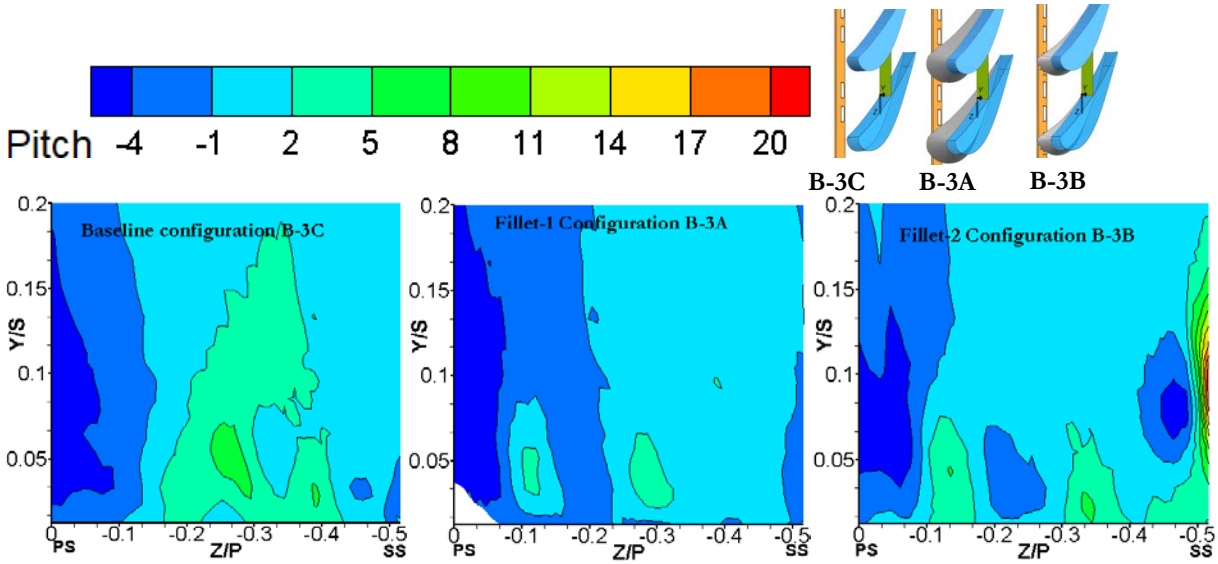

Figure C 3: Distributions of pitch angle in third plane for cases: Baseline Case 3-C, Fillet 1 Case B-3A and Fillet 2 Case B-3B at M=1.4.

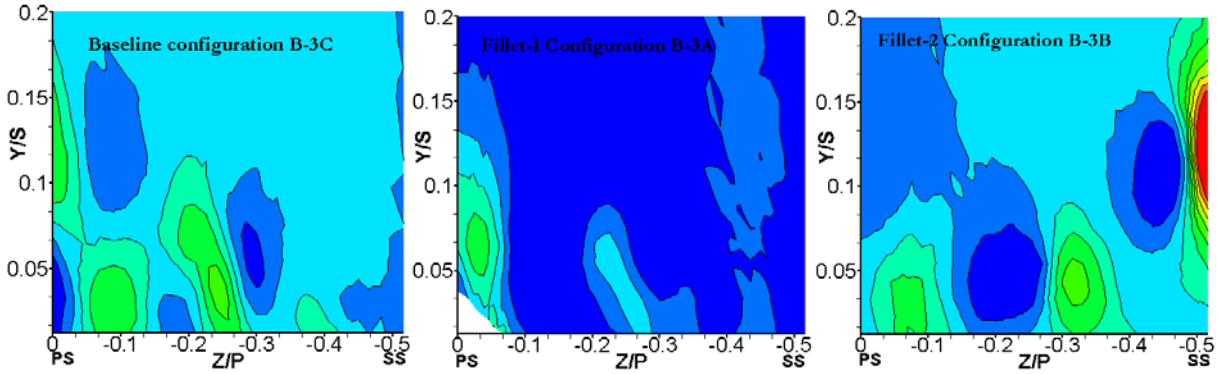

Figure C 4: Distributions of pitch angle in third plane for cases: Baseline Case 3-C, Fillet -1 Case B-3A and Fillet 2 Case B-3B at M=2.2.

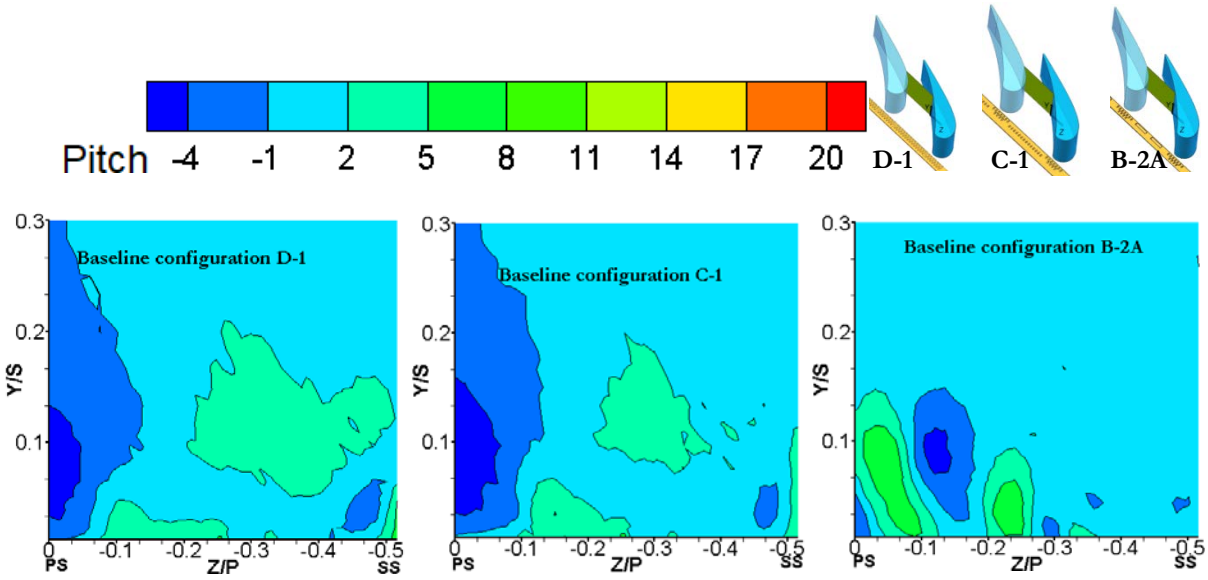

Figure C 5: *Distributions of pitch angle in third plane for cases: Baseline Case D-1, Baseline Case C-1and Baseline Case B-2A at M=2.2.*

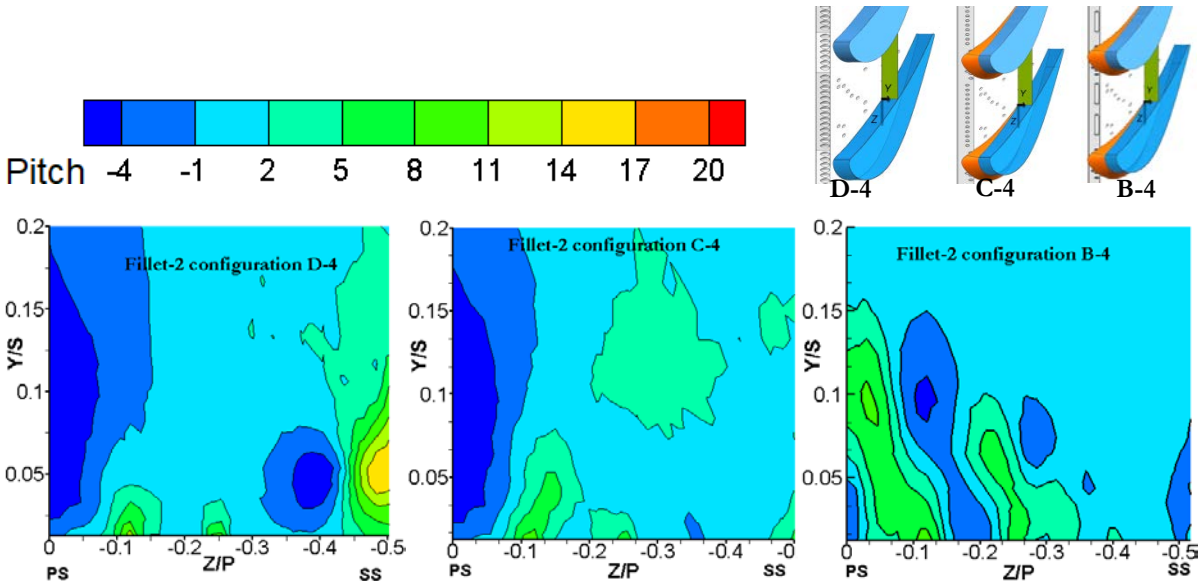

Figure C 6: *Distributions of pitch angle in third plane for cases: Fillet 2 Case D-4, Fillet 2 Case C-4and Fillet 2 Case B-2A at M=2.2.*

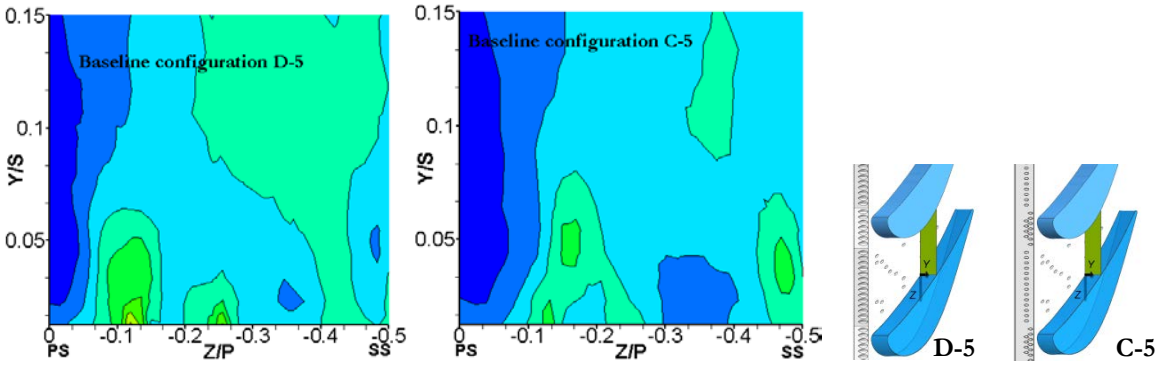

Figure C 7: *Distributions of pitch angle in third plane for cases: Baseline Case D-5 and Baseline Case C-5 at M=2.2.*

C.3 Total pressure coefficient contours

Figure C 8 shows the total pressure coefficient contours in the third plane for case B-2A and B-2B. In case B-2B, the effect of closing the LE edge holes, where the Fillet 2 rested, is to increase the total pressure coefficient towards the SS.

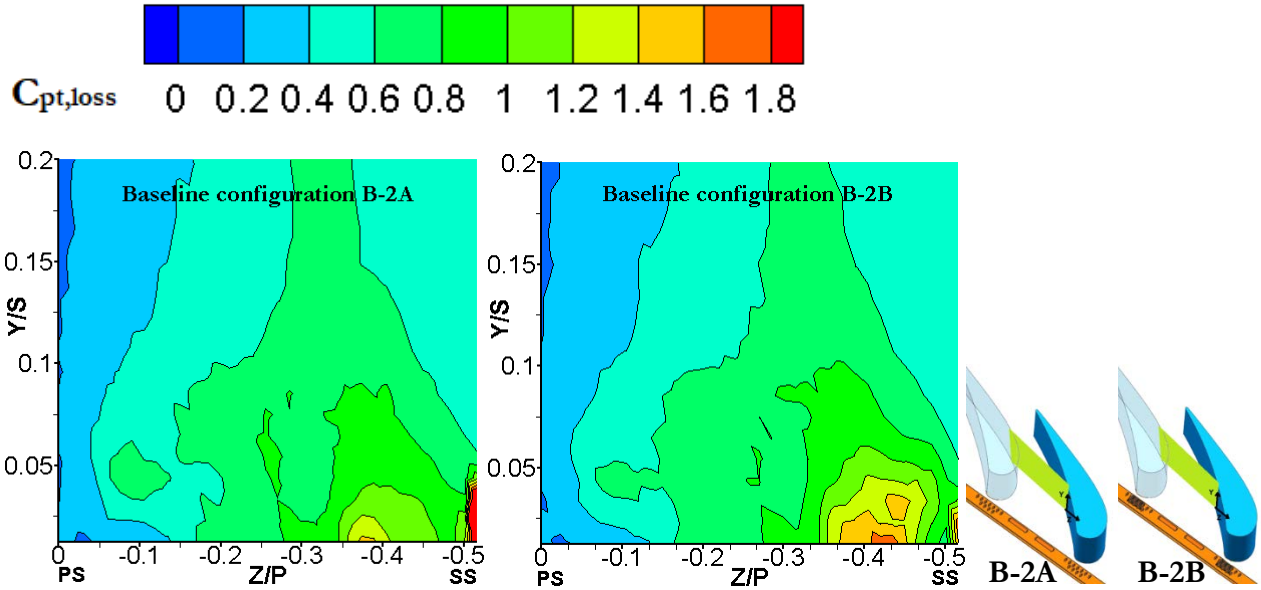

Figure C 8: *Distributions of total pressure loss coefficient, $C_{pt,\,loss}$ in third plane for cases: two bleed cooling slots and cylindrical holes (B-2A) and two bleed cooling slots and cylindrical holes partially closed (B-2B) at M=1.4.*

Figure C 9, ***Figure C 10*** and ***Figure C 11*** show the baseline configurations B-2A, C-1, D-1, and E without fillet at the exit plane. The LE edge cooling configuration of slots and holes seems to provide less loss when compared to other baseline cooling configurations. The passage vortex core is, at given blow ratio, weaker and the boundary layer mixing losses are reduced. The LE cylindrical holes display boundary layer mixing losses all along the endwall.

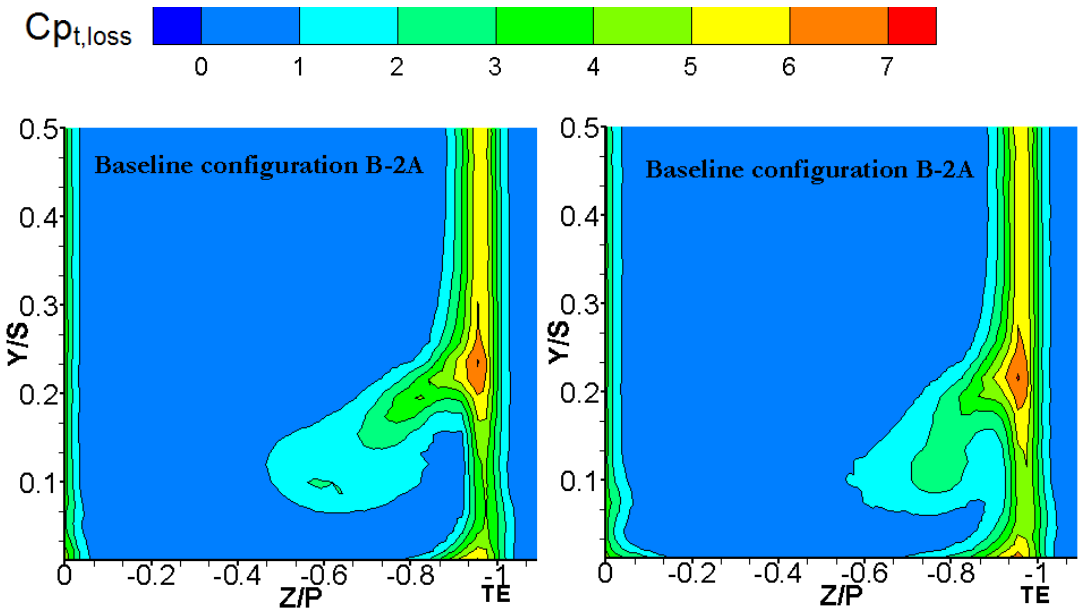

Figure C 9: *Total pressure loss coefficient, $C_{pt,\,loss}$ in exit plane for Case B-2A at a) M=1.4, b) M=2.2.*

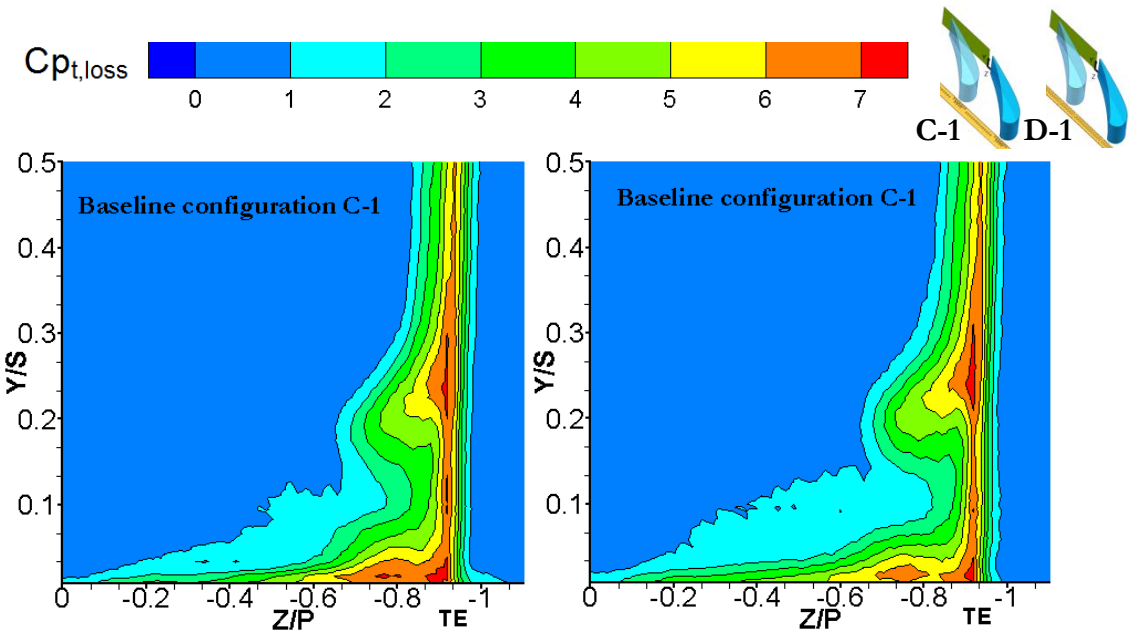

Figure C 10: Total pressure loss coefficient, $C_{pt,\,loss}$ in exit plane for Case C-1at a) M=1.4, b) M=2.2.

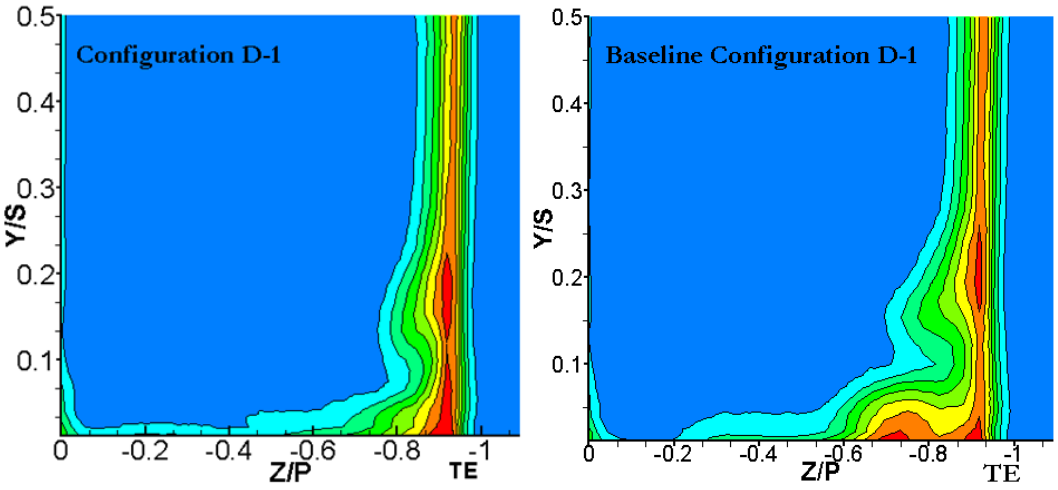

Figure C 11: Total pressure loss coefficient, $C_{pt,\,loss}$ in exit plane for Case D-1at M=1.4, b) M=2.2.

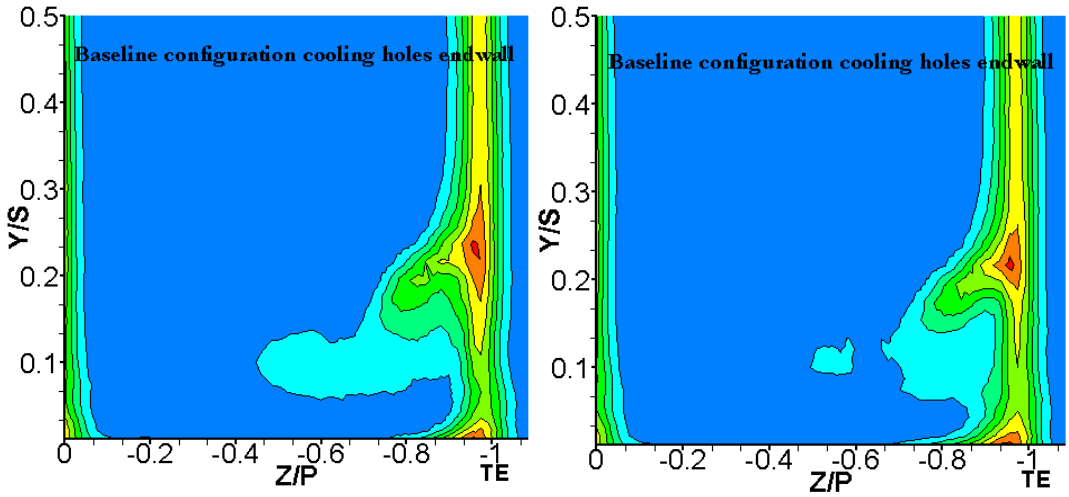

Figure C 12: Total pressure loss coefficient, $C_{pt,\,loss}$ in exit plane for Case E at M=1.4, b) M=2.2.

The filleted cooling configuration B-3B was tested in the exit plane, shown in ***Figure C 13*** and D-1 with Fillet 2, shown in ***Figure C 14***.

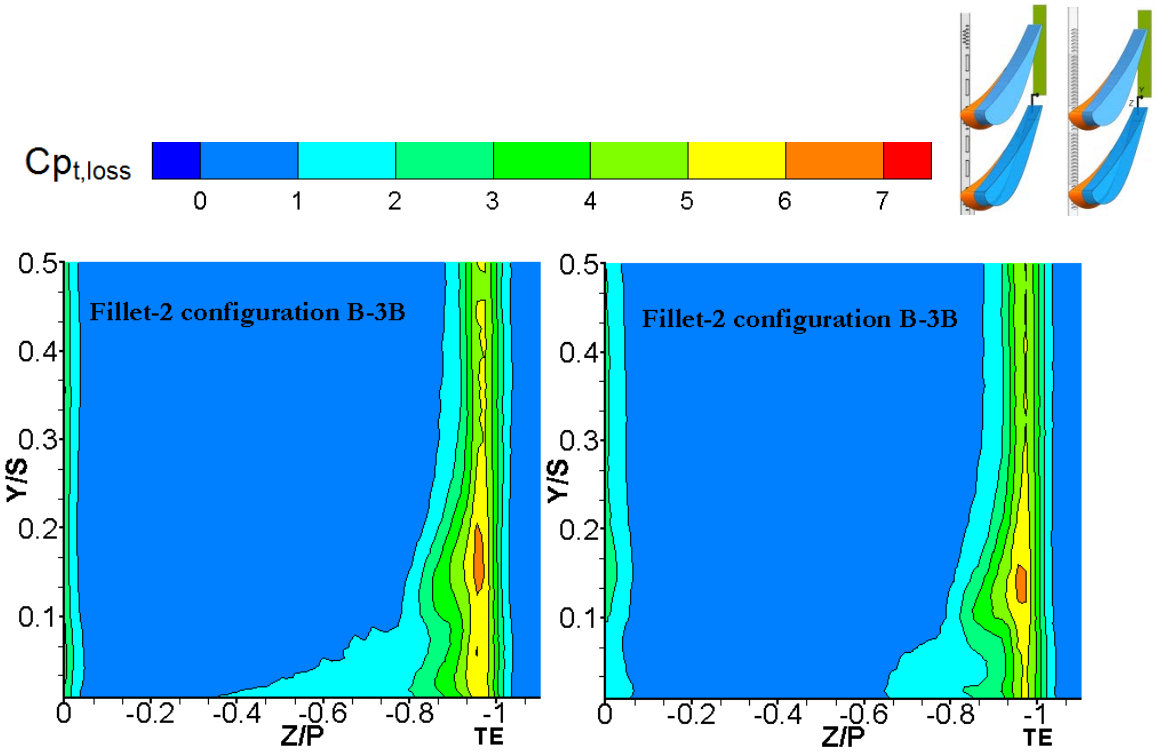

Figure C 13: *Total pressure loss coefficient, $C_{pt,\,loss}$ in exit plane for Case B-3B with Fillet-2, a) M=1.4, b) M=2.2.*

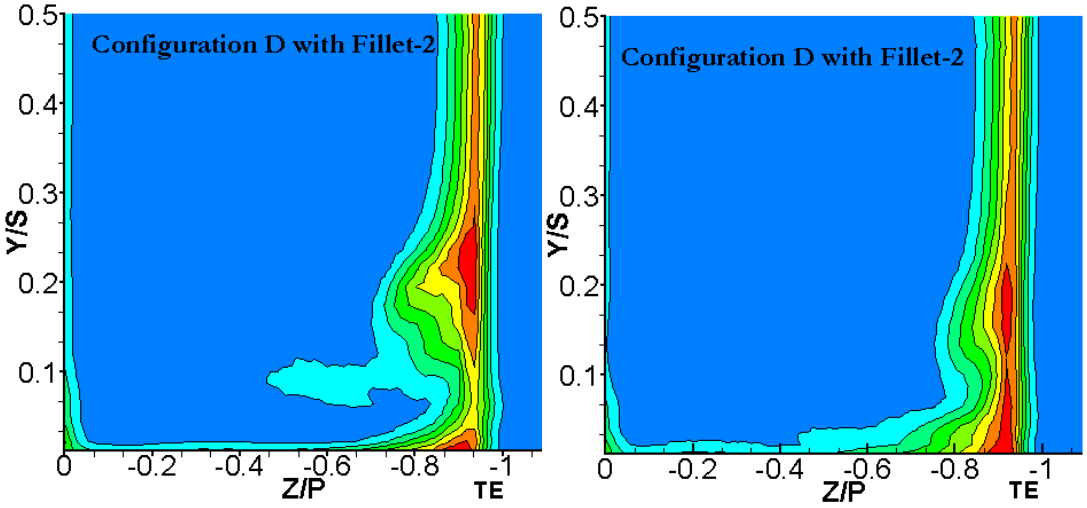

Figure C 14: *Total pressure loss coefficient, $C_{pt,\,loss}$ in exit plane for Case D-1 with Fillet-2, a) M=1.4, b) M=2.2.*

As has been seen for the baseline case, ***Figure 9*** and ***Figure 11***, the passage vortex core is smaller for the LE slots and holes configuration than the LE cylindrical diffused holes. When compared to the baseline cases, the fillet seems to decrease the passage vortex in both configurations B-3B and D-1 with the Fillet-2.